Journal Information

Maejo International Journal of Science and Technology (ISSN 1905-7873 © 2015), the international journal for preliminary communications in Science and Technology is the first peer-refereed scientific journal of Maejo University (www.mju.ac.th). Intended as a medium for communication, discussion, and rapid dissemination of important issues in Science and Technology, articles are published online in an open access format, which thereby gives authors the chance to communicate with a wide range of readers in an international community.

Publication Information

MIJST is published triannually. Articles are available online and can be accessed free of charge at http://www.mijst.mju.ac.th. Printed and bound copies of each volume are produced and distributed to selected groups or individuals.

Abstracting/Indexing Information

MIJST is covered and cited by Science Citation Index Expanded, SCOPUS, Journal Citation Reports/Science Edition, Zoological Record, Directory of Open Access Journals (DOAJ), CAB Abstracts, ProQuest, Google Scholar and EBSCO.

Contact Information

Editorial office: Maejo International Journal of Science and Technology (MIJST), 1st floor, Orchid Building, Maejo University, San Sai, Chiang Mai 50290, Thailand

Tel: +66-53-87-3880; Fax: +66-53-49-8133
E-mail: duang@mju.ac.th

MAEJO INTERNATIONAL JOURNAL OF SCIENCE AND TECHNOLOGY

MAEJO INTERNATIONAL JOURNAL OF SCIENCE AND TECHNOLOGY

The International Journal for the Publication of Preliminary Communications in Science and Technology

http://www.mijst.mju.ac.th
ISSN 1905-7873

MAEJO INTERNATIONAL JOURNAL
OF SCIENCE AND TECHNOLOGY

Volume 9, Issue 1 (January – April 2015)

CONTENTS

http://www.mijst.mju.ac.th
ISSN 1905-7873

http://www.mijst.mju.ac.th
ISSN 1905-7873

MAEJO INTERNATIONAL JOURNAL
OF SCIENCE AND TECHNOLOGY

Volume 9, Issue 1 (January – April 2015)

Author Index

Instructions for Authors

A proper introductory e-mail page containing the title of the submitted article and certifying its originality should be sent to the editor (Duang Buddhasukh, e-mail: duang@mju.ac.th). The manuscript proper together with a list of suggested referees should be attached in separate files. The list should contain at least 5 referees with appropriate expertise. Three referees should be non-native from 3 different countries. Each referee's academic/professional position, scientific expertise, affiliation and e-mail address must be given. The referees should not be affiliated to the same university/institution as any of the authors, nor should any two referees come from the same university/institution. The editorial team, however, retain the sole right to decide whether or not the suggested referees are approached.

Failure to conform to the above instructions will result in non-consideration of the submission.

Please also ensure that English and style is properly edited before submission. UK style of spelling should be used. Authors who would like to consult a professional service can visit www.editage.com/?ref=referral, www.bioedit.co.uk (bioscience and medical papers), www.scribendi.com, www.letpub.com, www.papersconsulting.com, www.stickleredit ing.com, Cambridge Proofreading (http://proofreading.org/), www.ProofreadingServices.com, www.horizonproofreading.org, Help.Plagtracker, www.ninjaessays.com/editing/, http://bid4papers.com/editing-services.html, www.enago.com, www.medsciediting.com, www.manuscriptedit.com, http://www.proofreadmyfile.com, ProofreadMyDocument, www.24x7editing.com, www.tulyasys.com, ww.regentediting.co.uk or www.editnpublish.com.

Important : Manuscript with substandard English and style will not be considered.

Warning : Plagiarism (including self-plagiarism) may be checked for at *the last* stage of processing and, if detected, will result in a rejection and blacklisting.

Manuscript Preparation

Manuscripts must be prepared in English using a word processor. MS Word for Macintosh or Windows, and .doc or .rtf files are preferred. Manuscripts may be prepared with other software provided that the full document (with figures, schemes and tables inserted into the text) is exported to a MS Word format for submission. Times or Times New Roman font is preferred. The font size should be 12 pt and the line spacing 'at least 17 pt'. A4 paper size is used and margins must be 1.5 cm on top, 2.0 cm at the bottom and 2.0 cm on both left and right sides of the paper. Although our final output is in .pdf format, authors are asked NOT to send manuscripts in this format as editing them is much more complicated. Under the above settings, a manuscript submitted should not be longer than **15 pages** for a full paper or **20 pages** for a review paper.

A template file may be downloaded from the *Maejo Int. J. Sci. Technol.* homepage. (DOWNLOAD HERE)

Authors' full mailing addresses, homepage addresses, phone and fax numbers, and e-mail addresses homepages can be included in the title page and these will be published in the manuscripts and the Table of Contents. The corresponding author should be clearly identified. It is the corresponding author's responsibility to ensure that all co-authors are aware of and approve of the contents of a submitted manuscript.

A brief (200 word maximum) Abstract should be provided. The use in the Abstract of numbers to identify compounds should be avoided unless these compounds are also identified by names.

A list of three to five keywords must be given and placed after the Abstract. Keywords may be single words or very short phrases.

Although variations in accord with contents of a manuscript are permissible, in general all papers should have the following sections: Introduction, Materials and Methods, Results and Discussion, Conclusions, Acknowledgments (if applicable) and References.

Authors are encouraged to prepare Figures and Schemes in colour. Full colour graphics will be published free of charge.

Tables and Figures should be inserted into the main text, and numbers and titles supplied for all Tables and Figures. All table columns should have an explanatory heading. To facilitate layout of large tables, smaller fonts may be used, but in no case should these be less than 10 pt in size. Authors should use the Table option of MS Word to create tables, rather than tabs, as tab-delimited columns are often difficult to format in .pdf for final output.

Figures, tables and schemes should also be placed in numerical order in the appropriate place within the main text. Numbers, titles and legends should be provided for all tables, schemes and figures. Chemical structures and reaction schemes should be drawn using an appropriate software package designed for this purpose. As a guideline, these should be drawn to a scale such that all the details and text are clearly legible when placed in the manuscript (i.e. text should be no smaller than 8-9 pt).

For bibliographic citations, the reference numbers should be placed in square brackets, i.e. [ ], and placed before the punctuation, for example [4] or [1-3], and all the references should be listed separately and as the last section at the end of the manuscript.

Format for References

Journal :

1. D. Buddhasukh, J. R. Cannon, B. W. Metcalf and A. J. Power, "Synthesis of 5-n-alkylresorcinol dimethyl ethers and related compounds *via* substituted thiophens", *Aust. J. Chem.*, **1971**, *24*, 2655-2664.

Text :

2. A. I. Vogel, "A Textbook of Practical Organic Chemistry", 3rd Edn., Longmans, London, **1956,** pp. 130-132.

Chapter in an edited text :

3. W. Leistritz, "Methods of bacterial reduction in spices", in "Spices: Flavor Chemistry and Antioxidant Porperties" (Ed. S. J. Risch and C-T. Ito), American Chemical Society, Washington, DC, **1997**, Ch. 2.

Thesis / Dissertation :

4. W. phutdhawong, "Isolation of glycosides by electrolytic decolourisation and synthesis of pentinomycin", *PhD Thesis*, **2002**, Chiang Mai University, Thailand.

Patent :

5. K. Miwa, S. Maeda and Y. Murata, "Purification of stevioside by electrolysis", *Jpn. Kokai Tokkyo Koho 79 89,066* (**1979**).

Proceedings :

6. P. M. Sears, J. Peele, M. Lassauzet and P. Blackburn, "Use of antimicrobial proteins in the treatment of bovine mastitis", Proceedings of the 3rd International Mastitis Seminars, **1995**, Tel-Aviv, Israel, pp. 17-18.

Websites :

7. S. Simon, "What is an odds ratio?", **2008**, http://www.childrensmercy.org/stats/definitions/or.htm (Accessed: October 2011).

Manuscript Revision Time

Authors who are instructed to revise their manuscript should do so within **45** days. Otherwise the revised manuscript will be regarded as a new submission.

Manuscript Processing Time

As a result of a large number of submissions, there may be a long delay in the evaluation or publication of a paer. A duration of at least 6-8 mouths between submission and acceptance (or rejection) can normally be expected.

Maejo International Journal of Science and Technology

ISSN 1905-7873
Available online at www.mijst.mju.ac.th

EDITORIAL

Act of Evil

E. F. Shumacher once remarked in one of his famous books to the effect that people were sometimes willing to die economically rather than go on living uneconomically, meaning that even though they knew something was bad for them, yet they went on doing it for economic reason. That, however, was a noble act compared to what is happening today. More and more people now seem to believe in living economically, even though in doing so others may die or suffer.

An example of this happened recently in Chacheungsao, an agricultural province near Bangkok. In an attempt to save cost, a liquid chemical waste was sneakily siphoned into a communal pond and rice paddies, permanently fouling both the paddies and the source of clean water for a community, rendering it cursed with hardships thereafter. In another incidence, another kind of industrial effluent was pumped directly from the trucks into a city underground drain, unknown to the police at first of course.

This sort of evil act nowadays seems to become more common in this country, especially in those provinces in the vicinity of an industrial estate. However, the practice is not limited locally to within a country like Thailand or other countries of similar rank. As is well known, a few so-called 'developed' nations have actually done it before. However, since they know better, they commit a badder sin by trying to get rid of their wastes anywhere in the world except in their own homes.

The Buddha taught us 2600 years ago to do three things: do good, avoid doing evil, and try to purify your mind. The people in his time seemed to fully believe in him and act accordingly. Even a hundred-odd years ago, people still seemed to believe in him. The steady decline of our faith in him seemed to uncannily coincide with the entering of modern science and technology into the world. Could this be just coincidence? Or could one thing be the cause of the other?

When you are angered by someone or something, are they to blame for your anger? When you have lustful thoughts, do you blame the sexual objects? And when you are possessed by greed, where does the greed come from? —"Show me the clues to these puzzles, and I'll show you the answers to the above questions."

Maejo Int. J. Sci. Technol. **2015**, *9*(01), 1-9; doi: 10.14456/mijst.2015.1

Maejo International Journal of Science and Technology

ISSN 1905-7873
Available online at www.mijst.mju.ac.th

Full Paper

Simple unstable baseline detection methods for perpendicular magnetic recording

Piya Kovintavewat [1,*], Santi Koonkarnkhai [1] and Aimamorn Suvichakorn [2]

[1] Data Storage Technology Research Centre, Nakhon Pathom Rajabhat University, Nakhon Pathom, Thailand

[2] Department of Advanced Channel Failure Analysis, Western Digital (Thailand) Company Ltd., Phra Nakhon Si Ayutthaya, Thailand

* Corresponding author, e-mail: piya@npru.ac.th

Received: 12 March 2013 / Accepted: 13 January 2015 / Published: 16 January 2015

Abstract: Current hard disk drives employ a magneto-resistive head to read and write data. During the reading process, if the magneto-resistive head is unstable or has some defects, the readback signal will experience some missing data zones known as an unstable baseline (UB) event, which causes the signal amplitude to drop drastically and vary around the baseline at 0 volt. Thus, such defective heads must be detected and taken care of during the testing process before assembling a hard disk drive. This paper proposes three simple methods to detect the UB event that can be employed in the testing process when the data have a specific pattern, i.e. 4*T*-pattern, where *T* is the bit period. The proposed methods can also be utilised to detect the UB event during normal operation when the data are random. Simulation results indicate that the methods can detect the short UB event (4-bit duration) with 4*T*-pattern data and the 25-bit UB event with random data at 100% of detection.

Keywords: head instability, magneto-resistive head, perpendicular magnetic recording, unstable baseline

INTRODUCTION

In perpendicular magnetic recording systems, when the magneto-resistive read head senses the change in a magnetic flux via the transition of the magnetisation pattern, an induced voltage pulse called a transition pulse is produced. Then a read channel transforms this induced voltage pulse into the output response known as a readback signal. If the magneto-resistive read head has some defects that come from the manufacturing process or are caused by electrostatic discharge effects, the quality of the readback signal will be poor, thus making a detector unable to decode data

correctly. This problem is usually referred to as head instability, which yields several impacts in the hard disk drive (HDD), e.g. baseline popping (BLP), writer-induced instability, permanent magnet reversal instability, spiking noise, random telegraph noise and amplitude asymmetry of a signal [1-6]. Thus, it is apparent that the head instability can degrade the system performance significantly.

Generally, the head instability resulting from an electrostatic discharge effect primarily yields two disturbances, viz. an amplitude spike caused by some defects inside the head [4, 7] and an unstable baseline (UB) caused by dielectric breakdown in the head [8, 9]. This paper focuses only on the UB problem, which causes the amplitude of the readback signal to drop dramatically and vary around 0 volt for many bit periods, as illustrated in Figure 1. Note that the UB event in fact occurs randomly throughout the magnetic medium because it is caused by the read head. Specifically, the UB event will not always occur at the same location on the medium. In practice, the UB event can cause an error burst in the data detection process, which can easily exceed the correction capability of an error-correction code and thus result in a sector read failure and degrade the disk drive reliability. It is inevitable that the UB effect becomes worse as the recording density increases. Consequently, the UB detection method is essential in the testing process before assembling the HDDs in a clean room.

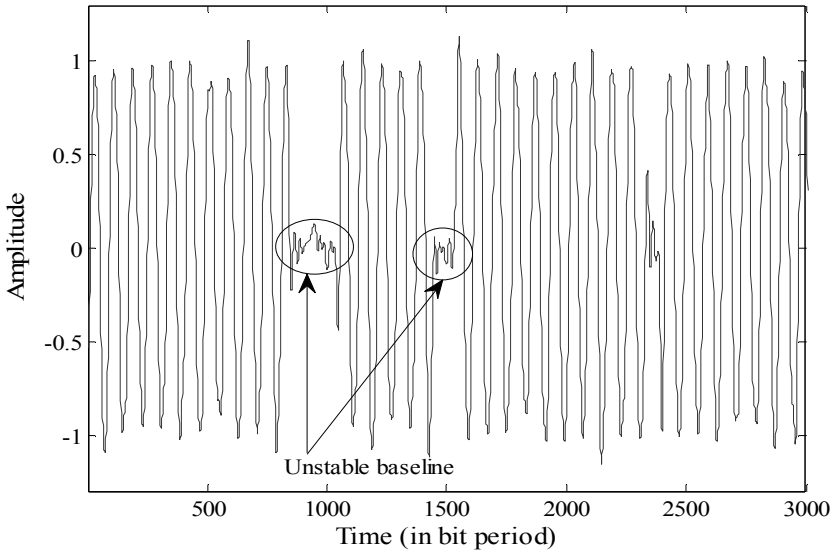

Figure 1. The UB-affected readback signal at SNR = 28 dB

To test whether the read head is stable, a square-wave signal of 2*T* or 4*T* pattern (*T* = bit period) depending on the write frequency and recording capacity, which corresponds to the binary sequence of [0 0 ... 1 1 0 0 1 1 ... 0 0] or [0 0 0 0 ... 1 1 1 1 0 0 0 0 1 1 1 1 ... 0 0 0 0] respectively, is written into the medium. Note that current high-density HDDs employ a 4*T* pattern signal to test the performance of the read head. Then the read head reads these specific data and sends the readback signal to a testing engineer to check if it looks normal or not. If the amplitude in some portions of the readback signal suddenly drops and varies around 0 volt for several bit periods, the read head is declared unstable. In other words, the read head contains the UB event. When this occurs, that read head will be discarded from the manufacturing process. Therefore, an efficient UB detection method is necessary for the testing process to ensure that all commercial HDDs do not have any defective read head inside.

Sometimes the read head may start having some defects after a customer uses the HDD for a while. When this happens, the read head starts to malfunction and thus creates some UB events in the readback signal. This problem is unwanted because it renders the customer unable to retrieve some important data from the HDD. Again, an efficient UB detection method is needed in this case because if we can detect the UB event and it is not too severe, we might be able to recover the data by re-reading the data sector or forcing the iterative decoding to increase the number of error-correction iterations.

Several studies related to the detection and the root cause of head instability have appeared in the literature. For example, Chen et al. [1] investigated the types of head instability in perpendicular magnetic recording, which include BLP, writer-induced instability, permanent magnet reversal instability, spiking noise and random telegraph noise. Yang [4] presented a method to restore the head stability by automatically applying a bias shock current to the head according to the information received from a thermal asperity detection method. Zafer [5] introduced a method to detect BLP during servo reads by passing the readback signal through a digital filter and then computing the absolute value of the resulting signal before feeding it to a threshold detector. Song and Madden [6] presented a technique to correct the BLP event in the readback signal during acquisition mode. Li et al. [8] proposed the employment of a track average amplitude technique and a threshold detector to detect both the BLP and the UB. Finally, Du [9] introduced a method to detect the UB and the baseline shift in the readback signal by using an adjustable filter, which is placed between a pre-amplifier circuit and a servo circuit.

In this paper we propose three simple methods to detect the UB event caused by an unstable read head that loses an insulator state. Specifically, this type of read head will cause the amplitude of the readback signal to drop considerably and fluctuate around 0 volt for many bit periods. Also, we suggest some possible solutions to solve the UB problem in perpendicular magnetic recording systems.

CHANNEL MODEL

To investigate the performance of the proposed UB detection methods, we use the simulated signal generated from a channel model shown in Figure 2. A data input sequence $a_k \in \{-1, 1\}$ with bit period T is filtered by an ideal differentiator $(1-D)/2$, where D is the unit delay operator, to form a transition sequence $d_k \in \{-1, 0, 1\}$, when $d_k = \pm 1$ corresponds to a positive or a negative transition, and $d_k = 0$ corresponds to the absence of a transition. Hence the transition sequence d_k passes through a magnetic recording channel represented by $g(t)$. The transition response $g(t)$ for perpendicular recording is given [10] by:

$$g(t) = \mathrm{erf}\left(\frac{2t\sqrt{\ln 2}}{\mathrm{PW}_{50}}\right) \tag{1}$$

where erf(.) is an error function and PW_{50} determines the width of the derivation of $g(t)$ at half of its maximum. In the context of magnetic recording, a normalised recording density is defined as $\mathrm{ND} = \mathrm{PW}_{50}/T$.

The UB-affected readback signal, $y(t)$, can be expressed as:

$$y(t) = \sum_k d_k g(t - kT) + n(t) + u(t) \tag{2}$$

where $n(t)$ is additive white Gaussian noise with two-side power spectral density $N_0/2$, and $u(t)$ represents the UB signal. Specifically, to simulate the signal $y(t)$, we assume that there is no

transition (i.e. $d_k = 0$ for many bit periods kT's) during the UB event. Then the UB-affected readback signal $y(t)$ is filtered by a seventh-order Butterworth lowpass filter and is sampled at time kT, assuming perfect synchronisation. Here, the sampler output y_k is sent to the UB detection block to determine if the readback $y(t)$ contains the UB event, where Z in Figure 2 is a UB indicator such that $Z = 1$ means the presence of UB and $Z = 0$ means its absence. Then the sequence x_k is further processed by an equaliser and the Viterbi detector [11] to output the most likely input sequence a_k.

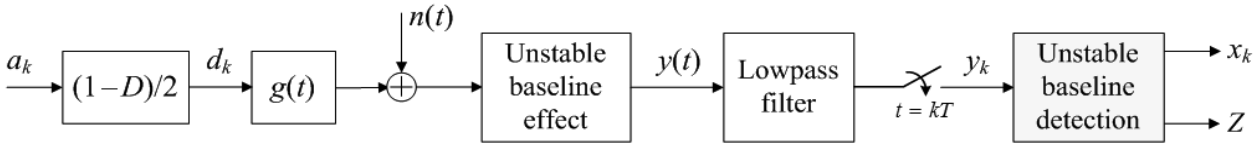

Figure 2. A perpendicular recording channel model with UB effect

UNSTABLE BASELINE DETECTION ALGORITHMS

Based on an averaging filter and the sequence $\{y_k\}$, three simple methods are proposed to detect the UB event. Each can be explained as follows.

Method 1

This method makes use of an envelope detector, as demonstrated in Figure 3. The received sequence $\{y_k\}$ is sent to the envelope detector, which attempts to detect the envelope of $\{y_k\}$, to obtain a sequence $\{p_k\}$. Note that the sequence $\{p_k\}$ comprises two components, namely an upper enveloped signal u_k and a lower enveloped signal l_k, as depicted in Figure 4.

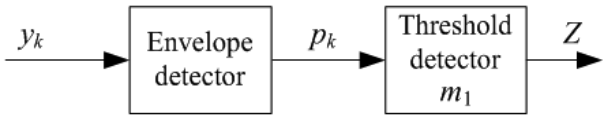

Figure 3. Method 1 for UB detection

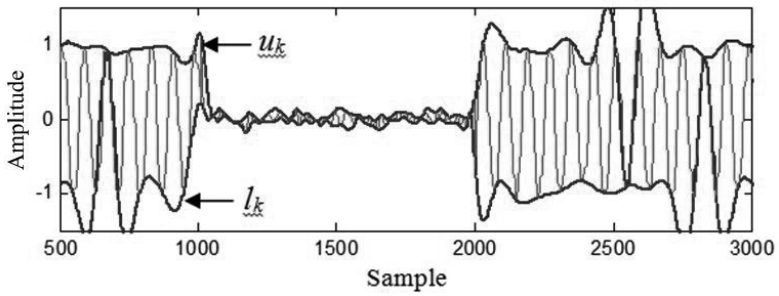

Figure 4. The upper (u_k) and lower (l_k) enveloped signals for Method 1

To detect the UB event, the signals u_k and l_k are used to compare with the threshold value m_1. Specifically, the UB is detected if there exists the signal at time kT that results in $u_k < m_1$ and $| l_k | < m_1$, where $| l_k |$ is the absolute value of l_k. This method is simple but it is sensitive to the

amplitude fluctuation. Therefore, the method is in practice good for a 4*T*-patterned signal, not a random signal (or an actual user data).

Method 2

The second UB detection method is displayed in Figure 5. Here, the sequence $\{y_k\}$ is first passed through an absolute operator to obtain a signal $r_k = | y_k |$. Then the signal r_k is sent to an averaging filter with a window length of L samples to obtain the signal q_k [12] according to:

$$q_k = \frac{1}{L}\sum_{i=k-\beta}^{k+\beta} r_i \tag{3}$$

where $\beta = (L-1)/2$. Similarly, to detect the UB, the signal q_k is compared with the threshold value m_2. Specifically, the UB is detected if $q_k < m_2$. Figure 6 illustrates an example of the signals obtained from Method 2. In general, this method is more robust to signal fluctuation than Method 1 and also has low complexity.

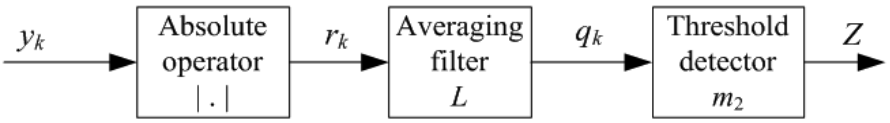

Figure 5. Method 2 for UB detection

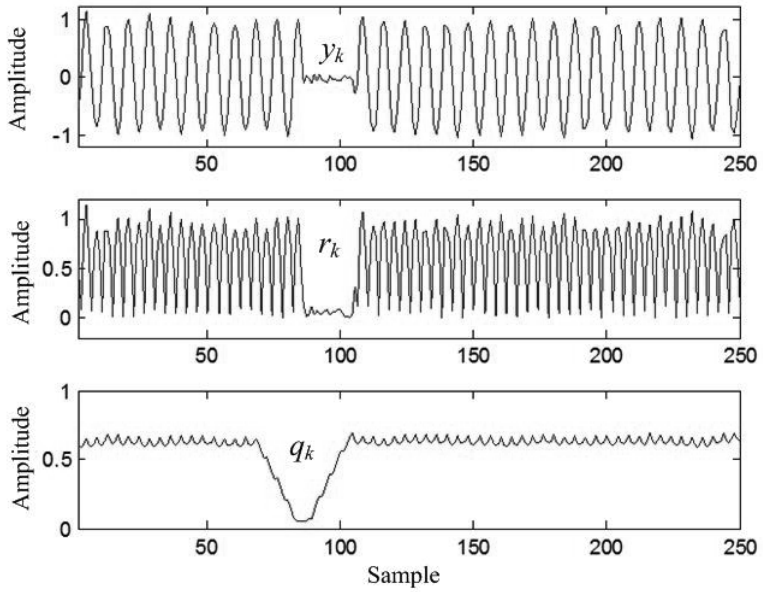

Figure 6. Example of signals $\{y_k, r_k, q_k\}$ from Method 2

Method 3

To improve the performance of Method 2, we propose Method 3 as depicted in Figure 7. Again, the signal y_k is passed through an absolute operator to obtain a signal $r_k = | y_k |$. Thus, the amplitude of the signal r_k at specific portions will be enlarged to ease the UB detection process. Specifically, the adjusted signal z_k is given by

$$z_k = \begin{cases} A+\Delta, & r_k > m_3 \\ r_k, & \text{else} \end{cases}, \tag{4}$$

where Δ is a large number (e.g. 10), $A = 1$ is assumed to be the peak amplitude of the UB-unaffected readback signal, and m_3 is a threshold value. After that the adjusted signal z_k is fed to an averaging filter with a window length of L samples to obtain the signal q_k according to (3).

Similarly, to detect the UB, the signal q_k is compared with the threshold value m_4. Specifically, the UB is detected if $q_k < m_4$ for three consecutive samples so as to make it more robust to false alarm. Note that with enlarged signal, Method 3 can now utilise a smaller L than that in Method 2 for averaging the signal. Figure 8 shows an example of the signals obtained from Method 3.

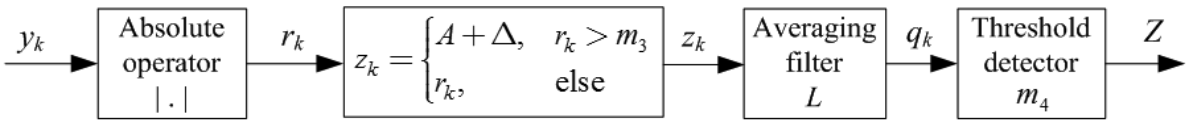

Figure 7. Method 3 for UB detection

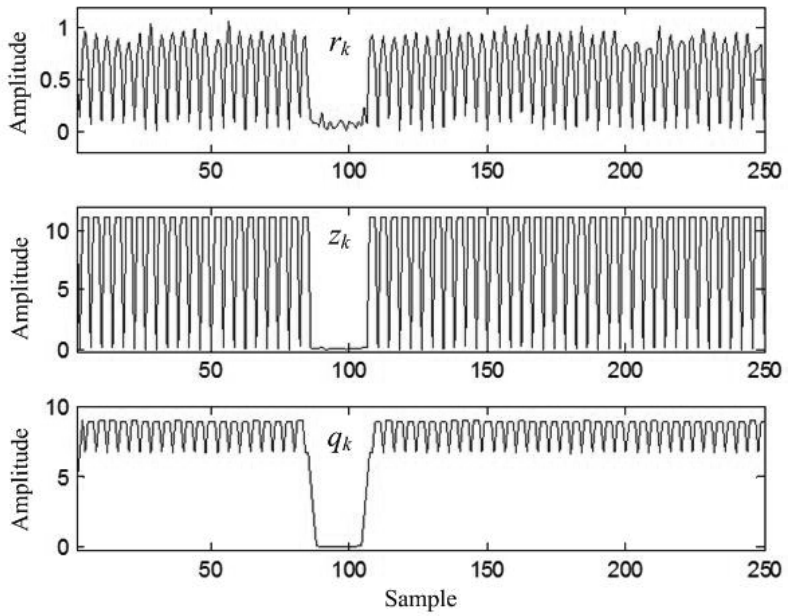

Figure 8. Example of the signals $\{r_k, z_k, q_k\}$ from Method 3

NUMERICAL RESULTS

Consider the perpendicular recording channel in Figure 2 at ND = 2 and signal-to-noise ratio (SNR) = 21 dB, where bit-error rate (BER) = 10^{-5} at the output of the sequence detector when the readback signal has no UB event. Here, SNR = $10\log_{10}(E_i/N_0)$ in decibel (dB), where E_i is the energy of the channel impulse response. We use the partial-response target $H(D) = 1 + 2D + D^2$ at ND = 2 [13]. The 11-tap finite impulse response equaliser is designed based on a minimum mean-squared error approach [14]. We also assume that each data sector contains one UB event starting at the 100th bit.

Figure 9 illustrates the system performance in terms of BER at the output of the Viterbi detector for different UB events. Each BER point was computed using as many 4096-bit data sectors as needed to collect 1000 error bits. Because each data sector contains one UB event, we

call the BER as 'UB-given BER.' It is apparent that the UB event degrades the system performance, especially when it covers several bit durations.

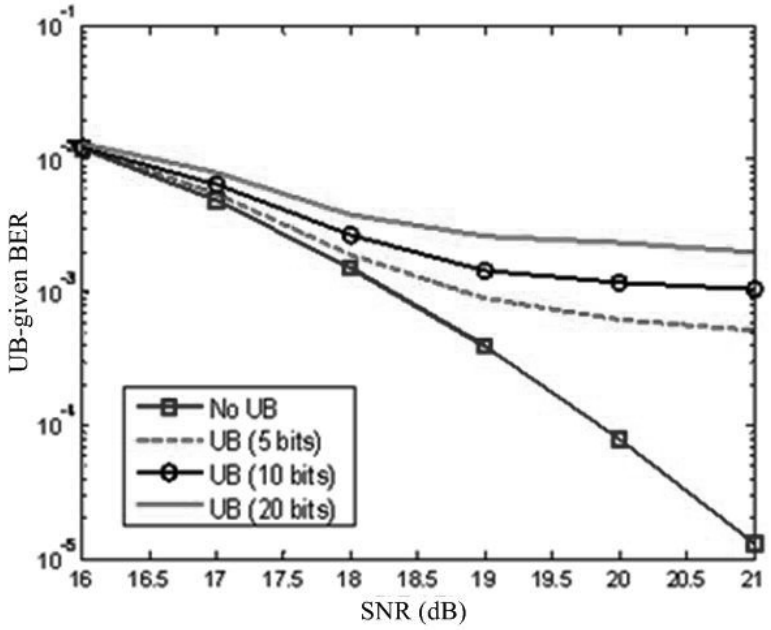

Figure 9. BER performance for different lengths of UB event

Here, we compare the performance of the three proposed UB detection methods, all of which are designed to detect the UB event only, without finding its exact location. Two cases are considered, viz. when the data input is 4*T* pattern (used in the testing process) and when the data input is random (after a customer uses the HDD). The parameters utilised for each method (optimised at ND = 2 and SNR = 21 dB by maximising the percentage of detection and minimising the percentage of false alarm) are the following:

- Method 1: $m_1 = 0.15$ for both random data and 4*T*-pattern data
- Method 2: $\{L = 31, m_2 = 0.12\}$ for random data, and $\{L = 15, m_2 = 0.5\}$ for 4*T*-pattern data
- Method 3: $\{L = 21, \Delta = 10, m_3 = 0.3, m_4 = 2\}$ for random data, and $\{L = 5, \Delta = 10, m_3 = 0.3, m_4 = 3\}$ for 4*T*-pattern data

4T-Pattern Data

Practically, when the read head is in the testing process to check whether it is defective, the 4*T*-pattern data is usually written into a disk and read out by the tested read head. If there are some portions of the readback signal that have very small amplitude for several bit periods (see Figure 1 for example), the UB event is identified.

Figure 10 compares the performance of each method by plotting the percentage of detection as a function of the number of missing bits (in the UB event). For each performance point, we ran 1000 data sectors (each with one UB event). Then we counted the number of data sectors for which the proposed methods can detect the UB event correctly and computed the percentage of detection. Clearly, Method 3 can detect the UB event better than the others, followed by Method 2. Both Method 2 and Method 3 performed well and could detect the UB event that contained at least four missing bits. On the other hand, Method 1 could only detect the UB event efficiently when the number of missing bits was greater than 10 bits.

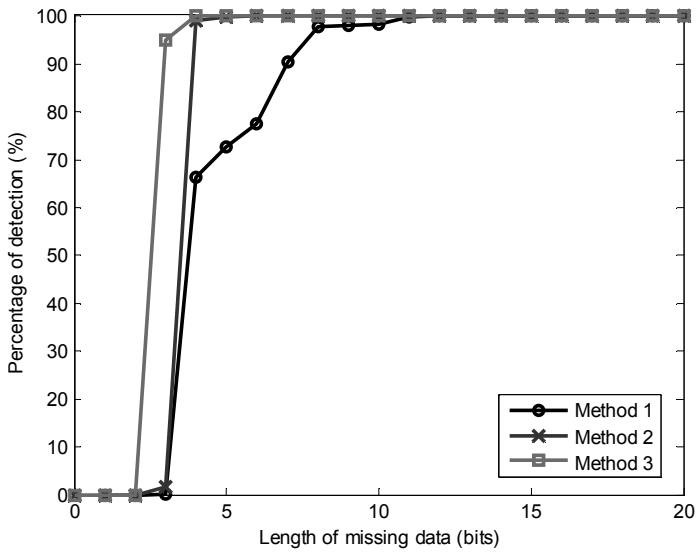

Figure 10. Performance comparison between UB detection methods based on 4*T*-pattern data

Random Data

When the UB event occurs in random data $\{a_k\}$, it is difficult to notice its existence in the readback signal, especially when the number of missing bits in the UB event is small as illustrated in Figure 11. With random data, we found that (not shown here) Method 1 does not work (even if the number of missing bits is large) because it relies merely on the enveloped signals u_k and l_k.

Figure 11 compares the performance of Method 2 and Method 3. Apparently, Method 3 can detect the presence of the UB event better than Method 2. Nonetheless, both methods can detect the UB event efficiently when the number of missing bits in the UB event is greater than 30 bits.

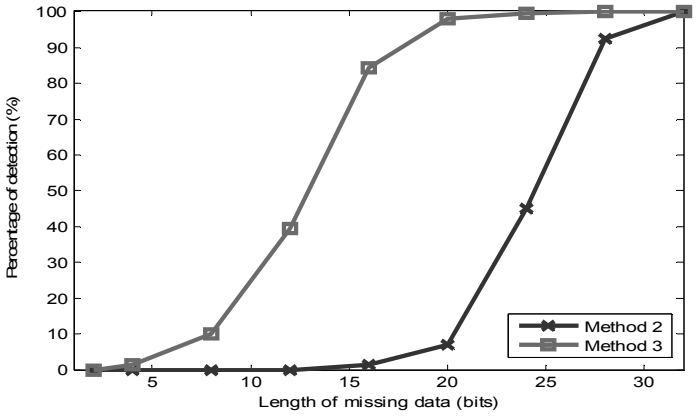

Figure 11. Performance comparison of Method 2 and Method 3 based on random data

CONCLUSIONS

Instability of the magneto-resistive head can cause a spike baseline or a UB, depending on the type of the defective head. This paper focuses on the UB and proposes three simple methods to detect it. Results show that all methods can detect the UB event for 4*T*-pattern data that is employed during the testing process, with Method 3 performing best. However, for random data, Method 1 can no longer work, and Method 3 performs better than Method 2. It should be pointed out that in

real hard disk drives, the UB detection can be further used to determine the number of error-control iterations for correcting the lost bits. Additionally, it can also be employed to indicate whether the drive is needed to re-read the data sector that contains the UB event.

ACKNOWLEDGEMENTS

We thank the Advanced Channel Failure Analysis team, Western Digital (Thailand) Company Ltd. for their discussion on the unstable baseline effect in the readback signal.

REFERENCES

1. L. Chen, E. Chen, J. Giusti, J. Fernandez de Castro and D. Saunders, "Micro-magnetic and electric analysis on MR head baseline popping and instabilities", *IEEE Trans. Magnet.*, **2001**, *37*, 1343-1345.
2. E. Chen, D. Saunders and J. Fernandez de Castro, "Junction edge instability in simple spin valve recording heads", *IEEE Trans. Magnet.*, **2000**, *36*, 2581-2583.
3. L. Chen, J. Fernandez de Castro, J. Giusti, H. Fang and M. Hurben, "Telegraph noise mechanism and LLG noise model", *IEEE Trans. Magnet.*, **2000**, *36*, 3195-3198.
4. W. C. Yang, "Method and apparatus to control head instability in data storage system", *U.S. Patent* 7,062,698 B2 (**2006**).
5. B. Zafer, "Baseline popping noise detection circuit", *U.S. Patent* 0165444 A1 (**2008**).
6. H. Song and M. Madden, "ACQ in the presence of baseline popping", *U.S. Patent* 8,625,218 B1 (**2014**).
7. H. Y. Bang, L. Ro, R. Wang and J. Yun, "Amplitude spike detector for head instability", *U.S. Patent* 0030660 A1 (**2005**).
8. Z. Li, A. Kao and K. Y. Cho, "Method for magneto-resistive head electrostatic popping detection", *U.S. Patent* 6,556,001 B1 (**2003**).
9. K. Du, "Low frequency signal baseline shift compensation in a disk drive", *U.S. Patent* 6,628,468 B1 (**2003**).
10. T. A. Roscamp, E. D. Boerner and G. J. Parker, "Three-dimensional modeling of perpendicular reading with a soft underlayer", *J. Appl. Phys.*, **2002**, *91*, 8366-8368.
11. G. D. Forney, "Maximum-likelihood sequence estimation of digital sequences in the presence of intersymbol interference", *IEEE Trans. Inform. Theory*, **1972**, *18*, 363-378.
12. P. Kovintavewat and S. Koonkarnkhai, "Thermal asperity suppression based on least-squares fitting in perpendicular magnetic recording systems", *J. Appl. Phys.*, **2009**, *105*, 07C114-07C114-3.
13. P. Kovintavewat and S. Koonkarnkhai, "Joint TA suppression and turbo equalization for coded partial response channels", *IEEE Trans. Magnet.*, **2010**, *46*, 1393-1396.
14. J. Moon and W. Zeng, "Equalization for maximum likelihood detectors", *IEEE Trans. Magnet.*, **1995**, *31*, 1083-1088.

Maejo Int. J. Sci. Technol. **2015**, *9*(01), 10-20; doi: 10.14456/mijst.2015.2

Maejo International Journal of Science and Technology

ISSN 1905-7873
Available online at www.mijst.mju.ac.th

Full Paper

Performance investigation of a modified small engine fueled with producer gas

Nigran Homdoung [1], Nakorn Tippayawong [1,*] and Natthawud Dussadee [2]

[1] Department of Mechanical Engineering, Chiang Mai University, Chiang Mai 50200, Thailand
[2] School of Renewable Energy, Maejo University, Chiang Mai 50290, Thailand
* Corresponding author, e-mail: n.tippayawong@yahoo.com

Received: 18 February 2014 / Accepted: 19 January 2015 / Published: 27 January 2015

Abstract: Producer gas from biomass gasification can be used as a replacement fuel in spark-ignition engines. In this study, a small, single-cylinder, naturally aspirated diesel engine was modified into a spark-ignition engine. A conventional swirl chamber was replaced by a bath tube combustion chamber. Optimum spark ignition time was set for each engine speed to give maximum brake torque. It was fueled with 100% producer gas and coupled to a 5.0-kW dynamometer. A downdraft gasifier was used to generate producer gas from charcoal. Engine performance in terms of engine torque, brake power, brake thermal efficiency and brake specific fuel consumption were evaluated at variable compression ratios between 9.7:1-17:1. Engine speed and load were varied between 1100-1900 rpm and 20-100% respectively. At a certain combination of compression ratio, engine speed and load, deceleration and knocking were detected. Maximum engine torque and brake power were 18.6 Nm and 3.3 kW respectively, at a compression ratio of 14:1, full load and 1700 rpm. The best specific fuel consumption of 0.94 kg/kWh and maximum brake thermal efficiency of about 19% were obtained.

Keywords: small engine, producer gas, compression ratio, spark ignition, renewable energy

INTRODUCTION

Escalating oil prices and increasingly scarce fossil fuels, coupled with an exploding population, have created an energy crisis, especially in developing countries where machines are used in food production. In Thailand, the agricultural sector commonly uses small, internal combustion engines, with power and speed mostly in the range of 2.2-10.4 kW and 1000-2000 rpm respectively [1]. Farms use them for mechanical work, pumping, power generation and plowing. Using producer gas in engines offers an alternative energy source, reducing dependence on fossil fuels. However, producer gas poses a problem as more combustible carbon monoxide content is needed to produce a similar output to gasoline. This is because the engine operates at a lower

thermal efficiency with power de-rated by more than 30% due to the lower energy density of producer gas compared to that of gasoline and diesel fuels [2].

Attempts to develop internal combustion engines, especially for producer gas as fuel, are ongoing, with three primary types: (i) spark ignition (SI) engines using gas, (ii) compression ignition (CI) engines using gas and diesel in dual fuel mode, and (iii) engines converted from CI to SI using 100% gas. Based on previous researches, converting a CI engine into an SI engine operated at medium and high levels of compression ratio (CR) shows promise. A number of studies of SI engines fueled by producer gas have been carried out. Parke and Clark [3] and Martin and Wauters [4] showed that the engine power was 34-50% less than gasoline engines at conventional CR [5]. Munoz et al. [6] reported test results on a small SI engine at a CR of 8.2: 1. A power de-rating of 50% was observed. Ando et al. [7] reported that SI engines using producer gas at a CR of 9.4:1 caused a 45% average power reduction at all engine speeds. Shah et al. [8] found that a small SI engine using producer gas at a low CR had 1.8 times less power than using gasoline. Dasappa et al. [9] studied the use of producer gas with a 100-kW SI engine at a CR of 9.7:1. The maximum thermal efficiency was 18% and at low CR the engine power was reduced.

Ramachandra [10] studied medium and high CRs in a converted SI engine and found that the engine ran smoothly, with power output reduced by 20% compared to the original CI engine [5]. Shasikantra et al. [11] converted a CI engine to operate as an SI engine with producer gas as fuel at a CR of 11:1. They obtained a high thermal efficiency in the range of 20-24%. Aung [12] adapted a producer gas engine converted from a CI engine at a CR of 10:1. The power and torque output were 40% less than that with diesel mode. Raman and Ram [13] reported on an SI engine using producer gas at a CR of 12:1. The maximum thermal efficiency was 21% at 85% of full load. Sridhar et al. [5] modified a CI engine into an SI engine and used producer gas as fuel at a CR of 17:1. The engine brake power was reduced by 20% and the maximum overall efficiency obtained was 21%.

Most of these studies used medium to large engines. There have been very few studies on small engines. The objective of this research is to analyse the performance of a small engine fueled with 100% producer gas and determine the most appropriate CR, load and engine speed.

MATERIALS AND METHODS

Experimental Set-up

A schematic diagram of the gas generator system used in this study is shown in Figure 1. The gas generator design is based on a downdraft gasifier [14], and configured to operate on charcoal or wood. It consists of a gasifier, a gas conditioner and gas filters. The producer gas can be produced with a charcoal consumption rate between 5-6 kg/h. The efficiency of the gasification system is 70-75% and can generate up to 27 Nm^3/h of producer gas. The conditioning system improves the quality of the producer gas to ensure that the engine runs smoothly. The gas conditioning system consists of a heat exchanger, cyclone, Venturi scrubber, tar box, moisture separator, biomass filter, fabric filter and paper filter. The set-up also includes a water treatment plant for closed-loop water re-circulation.

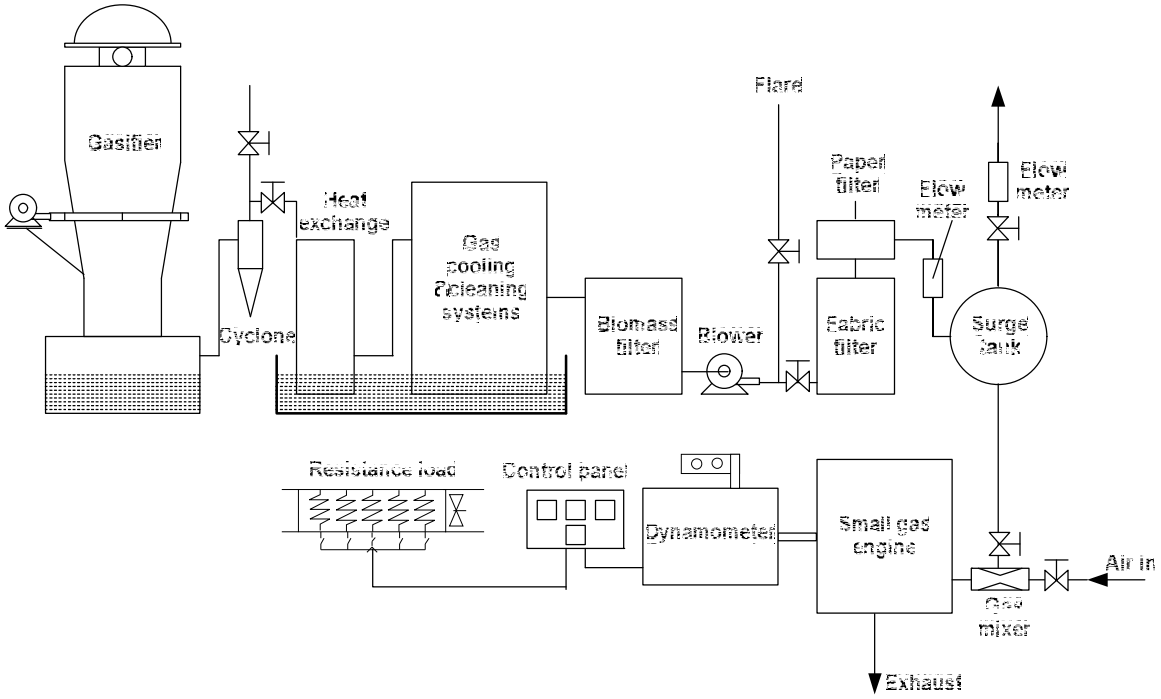

Figure 1. Schematic diagram of the experimental set-up for gas generator system

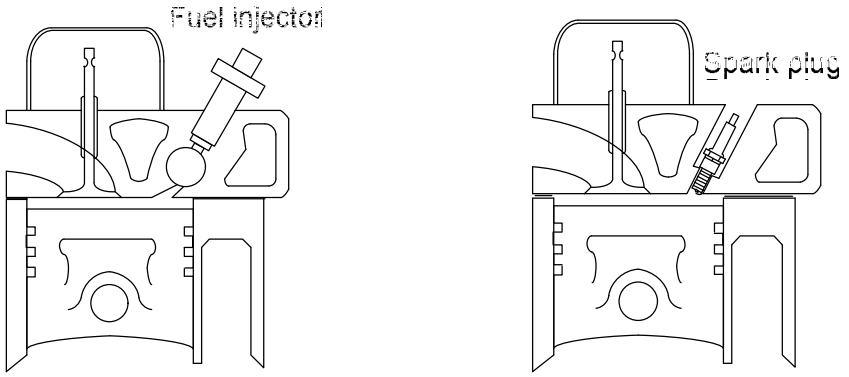

(a) before (b) after

Figure 2. Small producer gas engine before and after modification of cylinder head

Engine Modification

A conventional, small, agricultural, water-cooled diesel engine with a CR of 21:1 was used in this experiment. The four-stroke, single cylinder, indirect injection engine was capable of producing a maximum power output of 8.2 kW. The engine specifications are given in Table 1. For the producer gas feeding system, a gas mixer was designed, manufactured and installed. The original diesel injection system was replaced with a spark plug as shown in Figure 2. The distributor and ignition coil were taken from a Mitsubishi 4G15 engine. The vacuum and centrifugal advances were disabled because the engine ran at a constant speed. The distributor was modified by replacing the magnetic pick-up with a spark timing plate stuck to the flywheel. The spark-ignition timing could be adjusted between 0-60°. The CR was adjusted to a range of 9.7-17: 1. Variable CR was achieved by using a thicker head gasket (between 4.7-8.2 mm). The volumes of the cylinder head

and piston head were measured using a hypodermic syringe with low-viscosity oil. The cylinder head bolts and push rods were modified and the stoichiometric ratio of air to producer gas was approximately 1: 1.2. This volume ratio was used in the design of the gas mixer, which was based on Janisch [15] and used to supply the engine operating between 1000-2000 rpm with the appropriate mixture of air and gas. The air mixer was a Venturi with a throat diameter of 25 mm. Producer gas and air could be controlled by adjusting two screws.

Table 1. Specifications of original engine dynamometer set-up

Engine make, model	Kubota, ET11
Engine power	8.2 kW
Bore × Stroke	92×90 mm^2
Number of cylinder	1
Engine arrangement	Horizontal
Type of cooling	Water, thermo siphon system
CR	21:1
Combustion chamber	Pre-chamber
Ignition system	Compression ignition
Alternator efficiency	85%

Experimental Apparatus and Procedure

All experiments involving the engine were performed only after the gasifier system stabilised, normally about 1 hour from start-up. The stability of the gasifier system was achieved when the temperatures of the gasification zone and burner flame stabilised. The gas generator was operated using charcoal (size 25×25×25–50×50×50 mm according FAO [2] and Shaw [16]) which was available locally. Its density and average moisture content were measured based on ASTM C373-88 and ASTM D 2016-74 [17] and were found to be 250-300 kg/m^3 and 7% respectively. The gas composition was determined at random intervals using a Shimadzu GC-8A gas chromatography fitted with a ShinCarbon ST Micropacked column and a thermal conductivity detector. The conditions used were similar to those reported previously [18, 19]. The average chemical composition was 30.5±2% CO, 8.5±2% H_2, 0.35% CH4, 4.8±1% CO_2, 6.3±0.5% O_2 and N_2 (balance). The calculated mean calorific value of the producer gas was 4.64 MJ/Nm^3. The tar and particulate matter in the producer gas was measured according to Hasler et al. [20] and found to be less than 50 mg/Nm^3. Experiments were conducted at CRs of 9.7:1, 14:1 and 17:1. A higher CR engine using producer gas is of interest as it might offer a higher efficiency with better tolerance to knocking. Modifying an engine to have a higher CR is straightforward by simply decreasing the thickness of the cylinder head gasket. Engine tests were carried out by varying engine speeds with rpm and loading range of 1100-1900 and 20-100% respectively. The data were acquired at the corresponding maximum brake torque timing for each 1100, 1300, 1500, 1700 and 1900 rpm of the engine speed test condition. The air and fuel were tuned to achieve maximum power and after a stable operation, several measurements were taken over an average of 10-min. interval. Charcoal consumption at different loads was monitored by weighing the amount fed into the gasifier. The producer gas and airflow rates were measured using a Lutron YK-80 flow meter. The electrical load consisted of ten 100W bulbs with ten 500W heaters; a F609 Chauvin Arnoux watt meter was used

for monitoring the load. The engine torque was measured using a load cell. The brake power, thermal efficiency and fuel consumption were evaluated using the following equations [21]:

$$P = 2\pi N\tau \quad (1)$$

where P is the brake power, τ is the engine torque (Nm) and N is the engine speed (s^{-1});

$$BSFC = \frac{m_f^{\bullet}}{P} \quad (2)$$

where *BSFC* is the brake specific fuel consumption and $m_f^{\bullet}$ is the mass flow rate of biomass (kg/h);

$$BTE = \frac{P}{V_{pg}^{\bullet} LHV_{pg}} \quad (3)$$

where *BTE* is the brake thermal efficiency, expressed as ratio of the output power to the power supplied by the fuel, $V_{pg}^{\bullet}$ is the producer gas flow rate (m^3/s) and LHV_{pg} is the lower heating value of the producer gas (MJ/Nm^3).

RESULTS AND DISCUSSION

Gas Engine Operation

Table 2 provides a general overview of operation of a small engine with producer gas. It is representative of the results of analysing the engine performance. It can be observed that, at a low CR (9.7:1), the engine was able to be gradually loaded and stabilised up to 1500 rpm. With increasing engine speed, acceleration was good and the engine power increased. The engine decelerated and became unstable when the speed was increased to 1700-1900 rpm. The observed deceleration might be due to a reduced energy density compared to gasoline. The low CR of the engine might cause a lower pressure inside the combustion chamber [22] and affect flammability of the producer gas [7]. The lower volumetric efficiency might be reduced for gaseous fuel operation compared to conventional liquid fuels [23]. At a medium CR (14:1), however, the engine was observed to have good acceleration stability and its power increased with speed, although knocking occurred at full load and 1900 rpm. Finally, at a high CR (17:1), the small engine operated well between 1100-1500 rpm, but severe knocking symptoms occurred at 1700-1900 rpm and 80-100% of full load. Knocking might result from the increasing compression ratio, as well as increasing load and engine speed, leading to an increase in gas density, temperature and ignition lag in the combustion chamber [21].

Engine Brake Torque

Figure 3 shows the variation in engine torque of the small producer gas engine at 1500 rpm with different engine loads and CRs. A maximum torque of 15.38 Nm was obtained at CR = 14:1 and full load. For all CRs, the brake torque was similar between 20-60% of load. Increasing load from 60 to 80% at medium CR increased brake torque significantly. The main reason for the increase in torque is that, compared to low CR, the work in expansion stroke exceeds that in the compression stroke [13]. At high CR, the engine torque was low due to abnormal combustion, leading to knocking [24]. Comparing engine torque versus speed at full load, the suitable CR for the small producer gas engine was found to be 14:1 at 1700 rpm and 18.61 Nm of maximum torque. At 1900 rpm, the engine was unable to operate due to severe knocking.

Table 2. Operation of modified small engine fueled with producer gas at different test conditions

Compression ratio	Load (%)	Engine operation				
		1100 rpm	1300 rpm	1500 rpm	1700 rpm	1900 rpm
9.7:1	20	✓	✓	✓	x	x
	40	✓	✓	✓	x	x
	60	✓	✓	✓	x	x
	80	✓	✓	✓	x	x
	100	✓	✓	✓	x	x
14:1	20	✓	✓	✓	✓	✓
	40	✓	✓	✓	✓	✓
	60	✓	✓	✓	✓	✓
	80	✓	✓	✓	✓	✓
	100	✓	✓	✓	✓	xx
17:1	20	✓	✓	✓	✓	✓
	40	✓	✓	✓	✓	✓
	60	✓	✓	✓	✓	✓
	80	✓	✓	✓	xx	xx
	100	✓	✓	✓	xx	xx

Note: ✓ = OK; x = Erratic; xx = Knocking

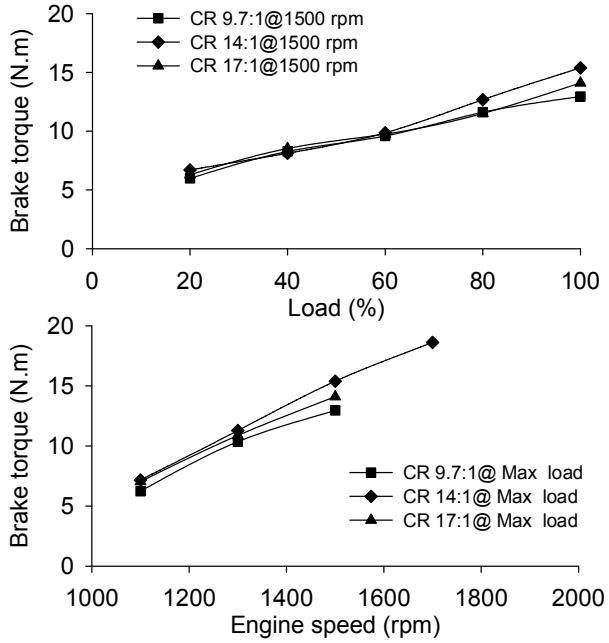

Figure 3. Engine brake torques at different loads and engine speeds

Brake Power

Figure 4 shows the effect of load and engine speed on the brake power for each CR considered. The engine brake power increased as engine load increased at all CRs. At 1500 rpm, an engine brake power of 2.41 kW was achieved at 14:1 of CR. The maximum engine brake power of 3.31 kW was achieved at 1700 rpm and medium CR.

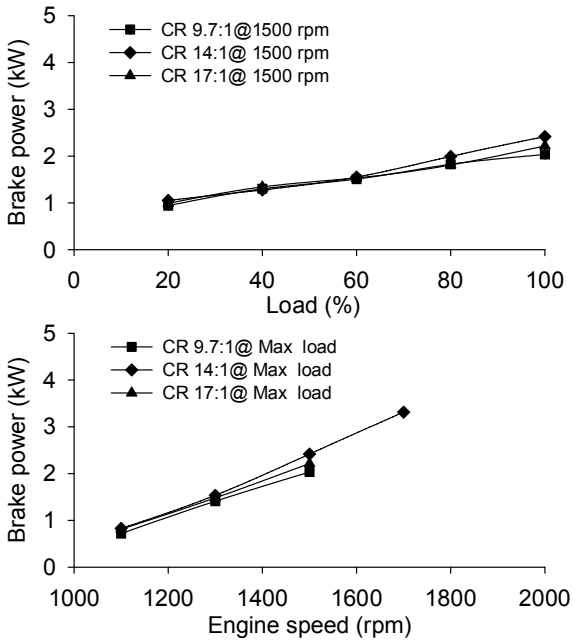

Figure 4. Engine brake power at different loads and engine speeds

Brake Thermal Efficiency

Figure 5 shows the BTE as a function of engine load and speed at different CRs. The efficiency tended to increase with engine load. This might be attributed to a better combustion of the relatively rich gas-air mixture at high loads. The BTE at medium CR was slightly higher than those at low and high CRs; reduction of BTE was due to a higher producer gas flow rate and poor combustion. At medium CR, a maximum BTE of 18.6% was obtained at full load. The small producer gas engine operated successfully at 1100-1500 rpm at both low and high CRs. The engine could operate up to 1700 rpm at medium CR, but at 1500-1700 rpm, the BTE tended to level off.

Brake Specific Fuel Consumption

The gasification rate from charcoal to producer gas was 25 Nm^3/h. The charcoal-to-gas conversion rate was arrived at by measuring the gas flow rate and fuel consumption rate. The specific charcoal consumption rate for the small producer gas engine was 0.94 kg/kWh. When the engine was operated at medium CR at full load (Figure 6), fuel consumption was reduced with increasing engine speed. The low and high CRs consumed more fuel than medium CR. Generally, the BSFC rate of the producer gas engine is in a range of 1.2-2 kg/kWh [9, 12]. At full load, the specific consumption rate decreased as engine speed increased. The lowest BSFC occurred between 1400-1500 rpm.

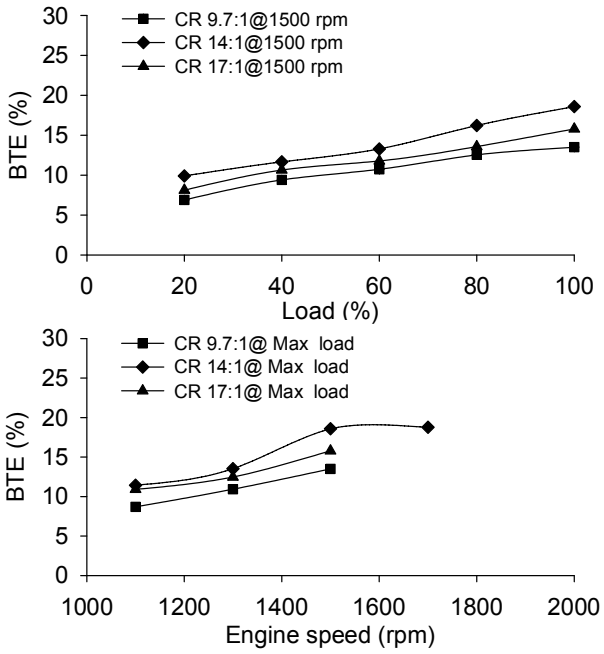

Figure 5. BTE at different loads and engine speeds

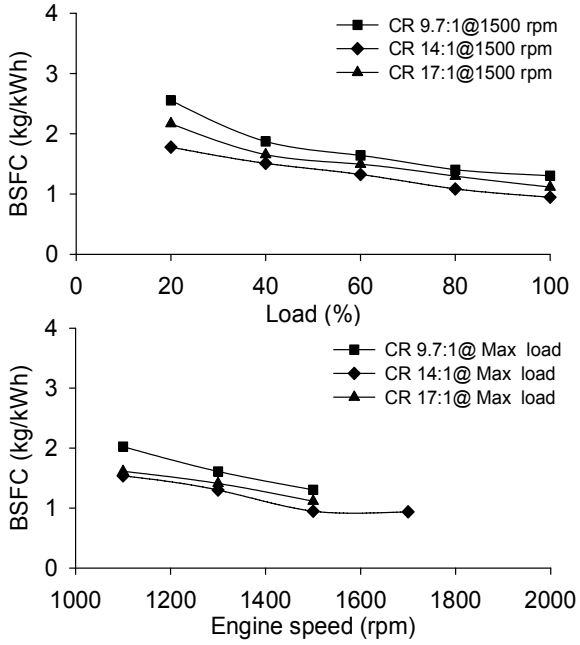

Figure 6. BSFC at different loads and engine speeds

Comparison with Previous Results

The performance of engines converted from CI or SI engines and fueled with producer gas at typical and high CRs, including that in this study, is summarised in Table 3. Most engines tested were large, with 2-6 cylinders and total engine displacement in the range of 1800-14000 cm^3, while that in this study was a small, single-cylinder engine with displacement of less than 600 cm^3. The CRs of the engines used were mostly low due to concerns about possible knocking [11] and the flexibility of using other fuels as primary fuel [12]. No sign of knocking at high CR was reported [9, 25]. Most reports on large engines did not provide information on torque and power. The overall

efficiency of these large engines was in a range of 18-21%, which is similar to the efficiency values obtained in this work. The BSFC of our small engine was lower than those reported for the large engines.

Table 3. Performance of modified engines operated on producer gas

Performance specifications	[5]	[9]	[12]	[13]	This study
Engine power (kW)	28	283.48	26.5	99.2	8.2
Total displacement (cm^3)	3307	14000	1853	12316	598
Bore x Stroke (mm)	110x116	140x152	100x118	132x150	92x90
Number of cylinder	3	6	2	6	1
CR	17:1	8.5	10:1	12:1	14:1
Max torque/engine speed (Nm/rpm)	-	-	64/1400	-	18.6/1700
Max brake power/engine speed (kW/rpm)	-	-	12/1400	-	3.3/1700
BTE (%)	21	18	-	20.7	18.58
BSFC (kg/kWh)	-	1.36	2	1.2	0.94

Note: '-' = not available

CONCLUSIONS

We converted a small diesel engine into an SI gas engine. The modified engine successfully ran with 100% producer gas at high CRs. The most appropriate CR was 14:1 at full load with a maximum engine speed of 1700 rpm. The maximum engine torque and brake power was 18.61 Nm and 3.31 kW respectively.

ACKNOWLEDGEMENTS

We acknowledge support from Chiang Mai University and the Energy Policy and Planning Office, Ministry of Energy. The authors also thank the Energy Research Centre, Maejo University for providing test facilities.

REFERENCES

1. S. Siripornakarachai and T. Sucharitakul, "Modification and tuning of diesel bus engine for biogas electricity production", *Maejo Int. J. Sci. Technol.*, **2007**, *1*, 194-207.
2. FAO Forestry Department, "Wood Gas as Engine Fuel", Food and Agriculture Organization of the United Nations, **1986**, pp.7-21.
3. P. P. Parke and S. J. Clark, "Biomass producer gas fueling of internal combustion engines naturally aspirated and supercharged mixtures", *J. ASAE Technol.*, **1981,** *1*, 1-35.
4. J. Martin and P. Wauters, "Performance of charcoal gas internal combustion engines", Proceedings of International Conference on New Energy Conversion Technologies and Their Commercialization, **1981**, Berlin, Germany, pp.1415-1424.
5. Q. Sridhar, P. J. Paul and H. S. Mukunda, "Biomass derived producer gas as a reciprocating engine fuel—an experimental analysis", *Biomass Bioener.*, **2000**, *21*, 61-72.
6. M. Munoz, F. Moreno, J. Morea-Roy, J. Ruiz and J. Arauzo, "Low heating value gas on spark ignition engines", *Biomass Bioener.*, **2000**, *18*, 431-439.

7. Y. Ando, K. Yoshikawa, M. Beck and H. Endo, "Research and development of a low BTU gas-driven engine for waste gasification and power generation", *Energy*, **2005**, *30*, 2206-2218.
8. A. Shah, R. Srinivasan, S. D. F. To and E. P. Columbus, "Performance and emissions of a spark-ignited engine driven generator on biomass based syngas", *Bioresour. Technol.*, **2010**, *101*, 4656-4661.
9. S. Dasappa, D. N. Subbukrishna, K. C. Suresh, P. J. Paul and G. S. Prabhu, "Operational experience on a grid connected 100 kWe biomass gasification power plant in Karnataka, India", *Energy Sustain. Develop.*, **2011**, *15*, 231-239.
10. A. Ramachandra, "Performance studies on a wood gas run IC engine", Proceedings of 4th National Meet on Biomass Gasification and Combustion, **1993**, Mysore, India, pp.213-218.
11. T. Shashikantha, W. Klose and P. P. Parikh, "Development of a 15-kWe spark-ignition producer gas engine and some investigations of its in-cylinder processes", *Renew. Ener.*, **1994**, *5*, 835-837.
12. N. Z. Aung, "Modification of diesel engine to producer gas engine", *J. ilmiah Teknol. Ener.*, **2008**, *1*, 29-41.
13. P. Raman and N. K. Ram, "Performance analysis of an internal combustion engine operated on producer gas, in comparison with the performance of the natural gas and diesel engines", *Energy*, **2013**, *63*, 317-333.
14. T. B. Reed and A. Das, "Handbook of Biomass Downdraft Gasifier Engine Systems", U.S. Government Printing Office, Washington D.C., **1988**, pp.32-42.
15. D. G. Janisch, "Air fuel mixing device for producer gas", *US Patent 5070851* (**1991**),
16. L. N. Shaw, J. D. Whitney, S. L. Hedden and D. B. Churchill, "Operating a diesel irrigation pump on citrus-wood producer gas", *Appl. Eng. Agric.*, **1990**, *6*, 376-381.
17. N. Dussadee, N. Homdoung, R. Ramaraj, K. Santisouk and I. Inthavideth, "Performance analysis of power generation by producer gas from refuse derived fuel-5 (RDF-5)", *Int. J. Sustain. Green Ener.*, **2014**, *4*, 44-49.
18. N. Tippayawong, C. Chaichana, A. Promwungkwa and P. Rerkkriangkrai, "Gasification of cashew nut shells for thermal application in local food processing factory", *Ener. Sustain. Develop.*, **2011**, *15*, 69-72.
19. N. Tippayawong, C. Chaichana, A. Promwungkwa and P. Rerkkriangkrai, "Investigation of a small biomass gasifier – engine system operation and its application to water pumping in rural Thailand", *Ener. Sources A*, **2013**, *35*, 476-486.
20. P. Hasler, R. Salzmann, H. Kaufmann and T. Nussbaumer, "Guideline for Sampling and Analysis of Tars Condensates and Particulates from Biomass Gasifiers", Swiss Federal Institute of Technology Zürich and Verenum Research Zürich, Switzerland, **1998**, Ch.3.
21. J. B. Heywood, "Internal Combustion Engine Fundamentals", McGraw-Hill, Singapore, **1989**, pp.41-52.
22. M. E. Kassaby, M. A. Nemit allah, "Studying the effect of compression ratio on an engine fueled with waste oil produced biodiesel/diesel fuel", *Alexandria Eng. J.*, **2013**, *52*, 1-11.
23. N. N. Mustafi, Y. C. Miraglia, R. R. Raine, P. K. Bansal and S. T. Elder, "Spark-ignition engine performance with 'Powergas' fuel (mixture of CO/H_2): A comparison with gasoline and natural gas", *Fuel*, **2006**, *85*, 1605-1612.
24. D. M. Wise, "Investigation into producer gas utilization in high performance natural gas engines", *PhD Thesis*, **2005**, Colorado State University, USA.

25. G. Sridhar, H. V. Sridhar, S. Dasappa, P. J. Paul, N. K. S. Rajan and H. S. Mukunda, "Development of producer gas engines", *Proc. Inst. Mech. Eng. D: J. Autom. Eng.*, **2005**, *219*, 423-438.

Maejo Int. J. Sci. Technol. **2015**, *9*(01), 21-31; doi: 10.14456/mijst.2015.3

Maejo International Journal of Science and Technology

ISSN 1905-7873
Available online at www.mijst.mju.ac.th

Full Paper

Aromaticity of a series of poly-2,7-[N]calicenes

Thawalrat Ratanadachanakin [1,*] and Willard E. Collier [2]

[1] Faculty of Science, Maejo University, Sansai, Chiang Mai, 50290, Thailand
[2] Department of Chemistry, College of Arts and Sciences, Tuskegee University, Tuskegee, AL, 36088, USA

* Corresponding author, e-mail: thawalrat@mju.ac.th; fax: 66 5387 3548; tel.: 668 7504 3314

Received: 1 July 2014 / Accepted: 10 February 2015 / Published: 12 February 2015

Abstract: The nucleus independent chemical shift (NICS) criterion of aromaticity is used to evaluate the aromaticity of a series of poly-2,7-[N]calicenes. The geometry and NICS values of all poly-2,7-[N]calicenes and reference molecules (calicene, bicalicene, benzene, cyclopentadienyl anion and cyclopropenyl cation) are evaluated at the B3LYP/6-31G(d,p) level of computational theory. The NICS data indicate that all poly-2,7-[N]calicenes studied are aromatic, and aromaticity increases as the number of calicene units (N) increases.

Keywords: polycalicenes, aromaticity, nucleus independent chemical shift, B3LYP

INTRODUCTION

Aromaticity is one of the foundational concepts in chemistry, but after almost 150 years of research, aromaticity still elicits spirited debates and has yet to be definitively defined [1-3]. Many criteria of aromaticity have been proposed such as chemical reactivity, aromatic stabilisation energy, bond length equalisation and various magnetic properties such as ^{1}H chemical shift, but no criterion has been accepted to be definitive [4-6]. Some lament the lack of agreement, but as pointed out by others this inability to reach a consensus has spurred research and led to many discoveries.

While benzene is the archetypal aromatic molecule, non-benzenoid aromatic compounds are intrinsically interesting and provide insight into the scope of aromatic character. The aromaticities of a novel series of poly-2,7-[N]calicenes (**1-4**, Figure 1), where 2,7 designates the location of the bond between calicene monomers and [N] is the number of calicene monomers, are investigated in this paper**.** Poly-2,7-[N]calicenes **1-4**, having N values of 2, 3, 4 and 5 respectively, have not been synthesised.

Poly-2,7-[N]calicenes are polymers of calicene (**5**, Figures 2 and 3), also known as triapentafulvalene. Calicene is frequently mentioned in organic chemistry textbooks as an aromatic molecule due to its dipolar resonance form (**5b**, Figure 2). With 4n + 2 π electrons in both of its five-membered ring (6 electrons) and three-membered ring (2 electrons), **5b** is expected to be the major contributor to the electronic structure of calicene. If **5b** is a major contributor, **5** would be

expected to have a large dipole moment due to the dipolar character of **5b**. Intriguingly, calicene has never been synthesised, but substituted calicenes such as 2,3-dicyano-5,6-diphenylcalicene and 1,2,3,4-tetrachloro-5,6-diphenylcalicene are known and have large dipole moments [7, 8]. Even more surprisingly, bicalicene (**6**, Figure 3), a cyclic dimer of calicene with a 16-π peripheral electron system and expected to be anti-aromatic according to the 4n + 2 aromatic rule, was synthesised and characterised to be aromatic [9, 10].

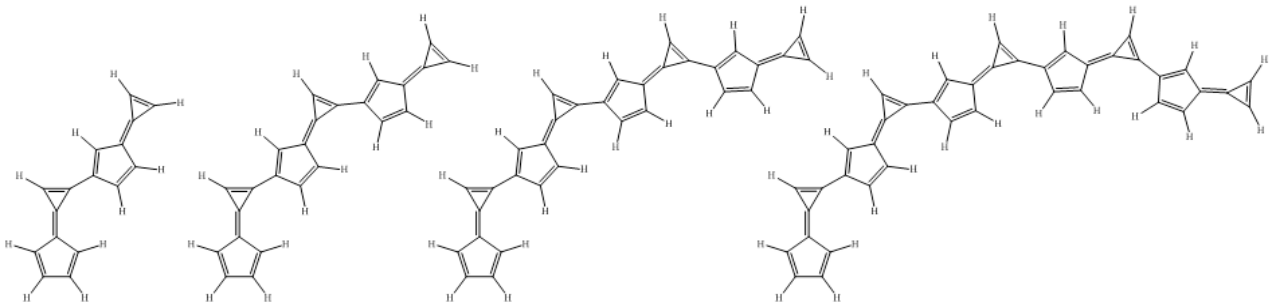

1 **2** **3** **4**

Figure 1. A series of poly-2,7-[N]calicenes

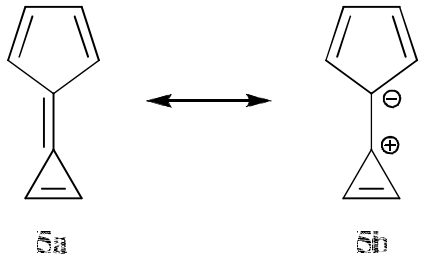

5a **5b**

Figure 2. Two main resonance forms of calicene (**5**)

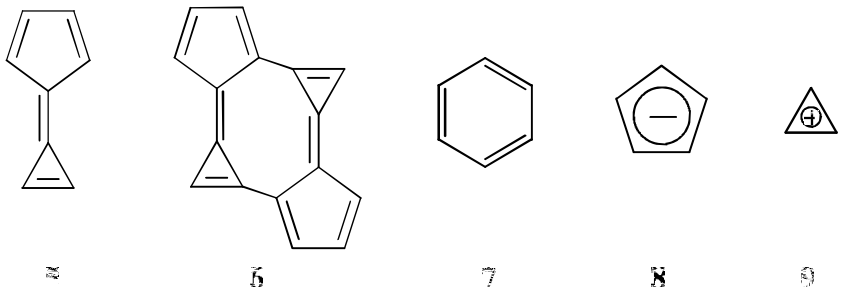

5 **6** **7** **8** **9**

Figure 3. Reference molecules used in this study

This work is a continuation of previous investigations into the structure and aromaticity of various polycalicene families that result from different bonding motifs between the calicene monomers [11-12]. The poly-2,7-[N]calicenes are only one example of the rich variety of molecules that can be constructed from calicene building blocks. Polycalicenes are an unexplored region of chemical space, and the possibility that some polycalicenes are non-benzenoid aromatic molecules

is inherently fascinating. Thus, the aromaticities of poly-2,7-[N]calicenes are evaluated in this paper using Schleyer's nucleus independent chemical shifts (NICS) [13]. The NICS values of calicene (**5**), bicalicene (**6**), benzene (**7**), cyclopentadienyl anion (**8**) and cyclopropenyl cation (**9**) (Figure 3) are calculated as references.

METHODS

The geometries of poly-2,7-[N]calicenes (**1-4**) were optimised using the density functional theory method composed of B3LYP functional [14, 15] and 6-31G(d,p) basis set [16, 17]. Harmonic vibrational frequency calculations were performed at the same level for all molecules to confirm that the molecules are of minimum energy conformations. NICS, defined as the negative of the calculated isotropic shielding [13], were evaluated at selected points (Figure 4). NICS(0) values (z=0) were calculated at points located at the centre (non-weighted average of ring atom coordinates) of the three-membered rings (cpro) and five-membered rings (cpent), and in the plane of each ring. NICS(1) values (z=1) were calculated at 1 Å above the NICS(0) point located at the ring centre and in the molecular plane of each ring. The geometries of all reference molecules, viz. calicene (**5**), bicalicene (**6**), benzene (**7**), cyclopenta-dienyl anion (**8**) and cyclopropenyl cation (**9**), were optimised at the same level of computational theory. NICS(0) and NICS(1) values for the reference molecules were calculated for comparison with the NICS results of **1-4**. All calculations were carried out using the Gaussian 09 suite of quantum mechanical programmes [18].

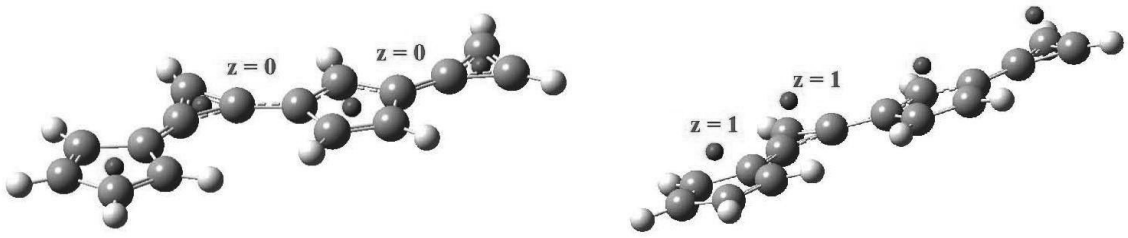

Figure 4. Location of NICS points, z=0 and z=1, for poly-2,7-[2]calicene (**1**)

RESULTS AND DISCUSSION

NICS Criterion of Aromaticity

NICS are a simple and robust criterion of aromaticity [13, 19]. NICS values are defined as the negative of the absolute magnetic shieldings computed at the 'ring centres (non-weighted mean of the heavy atom coordinates)'. Initially, NICS values were calculated only for points in the plane of the ring, designated as NICS(0) [13]. Negative NICS values indicate aromaticity and positive NICS values indicate anti-aromaticity. Since its introduction in 1996, there have been many refinements to the NICS method. Due to concerns over σ-electron contribution, it was proposed that NICS values be calculated 0.5 Å above the ring centre [20]. Next, NICS values are calculated 1 Å above the ring centre to further reduce the σ-electron contribution and are referred to as NICS(1) [21]. Further refinements have been proposed [20, 22, 23], such as separating the NICS values into σ- and π-electron contributions [20], but these 'refinements' detract from the simplicity of the original NICS method. Apart from the simplicity factor, the reliability of some of the latest refinements (e.g. NICS scan) [24] has been questioned.

Qualitative assignment of aromaticity is simple using NICS values, but quantitatively assessing the aromaticity is more complicated. Generally, the more negative the NICS value is, the

more aromatic the system becomes. However, ring size and electron density also play a major role. Because of these concerns we always include, as reference molecules, well-known aromatic molecules (for example benzene) and, more importantly, aromatic molecules that are similar to the molecules under evaluation.

Despite its widespread use, some have questioned the reliability and even the fundamental wisdom of assessing aromaticity using the NICS criterion [25]. However, we have used the NICS criterion of aromaticity extensively and have refuted one purported failure of the NICS method touted by its critics [11]. We maintain that NICS(0) and NICS(1) values alone are a reliable and simple method of assessing aromaticity without resorting to complicated and arbitrary refinements. This study, therefore, focuses on the NICS(0) and NICS(1) values of the poly-2,7-[N]calicenes (**1-4**).

Poly-2,7-[N]calicene Ring Designations

Each poly-2,7-[N]calicene contains two or more calicene subunits that are numbered as illustrated in Figure 5 for the longest poly-2,7-[N]calicene studied, poly-2,7-[5]calicene (**4**). The calicene subunit that is bonded by its three-membered ring to the five-membered ring of the next calicene subunit is designated the first calicene subunit. The first calicene subunit is identified by no prime, the second calicene subunit by one prime (i.e. '), the third calicene subunit by two primes (i.e. "), and the progression continues as each calicene subunit is added. In addition, each calicene subunit has a three-membered ring (cpro) and a five-membered ring (cpent), so when combined, the numbering scheme and ring designation allows each ring to be identified uniquely. It is noted that when all three-membered rings are collectively described, cpro is used, but when three-membered rings are individually distinguished, cpro designates the three-membered ring of the first calicene subunit. Likewise when all five-membered rings are collectively described, cpent is used, but when five-membered rings are individually distinguished, cpent designates the five-membered ring of the first calicene subunit.

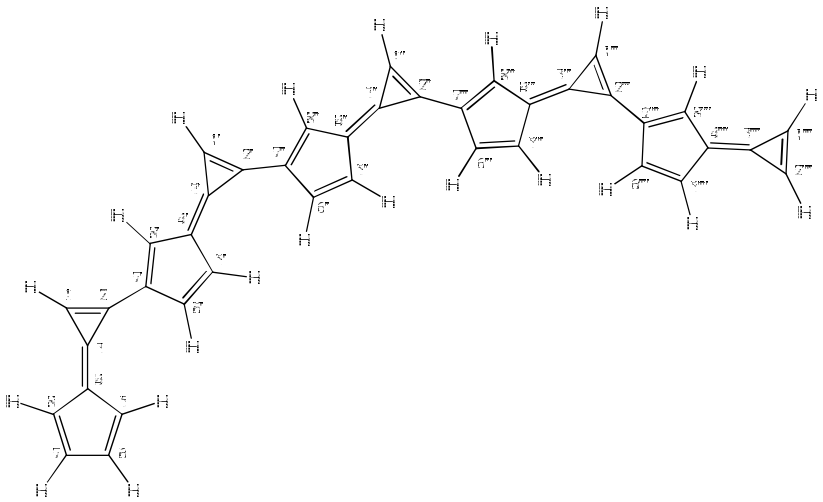

Figure 5. Numbering scheme of poly-2,7-[N]calicenes (**1-4**), illustrated by poly-2,7-[5]calicene (**4**)

Basis Set Choice

The calicene subunits of poly-2,7-[N]calicenes (**1-4**) are expected to have significant dipolar character with a five-membered ring that has significant cyclopentadienyl anion character and a three-membered ring that has significant cyclopropenyl cation character (Figure 2). Diffuse

functions are recommended for calculations involving anions; therefore, it is best to use the larger 6-31+G(d,p) basis set that includes diffuse functions on the second row atoms [26]. Poly-2,7-[N]calicenes **1-3** were indeed studied using the 6-31+G(d,p) basis set; however, poly-2,7-[5]calicene (**4**) could not be optimised using the 6-31+G(d,p) basis set. We have consistently found that calculations involving polycalicene molecules (even those with different bonding motifs) as large as poly-2,7-[5]calicene (**4**) or larger using the 6-31+G(d,p) basis set generate a numerical error [11-12]. To demonstrate the reliability of the 6-31G(d,p) NICS data, we have included the B3LYP/6-31+G(d,p) NICS(0) and NICS(1) data for poly-2,7-[N]calicenes **1-3** in Table 1 and the same data for reference molecules **5-9** in Table 2.

Table 1. B3LYP/6-31+G(d,p) NICS(0) and NICS(1) data for poly-2,7-[N]calicenes (**1-3**)

Ring	**NICS(0) (ppm)**				**NICS(1) (ppm)**			
	1	**2**	**3**	**4**	**1**	**2**	**3**	**4**
cpro	-22.9	-23.2	-23.4		-7.4	-7.5	-7.6	
cpro'	-21.2	-23.4	-23.8		-7.9	-8.1	-8.2	
cpro"		-21.5	-23.8			-8.3	-8.5	
cpro"'			-21.7				-8.6	
cpro""								
cpent	-5.6	-6.1	-6.6		-5.9	-6.2	-6.5	
cpent'	-4.7	-5.7	-6.2		-5.6	-6.2	-6.6	
cpent"		-4.8	-5.8			-5.6	-6.4	
cpent"'			-4.9				-5.8	
cpent""								

Table 2. B3LYP/6-31+G(d,p) NICS(0) and NICS(1) data for reference molecules (**5-9**)

Molecule		**Ring**	**NICS(0) (ppm)**	**NICS(1) (ppm)**
Calicene	**5**	Cpro	-20.5	-6.9
		Cpent	-4.5	-5.1
Bicalicene	**6**	Cpro	-23.3	-7.5
		Cpent	-4.7	-5.7
Benzene	**7**	Chex*	-8.1	-10.2
Cyclopentadienyl anion	**8**	Cpent	-12.8	-9.6
Cyclopropenyl cation	**9**	Cpro	-22.4	-14.5

* = six-membered ring

These data have been included to show that while the absolute values of the NICS data are different, essentially every trend (to be discussed) using the 6-31G(d,p) NICS data (Tables 3 and 4) is also found in the 6-31+G(d,p) NICS data in Tables 1 and 2. This validates the reliability of using

the 6-31G(d,p) NICS data compared to the 6-31+G(d,p) NICS data. Therefore, the discussion will only focus on the B3LYP/6-31G(d,p) NICS(0) and NICS(1) data because those results are complete and more detailed comparisons can be made.

B3LYP/6-31G(d,p) NICS Data

The B3LYP/6-31G(d,p) NICS(0) and NICS(1) data for poly-2,7-[N]calicenes (**1-4**) are detailed in Table 3 and the same data for reference molecules (**5-9**) are listed in Table 4.

Table 3. B3LYP/6-31G(d,p) NICS(0) and NICS(1) data for poly-2,7-[N]calicenes (**1-4**)

Ring	NICS(0) (ppm)				NICS(1) (ppm)			
	1	**2**	**3**	**4**	**1**	**2**	**3**	**4**
cpro	-23.5	-24.0	-24.3	-24.4	-7.9	-8.1	-8.2	-8.2
cpro'	-22.0	-24.0	-24.5	-24.6	-8.3	-8.6	-8.8	-8.9
cpro"		-22.2	-24.3	-24.7		-8.7	-9.0	-9.1
cpro"'			-22.4	-24.3			-8.9	-9.1
cpro""				-22.4				-9.0
cpent	-7.2	-7.7	-8.2	-8.3	-7.0	-7.3	-7.6	-7.7
cpent'	-6.0	-7.1	-7.6	-7.9	-6.6	-7.3	-7.7	-7.8
cpent"		-6.0	-7.2	-7.7		-6.7	-7.5	-7.8
cpent"'			-6.0	-7.2			-6.8	-7.5
cpent""				-6.2				-6.9

Table 4. B3LYP/6-31G(d,p) NICS(0) and NICS(1) data for reference molecules (**5-9**)

Molecule		Ring	NICS(0) (ppm)	NICS(1) (ppm)
Calicene	**5**	Cpro	-21.6	-7.6
		Cpent	-6.1	-6.4
Bicalicene	**6**	Cpro	-23.9	-8.0
		Cpent	-6.0	-6.8
Benzene	**7**	Chex*	-9.8	-11.3
Cyclopentadienyl anion	**8**	Cpent	-17.5	-12.5
Cyclopropenyl cation	**9**	Cpro	-22.4	-14.4

* = six-membered ring

The first and most notable overall trend revealed by the NICS results in Table 3 is that poly-2,7-[N]calicenes (**1-4**) are all aromatic according to the NICS criterion of aromaticity. All NICS values detailed in Table 3, both NICS(0) and NICS(1), are negative.

Before any discussion of how the aromaticity of the poly-2,7-[N]calicene varies with the length of the molecule and in particular how the aromaticity of the rings making up each molecule varies among **1-4**, it is logical to compare and contrast the NICS values of the reference molecules (Table 4) among themselves and how the NICS values of **1-4** compare to the reference molecules.

Benzene (**7**) is the archetypal aromatic molecule with an NICS(0) value of -9.8 ppm and NICS(1) value of -11.3 ppm and is included for completeness and illustration of the NICS method. However, none of the rings in the poly-2,7-[N]calicenes are benzene-like; instead, the rings are either three-membered or five-membered. The cyclopentadienyl anion (**8**) and cyclopropenyl cation (**9**) are more appropriate reference molecules, especially since the poly-2,7-[N]calicenes are expected to have significant charge separation.

The NICS(0) and NICS(1) values of cyclopentadienyl anion (**8**) (-17.5 ppm and -12.5 ppm respectively) are significantly lower than all cpent NICS(0) and NICS(1) values of **1-4**. This indicates that all cpent rings in **1-4** are significantly less aromatic than the cyclopentadienyl anion. This is reasonable since it is not expected that **1-4** would have complete charge separation between the cpro and cpent rings.

The NICS(0) value of cyclopropenyl cation (**9**) (-22.4 ppm) is higher than all the cpro NICS(0) values of **1-4** except for the cpro' NICS(0) of **1** (-22.0 ppm) and cpro" NICS(0) of **2** (-22.2 ppm). These results indicate that the cpro rings of **1-4** are as aromatic as the cyclopropenyl cation or in some cases even more aromatic. However, the NICS(1) value of **9** (-14.4 ppm) is significantly lower than the cpro NICS(1) values of **1-4** (all between -7.9 to -9.1 ppm). The cpro NICS(1) data indicate that the cpro rings of **1-4** are significantly less aromatic than the cyclopropenyl cation. The discrepancy between the cpro NICS(0) and NICS(1) data of **1-4** can be explained since NICS(0) values are known to be influenced by the σ-electrons and the extended conjugation found in **1-4** would distort the molecular framework and the σ-electrons. As mentioned earlier, NICS(1) values are regarded as more reliable since they are mainly influenced by the π-electrons.

While the cyclopentadienyl anion and the cyclopropenyl cation are better reference molecules than benzene, they are still isolated small ring molecules and do not fully reflect the molecular environment of the poly-2,7-[N]calicenes. Two better reference molecules are calicene (**5**) and bicalicene (**6**). These two molecules are expected to have significant dipolar character with a five-membered ring that has significant cyclopentadienyl anion character and a three-membered ring that has significant cyclopropenyl cation character, just as expected for poly-2,7-[N]calicenes (**1-4**).

The case for **1-4** being aromatic is strengthened because their NICS values are more negative than almost all of their corresponding NICS values in calicene (**5**). For example, **5** has a cpro NICS(0) of -21.6 ppm, compared to -22.0 ppm for cpro' of **1**, the highest NICS(0) value for all the cpro rings (cpro, cpro', cpro", cpro"' and cpro"") of **1-4**. The cpro NICS(1) value of **5** (-7.6 ppm) is also higher than the highest cpro NICS(1) value of **1-4** (-7.9 ppm) found in cpro of **1**. The cpent NICS(0) and NICS(1) values of **5** (-6.1 ppm and -6.4 ppm respectively) are higher than all but the respective terminal cpent NICS(0) values of **1-3** (all -6.0 ppm).

The most telling comparison is between the NICS(0) and NICS(1) values of **1-4** and those of bicalicene (**6**), because bicalicene was shown to be aromatic experimentally and a recent theoretical examination confirms the aromaticity of bicalicene [27]. Considering the cpro NICS results, only cpro **1** and the terminal cpro rings of **1-4** have higher NICS(0) values than the -23.9 ppm for the cpro of **6**. Even more important, the cpro NICS(1) of **6** (-8.0 ppm) is lower than only one of the total cpro NICS(1) values for **1-4**, the NICS(1) value of cpro **1** (-7.9 ppm). The cpent NICS(0) of **6** (-6.0

ppm) is higher than all but the terminal cpent NICS(0) values of **1-3** (all -6.0 ppm). Likewise, the cpent NICS(1) of **6** (-6.8ppm) is higher than all but the terminal cpent NICS(1) values of **1-3** (-6.6 ppm, -6.7 ppm and -6.8 ppm respectively).

The second main trend revealed by the data is that the molecules become more aromatic as the length of the poly-2,7-[N]calicene increases. This trend is easily confirmed by comparing either the NICS(0) or NICS(1) values of a specific ring across all poly-2,7-[N]calicenes containing that ring. All poly-2,7-[N]calicenes **1-4** have cpent, cpro, cpent′, and cpro′ rings so these are the most important rings to compare.

Looking at the first ring in **1-4**, the cpent NICS(0) values for (-7.2 ppm, -7.7 ppm, -8.2 ppm and -8.3 ppm respectively) and the cpent NICS(1) values (-7.0 ppm, -7.3 ppm, -7.6 ppm and -7.7 ppm respectively) all increase as the length of the molecule increases. The data for the second ring in **1-4** continues the trend with cpro NICS(0) values of -23.5 ppm, -24.0 ppm, -24.3 ppm and -24.4 ppm respectively, and cpro NICS(1) values of -7.9 ppm, -8.1 ppm, -8.2 ppm and -8.2 ppm respectively. The increase in aromaticity with the length of the molecule is also evident when comparing the second calicene subunit of **1-4,** with cpent′ NICS(0) values of -6.0 ppm, -7.1 ppm, -7.6 ppm and -7.9 ppm respectively, and cpent′ NICS(1) values of -6.6 ppm, -7.3 ppm, -7.7 ppm and -7.8 ppm respectively. The cpro′ NICS(0) values for **1-4** of -22.0 ppm, -24.0 ppm, -24.5 ppm and -24.6 ppm respectively, and the cpro′ NICS(1) values of -8.3 ppm, -8.6 ppm, -8.8 ppm and -8.9 ppm respectively, again reveal increasing aromaticity as the length of molecule increases.

The trend of increasing aromaticity as the length of the molecule increases also holds for the rings shared by the longer poly-2,7-[N]calicenes (**2-4**). The cpent" NICS(0) values for **2-4** of -6.0 ppm, -7.2 ppm and -7.7 ppm respectively, and cpent" NICS(1) values of -6.7 ppm, -7.5 ppm and -7.8 ppm respectively, all reflect the trend of increasing aromaticity as the length of the molecule increases. Likewise this trend is found in the cpro" NICS(0) values (-22.2 ppm, -24.3 ppm and -24.7 ppm respectively) and the cpro" NICS(1) values for **2-4** (-8.7 ppm, -9.0 ppm and -9.1 ppm respectively).

Even the rings shared by the longest poly-2,7-[N]calicenes (**3-4**) reflect the trend of increasing aromaticity as the length of the molecule increases, as shown by the cpent'" NICS(0) values (-6.0 ppm and -7.2 ppm respectively) and cpent'" NICS(1) values for **3-4** (-6.8 ppm and -7.5 ppm respectively. This trend is also found in the cpro'"NICS(0) values (-22.2 ppm and -24.3 ppm respectively) and cpro'" NICS(1) values for **3-4** (-8.9 ppm and -9.1 ppm respectively).

The data detailed above confirm that poly-2,7-[N]calicene increases in aromaticity as the length of the molecule increases. The only exception to this trend is found for the cpro NICS(1) values of **3** and **4** that remain the same (-8.2 ppm).

One of the two minor trends that can be teased out from the data, but only by majority consensus, is that the terminal cpro and cpent rings of each poly-2,7-[N]calicene (**1-4**) are the least aromatic of all the cpro and cpent rings in that poly-2,7-[N]calicene. This conclusion is supported by all the cpro NICS(0) values for **1-4**; for example, the cpro"" NICS(0) value of **4** is -22.4 ppm, compared to -24.4 ppm, -24.6 ppm, -24.7 ppm and -24.3 ppm for its other cpro NICS(0) values. The cpent NICS(0) values for **1-4** also reveal this trend; for example, the cpent"" NICS(0) value of **4** is -6.2 ppm, compared to -8.3 ppm, -7.9 ppm, -7.7 ppm and -7.2 ppm for its other cpent NICS(0) values. Likewise, the cpent NICS(1) values for **1-4** support the conclusion that the terminal rings of each poly-2,7-[N]calicene are less aromatic than their counterparts; for example, the cpent""

NICS(1) value of **4** is -6.9 ppm, compared to -7.7 ppm, -7.8 ppm, -7.8 ppm and -7.5 ppm for its other cpent NICS(1) values.

While the cpro NICS(0), cpent NICS(0) and cpent NICS(1) data support our conclusion that the terminal cpro and cpent rings of each poly-2,7-[N]calicene (**1-4**) are the least aromatic of all the cpro and cpent rings in that poly-2,7-[N]calicene, the cpro NICS(1) data contradict this conclusion. For example, the terminal cpro' of **1** has an NICS(1) value of -8.3 ppm while the cpro NICS(1) value is -7.9 ppm. Likewise the terminal cpro" of **2** has an NICS(1) value of -8.7 ppm compared to -8.6 ppm for cpro' and -8.1 ppm for cpro of **2**. The terminal cpro"' of **3** has an NICS(1) value of -8.9 ppm that is less aromatic than its cpro" at -9.0 ppm, but more aromatic than either the cpro' at -8.8 ppm or cpro at -8.2 ppm. Similar to **3**, the terminal cpro"" has an NICS(1) value of -9.0 ppm, which is less aromatic than either its cpro"' or cpro", both having an NICS(1) value of -9.1 ppm, but more aromatic than its cpro' at -8.9 ppm or cpro at -8.2 ppm. Note that as the length of the molecule increases, the cpro NICS(1) results become less of an exception to the trend that the terminal cpro and cpent rings of each poly-2,7-[N]calicene are the least aromatic of all the cpro and cpent rings in that poly-2,7-[N]calicene.

The second minor trend, by a slim majority of data and more correctly titled 'emerging trend', is that as the length of the molecule increases, the cpro and cpent rings near the middle of a poly-2,7-[N]calicene become more aromatic than their counterparts at either end of the same molecule. This emerging trend can be seen in the cpro NICS(0), cpro NICS(1) and cpent NICS(1) data. This trend is contradicted by the consistently decreasing cpent (cpent, cpent', cpent", cpent"' and cpent"") NICS(0) values for molecules **1-4**, for example -8.2 ppm, -7.6 ppm, -7.2 ppm and -6.0 ppm for cpent, cpent', cpent" and cpent"' respectively of **3**. However, a closer examination of the cpent NICS(0) results shows tantalising evidence that the terminal cpent rings are becoming more negative at a slower rate than the middle cpent rings. It is predicted that if longer poly-2,7-[N]calicenes were studied, this trend of the cpro and cpent rings near the middle of a poly-2,7-[N]calicene being more aromatic than their respective counterparts in the same molecule would be confirmed. It is planned to investigate longer poly-2,7-[N]calicenes and the results obtained should resolve the validity of both minor trends described above.

CONCLUSIONS

The NICS data indicate that poly-2,7-[N]calicenes (**1-4**) are aromatic, and the aromaticity increases as the number of calicene units (N) increases. These results reveal that poly-2,7-[N]calicenes are a novel family of non-benzenoid aromatic molecules and therefore are intriguing synthetic targets.

ACKNOWLEDGEMENTS

The computer time for this research was provided by the Mississippi Centre for Supercomputing Research.

REFERENCES

1. D. Lloyd, "What is aromaticity?", *J. Chem. Inf. Comput. Sci.*, **1996**, *36*, 442-447.
2. P. von Rague Schleyer and H. Jiao, "What is aromaticity?", *Pure Appl. Chem.*, **1996**, *68*, 209-218.
3. A. T. Balaban, "Is aromaticity outmoded?", *Pure Appl. Chem.*, **1980**, *52*, 1409-1429.

4. M. K. Cyranski, T. M. Krygowski, A. R. Katritzky and P. von Rague Schleyer, "To what extent can aromaticity be defined uniquely?", *J. Org. Chem.*, **2002**, *67*, 1333-1338.
5. T. M. Krygowski, M. K. Cyranski, Z. Czarnocki, G. Hafelinger and A. R. Katritzky, "Aromaticity: A theoretical concept of immense pratical importance", *Tetrahedron*, **2000**, *56*, 1783-1796.
6. V. I. Minkin, M. N. Glukhovtsev and B. Ya. Simkin, "Aromaticity and Antiaromaticity: Electronic and Structural Aspects", John Wiley and Sons, New York, **1994**.
7. B. Halton,"The fulvalenes", *Eur. J. Org. Chem*., **2005**, *16*, 3391-3414.
8. A. Al-Dulayymi, X. Li and M. Neuenschwander, "Further synthetic attempts towards calicene", *Helv. Chim. Acta*, **2000**, *83*, 1633-1644.
9. Z. -i. Yoshida, "Novel pi systems possessing cyclopropenylidene moiety", *Pure Appl. Chem.*, **1982**, *54*, 1059-1074.
10. S. Yonedo, M. Shibata, S. Kida, Z. Yoshida, Y. Kai, K. Miki and N. Kasai, "A novel aromatic hydrocarbon with 16π-electron periphery: Cyclic bicalicene", *Angew. Chem. Int. Ed. Engl.*, **1984**, *23*, 63-64.
11. W. E. Collier, "A computational investigation of some polycalicenes as novel nonbenzenoid aromatic molecules and the strange case of the cyclopropenyl anion", *PhD Dissertation*, **2009**, Mississippi State University, USA.
12. W. E. Collier and T. Ratanadachanakin, "The Potential of Bandcalicenes as carbon dioxide hosts", *J. Interdiscipl. Networks*, **2013**, *2*(Sp. Iss.), 112-117.
13. P. von Rague Schleyer, C. Maerker, A. Dransfeld, H. Jiao and N. J. R. van Eikema Hommes, "Nucleus-independent chemical shifts: A simple and efficient aromaticity probe", *J. Am. Chem. Soc.*, **1996**, *118*, 6317-6318.
14. A. D. Becke, "Density-functional thermochemistry. III. The role of exact exchange", *J. Chem. Phys.*, **1993**, *98*, 5648-5652.
15. C. Lee, W. Yang and R. G. Parr, "Development of the Colle-Salvetti correlation-energy formula into a functional of the electron density", *Phys. Rev. B*, **1988**, *37*, 785-789.
16. W. J. Hehre, R. Ditchfield, R. F. Stewart and J. A. Pople, "Self-consistent molecular orbital methods. IV. Use of gaussian expansions of slater-type orbitals. Extension to second-row molecules", *J. Chem. Phys.*, **1970**, *52*, 2769-2773.
17. R. Ditchfield, W. J. Hehre and J. A. Pople, "Self-consistent molecular orbital methods. IX. An extended gaussian-type basis for molecular-orbital studies of organic molecules", *J. Chem. Phys.*, **1971**, *54*, 724-728.
18. M. J. Frisch, G. W. Trucks, H. B. Schlegel, G. E. Scuseria, M. A. Robb, J. R. Cheeseman, G. Scalmani, V. Barone, B. Mennucci, G. A. Petersson, H. Nakatsuji, M. Caricato, X. Li, H. P. Hratchian, A. F. Izmaylov, J. Bloino, G. Zheng, J. L. Sonnenberg, M. Hada, M. Ehara, K. Toyota, R. Fukuda, J. Hasegawa, M. Ishida, T. Nakajima, Y. Honda, O. Kitao, H. Nakai, T. Vreven, J. A. Montgomery, Jr., J. E. Peralta, F. Ogliaro, M. Bearpark, J. J. Heyd, E. Brothers, K. N. Kudin, V. N. Staroverov, R. Kobayashi, J. Normand, K. Raghavachari, A. Rendell, J. C. Burant, S. S. Iyengar, J. Tomasi, M. Cossi, N. Rega, J. M. Millam, M. Klene, J. E. Knox, J. B. Cross, V. Bakken, C. Adamo, J. Jaramillo, R. Gomperts, R. E. Stratmann, O. Yazyev, A. J. Austin, R. Cammi, C. Pomelli, J. W. Ochterski, R. L. Martin, K. Morokuma, V. G. Zakrzewski, G. A. Voth, P. Salvador, J. J. Dannenberg, S. Dapprich, A. D. Daniels, O. Farkas, J. B. Foresman, J. V. Ortiz, J. Cioslowski and D. J. Fox, "Gaussian 09, Revision A.1", Gaussian Inc., Wallingford (CT), **2009**.

19. Z. Chen, C. S. Wannere, C. Corminboeuf, R. Puchta and P. von Rague Schleyer, "Nucleus-independent chemical shifts (NICS) as an aromaticity criterion", *Chem. Rev.*, **2005**, *105*, 3842-3888.
20. P. von Rague Schleyer, K. Najafian, B. Kiran and H. Jiao, "Are oxocarbon dianions aromatic?", *J. Org. Chem.*, **2000**, *65*, 426-431.
21. P. von Rague Schleyer, H. Jiao, N. J. R. van Eikema Hommes, V. G. Malkin and O. L. Malkina, "An evaluation of the aromaticity of inorganic rings: Refined evidence from magnetic properties", *J. Am. Chem. Soc.*, **1997**, *119*, 12669-12670.
22. S. Noorizadeh and M. Dardab, "A new NICS-based aromaticity index; NICS rate", *Chem. Phys. Lett.*, **2010**, *493*, 376-380.
23. A. Stanger, "Nucleus-independent chemical shifts (NICS): Distance dependence and revised criteria for aromaticity and antiaromaticity", *J. Org. Chem.*, **2006**, *71*, 883-893.
24. P. Seal and S. Chakrabarti, "Is nucleus-independent chemical shift scan a reliable aromaticity index for planar heteroatomic ring systems?", *J. Phys. Chem. A*, **2007**, *111*, 9988-9994.
25. P. Lazzeretti, "Assessment of aromaticity via molecular response properties", *Phys. Chem. Chem. Phys.*, **2004**, *6*, 217-223.
26. T. Clark, J. Chandrasekhar, G. W. Spitznagel and P. von Rague Schleyer, "Efficient diffuse function-augmented basis sets for anion calculations. III. The 3-21+G basis set for first-row elements, Li-F", *J. Comput. Chem.*, **1983**, *4*, 294-301.
27. W. P. Oziminski, M. Palusiak, J. Dominikowska, T. M. Krygowski, R. W. A. Havenith, C. M. Gibson and P. W. Fowler, "Capturing the elusive aromaticity of bicalicene", *Phys. Chem. Chem. Phys*., **2013**, *15*, 3286-3293.

Maejo Int. J. Sci. Technol. **2015**, *9*(01), 32-42; doi: 10.14456/mijst.2015.4

Maejo International Journal of Science and Technology

ISSN 1905-7873

Available online at www.mijst.mju.ac.th

Report

Diversity of phytoplankton in Kucukcekmece Lagoon channel, Turkey

Nese Yilmaz

Department of Freshwater Biology, Fisheries Faculty, Istanbul University, Ordu St. No: 200 Laleli, Istanbul, Turkey

E-mail: nyilmaz@istanbul.edu.tr; tel: +90 212 455 57 00; fax: +90 212 514 03 79

Received: 14 January 2014 / Accepted: 20 February 2015 / Published: 24 February 2015

Abstract: The composition and functional groups of phytoplankton in the channel from Kucukcekmece Lagoon to the Marmara Sea were investigated. Some water-quality parameters and nutrient variations were also recorded. Water samples were taken from the water surface between May-August 2008 at 5 sampling sites including the lake and the sea.

A total of 28 taxa were recorded, including Charophyta (1), Chlorophyta (4), Cryptophyta (1), Cyanophyta (3), Dinophyta (5), Euglenozoa (2) and Ochrophyta (12). According to the functional-group approach, the populations formed by 13 groups were most common in mesotrophic and eutrophic water.

The phytoplankton density (19-8842 individuals/cm^3) and chlorophyll-a content (4.45-40.36 mg/m^3) varied in broad ranges. The data from certain water-quality parameters and some nutrient experiments showed variations related to sampling points. As a result, the minimum and maximum water-quality parameters and nutrient concentrations were found to be in normal ranges. No high levels of nutrients were recorded. The presence of pollution indicated by freshwater and marine species with high chlorophyll-a concentrations showed that the study area was eutrophic.

Keywords: water quality, phytoplankton, Kucukcekmece Lagoon, Turkey

INTRODUCTION

Lagoon systems comprise approximately 13% of the earth's coastline. Coastal lagoons form a transition zone between terrestial and marine ecosystems, and are affected by physical, chemical and biological changes in both environments. They are unique and constitute very sensitive natural habitats for many life forms. They also have great socio-economic importance in terms of providing opportunities for agriculture, aquaculture, fishing, tourism and recreation [1]. Because of nutrient

richness, lagoons are one of the most productive coastal ecosystems, hosting a wide variety of species. Increasing pollution levels resulting from growing population and industrialisation pose a significiant threat to water quality and aquatic life in lagoons [2, 3].

Turkey is a coastal country surrounded by the sea on three sides and has a shoreline spanning about 7,816 km. There are 72 lagoon areas in Turkey [2]. Kucukcekmece Lagoon is in Marmara region and is considered to be a Class B wetland area. In the past the lake was a fishing area with a wide range of fish species as well as home to endemic plant species, migratory birds and waterfowls. The abolishment of its protected status, its opening to settlement in 1984, uncontrolled migration and consequent excessive construction have resulted in an increase in domestic pollution [4]. In addition, wastes from industrial establishments without treatment have caused further pollution [3].

Despite having great importance for Istanbul's metropolitan area, only a few limnological studies have been done in Kucukcekmece Lagoon. Some physico-chemical parameters were measured by Topcuoglu et al. [5]. The occurence of toxic cyanophytes was investigated by Albay et al. [6] and the water quality and heavy metal monitoring in water and sediment were done by Altun et al. [7]. Epipelic algae were studied by Polge et al. [8] and seasonal changes in zooplankton structures were examined by Ozcalkap and Temel [9]. A lagoon water quality index was applied to Kucukcekmece Lagoon by Taner et al. [1]. It was found that Kucukcekmece Lagoon is eutrophic and the level of eutrophication is gradually increasing. Topcuoglu et al. [5] found that the fish fauna has declined significantly. The increase of raw domestic sewage inputs from the growing lake-shore community has accelerated eutrophication. For public health Albay et al. [6] recommended monitoring cyanobacterial levels in the Kucukcekmece Lagoon, which is intensively used by Istanbul residents for recreational and fishery activities during the bloom seasons. Altun et al. [7] noted a remarkable increase in pollution and eutrophication since 1994 and high levels of heavy metal pollution in the sediment. Coskun et al. [10] pointed out an increase in pollution rate between 1992-2006 in urban areas of the Kucukcekmece Basin. Due to uncontrolled urban development especially on the southern part of the basin and motorway construction at the northern part of the basin, shoreline changes have occurred [10]. Ozcalkap and Temel [9] found high chlorophyll-*a* and nutrient concentrations in the water and the presence of indicator zooplankton species in the lake, indicating that it was being polluted by household wastes. However, information on water quality of this narrow channel where Lake Kucukcekmece opens into the Marmara sea is lacking.

In aquatic ecosystems primary producers are phytoplankton species, which are used as indicator organisms for detection of water pollution because of their sensitivity towards rapid aquatic changes [11, 12]. Phytoplankton species are indicated by their functional groups in terms of their tolerance and sensivity level to different combinations of physicochemical and biological properties of aquatic systems [13, 14]. Dangerous pollution levels in Kucukcekmece Lagoon are anthropogenic [5, 7, 10]. Phytoplankton diversity, trophic structure, productivity and nutrient levels are important factors for determining and monitoring the pollution rate in the lagoon. This paper reports on the composition and functional groups of phytoplankton related to specific water quality parameters and nutrients along the channel joining Kucukcekmece Lagoon to the Marmara Sea.

STUDY AREA AND CLIMATE

Istanbul is situated on both the European (Thrace) and Asian (Anatolia) sides of the Bosphorus and is one of the most populous cities of Eurasia and Turkey's cultural and financial

centre [15]. The area of Istanbul is around 5,750 km^2 and has a population of 14,160,000 (2014), 99% of which live in the city centre or suburban zones [16, 17].

Kucukcekmece Lagoon, with a surface area of 15.22 km^2, is located in the south-western part of Istanbul (41º00' N-28º43' E). It has a water capacity of 145 million cubic metres and a maximum depth of 20 metres. The streams that feed the lake are Nakkas, Ispartakule and Sazlidere [18, 19]. The freshwater inflow was notably reduced after 1998 upon the opening of Sazlidere Dam. The dam, with an annual capacity of 55 million cubic metres, is used for supplying potable water for Istanbul [20]. Kucukcekmece Lagoon is eutrophic and algal blooms occur usually during early spring and late fall. The study area covers the 1.5-km-long narrow channel which connects the lagoon with the Marmara Sea (Figure 1).

Figure 1. Map of study area (prepared by using Google Earth Programme and sampling stations (St. 1-5)

The climate in the study area is a subtropical type of the Mediterranean macro-climate. In the region the averages of annual temperature and annual precipitation from 1990 to 2000 were 14.4ºC and 666.8 mm respectively [8]. The rain regime and type are winter-autumn-spring-summer and central Mediterranean rain type respectively. The relative humidity is between 73-77%, which decreases to 65-68% in summer. The dominant wind type in the city is north-east originated [21].

SAMPLING AND ANALYSES

Samples were taken from the surface water at 5 stations (Figure 1) between May-August 2008, using Nansen bottles. The samples were subjected to Lugol's iodine for phytoplankton identification. Phytoplankton were counted with an inverted microscope according to Lund et al. [22]. Phytoplankton species were identified through references including several comprehensive reviews [23-32]. Phytoplankton functional groups have been employed to indicate environmental

conditions and have proved to be more precise than phylogenetic grouping [33]. In the scheme proposed by Reynolds [34] and updated by Reynolds et al. [13], phytoplankton species are grouped into 33 functional groups, nominated by alphanumeric codes based on their survival strategies, tolerance and sensitivities. Such functional groups have been succesfully applied to both the freshwater phytoplankton and marine dinoflagellates that produce harmful algal blooms [35]. In this study phytoplankton assemblages were classified according to Reynolds et al. [13]. Chlorophyll-*a* concentrations were estimated according to Parsons and Strickland's methodology [36]. Salinity, conductivity and pH were measured on site using a WTW multi-meter. Concentrations of ortho-phosphate (PO_4-P), nitrate-nitrogen (NO_3-N) and nitrite nitrogen (NO_2-N) were determined in the laboratory by employing standard methods [37].

COMPOSITION, FUNCTIONAL GROUPS AND CHLOROPHYLL-*a* OF PHYTOPLANKTON

A total of 28 planktonic algae were identified, belonging to Charophyta (1), Chlorophyta (4), Cryptophyta (1), Cyanophyta (3), Dinophyta (5), Euglenozoa (2) and Ochrophyta (12). The distribution of phytoplankton groups is shown in Figure 2 and the list of recorded taxa according to sampling sites is given in Table 1. Ochrophyta was dominant in terms of species numbers. Dinophyta and Cyanophyta were highest in density. *Peridinium bipes* and *Prorocentrum micans* (Dinophyta) were dominant species while *Euglena gracilis* (Euglenozoa) and *Merismopedia glauca* (Cyanophyta) were subdominant species.

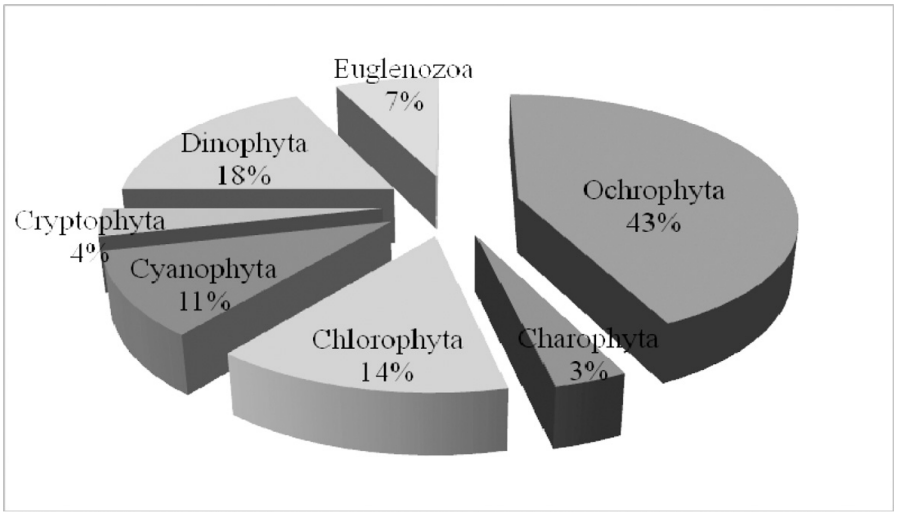

Figure 2. Diversity of phytoplankton groups in Kucukcekmece Lagoon channel

The density and chlorophyll-*a* content of the phytoplankton varied between 19-8842 individuals/cm^3 and 4.45-40.36 mg/m^3 respectively. The maximun phytoplankton density was recorded as 8842 individuals/cm^3 at station 3 in May 2008. *Peridinium bipes* and *Prorocentrum micans* were determined as dominant and subdominant species respectively. The minimum phytoplankton density was recorded as 19 individuals/cm^3 at station 4 in June 2008. *Prorocentrum micans* was recorded as the dominant species. The phytoplankton functional groups comprised more than 45 assemblages that were identified by alphanumerical codes in terms of their sensitivity and tolerance levels [13, 14]. In terms of functional group, the phytoplankton formed in 13 groups: B, C, D, N, X1, Y, F, J, Lo, M, MP, W1 and W2. These are typical for mesotrophic and eutrophic waters, tolerant to light and nutrient deficiencies and sensitive to nutrient depletion and increased

pH (Table 2). The Lo assemblage (*Peridinium bipes*, *Peridinium conicum and Merismopedia glauca*), which constituted a great part of the phytoplankton, is mostly found in summer epilimnia in mesotrophic lakes. It is tolerant to segregated nutrients and sensitive to prolonged or deep mixing. *Prorocentrum micans*, *Prorocentrum minimum* and *Peridinium bipes* may cause red tides under appropriate conditions. These species of dinoflagellates are considered harmful phytoplankton [38].

Table 1. List of recorded taxa at the five sampling sites (M: May 2008, J: July 2008, A: August 2008)

	St. 1			St. 2			St. 3			St. 4			St. 5		
	M	J	A	M	J	A	M	J	A	M	J	A	M	J	A
DIVISION:CHAROPHYTA															
Order: Desmidiales															
Cosmarium formosulum Hoff.	+	-	-	-	-	-	-	-	-	+	-	-	-	-	-
DIVISION:CHLOROPHYTA															
Order: Chlorococcales															
Monoraphidium falcatus Corda) Ralfs	-	+	+	-	-	-	+	-	-	+	-	-	+	-	-
Oocystis borgei J. Snow	-	-	-	+	-	-	-	-	-	-	-	-	-	+	-
Pediastrum dublex Meyen	-	+	-	-	-	-	-	-	-	-	-	-	-	-	-
Scenedesmus sp.	-	-	-	-	-	-	-	-	-	+	-	-	-	-	-
DIVISION: CRYPTOPHYTA															
Order: Cryptomonadales															
Cryptomonas ovata Ehr.	+	-	+	-	-	+	-	-	-	+	-	-	-	-	-
DIVISION: CYANOPHYTA															
Order: Chroococcales															
Merismopedia glauca (Ehr.) Naeg.	-	-	+	-	-	+	-	-	+	+	-	-	-	-	-
Microcystis aeruginosa (Kütz.) Kütz	+	-	-	-	-	-	-	-	-	+	-	-	-	-	-
Order: Oscillatoriales															
Oscillatoria tenuis C.Agarth Gomont	-	-	-	-	-	-	+	+	+	-	-	+	-	-	+
DIVISION: DINOPHYTA															
Order: Peridiniales															
Peridinium bipes F.Stein	+	-	-	+	-	+	+	-	-	+	-	-	+	-	-
Peridinium conicum (Gran) Ostenfeld & Schmidt	+	-	-	+	-	+	+	-	-	+	-	-	+	-	-
Prorocentrum concavum Fukuyo	-	-	+	+	-	+	-	-	+	-	+	+	-	-	+
Prorocentrum micans Ehr.	-	-	+	+	-	+	-	-	+	-	+	+	-	-	+
Prorocentrum minimum (Pavillard) J.Schiller	-	-	+	+	-	+	-	-	+	-	+	+	-	-	+
DIVISION: EUGLENOZOA															
Order: Euglenales															
Euglena gracilis G. A. Klebs	+	-	+	-	-	+	+	-	+	+	+	-	+	-	-
Trachelomonas hispida (Perty) F. Stein	+	-	-	+	-	+	+	-	-	-	-	-	-	-	-
DIVISION:OCHROPHYTA															
Order: Centrales															
Aulocoseira italica (Ehr.) Simonsen	-	-	-	-	-	-	-	+	-	-	-	-	-	-	-
Cyclotella atomus Hust.	+	-	+	+	-	+	+	-	-	+	-	-	-	-	-
Cyclotella ocellata Pant.	+	-	+	+	-	+	+	-	-	+	-	-	-	-	-
Order: Pennales															
Achnanthes lanceolata (Brébisson ex Kützing) Grunow	-	-	-	-	-	-	-	+	-	-	-	-	-	-	-
Asterionella formosa Hassal	+	-	-	+	-	-	-	-	-	-	-	-	-	-	-
Cocconeis placentula Ehr.	-	-	+	+	-	-	-	-	-	-	-	-	-	+	-
Cymbella affinis Kütz.	-	-	-	-	+	-	+	-	-	-	-	-	+	+	-
Diatoma vulgaris Bory de Saint-Vincent	+	-	-	-	-	-	-	-	-	-	-	-	-	-	-
Navicula cuspidata(Kütz.) Kütz.	+	-	+	-	-	-	-	+	-	-	+	-	-	-	-
Pinnularia viridis (Nitzsch) Ehr.	-	-	-	-	+	-	-	-	-	-	-	-	-	-	-
Ulnaria acus (Kutz.) M.Aboal	-	-	-	-	-	-	-	-	-	+	-	-	-	-	-
Ulnaria ulna (Nitzsch) P.Compere	-	-	+	-	+	+	-	+	+	-	-	-	+	-	-

According to previous studies carried out in the freshwaters in the Marmara region, Ochrophyta members were found to be the commonest group [8, 39-43]. Ochrophyta was represented by 12 species. *Cyclotella atomus* and *Cyclotella ocellata* (Centrales) were recorded at stations 1-4. These centric diatoms are typical components of oligotrophic lakes. *Cyclotella* species indicate mesotrophic lakes with species sensitive to the onset of stratification [44, 45]. *Aulocoseira italica* was only found at station 3. *Aulocoseira* spp. are found in mesotrophic and eutrophic waters [13]. Codon B was represented by *Cyclotella atomus*, *Cyclotella ocellata* and *Aulocoseira italica*— all centric diatoms. This group is tolerant to light deficiency and sensitive to a rise in pH. Codon C was represented by *Asterionella formosa* (Pennales), a species of small and medium eutrophic lakes [13], recorded at stations 1-2. *Ulnaria ulna* was found at all sampling points except station 4. It is a characteristic inhabitant of eutrophic lakes and prefers inorganically turbid, shallow lakes [13, 44, 46]. *Ulnaria acus* was only found at station 4. Codon D was represented by *U. acus* and *U. ulna* (pennate diatoms). They usually occur in shallow, enriched turbid waters and are sensitive to nutrient depletion [13, 14]. *Pinnularia viridis*, *Cocconeis placentula*, *Cymbella affinis* and *Navicula cuspidata* were recorded at station 2, stations 1, 2 and 5, stations 2, 3 and 5, and stations 1, 3 and 4 respectively. It has been determined that the numbers of diatom taxa are higher in water samples taken in May 2008 and July 2008. In general, increases in light and temperature lead to phytoplankton accumulation, especially to high diatom abundance in the spring [47].

Table 2. Functional groups of recorded phytoplankton species [13]

Codon	Habitat	Typical Representatives	Tolerance	Sensitivities
B	Vertically mixed, mesothrophic, small to medium lakes	*Aulocoseira italica* *Cyclotella atomus* *Cyclotella ocellata*	Light deficiency	pH rise, Si depletion stratification
C	Eutrophic, small- and medium-sized lakes	*Asterionella formosa*	Light, C deficiency	Onset of stratification
D	Shallow, enriched turbid waters including rivers	*Ulnaria acus* *Ulnaria ulna*	Flushing	Nutrient depletion
N	Mesotrophic epilimnia	*Cosmarium formosulum*	Nutrient deficiency	Stratification, pH rise
X1	Shallow, mixed layers in enriched conditions	*Monoraphidium falcatus*	Stratification	Nutrient depletion
Y	Usually small, enriched lakes	*Cryptomonas ovata*	Low light	Phagothrophs
F	Clear epilimnia	*Oocystis borgei*	Low nutrients high turbidity	CO_2 deficiency
J	Shallow, enriched lakes, ponds and rivers	*Pediastrum dublex* *Scenedesmus* sp.	-	Settling into low light
Lo	Summer epilimnia in mesotrophic lakes	*Peridinium bipes* *Peridinium conicum* *Merismopedia glauca*	Segregated nutrients	Prolonged or deep mixing
M	Dielly mixed layers of small, eutrophic, low latitude lakes	*Microcystis aeruginosa*	High insolation	Mixing, poor light stratification
MP	Frequently-stirred-up, inorganically turbid shallow lakes	*Achnanthes lanceolata* *Cymbella affinis* *Navicula cuspidata* *Oscillatoria tenuis*	-	-
W1	Small organic ponds	*Euglena gracilis*	High BOD	Grazing
W2	Shallow mesotrophic lakes	*Trachelomonas hispida*	-	-

Chlorophyta are usually found in abundance in mesotrophic and eutrophic lakes [40]. Chlorococcales have been recorded in aquatic environments which are transitioning from oligotrophic to eutrophic [45]. In this study Chlorococcales are represented by 4 species. The X1 assemblage includes *Monoraphidium falcatus*, which was recorded at all stations except station 2. Members of codon X1, found in shallow water in enriched conditions, are tolerant to stratification and sensitive to nutrient depletion. Members of the F group are tolerant to deep mixing and are present in clear water, with high diversity in mesotrophic lakes. The F assemblage, which can develop in clear epilimnia, is tolerant to low nutrients and high turbidity. It includes *Oocystis borgei*, which was only recorded at stations 2 and 5, and only a small increase was observed in July 2008 at station 5 (58 individuals/cm^3). The J assemblage consisted of *Pediastrum dublex* and *Scenedesmus* sp. (Chlorococcales), which are characteristic of shallow, enriched lakes, ponds and rivers. *Pediastrum dublex* and *Scenedesmus* sp. were only found at stations 1 and 4 respectively. *Scenedesmus* spp. are prominent in shallow, highly enriched systems [13] and are frequently dominant in freshwater lakes and rivers [48]. In the present study, *Scenedesmus* sp. was only recorded in low number (12 individuals/cm^3) in May 2008.

Cosmarium formosulum (Charophyta) is a member of the functional N group, tolerant to nutrient deficiency and sensitive to rises in pH and indicates mesotrophic waters. This species was recorded in low numbers at station 1 (35 individuals/cm^3) and station 4 (23 individuals/cm^3) in May 2008. Desmidiales members are very sensitive to chemical variations of water. Generally, they prefer acidic water and are used as indicators in aquatic systems [46].

Cyanophyta is represented by 3 taxa which usually prefer eutrophic environments [49]. *Merismopedia glauca*, a charachteristic of summer epilimnia in mesotrophic lakes, was recorded at stations 1-4. It is in the Lo assemblage and is tolerant to segregated nutrients and sensitive to prolonged or deep mixing [49]. Codon MP includes *Oscillatoria tenuis*, a typical filamentous cyanophyte of inorganically turbid shallow lakes, and was found at stations 3-5. The M assemblage is represented by *Microcystis aeruginosa*. It was recorded at stations 1 and 4. It is tolerant to high insolation and sensitive to mixing and poor light stratification. Species of *Oscillatoria* and *Microcystis* are known to be the cause of excessive blooms. *M. aeruginosa*, which usually inhabits eutrophic waters, is a cyanobacterium notorious for forming toxic water blooms all over the world. Shallow, warm and eutrophic reservoirs provide the most favourable conditions for its development [13, 14, 50]. *Microcystis* is a danger to public health, as well as all aquatic organisms and migratory birds, by secreting a toxin called microcystin into the water. Albay et al. [6] recorded microcystin at high levels in Kucukcekmece Lagoon.

Chlorophyll-*a* increased along the canal from the sea to the lagoon. Sokamoto [47] expressed that the chlorophyll-*a* content of eutrophic lakes is between 5-140 mg/m^3. Based on the chlorophyll-*a* values, it can be said that the study area is eutrophic.

PHYSICO-CHEMICAL PROPERTIES

The data for some water quality parameters and nutrients showed some differences which depend on the sampling points. The minimum and maximum water quality parameters and nutrient concentrations of water samples are shown in Table 3.

During this study, the average pH was 7.59. It is known that pH varies between 6-9 in clear waters [46]. Salinity and conductivity were lower than those of the sea and the lagoon. Phosphate concentration increased along the channel and the highest concentration was recorded in the lagoon. Maximum nitrite and nitrate concentrations were detected at stations 3-5. The minimum and

maximum water-quality parameters and nutrient concentrations were found to be in normal ranges. No high levels of nutrients were recorded.

Table 3. Minimum and maximum measured values of some physico-chemical parameters, nutrients and chlorophyll-*a* in Kucukcekmece Lagoon channel

	Minimum	**Maximum**
pH	6.27	8.31
Salinity (%)	11.8	24.9
Conductivity (mS/cm)	19.7	39.2
Nitrite (µg/L)	0.27	5.63
Nitrate (µg/L)	0.109	15.034
Ortho-phosphate (µg/L)	0.061	0.083
Chlorophyll-*a* (mg/m^3)	4.45	40.36

CONCLUSIONS

The functional group approach constitutes a useful means of understanding phytoplankton communities. Determining the trophic structure and pollution levels of aquatic environments in aquatic systems is a means of determining the health of aquatic systems. The presence of pollution indicated by freshwater and marine species with high chlorophyll-*a* concentrations shows that the study area was eutrophic. Continued studies and monitoring of phytoplankton are needed in the Kucukcekmece Basin.

ACKNOWLEDGEMENT

I am grateful to Mr. James Franklin Maxwell for language editing.

REFERENCES

1. M. U. Taner, B. Ustun and A. Erdincler, "A simple tool for the assessment of water quality in polluted lagoon systems: A case study for Kucukcekmece lagoon, Turkey", *Ecol. Indicat.*, **2011**, *11*, 749-756.
2. A. Kocatas, "Ecology, Environmental Biology", Ege University Faculty of Fisheries Publications, Izmir (Turkey), **2008** (in Turkish).
3. M. Kislalioglu and F. Berkes, "Ecology and Environmental Sciences", Remzi Bookstore, Istanbul, **2001** (in Turkish).
4. Istanbul Enviromental Status Report 2010-2011, TC Istanbul Governorship Environment and Urban Planning Directorate, **2011**.
5. S. Topcuoglu, N. Gungor and C. Kirbasoglu, "Physical and chemical parameters of brackish water lagoon, Kucukcekmece Lake, in northwestern Turkey", *Toxicol. Environ. Chem.*, **1999**, *69*, 101-108.
6. M. Albay, A. Matthiensen and G. A. Codd, "Occurence of toxic blue-green algae in the Kucukcekmece lagoon (Istanbul, Turkey)", *Environ. Toxicol.*, **2005**, *20*, 277-284.
7. O. Altun, M. T. Sacan and A. K. Erdem, "Water quality and heavy metal monitoring in water and sediment samples of the Kucukcekmece lagoon, Turkey (2002–2003)", *Environ. Monit. Assess.*, **2009**, *151*, 345-362.

8. N. Polge, A. Sukatar, E. N. Soylu and A. Gonulol, "Epipelic algal flora in the Kucukcekmece lagoon", *Turk. J. Fish. Aquatic Sci.*, **2010**, *10*, 39-45.
9. S. Ozcalkap and M. Temel, "Seasonal changes in zooplankton community structure in Lake Kucukcekmece, Istanbul, Turkey", *Turk. J. Zool*., **2011**, *35*, 689-700.
10. H. G. Coskun, U. Alganci and G. Usta, "Analysis of land use change and urbanization in the Kucukcekmece water basin (Istanbul, Turkey) with temporal satellite data using remote sensing and GIS", *Sensors*, **2008**, *8*, 7213-7223.
11. G. Nygaard, "Hydrobiological studies on some Danish ponds and lakes, part II: The quotient hypothesis and some new of little known phytoplankton organisms", Munksgaard, Kobenhavn (Denmark), **1949**.
12. C. S. Reynolds, "What factors influence the species composition of phytoplankton in lakes of different trophic status?", *Hydrobiologia*, **1998**, *369-370,* 11-26.
13. C. S. Reynolds, V. Huszar, C. Kruk, L. Naselli-Flores and S. Melo, "Towards a functional classification of the freshwater phytoplankton", *J. Plankton Res*., **2002**, *24*, 417-428.
14. J. Padisak, L. O. Crossetti and L. Naselli-Flores, "Use and misuse in the application of the phytoplankton functional classification: A critical review with updates", *Hydrobiologia*, **2009**, *621*, 1-19.
15. V. Altay, I. I. Ozyigit and C. Yarici, "Urban ecological characteristics and vascular wall flora on the Anatolian side of Istanbul, Turkey", *Maejo Int. J. Sci. Technol*., **2010**, *4*, 483-495.
16. E. Osma, I. I. Ozyigit, V. Altay and M. Serin "Urban vascular flora and ecological characteristics of Kadikoy district, Istanbul, Turkey", *Maejo Int. J. Sci. Technol*., **2010**, *4*, 64-87.
17. Turkish Republic Office of Prime Ministry Statistical Institute, http://www.tuik.gov.tr (Accessed: June 2014**)**.
18. F. Oktay and R. H. Eren, "The geology of the Istanbul metroploitan area", Istanbul Metropolitan Municipality Department of Reconstruction, City Planning Directorate, Istanbul, **1994** (in Turkish).
19. C. Senduran, "Investigation on limnological features and sediment transport in Kucukcekmece lagoon", *Master Thesis*, **2007** (in Turkish), Yildiz Technical University, Turkey.
20. N. Yilmaz, "Phytoplankton composition of Sazlidere Dam lake, Istanbul, Turkey", *Maejo Int. J. Sci. Technol*., **2013**, *7*, 203-211.
21. U. Yasar, I. I. Ozyigit and M. Serin, "Judas tree (*Cercis siliquastrum* L. subsp. *siliquastrum*) as a possible biomonitor for Cr, Fe and Ni in Istanbul (Turkey)", *Rom. Biotechnol. Lett*., **2010**, *15*, 4983-4992.
22. J. W. G. Lund, C. Kipling and E. D. Le Cren, "The inverted microscope method of estimating algal numbers and the statiscal basis of estimations by counting", *Hydrobiologia*, **1958**, *11*, 143-170.
23. F. Hustedt, "Bacillariophyta (Diatomeae) heft 10", in "Die Süsswasser-flora Mitteleuropas" (Ed. A. Pascher), Gustav Fischer Pub., Jena (Germany), **1930**.
24. T. V. Desikachary, "Cyanophyta", Monograph on Algae, Botany Department, University of Madras, New Delhi, **1959**.
25. G. W. Prescott, "Algae of Western Great Lake Area", W.M.C. Brown Co. Publishers, Dubuque (IA), **1961**.
26. G. W. Prescott, "Fresh Water Algae", W.M.C. Brown Co. Publishers, Dubuque (IA), **1964**.

27. R. Patrick and C. W. Reimer, "The Diatoms of the United States: Exclusive of Alaska and Hawaii", Vol. 1, The Academy of Natural Sciences, Philadelphia (PA), **1966**.
28. R. Patrick and C. W. Reimer, "The Diatoms of the United States: Exclusive of Alaska and Hawaii", Vol 2, The Academy of Natural Sciences, Philadelphia (PA), **1975**.
29. G. Huber-Pestalozzi, "Das Phytoplankton des Süsswassers: Systematik und Biologie: 2. Teil, 2. Halfte: Diatomeen, in Die Binnengewasser (Ed. A. Thienimann Teil 2 Diatomeen", E. Schweizerbartsche Verlagsbuchhandlung, Stuttgard, **1942**.
30. F. Hustedt, "The Pennate Diatoms", Koeltz Scientific Books, Koeningstein, **1985**.
31. K. Krammer and H. Lange-Bertalot, "Bacillariophyceae: Teil 3. Centrales, Fragilariaceae, Eunotiaceae", Gustav Fischer Verlag, Jena, **1986**.
32. D. M. John, B. A. Whitton and A. J. Brook, "The Freshwater Algal Flora of the British Isles", Cambridge University Press, New York, **2003**.
33. C. Kruk, N. Mazzeo, G. Lacerot and C. S. Reynolds, "Classification schemes for phytoplankton: A local validation of a functional approach to the analysis of species temporal replacement", *J. Plankton Res.*, **2002**, *24*, 901-912.
34. C. S. Reynolds, "Vegetation processes in the pelagic: A model for ecosystem theory", Ecology Institute, Oldendorf, **1997**.
35. C. Alves-de-Souza, M. T. Gonzalez and J. L. Iriarte, "Functional-groups in marine phytoplankton assemblages dominated by diatoms in fjord of southern Chile", *J. Plankton Res.*, **2008**, *30*, 1233-1243.
36. T. R. Parsons and J. D. H. Strickland, "Discussion of spectrophotometric determination of marine plant pigments, with revised equations for ascertaining chlorophylls and carotenoids", *J. Marine Res.*, **1963**, *21*, 155-163.
37. A. Greenberg (Ed.), "Standard Methods for the Examination of Water and Wastewater", 16th Edn., American Public Health Association, Washington, D.C., **1985**.
38. C. Alves-de-Souza, M. Menezes and V. Huszar, "Phytoplankton composition and functional-groups in a tropical humid coastal lagoon, Brazil", *Acta Bot. Bras*., **2006**, *20*, 701-708.
39. M. Temel, "The phytoplankton of lake Buyukcekmece, Istanbul, Turkey", *Pak. J. Bot*., **2002**, *34*, 81-91.
40. D. Karacaoglu, S. Dere and N. Dalkiran, "A taxonomic study on the phytoplankton of Lake Uluabat (Bursa)", *Turk. J. Bot*., **2004,** *28*, 473-485.
41. N. Yilmaz and G. Aykulu, "An investigation on the seasonal variation of the phytoplankton density on the surface water of Sapanca Lake, Turkey", *Pak. J. Bot*., **2010**, *42*, 1213-1224.
42. N. Yilmaz and Y. Gulecal, "Phytoplankton community of Terkos Lake and its influent streams, Istanbul, Turkey", *Pak. J. Bot*., **2012**, *44*, 1135-1140.
43. N. Yilmaz, "Phytoplankton composition of Sazlidere Dam lake, Istanbul, Turkey", *Maejo Int. J. Sci. Technol.*, **2013**, *7*, 203-211.
44. G. E. Hutchinson, "A Treatise on Limnology. Vol. II. Introduction to Lake Biology and the Limnoplankton", John Wiley and Sons, New York, **1967**.
45. I. S. Trifonova, "Phytoplankton composition and biomass structure in relation to trophic gradient in some temperate and subarctic lakes of north-western Russia and the Prebaltic", *Hydrobiologia*, **1998**, *369-370*, 99-108.
46. S. Cirik and S. Cirik, "Limnology", Ege University Faculty of Fisheries Publications, Izmir, **1991** (in Turkish).

47. S. Cirik and S. Gokpinar, "Plankton Knowledge and Culture", Ege University Faculty of Fisheries Publications, Izmir, **2006** (in Turkish).
48. M. K. Kim, J. W. Park, C. S. Park, S. J. Kim, K. H. Jeune, M. U. Chang and J. Acreman, "Enhanced production of *Scenedesmus* spp. (green microalgae) using a new medium containing fermented swine wastewater", *Bioresour. Technol.*, **2007**, *98*, 2220-2228.
49. J. Padisak and C. S. Reynolds, "Selection of phytoplankton associations in Lake Balaton, Hungary, in response to eutrophication and restoration measures, with special reference to the cyanoprokaryontes", *Hydrobiologia*, **1998**, *384*, 41-53.
50. N. A. Gaevsky, V. I. Kolmakov, O. I. Belykh, I. V. Tikhonova, Y. Joung, T. S. Ahn, V. A. Nabatova and A. S. Gladkikh, "Ecological development and genetic diversity of *Microcystis aeruginosa* from artificial reservoir in Russia", *J. Microbiol.*, **2011,** *49*, 714-720.

Maejo Int. J. Sci. Technol. **2015**, *9*(01), 43-53; doi: 10.14456/mijst.2015.11

Maejo International Journal of Science and Technology

ISSN 1905-7873

Available online at www.mijst.mju.ac.th

Full Paper

Microwave irradiation improves physico-chemical properties of soya meal for economic freshwater fish

Karun Thongprajukaew [1, 2,*], Uthaiwan Kovitvadhi [2, 3] and Pipatpong Chandang [4]

[1] Department of Applied Science, Faculty of Science, Prince of Songkla University, Songkhla, 90112, Thailand

[2] Biochemical Research Unit for Feed Utilisation Assessment, Faculty of Science, Kasetsart University, Bangkok, 10900, Thailand

[3] Department of Zoology, Faculty of Science, Kasetsart University, Bangkok, 10900, Thailand

[4] Interdepartmental Multidisciplinary Graduate Programme in Bioscience, Faculty of Science, Kasetsart University, Bangkok, 10900, Thailand

* Corresponding author, e-mail: karun.t@psu.ac.th

Received: 17 September 2013 / Accepted: 6 February 2015 / Published: 9 March 2015

Abstract: The effects of microwave heating time on the chemical composition, physico-chemical properties and *in vitro* digestibility of soya meal are investigated. Heating time has no effect on the protein, carbohydrate, fibre and ash content ($P > 0.05$), but microwave irradiation reduces the lipid content significantly ($P < 0.05$). The hydrolytic properties are different between raw and microwave-irradiated soya meals. The irradiation increases the degree of starch gelatinisation and water solubility of nutrients. Diffraction patterns show the same characteristics for all treatments, but relative crystallinity decreases dramatically. For nutrient utilisation, microwave irradiation of soya meal improves the *in vitro* digestibility of protein and carbohydrate for three economic fish species (Nile tilapia, broadhead catfish and striped snakehead). The changes in all observed parameters indicate that microwave irradiation for an appropriate time improves the physico-chemical properties of soya meal including the enhancement of enzymatic hydrolysis of its protein and carbohydrate.

Keywords: soya meal, microwave irradiation, Nile tilapia, broadhead catfish, striped snakehead

INTRODUCTION

The global utilisation of soya meal as a feed ingredient has progressively increased. Soya meal has been successfully used as a feedstuff for culturing various fish species. However, its nutritional content is limited due to a large amount of anti-nutritional compounds including goitrin,

phytohaemagglutinins, lectins, non-starch polysaccharides, phytate, phytoestrogens, protein antigens, saponins and trypsin inhibitor [1, 2]. These compounds can play a significant role in suppressing the growth and development of animals. Conventional heat treatment is used to reduce the toxic effects of these compounds and promote the utilisation of nutrients from the feedstuff [1, 3].

Microwave heating has been used to treat various food and feed for industries. In comparison to the conventional heating processes, the microwaves provide rapid heating characteristics and reduce energy costs [4]. Microwave irradiation has been practically used for improving the digestibility of protein [3, 5-8] and carbohydrate [5-7, 9-11] in various feedstuffs as well as in fish diet [12]. Pre-treatment of raw feedstuffs using microwave irradiation can enhance the enzymatic digestion by altering their physico-chemical properties such as protein and starch degradability [7], starch gelatinisation and water solubility [10-12], lignocellulosic content [9, 13] and relative crystallinity [9-11, 14]. However, the beneficial alterations of appropriate properties specifically occur at some optimal heating time that varies with different feedstuffs [7, 8, 11, 12, 15].

The effects of microwave heating time on the nutritional utilisation of soya meal for specific aquatic animals have not been evaluated previously. The main purpose of this study is therefore to improve the feed quality of soya meal using microwave irradiation. Three species of fish of high economic importance, namely Nile tilapia, broadhead catfish and striped snakehead, are used as sources of digestive enzymes to determine the protein and carbohydrate digestibility *in vitro* of the treated feedstuff.

MATERIALS AND METHODS

Preparation of Microwave-Irradiated Soya Meal

One hundred grams of unprocessed soya meal (Phatthalung Livestock Co., Phatthalung, Thailand) were placed in a plastic box (20-cm diameter × 10-cm height), mixed with distilled water (400 mL) and heated at 700W in a 20-L microwave oven (Sanyo, Model EM-700T, 2450 MHz). The box was covered with a lid during the microwave process. Uncooked raw soya meal was used as control. The control and microwave-irradiated soya meals were dried with a freeze dryer (Heto FD3, Heto-Holten, Denmark) for 48 hr and then ground, sieved and kept in a desiccator prior to investigations of their chemical composition, physico-chemical properties and *in vitro* digestibility.

Chemical Composition, Gelatinisation and Water Solubility

Raw and microwave-irradiated soya meals were analysed for their protein, lipid, fibre and ash contents as described by AOAC [16]. Carbohydrate or nitrogen-free extract was obtained by subtraction. Gross energy values were calculated from the combined amounts of crude protein, crude lipid and nitrogen-free extract. The degree of starch gelatinisation was determined spectrophotometrically at 600 nm according to Guraya and Toledo [17]. Water solubility was measured gravimetrically according to the method of Chung et al. [18] by calculating from the ratio of the weight of the dissolved solids in the supernatant to the weight of dry solids in the original sample.

Scanning Electron Microscopy and X-ray Diffraction

Micrographs were taken using a scanning electron microscope (Jeol JSM-5410W, Jeol Ltd., Japan) at magnifications of 750 and 3500, with the electric potential set at 15 kV. The soya meal samples were mounted on an aluminum stub using two-sided adhesive tape, with the sample then

coated with gold. X-ray diffraction patterns were observed with an X-ray diffractometer (X'Pert MPD, Philips, Netherlands) operating at a 40 kV and 40 mA. Diffractograms were recorded for 2θ in the range of 4–35°, with a scanning rate of 1^{o}/min. The relative crystallinity (%) was calculated from the ratio of the peak area to the total area (sum of peak areas and amorphous areas) of a diffractogram using Microsoft Excel 2007 (Microsoft Corp., USA).

Fish Preparation and *In Vitro* Digestibility

Fish preparation

Adult samples of the economic fish, namely Nile tilapia (*Oreochromis niloticus*), broadhead catfish (*Clarias macrocephalus*) and striped snakehead (*Channa striata*), were obtained from a farm in Songkhla province. The fish (n = 3) were acclimatised for 14 days in tanks (80-cm diameter × 40-cm height). The tank water was maintained at a temperature of 27.40 ± 0.30°C and a pH of 7.03 ± 0.07. The lighting was controlled at a diurnal cycle of 12-hr light/12-hr dark. All fish were fed *ad libitum* twice daily (08:00 hr and 18:00 hr) with commercial diet containing 20% crude protein (for Nile tilapia) and 37% crude protein (for broadhead catfish and striped snakehead). At the end of acclimatisation, all fish were starved for 24 hr prior to sampling. The fish were sacrificed by chilling in ice according to "Ethical Principles and Guidelines for the Use of Animals for Scientific Purposes" developed by the National Research Council of Thailand. The intestines of each fish were carefully collected and kept at –80°C until use.

Digestive enzyme extraction

The digestive enzyme from the small intestine of each fish species was extracted in 50 mM Tris-HCl buffer (pH 8) containing 200 mM NaCl (intestine: buffer = 1: 4) using a micro-homogeniser (Model THP-220, Omni International, USA). The homogenate was centrifuged at 15000*g* for 30 min. at 4^{o}C. The lipid portion (the upper layer) of the supernatant was carefully removed and the supernatant was collected and kept at -80^{o}C prior to *in vitro* digestibility test.

In vitro digestibility

Each enzyme extract was dialysed overnight against an extraction buffer (50 mM Tris-HCl buffer pH 8 containing 200 mM NaCl) a proportion of 1: 50 (enzyme extract: buffer). The protein and carbohydrate digestibility of the soya meals were then determined using the method described by Thongprajukaew et al. [12], with the reaction mixture containing the feedstuff (5 mg), 50 mM phosphate buffer pH 8.2 (10 ml), 0.5% chloramphenicol (50 µL) and the dialysed crude enzyme extract (125 µL). The protein and carbohydrate digestibility were determined by measuring the increase in the liberated reactive amino groups of cleaved peptides and the reducing sugar respectively after incubation with the digestive enzyme. The *in vitro* digestibility of protein and carbohydrate were expressed as mmol *DL*-alanine equivalent/g and µmol maltose/g respectively.

Statistical Analysis

Data were expressed as mean ± standard error of mean (SEM). All average values were calculated from triplicate observations (n = 3). A one-way ANOVA was used to evaluate the effects of microwave irradiation on the chemical composition, physicochemical properties and *in vitro* digestibility. Significant differences between the mean values were ranked using Duncan's Multiple Range Test at 95% significance level.

RESULTS AND DISCUSSION

Chemical Composition

No significant difference was found in the contents of protein, carbohydrate, fibre and ash in the raw and microwave-irradiated soya meals (Table 1). This is similar to the results obtained after microwave pre-treatment of leguminous seeds such as Bengal gram, green gram and horse gram [6] and canola seed [19] as well as fish diet [12]. However, the available carbohydrates were relatively higher after heating times of 15-20 min., and crude fibre was relatively higher after a 5-10-min. heating time when compared to the control ($P > 0.05$). This shows that microwave irradiation of soya meal could partially disrupt unavailable components in feedstuff, especially cell wall constituents, that to some extent govern the quality of nutrient utilisation [10, 11].

The lipid content of the microwaved soya meals significantly decreased after all heating times when compared with the control (Table 1). Similar reduction in fatty acid content have also been observed in soya bean and olive oil and found to depend on irradiation time and temperature [20, 21]. Irradiation activates the release of free unsaturated fatty acids and causes the formation of secondary oxidation products, decreasing the level of total fatty acids [20]. However, microwave treatment has been reported to have no effect on the crude lipid content of rice bran [11] or the saturated fatty acids in fish diet [22].

Physico-chemical Properties

Gelatinisation and water solubility

Microwaved soya meal had a significantly higher degree of gelatinisation than did the unmodified meal while the water solubility of the irradiated soya meal slightly increased (Table 1). These properties are important for starch digestibility and utilisation of feeds and feedstuffs [12, 22, 23], and contribute to the hydrolytic capacity of digestive enzymes, as observed by Thongprajukaew et al. [12], Chung et al. [18] and Lee et al. [24]. Increased gelatinisation and solubility of the microwave-treated soya meal may therefore improve digestion in animals.

Microstructure

With a small amount of starch, the macrostructure of soya meal during heating was coarse but not clotting. As for the microstructure, a rough surface was observed in the control (Figures 1a-b) and the microwaved samples with heating time of 5-10 min. (Figures 1c–f), while a smooth surface was mainly observed for the meal heated for 15-20 min. (Figures 1g-j). These findings show that the microwave treatment of soya meal has changed the architecture of the feedstuff. Similar observations have been reported with increased hydrolytic properties of the feedstuffs [25, 26].

Diffraction pattern

The diffraction patterns of raw and microwave-irradiated soya meals have similar characteristics in terms of position and strength of their peaks (Figure 2). Similar findings were reported by Thongprajukaew [22] and by other researchers in other raw and modified feedstuffs [18, 25, 27]. This indicates that microwave irradiation mainly affects the amorphous regions of the starch. As seen in Table 1, relative crystallinity decreased dramatically: 3.9- and 4.7-fold after 10- and 15-min. heating respectively. This probably occurred through a partial disruption of the crystalline regions after microwave irradiation. Therefore, the decrease in crystallinity of the

Maejo Int. J. Sci. Technol. **2015**, *9*(01), 43-53; doi: 10.14456/mijst.2015.11

Table 1. Chemical composition and physico-chemical properties of raw and microwave-irradiated soya meals with different heating times. Average values were obtained from triplicate determinations and are expressed on a dry-matter basis.

Composition/Property	Raw soya meal	Microwave-irradiated soya meal at different heating times				Pooled SEM
		5 min.	10 min.	15 min.	20 min.	
Chemical composition (%)						
Crude protein	45.28	45.81	45.82	45.28	44.61	< 0.001
Carbohydrate	35.53	35.04	35.89	36.55	37.43	< 0.001
Crude lipid	1.15[a]	0.70[b]	0.59[b]	0.72[b]	0.83[b]	0.004
Crude fibre	10.84	11.59	11.28	10.82	10.28	< 0.002
Crude ash	7.20	6.86	6.42	6.63	6.85	< 0.001
Gross energy (kJ/g)	18.37	18.22	18.34	18.38	18.42	< 0.001
Physico-chemical properties (%)						
Degree of gelatinisation	46.29[a]	52.70[b]	52.53[b]	50.75[b]	53.70[b]	0.960
Water solubility	7.74	7.83	8.79	8.61	8.28	0.200
Relative crystallinity	29.25	16.28	6.61	5.54	19.77	_

Note: Relative crytallinity was calculated from only one sample of each condition.
Values with different superscripts in the same row indicate significant difference ($P < 0.05$).

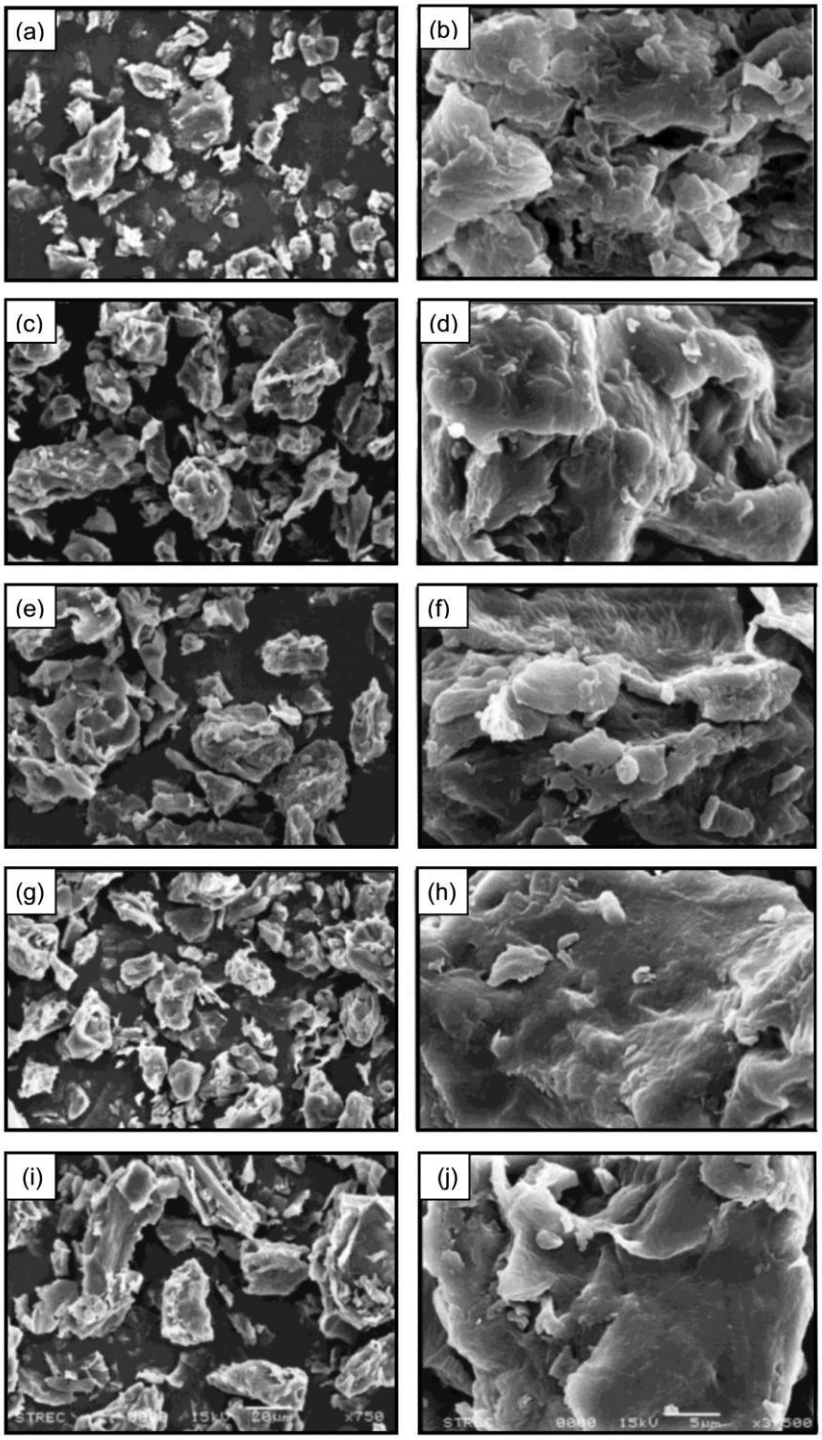

Figure 1. Scanning electron micrographs of raw soya meal (a and b) and soya meal microwave-irradiated for 5 min. (c and d), 10 min. (e and f), 15 min. (g and h) and 20 min. (i and j). The magnifications are 750× (left panel) and 3500× (right panel).

microwave-modified soya meal was due to an increase in the amorphous regions, which matches the observed increase in its starch gelatinisation and water solubility. This allows water to penetrate and increase the rate of hydrolytic reaction. On the other hand, crystallinity sharply increased again after a 20-min. heating. This result is similar to that found in rice straw after modifications by an

electron beam [28]. It is possible that prolonged microwave treatment might have induced a molecular reorganisation or transformation of cell wall constituents, especially cellulose, which is crystalline in nature.

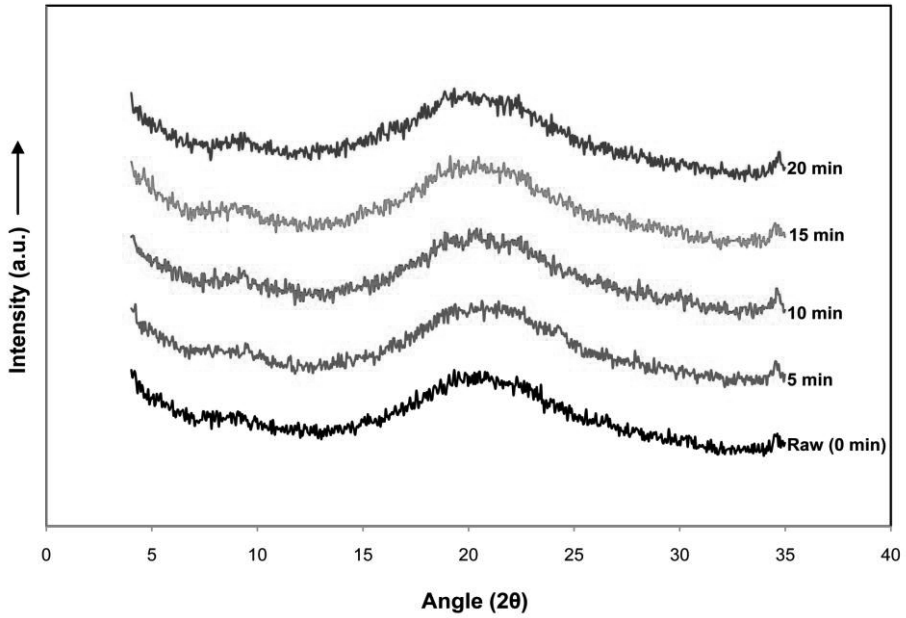

Figure 2. Diffraction patterns of raw and microwave-irradiated soya meal at different heating times

In Vitro Digestibility

Protein digestibility

Improved protein digestibility of various feedstuffs after microwave irradiation has been reported previously [3, 5, 6]. In this study, no significant difference was observed in the protein digestibility of treated and untreated soya meals for Nile tilapia (Table 2, $P > 0.05$), although a significant increase ($P < 0.05$) in digestibility of the treated meals was observed for both of the carnivorous fish, i.e. the broadhead catfish and the striped snakehead. Protein digestibility also tended to increase with heating time. Digested products for both species at the optimal heating time (15 min.) increased 1.17-fold on average when compared with the control. Differences in heating time for optimal protein digestibility have been reported [8, 12, 19]. They seem to be influenced by the method of material preparation including microwave intensity and substrate concentration [15], as well as by the source of digestive enzymes tested [8, 10]. Increased digestibility might stem from the unfolding of the protein, which exposes hydrophobic amino acids that act as active sites for pepsin and trypsin activities [29].

Upon prolonged heating, however, protein digestibility tended to decrease (Table 2). A decrease in *in vitro* protein digestibility after a 6-min. microwave irradiation of cottonseed meal when compared with a 4-min. irradiation has also been observed [8]. This phenomenon could be an effect of prolonged heating on the protein molecules, which results in, among other transformations, the formation of cross-linkage to a higher molecular weight aggregate and subsequent indigestibility. For soya meal, for example, a 6-min.-irradiated sample containing two subunits of β-conglycinin has been found to be more resistant to ruminal degradation than the one

Table 2. *In vitro* digestibility of protein (mmol *DL*-alanine equivalent/g) and carbohydrate (μmol maltose/g) of raw and microwave-irradiated soya meals using digestive enzyme extracts from Nile tilapia (100 U trypsin and 2000 U amylase), broadhead catfish (100 U trypsin and 1000 U amylase) and striped snakehead (100 U trypsin and 100 U amylase)

Digestibility	Raw soya meal	Microwave-irradiated soya meal at different heating times				Pooled SEM
		5 min.	10 min.	15 min.	20 min.	
Protein digestibility						
Nile tilapia	53.51	55.57	56.26	52.19	52.55	1.29
Broadhead catfish	16.29^{c}	18.29^{ab}	17.09^{bc}	18.49^{a}	17.41^{abc}	0.12
Striped snakehead	63.37^{b}	67.17^{a}	73.34^{ab}	75.46^{a}	68.15^{ab}	10.51
Carbohydrate digestibility						
Nile tilapia	57.82^{bc}	53.16^{c}	76.15^{ab}	90.37^{a}	54.99^{c}	27.67
Broadhead catfish	180.14^{bc}	134.08^{c}	208.80^{ab}	240.52^{a}	197.54^{ab}	160.82
Striped snakehead	50.74^{b}	46.39^{b}	86.50^{a}	88.43^{a}	76.83^{a}	15.09

Note: Different superscripts within the same row indicate a significant difference ($P < 0.05$).

Maejo Int. J. Sci. Technol. **2015**, *9*(01), 43-53; doi: 10.14456/mijst.2015.11

undergoing 4-min. irradiation [30]. This valuable characteristic increases the escape of protein from the rumen to the intestine for microbial fermentation [7, 8, 30]. In contrast, for monogastric animals, this change has a negative effect on the protein digestion along the alimentary tract.

Carbohydrate digestibility

The use of microwave irradiation for increasing the apparent digestibility of carbohydrates has been reported for various leguminous seeds such as moth bean [5], green gram, Bengal gram and horse gram [6]. From Table 2, carbohydrate digestibility of the treated and untreated soya meals was statistically different in the three fish species ($P < 0.05$). The highest values of digestion were observed in samples heated for 15 min., which increased the digestibility 1.56- and 1.34-fold on average for Nile tilapia and broadhead catfish respectively when compared with control samples. For striped snakehead, carbohydrate digestibility was unchanged in the range of 10–15 min. heating time ($P > 0.05$). On average, heating improved digestibility 1.72-fold when compared with control. Decreased digestibility of all samples subjected to prolonged heating (20-min.) may be associated with increased relative crystallinity (Table 1).

In a previous study of Nile tilapia, improved carbohydrate digestibility was observed for a 5-min. microwave-irradiated coconut meal (feedstuff: water = 1: 9) [10] as well as a 10-min. microwave-irradiated rice bran (feedstuff: water = 1: 3) [11], in comparison with the raw material. Similar results for catfish and striped snakehead were also reported using a 4-min. microwave-irradiated palm kernel meal (feedstuff: water = 1: 2) [9]. These differences in optimal irradiation time were due to the differences in type of feedstuff, ratio of feedstuff to water and source of digestive enzymes.

CONCLUSIONS

Microwave irradiation of soya meal for economic freshwater fish seems to have no significant effect on most of its chemical composition or its gross energy, except for a reduced lipid content of the meal. Irradiation for an appropriate time can improve its physico-chemical properties in such a way that its enzymatic hydrolysis is enhanced. These findings show that microwave irradiation of soya meal can improve nutrient utilisation, although the irradiation time should be optimised for each fish species. The use of microwave irradiation to modify soya meal for fish in aquaculture therefore appears to have significant potential.

ACKNOWLEDGEMENTS

This research is partially supported by the Department of Applied Science, Faculty of Science, Prince of Songkla University. The authors thank the Scientific Equipment Centre, Prince of Songkla University for help in sample analysis, and Assoc. Prof. Dr. Seppo Karrila of Research and Development Office, Prince of Songkla University and Dr. Brian Hodgson of the Faculty of Pharmaceutical Sciences for assistance with English proofreading.

REFERENCES

1. A. A. Sindhu, M. A. Khan, M. U. Nisa and M. Sarwar, “Agro-industrial by-products as a potential source of livestock feed”, *Int. J. Agric. Biol.*, **2002**, *4*, 307-310.
2. M. D. Drew, T. L. Borgeson and D. L. Thiessen, “A review of processing of feed ingredients to enhance diet digestibility in finfish”, *Anim. Feed Sci. Technol.*, **2007**, *138*, 118-136.

3. S. A. Alajaji and T. A. El-Adawy, "Nutritional composition of chickpea (*Cicer arietinum* L.) as affected by microwave cooking and other traditional cooking methods", *J. Food Comp. Anal.*, **2006**, *19*, 806-812.
4. N. H. Mermelstein, "How food technology covered microwaves over the years", *Food Technol*., **1997**, *51*, 82-84.
5. A. Negi, P. Boora and N. Khetarpaul, "Effect of microwave cooking on the starch and protein digestibility of some newly released moth bean (*Phaseolus aconitifolius* Jacq.) cultivars", *J. Food Comp. Anal.*, **2001**, *14*, 541-546.
6. N. Khatoon and J. Prakash, "Nutrient retention in microwave cooked germinated legumes", *Food Chem.*, **2006**, *97*, 115-121.
7. A. A. Sadeghi and P. Shawrang, "Effects of microwave irradiation on ruminal protein and starch degradation of corn grain", *Anim. Feed Sci. Technol.*, **2006**, *127*, 113-123.
8. A. A. Sadeghi and P. Shawrang, "Effects of microwave irradiation on ruminal protein degradation and intestinal digestibility of cottonseed meal", *Livest. Sci.*, **2007**, *106*, 176-181.
9. K. Thongprajukaew, P. Yawang, L. Dudae, H. Bilanglod, T. Dumrongrittamatt, C. Tantikitti and U. Kovitvadhi, "Physical modification of palm kernel meal improved available carbohydrate, physicochemical properties and *in vitro* digestibility in economic freshwater fish", *J. Sci. Food. Agric*., **2013**, *93*, 3832-3840.
10. S. Chumwaengwapee, S. Soontornchai and K. Thongprajukaew, "Improving chemical composition, physicochemical properties, and *in vitro* carbohydrate digestibility of fish coconut meal", *ScienceAsia*, **2013**, *39*, 636-642.
11. K. Sansuwan, K. Thongprajukaew, S. Kovitvadhi, P. Somsueb and U. Kovitvadhi, "Improvement of carbohydrate quality in rice bran using microwave irradiation for Nile tilapia feed production", *Asian Fish. Sci*., **2014**, *27*, 104-116.
12. K. Thongprajukaew, U. Kovitvadhi, S. Kovitvadhi, P. Somsueb and K. Rungruangsak-Torrissen, "Effects of different modified diets on growth, digestive enzyme activities and muscle compositions in juvenile Siamese fighting fish (*Betta splendens* Regan, 1910)", *Aquaculture*, **2011**, *322–323*, 1-9.
13. G. Y. S. Mtui, "Recent advances in pretreatment of lignocellulosic wastes and production of value added products", *Afr. J. Biotechnol.*, **2009**, *8*, 1398-1415.
14. G. Lewandowicz, T. Jankowski and J. Fornal, "Effect of microwave radiation on physico-chemical properties and structure of cereal starches", *Carbohydr. Polym.*, **2000**, *42*, 193-199.
15. H. Ma, W. W. Liu, X. Chen, Y. J. Wu and Z. L. Yu, "Enhanced enzymatic saccharification of rice straw by microwave pretreatment", *Bioresour. Technol.*, **2009**, *100*, 1279-1284.
16. W. Horsitz (Ed.), "Official Methods of Analysis", 18th Edn., Association of Official Analytical Chemists (AOAC), Washington, DC., **2005**.
17. H. S. Guraya and R. T. Toledo, "Determining gelatinized starch in a dry starchy product", *J. Food Sci.*, **1993**, *58*, 888-889.
18. H. J. Chung, S. Y. Lee, J. H. Kim, J. W. Lee, M. W. Byun and S. T. Lim, "Pasting characteristics and *in vitro* digestibility of γ-irradiated RS_4 waxy maize starches", *J. Cereal Sci.*, **2010**, *52*, 53-58.
19. S. R. Ebrahimi, A. Nikkhah and A. A. Sadeghi, "Changes in nutritive value and digestion kinetics of canola seed due to microwave irradiation", *Asian-Australas. J. Anim. Sci.*, **2010**, *23*, 347-354.

20. O. J. Stewart, G. S. V. Raghavan, V. Orsat and K. D. Golden, "The effect of drying on unsaturated fatty acids and trypsin inhibitor activity in soybean", *Process Biochem.*, **2003**, *39*, 483-489.
21. R. Malheiro, I. Oliveira, M. Vilas-Boas, S. Falcão, A. Bento and J. A. Pereira, "Effect of microwave heating with different exposure times on physical and chemical parameters of olive oil", *Food Chem. Toxicol.*, **2009**, *47*, 92-97.
22. K. Thongprajukaew, "Feed development using digestive enzyme technology for successive growth in Siamese fighting fish (*Betta splendens* Regan, 1910)", *PhD Thesis*, **2011**, Kasetsart University, Thailand.
23. X. Y. Wu, Y. J. Liu, L. X. Tian, K. S. Mai and H. J. Yang, "Utilization of different raw and pre-gelatinized starch sources by juvenile yellowfin seabream *Sparus latus*", *Aquacult. Nutr.*, **2007**, *13*, 389-396.
24. Y. J. Lee, S. Y. Kim, S. T. Lim, S. M. Han, H. M. Kim and I. J. Kang, "Physicochemical properties of gamma-irradiated corn starch", *J. Food Sci. Nutr.*, **2006**, *11*, 146-154.
25. A. Lopez-Rubio, B. M. Flanagan, A. K. Shrestha, M. J. Gidlev and E. P. Gilbert, "Molecular rearrangement of starch during *in vitro* digestion: Toward a better understanding of enzyme resistant starch formation in processed starches", *Biomacromolecules*, **2008**, *9*, 1951-1958.
26. H. J. Chung and Q. Liu, "Molecular structure and physicochemical properties of potato and bean starches as affected by gamma-irradiation", *Int. J. Biol. Macromol.*, **2010**, *47*, 214-222.
27. M. Kaur, K. S. Sandhu and S. T. Lim, "Microstructure, physicochemical properties and *in vitro* digestibility of starches from different Indian lentil (*Lens culinaris*) cultivars", *Carbohydr. Polym*., **2010**, *79*, 349-355.
28. J. S. Bak, J. K. Ko, Y. H. Han, B. C. Lee, I. G. Choi and K. H. Kim, "Improved enzymatic hydrolysis yield of rice straw using electron beam irradiation pretreatment", *Bioresour. Technol.,* **2009**, *100*, 1285-1290.
29. R. K. Murray, D. K. Granner, P. A. Mayes and V. W. Rodwell, "Harper's Biochemistry", 26th Edn., McGraw-Hill, New York, **2003**.
30. A. A. Sadeghi, A. Nikkhah and P. Shawrang, "Effects of microwave irradiation on ruminal degradation and *in vitro* digestibility of soya-bean meal", *Anim. Sci*., **2005**, *80*, 369-375.

Maejo Int. J. Sci. Technol. **2015**, *9*(01), 54-63; doi: 10.14456/mijst.2015.6

Maejo International Journal of Science and Technology

ISSN 1905-7873
Available online at www.mijst.mju.ac.th

Full Paper

Influence of drying method on drying kinetics and qualities of longan fruit leather

Somkiat Jaturonglumlert [1,*], Jatuphong Varith [1] and Tanongkiat Kiatsiriroat [2]

[1] Division of Food Engineering, Faculty of Engineering and Agro-Industry, Maejo University, Chiang Mai, Thailand
[2] Department of Mechanical Engineering, Faculty of Engineering, Chiang Mai University, Chiang Mai, Thailand
* Corresponding author, e-mail: yaidragon@mju.ac.th

Received: 16 April 2014 / Accepted: 10 March 2015 / Published: 13 March 2015

Abstract: The effects of some drying techniques (hot-air drying, far-infrared drying and microwave-vacuum drying) on the qualities of longan fruit leather, as well as on the drying rate, specific energy consumption, and other properties of longan fruit leather were studied. The drying time for microwave vacuum drying was shortest and the specific energy consumption was also lowest. However, far-infrared drying gave products with the best qualities. It also reduced the drying time and specific energy consumption in comparison to hot-air drying and was found to be suitable for the production of longan fruit leather.

Keywords: longan fruit leather, hot-air drying, microwave-vacuum drying, far-infrared drying, fruit leather

INTRODUCTION

Drying is one of the most common methods of food preservation. The major aim is to remove moisture to the desirable level at which microbial spoilage and deteriorative chemical reactions are avoided or greatly minimised. Every drying technique has its own advantages and disadvantages. Hot air (HA) drying is a conventional method, but its long exposure times can cause serious damage to the flavour, colour, nutritional value and rehydration capacity of the dried products [1]. Drying by far-infrared (FIR) radiation is a technique for speeding up the conventional drying process as well as improving the quality of the dried product. FIR drying can be used to accelerate a drying process because this form of energy can be directly absorbed by the dried product without significant losses to the environment. The reduction in drying time for a variety of food products has been reported by many researchers. FIR drying has also been proven to be more effective with products that have a high moisture content [2-5]. Microwave vacuum (MWV) drying is a method that can be utilised at low temperatures in the absence of oxygen. MWV drying

combines the advantages of rapid volumetric heating by microwaves and low-temperature evaporation of moisture, with faster moisture removal than vacuum drying. This method can dry a product in a shorter time because microwaves penetrate into the interior of the product and cause the water to boil at a comparatively low temperature, owing to the reduced pressure in the drying chamber [6]. Due to the water boiling inside the product, there is a relative difference in pressure between the interior of the product and the environment, enabling extremely quick water vapour removal and producing favourable conditions for the occurrence of the puffing phenomenon [7].

Fruit leather is a dried sheet of fruit pulp that has a soft, rubbery texture and sweet taste. It can be made from most fruits, although mango, apricot, banana, tamarind and longan leathers are amongst the most popular [8]. Fruit leathers are made by removing moisture from a large flat tray of wet puree until the desired cohesive leathery composition is obtained [9]. The fruit leather should not be dried in direct sunlight as this will cause the fading of colour and reduction of the levels of vitamins A and C. Indirect solar dryers or mechanical dryers should be used [10, 11]. The objective of this study is to compare the effect of HA, FIR and MWV drying methods on the drying kinetics, physical characteristics and qualities of longan (*Dimocarpus longan*) fruit leather.

MATERIALS AND METHODS

Experimental Set-up

A double-function dryer, which can be used either as an HA or FIR dryer, is shown in Figure 1. The dryer consists of a blower for supplying air into the drying chamber. The entering air velocity can be varied between 0-4.5 m/s and the temperature can be controlled at 30-80^{o}C by an electrical heater. The drying chamber is a well-insulated rectangular duct equipped with an FIR ceramic heater (800W maximum power, Model EL-3, EDF Industrial Automation Co., Malaysia) and an intensity-level control. The sample to be dried is kept in a tray under the heater.

The weight of the sample can be recorded every 5 minutes during drying by an electronic balance (cp3202s, Sartorius, Germany) with an accuracy of ± 0.01 g. The air velocity is measured by an anemometer with an accuracy of ± 0.1 m/s at the position over the sample. The fan speed is controlled by a variable electronic transistor inverter (Model VFD-S, Delta Electronics Inc., Taiwan). The air temperature and relative humidity are controlled by a digital controller (Model MAC3F, Shimax Co., Japan).

A K-type thermocouple (30-gauge hypodermic needle probe, Omega Engineering Co., USA) is inserted from the top into the centre of the sample to be dried. The thermocouple wire is kept inside an aluminum rod that serves as a shield from radiation. The surface temperature is measured by an infrared optical pyrometer (Model OS550, Omega Engineering Co., USA), which is focused at a 0.009-m-diameter circle from a 0.61-m distance. The spot location is confirmed by a laser sighting viewer (Model OS550-LS, Omega Engineering Co., USA) prior to each run. A monitoring programme is used to log the data, which are then downloaded into a computer.

A 22-L, 800W MWV dryer with a 0.2-kW motor (Model R-254, Sharp Corp., Japan) used in this experiment is shown in Figure 2. The vacuum in the drying cavity is maintained by a vacuum pump (1.5 kW, ICME, TMB90LB4, Busch Vacuum Co., Italy). The dimensions of the microwave chamber are 500 x 500 x 500 mm. The plate in the chamber rotates at 10 rpm during its operation to even out the volumetric heating of the product. The microwave power density used is 1,000 W and the microwave frequency is 2,450 MHz. The maximum vacuum pressure is 15 inches Hg.

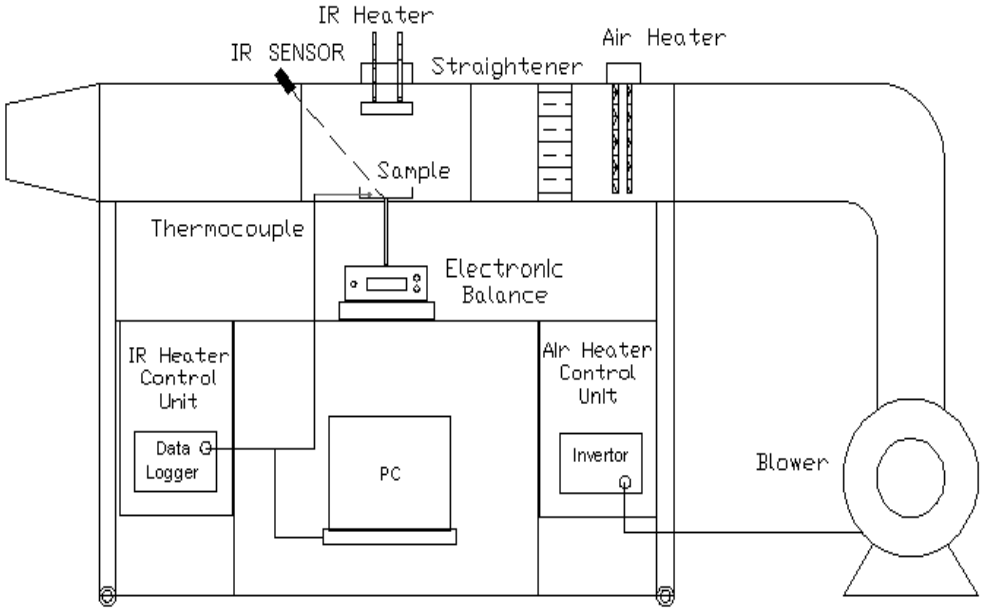

Figure 1. Schematic diagram of a double-function (HA/FIR) dryer [3]

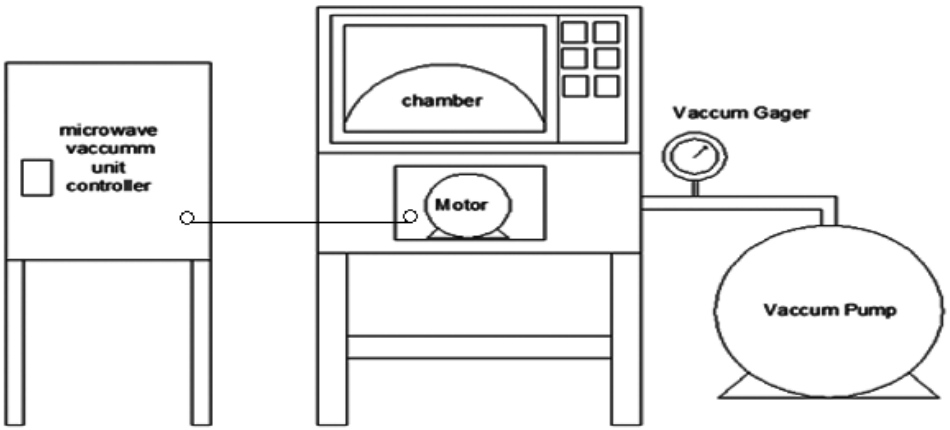

Figure 2. Schematic diagram of MWV dryer

Materials

Each sample of 150 g of longan puree was prepared by blending fresh longan and spreading the blend uniformly in a single layer in an aluminum tray (Figure 3) that was kept inside the drying chamber. The sample thickness was measured with a dial micrometer; at least five measurements of the thickness were made at different points and only 5% deviation of the average thickness was allowed for each sample. The final moisture content of the longan fruit leather was considered at a 13 % (dry basis) [10].

Methods

Drying

HA drying was done with hot air temperatures of 70^{o}, 75^{o} and 80^{o} C and air velocities of 0.50, 0.75 and 1.00 m/s. FIR drying was conducted at three radiator temperatures of 350^{o}, 400^{o} and

450^{o} C with distance between the samples and the infrared heat source of 15-25 cm. The inlet air temperature and velocity were kept constant at 30^{o}C and 0.5 m/s respectively. MWV drying was done at the microwave power densities of 60.8 and 121.7 W, and 10 and 15 inches of vacuum with a fixed mass load of product.

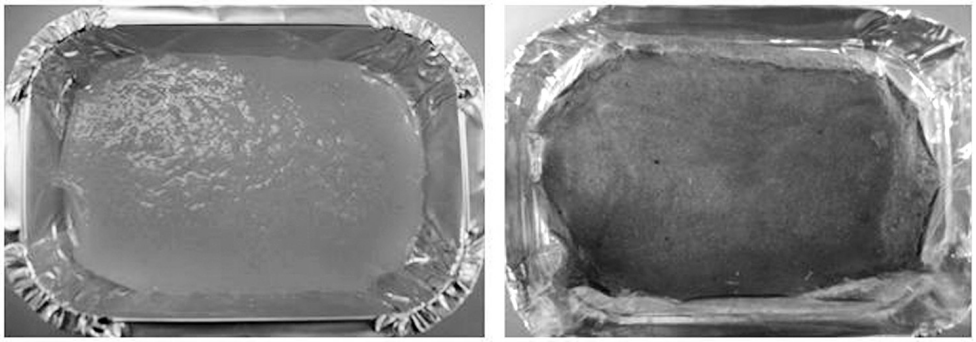

a) Longan puree b) Longan fruit leather

Figure 3. Longan fruit in drying tray

Moisture content

The moisture content was determined by the oven method. At regular time interval during the drying process, samples were taken out and dried in the oven for 3-4 hours at 105^{o} until a constant weight was achieved. Weighing was performed using a digital balance and the moisture content (wet basis) was calculated. The tests were performed in duplicate.

Colour

Colour measurements were performed using a colour difference meter (Model CR-200, Konica Minolta Co., Japan). The coordinates of the colour, viz. CIE L* (whiteness/darkness), a* (redness/greenness) and b* (yellowness/blueness), of the skin of the leather samples were obtained by reflection. Each sample was measured in quintuplicate. The total colour difference (ΔE) was determined as follows:

$$\Delta E = \sqrt{(L_0^* - L^*)^2 + (a_0^* - a^*)^2 + (b_0^* - b^*)^2},$$

where subscript 0 denotes the colour of the referenced classical production of longan fruit leather [8].

Texture

A texture analyser (Model TA-XT2i.plus, Stable Micro System Ltd., UK) was used to measure the hardness and gumminess in Newton (N) unit. A spherical stainless probe (2.5-mm diameter) was passed through the fruit leather sample with the test parameter set at 2 mm/s for pre-speed and post-speed, 2 mm/s for test speed and 20 g trigger. In penetration test, the hardness is the maximum force required to break the sample. Three samples were used in each treatment.

Specific energy consumption

The energy efficiency of the drying process was indicated in terms of specific energy consumption (SEC), which was calculated as: total energy used for drying (kJ) / total amount of water evaporataed from product (kg).

RESULTS AND DISCUSSION

Drying Kinetics of Longan Fruit Leather

Figure 4 shows the drying rates of the samples subjected to HA, FIR and MWV drying. For HA drying, at the same air velocity (0.5 m/s), the average drying rates at 70^o, 75^o and 80^o were 0.244, 0.269 and 0.358 $kg_{water}/h\ kg_{dry\ solid}$ respectively. It can be clearly seen that the drying rate increased with an increase in air velocity and hot air temperature. In the case of FIR drying, at the same distance (25 cm) between the samples and the infrared heat source, the average drying rates at 350^o, 400^o and 450^o were 0.255, 0.314 and 0.508 $kg_{water}/h\ kg_{dry\ solid}$ respectively. The drying rate was found to increase with increased radiator temperatures and decreased distance between the sample and the infrared heat source. For MWV drying, at the same vacuum level (10 in.Hg), the average drying rates at 60.8 W and 121.7 W were 0.815 and 1.952 $kg_{water}/h\ kg_{dry\ solid}$ respectively. The drying rates at 10 inches and 15 inches of vacuum were not significantly different.

Table 1 shows the drying kinetics data involved in producing longan fruit leather by HA, FIR and MWV drying. HA drying took the longest time while the drying time for MWV drying was the shortest (Table 1 and Figure 5). MWV drying is therefore the fastest drying option based solely on drying time. Note that drying by the classical method of longan fruit leather production by combining solar drying and HA drying takes roughly 32 hours [8].

The total energy used for HA drying was measured by the electric power supplied to the air heater and the air blower motor, while that for FIR drying was measured by the electric power supplied to the infrared heater and the air blower motor. For MWV drying, the electric power supplied to the microwave generator and the vacuum pump motor was taken into account in the energy analysis. Figure 6 shows that the SEC of MWV drying is lowest due to the least electric power consumed, while FIR drying exhibits lower SEC than does HA drying (more than 50% lower).

Qualities of Longan Fruit Leather

Table 2 and Figure 7 show experimental results on the qualities of longan fruit leather. Compare to fresh longan, the dried longan fruit leather gave a lower value of lightness and higher value of redness and yellowness. For FIR drying, the sample was brightest due to its lightness and yellowness values. Increasing higher power into FIR drying led to greater colour changes, indicating a phenomenon that accelerates non-enzymatic browning reactions. The same reason can also be applied to other methods. The colour difference (ΔE value) from the classical production of longan fruit leather [8] is an indication of the drying qualities. It was found that FIR drying gave the smallest colour difference values.

Texture is considered as one of the most important criteria for consumer acceptance of snack foods. As shown in Table 2, the texture of the fruit leather from MWV drying is harder than that from HA and FIR drying. MWV drying has also been reported to increase the hardness of texture and result in a more rigid structure of a dried product [7]. There is no significant difference between the gumminess values of the leather from different drying methods. Figure 7 shows the appearance of longan leather samples from HA, FIR and MWV drying methods. The surface of the fruit leather from MWV drying is rougher and more brittle than those from HA and FIR drying. It is also dense in structure and shows fractures, while the surface of the sample from FIR drying is smooth and bright.

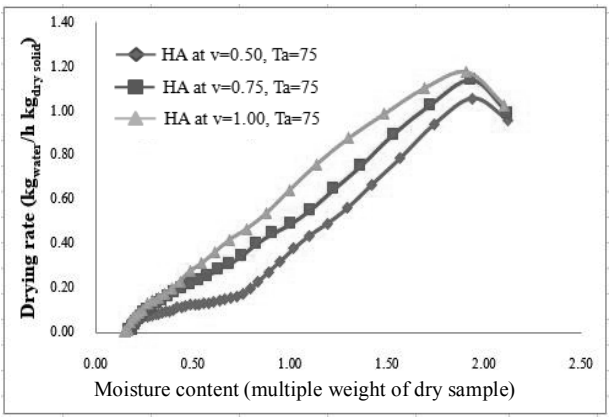

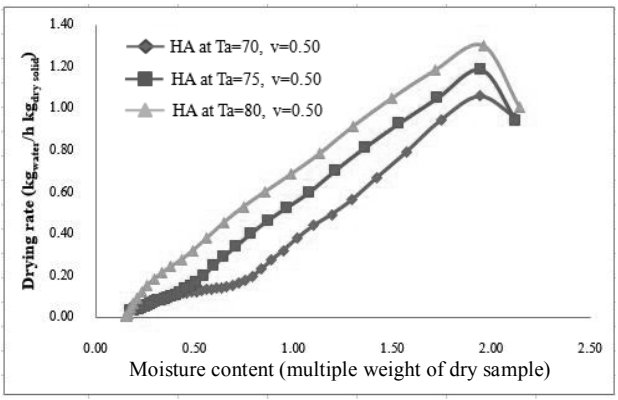

a) HA drying at constant hot air temperature and constant air velocity

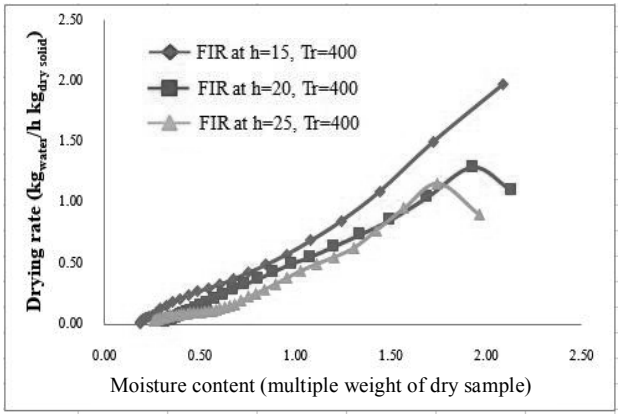

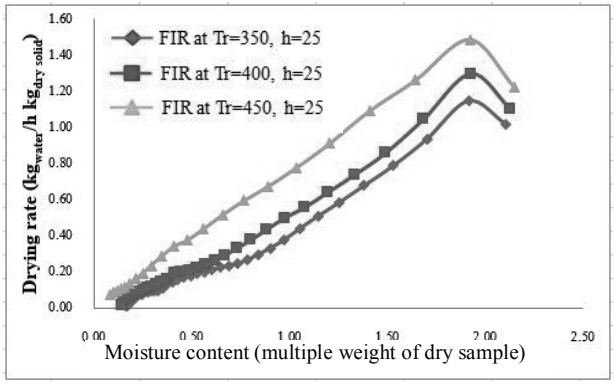

b) FIR drying at constant radiator temperature and constant distance between sample and infrared heat source

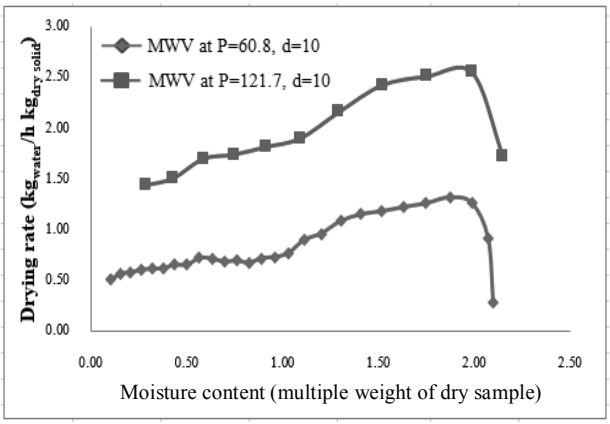

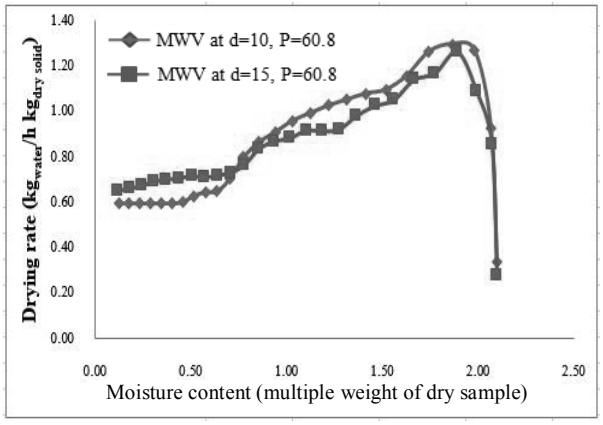

c) MWV drying at constant vacuum and constant microwave power density

Figure 4. Comparison of drying rate for (a) HA (b) FIR and (c) MWV drying.
Notation: Ta = hot air temperatures (^{o}C); v = air velocity (m/s); Tr = radiator temperature (^{o}C); h = distance between sample and infrared heat source (cm); P = microwave power density (W); d = vacuum degree (inches Hg)

Table 1. Drying times, drying rates and specific energy consumption during the drying process of longan fruit leather

Drying method		Drying kinetics		
		DT (hr)	DR (kg_{water}/h $kg_{dry\ solid}$)	SEC (kJ/ kg_{water})
HA	0.50 m/s, 70°C	24.0	0.244	6,555.2
	0.50 m/s, 75°C	22.0	0.269	6,447.8
	0.50 m/s, 80°C	20.0	0.358	6,179.1
	0.75 m/s, 70°C	22.0	0.269	5,319.4
	0.75 m/s, 75°C	19.5	0.310	5,050.8
	0.75 m/s, 80°C	18.0	0.416	4,889.6
	1.00 m/s, 70°C	20.0	0.380	4,567.2
	1.00 m/s, 75°C	18.5	0.420	4,513.4
	1.00 m/s, 80°C	17.0	0.450	4,405.9
FIR	15 cm, 350°C	12.5	0.394	1,714.8
	15 cm, 400°C	11.5	0.490	1,333.7
	15 cm, 450°C	10.0	0.530	952.7
	20 cm, 350°C	13.0	0.268	1,952.9
	20 cm, 400°C	12.5	0.375	1,714.8
	20 cm, 450°C	11.5	0.516	1,143.2
	25 cm, 350°C	14.5	0.255	2,191.1
	25 cm, 400°C	13.5	0.314	2,048.2
	25 cm, 450°C	12.5	0.508	1,428.9
MWV	10 inches Hg., 60.8 W	4.3	0.841	822.6
	15 inches Hg., 60.8 W	4.1	0.844	846.4
	10 inches Hg., 121.7 W	2.2	1.950	365.6
	15 inches Hg., 121.7 W	2.1	1.952	386.5
Sampanvejsobha et al. [8]		32.0	-	-

Notes: DT = drying time; DR = drying rate; SEC = specific energy consumption. Each value represents means of three replications and drying time is that taken to dry sample to 13% moisture (dry basis).

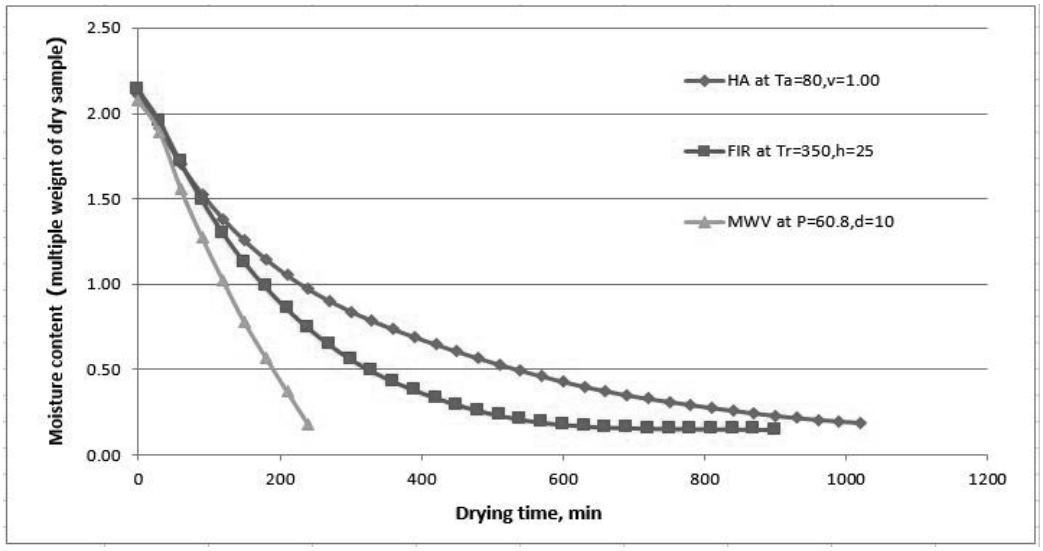

Figure 5. Comparison of drying curves for: 1) HA drying at 80°C and 1.00-m/s air velocity; 2) FIR drying at 350°C and 25-cm distance; 3) MWV drying at 60.8 W and 10-inch vacuum

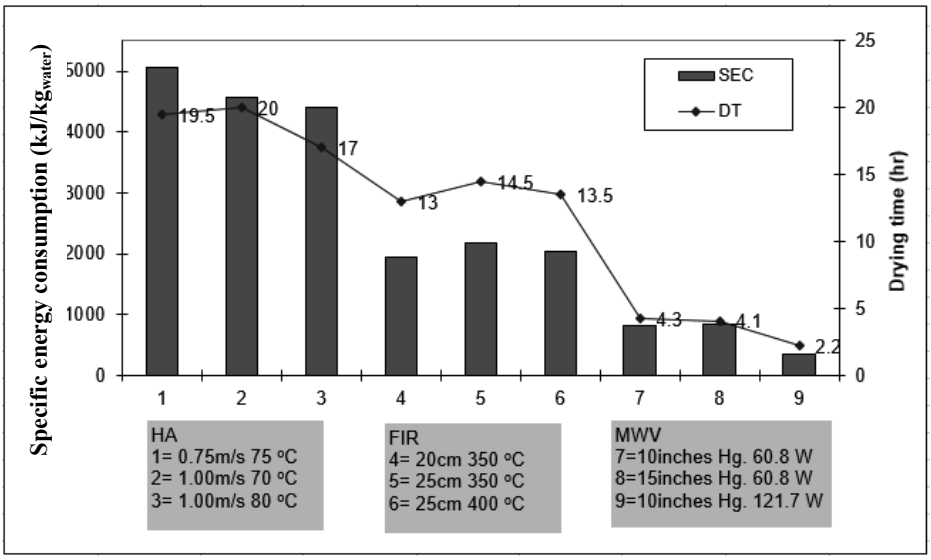

Figure 6. Comparison of drying time (DT) and SEC for HA, FIR and MWV drying

(a) (b) (c)

Figure 7. Surface appearance of longan leather samples from different drying methods: (a) HA drying; (b) FIR drying; (c) MWV drying

Table 2. Qualities of longan fruit leather

Drying method		Drying qualities					
		L*	a*	b*	ΔE	Hardness (N)	Gumminess (N)
HA	0.75 m/s, 75°C	40.43	12.70	26.61	15.50	5.47	1.77
	1.00 m/s, 70°C	40.76	13.61	26.77	16.61	1.84	1.60
	1.00 m/s, 80°C	48.04	11.10	31.98	14.69	2.57	1.01
FIR	20 cm, 350°C	47.26	9.69	25.55	9.09	2.41	2.08
	25 cm, 350°C	49.22	10.95	18.68	4.58	1.43	2.86
	25 cm, 400°C	46.65	12.43	24.64	9.36	2.39	2.30
MWV	10 in. vac., 60.8 W	48.85	4.83	27.90	11.14	19.09	1.35
	15 in. vac., 60.8 W	44.89	6.69	28.53	9.19	12.53	1.54
	10 in. vac., 121.7 W	39.79	11.11	24.59	14.95	12.39	1.76
Fresh longan		50.80	-1.50	12.20	-	-	-
Conventional method [8]		53.59	9.62	19.03	-	1.49	2.83

Note: Each value represents means of three replications.

CONCLUSIONS

Although MWV drying seems to be the fastest drying method, FIR drying gives longan fruit leather of apparently optimum qualities. It also displays important advantages over HA drying, viz. increased drying rate (hence shorter drying time) and substantially less energy consumption.

ACKNOWLEDGMENTS

The authors gratefully acknowledge the support provided by Maejo University.

REFERENCES

1. R. B. Keey, "Drying Principles and Practices", Pergamon Press, Oxford, **1972**, pp.197-203.
2. M. Adonis and M. T. E. Khan, "Combined convective and infrared drying model for food applications", Proceedings of 7th AFRICON Conference in Africa, **2004**, Gaborone, Botswana, vol. 2, pp.1049-1052.
3. S. Jaturonglumlert and T. Kiatsiriroat, "Heat and mass transfer in combined convective and far-infrared drying of fruit leather", *J. Food Eng*., **2010**, *100*, 254-260.
4. D. Nowak and P. P. Lewicki, "Infrared drying of apple slices", *Innov. Food Sci. Emerg. Technol*., **2004**, *5*, 353-360.
5. T. Swasdisevi, S. Devahastin, P. Sa-Adchom and S. Soponronnarit, "Mathematical modeling of combined far-infrared and vacuum drying banana slice", *J. Food Eng*., **2009**, *92*, 100-106.
6. S. Tontand and N. Therdthai, "Preliminary study of chili drying using microwave assisted vacuum drying technology", *Asian J. Food Agro-Ind.*., **2009**, *2*, 80-86.
7. J. Varith, P. Dijkanarukkul, A. Achriyaviriya and S. Achriyaviriya, "Combined microwave-hot air drying of peeled longan", *J. Food Eng*., **2007**, *81*, 459-468.
8. S. Sampanvejsobha, Y. Attabhanyo and A. Jangchud, "Effect of temperature on fruit leathers drying", *Agric. Sci. J*., **2006**, *37*, 21-27.

9. S. Jaturonglumlert and T. Kiatsiriroat, "Mass transfer kinetics of longan leather between hot air and far-infrared drying, Proceedings of 3rd International Symposium on Longan, Lychee and Other Fruit Trees in Sapindaceae Family, **2008**, Fuzhou, China, pp.119-129.
10. N. A. Q. Ruiz S. M. Demarchi and S. A. Giner, "Research on dehydrated fruit leathers: A review", Proceedings of 11th International Congress on Engineering and Food, **2011**, Athens, Greece, FPE398.
11. S. Jaturonglumlert and T. Kiatsiriroat, "Far-infrared radiation properties of longan leather drying", Proceedings of 8th Conference on Energy, Heat and Mass Transfer in Thermal Equipment, **2009**, Chiang Rai, Thailand, pp.193-197.

Maejo Int. J. Sci. Technol. **2015**, *9*(01), 64-81; doi: 10.14456/mijst.2015.5

Maejo International Journal of Science and Technology

ISSN 1905-7873
Available online at www.mijst.mju.ac.th

Full Paper

Hybrid framework for 3D colon model reconstruction from computed tomographic colonography

Pataraporn Promkumtan [1], Nagul Cooharojananone [1, *], Rajalida Lipikorn [1], Laddawan Vajragupta [2] and Bundit Chaopathomkul [2]

[1] Department of Mathematics and Computer Science, Faculty of Science, Chulalongkorn University, Thailand

[2] Department of Radiology, Faculty of Medicine, Chulalongkorn University, Thailand

* Corresponding author, e-mail: Nagul.C@chula.ac.th

Received: 10 December 2013 / Accepted: 13 March 2015 / Published: 16 March 2015

Abstract: A hybrid framework for an improved resolution of 3D-model colon reconstruction from computed tomographic colonography images is proposed. The framework is composed of three main parts: colon cleansing, colon-wall detection and colon segmentation followed by 3D model reconstruction. The first part, colon cleansing, was performed by applying a Laplacian operator combined with K-means clustering and morphological-based operations. An average Gaussian low-pass filter of two different sizes combined with a median filter was employed to reconstruct the colon wall as realistically as possible, and was evaluated on four data sets by an expert radiologist. The second part, colon-wall detection, utilised hybrid edge and enhanced gradient vector flow procedures to enhance the colon-wall detection, and the results were evaluated on eight data sets in comparison with two existing techniques by two expert radiologists. Finally, colon segmentation, based on anatomical structures and volume analysis, was applied and then 3D models were reconstructed. The colon cleansing was consistent across all data sets and gave satisfactory removal of all partial volume effects and contrast-enhancing material, whilst the proposed method gave better results for colon wall segmentation than the existing methods, even in special cases of unusually structured colons.

Keywords: computed tomographic colonography, colorectal cancer, polyps, colon cleansing, colon detection

INTRODUCTION

Colorectal cancer is a deadly disease in both men and women if the pathological symptoms are not diagnosed in the early stages [1]. Most colorectal cancers can be successfully treated if the pre-cancer cells (polyps) are detected and diagnosed at an initial stage. Virtual colonoscopy, also

called computed tomographic (CT) colonography, is used in colorectal cancer screening, which is performed by scanning the patient's abdomen to produce a series of cross sectional CT colonography images. This non-invasive technique is more comfortable for patients because they do not need a physical cleansing, which is comprised of either cleansing the colon with a large volume of liquids or taking medication and enemas to clear the colon lumen. Instead, the patient orally takes a contrast enhancement agent to make the retained residual materials (faeces and liquid stool) inside the colon radio-opaque so that they can be removed from the CT images by computerised cleansing [2].

However, CT colonoscopy has two main problems. The first is in cleaning up the colon images (colon cleansing) to eliminate any retained material of contrast-enhancing fluid (CEF) inside the colon lumen for reliable and accurate polyp detection. Although the intensities of these unwanted residual materials are enhanced, they do not show explicit boundaries due to the partial volume effect (PVE). Therefore, although applying simple threshold subtraction on the residual materials gives the fastest result, it cannot eliminate the PVE voxels at the interface region between the residual fluids and air, and it also increases aliasing effects at the surface of the colon wall.

The second problem is in the colon-wall detection and segmentation stage. The accuracy of the colon-wall detection is important in localising and identifying the size of polyps, but artefacts such as blurred surfaces where the colon lumen meets with air can reduce the accuracy of the colon-wall detection. Moreover, the colon is not the only air-filled organ in the abdomen. The lower portion of the lung, as well as the stomach and intestine are sometimes present in CT images. These air-filled organs make the task of accurate colon segmentation more difficult.

Many techniques for colon cleansing and PVE removal were reported previously. Typically, learning vector quantisation was applied for image classification and colon cleansing [3] whilst threshold value selection (based on the histogram of all the data intensity) and vertical filter were utilised for removing the CEF and PVE boundary [4]. However, these techniques did not address the effect of the sharpened intensity at the mucosal layers after colon cleansing. Segmentation ray casts with volume intensity distribution have been used to define the profile pattern for detecting the PVE whilst reconstruction graphs have been employed for removing the residuals [5]. Moreover, non-linear transfer function and morphological dilation operations have been used to find the intensity profile of the CEF [6] whilst a threshold function combined with triangular intensity transformation has been used for colon cleansing [7]. Similarly, half-sized data have been applied for generating the local and global histograms of the CEF to make a binary mask and then a morphological dilation operation is applied to seed the region growing [8]. Nevertheless, these methods require cautious selection of the optimal intensity for assigning the classification tasks.

Various techniques on automated colon-wall detection and segmentation have been developed. Although the basic techniques usually apply region growing [4, 8-9], these methods suffer from a limited capacity to find the optimal threshold setting and require refinement of the colon border. Another approach is to use the immersion-based watershed algorithm to compute the colon lumen border using a gradient map [6, 10-11]. Nevertheless, this method also has restrictions on their resolution of the complex contours of the colon border. Although level-set methods [12-15] have been used for colon segmentation, the identification of the decreasing shade intensity voxels on the border of the colon wall and the concave regions is still problematic. The traditional deformable model has the limitation of a small capture range and also has difficulties in driving into the concave boundary regions [16, 17]. Consequently, a gradient vector flow (GVF) deformable model has been developed to give a greater capture range in driving into concave regions [18, 19] in many

medical image segmentations [20-24]. However, the blurred area of low-intensity shading at the border of the colon wall still makes the edge detection difficult by the traditional GVF method.

For these reasons, we propose a hybrid framework for colon cleansing and colon-wall detection and segmentation to solve the described problems and to reconstruct a 3D colon model as realistically as possible. This will encourage radiologists to improve the diagnostic performance when performing a fly-through (the movement of virtual viewing inside colon) and displaying the entire 3D colon model with accurate surface and shape of colon. The proposed framework is composed of three main parts (Figure 1) and described as follows.

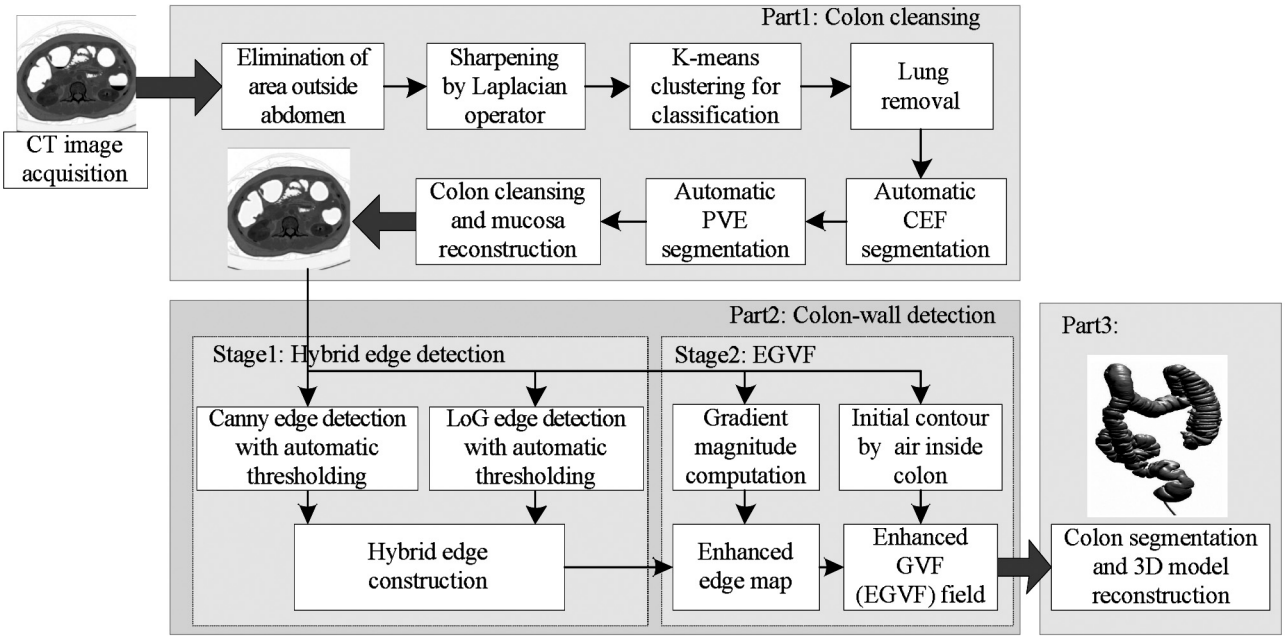

Figure 1. Proposed hybrid framework for colon cleansing and colon-wall detection and segmentation

The first part is the colon cleansing process, which uses a Laplacian operator combined with K-means clustering [25] to detect and eliminate the CEF and then applies morphological operations to remove the undesirable PVE. Moreover, the mucosal layers are reconstructed by an average Gaussian low pass filter of two different sizes combined with a median filter.

The second part is the colon-wall detection process, which uses an enhanced gradient vector flow (EGVF) to assist in the detection of the colon lumen. The proposed EGVF algorithm is composed of two stages. The first stage is the calculation of the hybrid edge, which is performed by combining the edge derived from the Canny edge detector [26] with automatic thresholding and that from the Laplacian of Gaussian (LoG) detectors [27] with automatic thresholding. In the second stage, the derived hybrid edge is then used as an edge mask to construct an enhanced edge map. This map is then applied to generate the EGVF for the detection of the colon wall.

The third part is the colon segmentation and 3D model reconstruction. The colon segmentation method is based on the anatomical structure of the colon and a volume analysis for the rendering of a 3D colon model.

MATERIALS AND METHODS

CT Image Acquisition and Elimination of Area Outside Abdomen

Since the retained faeces in the colon lumen can conceal polyps, all patients must undergo a standard bowel preparation involving a low-residue diet and take colonic lavage to make the retained faeces become more liquid. A contrast-enhancing agent such as barium sulphate was then taken to make the residual fluid radio-opaque and then the colon lumen was inflated to distend the colon and also to homogenise the residual material. After that, the CT colonographic scan was performed by a spiral CT scanner (Siemens SOMATOM Sensation 16, Technical Prospects, LLC, USA) to produce CT colonographic images. The acquired images were constructed at 1-mm intervals with 512×512 voxels, resulting in 500-700 slices. This approach had been approved by the Ethics Committee of the Faculty of Medicine, Chulalongkorn University.

The voxels outside the body were automatically detected and were discarded from the CT images in order to eliminate the extra computing time. The Otsu's method [28] was applied to separate the CT image into the foreground and the background. Afterwards, the areas outside the abdomen were discarded and all voxels inside the abdomen were preserved for the next process.

Image Sharpening by Laplacian Operator

Traditional K-means clustering is not precise at separating voxels that are located between two transitional regions and so small artifacts of CEF can be missed. Thus, the images were sharpened by Laplacian operator [27] via the highlighting of the discontinuity intensity levels. The sharpened image $I_{sh}(x,y)$ was acquired from Eq. (1):

$$I_{sh}(x,y) = I(x,y) - \nabla^2 I(x,y)\,, \tag{1}$$

where ∇^2 is the Laplacian operator and $I(x,y)$ is a CT image slice at coordinates x and y.

K-means Clustering for Colon Classification

Although applying thresholding is the simplest method in segmentation, each range of threshold intensities is sensitive to the intensity inhomogeneity. A slight change to these threshold values can affect the contour of colon, especially the thin tissue layers that may then disappear. Thus, it is not easy to select proper threshold intensities, and for this reason K-means clustering was applied to assist in image classification since the number of clusters for partitioning the regions is known and it converges to the optimal solution faster than the other pixel-based methods [25].

The intensity of each sharpened image was then used as feature vector $X = \{x_i \mid i = 1, 2, 3... n\}$ to classify into four main regions of (i) air, (ii) soft tissue and fat, (iii) muscle, and (iv) contrast-enhanced material and bones. The algorithm of K-means clustering was started by initialising the centroid of each cluster z_1, z_2, z_3 and z_4 at random from a range of data. At the p^{th} iteration, the feature vector x_i was assigned to the respective cluster C_j (j = 1, 2, 3 or 4) whose centroid was the nearest or whose Euclidean distance was the minimum, as expressed in Eq. (2):

$$x_i \in C_{j,p} \text{ if } \left\| x_i - z_{j,p} \right\| < \left\| x_i - z_{k,p} \right\|, \tag{2}$$

where $\|\cdot\|$ represents the Euclidean distance function, $C_{j,p}$ denotes a cluster j at the p^{th} iteration whose centroid is $z_{j,p}$, and k = 1, 2, 3 or 4 with the condition that $j \neq k$. Afterwards, the new centroid of each cluster, $z_{j,p+1}$ in the p+1th iteration, was recalculated to minimise the criterion function, as in Eq. (3)

$$J = \sum_{i=1}^{N_j} \left| x_{i,j} - z_{j,p+1} \right|, \tag{3}$$

where $x_{i,j}$ is in C_j and N_j is the number of voxels of cluster j. The value of $z_{j,p+1}$ which can minimise this criterion became the new centroid of the cluster and was computed by Eq. (4);

$$z_{j,p+1} = \frac{1}{N_j} \sum_{i=1}^{N_j} x_i \ , \tag{4}$$

The algorithm terminates if the centroids have not changed; otherwise, it will return to recalculate the clusters. To find the global minimum, several replications with random starting centroids were applied in order to converge the solutions to a global minimum. A sample image before and after performing K-means clustering is shown in Figures 2(a) and 2(b) respectively.

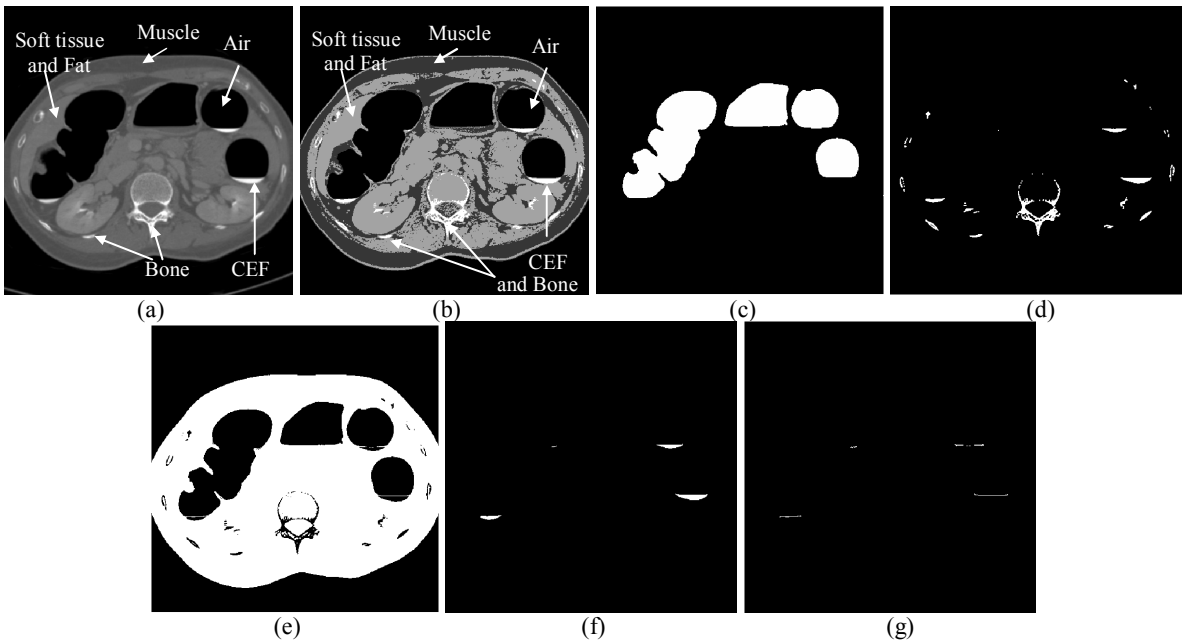

Figure 2. Original CT image slice (a) and that after K-means clustering (b), plus $Mask_{Air}$ (c), $Mask_{CEF\text{-}Bone}$ (d), $Mask_{Tissue}$ (e); $Mask_{CEF}$ (f) and $Mask_{PVE}$ (g)

Lung Removal

The prior removal of lungs was employed to eliminate the extra computation. Traditionally, a threshold setting is used to separate the lung tissue. In contrast, here the lungs were removed based upon their anatomical characteristic (they contain many blood vessels). Preliminarily, the air regions were constructed with a binary mask and labelled as $Mask_{Air}$. If a segment of $Mask_{Air}$ had holes inside, assumed to be blood vessels, it was designated as lung and ignored (Figure 3).

Automatic CEF Segmentation

The region of CEF and the bones were defined as $Mask_{CEF\text{-}Bone}$ (Figure 2(d)), whilst the regions of soft tissues and muscles were combined together and called $Mask_{Tissue}$ (Figure 2(e)). Since the CEF was concentrated at the lower part of the colon due to gravity and also appeared between the colon wall and the air region, then the voxels that surround the $Mask_{CEF\text{-}Bone}$ were examined for these restrictions to distinguish the CEF from bone and denoted as $Mask_{CEF}$ (Figure 2(f)).

(a) (b) (c)

Figure 3. CT image slice (a) and that for $Mask_{Air}$ before lung removal (b) and after lung removal (c)

Automatic PVE Segmentation

The PVE between air and CEF still remained in the $Mask_{Tissue}$. Then the boundary that included the interface layer of PVE voxels, assigned as $Mask_{Merge}$, was calculated by merging the boundaries of dilated masks of each segment of $Mask_{CEF}$ and their contiguous $Mask_{Air}$ with OR operation and applying morphological erosion afterwards, as in Eq. (5):

$$Mask_{Merge} = ((Mask_{Air,i} \oplus s_e) \vee (Mask_{CEF,i} \oplus s_e)) \ominus s_e, \quad (5)$$

where $\oplus$ and $\ominus$ represent the morphological dilation and erosion respectively, with a disk-shaped structuring element s_e whose radius size was equal to one. $Mask_{CEF,i}$ is each segment of $Mask_{CEF}$, $Mask_{Air,i}$ is a segment of $Mask_{Air}$ that is contiguous to $Mask_{CEF,i}$, and i represents each colon segment that has CEF. The symbol $\vee$ represents the OR operation. The suspected PVE that interfaced between the air and CEF, called $Mask_{TestPVE}$, was obtained by using the AND operation on $Mask_{Merge}$, $Mask_{Tissue}$ and the dilation of each segment of $Mask_{CEF}$, as given in Eq. (6):

$$Mask_{TestPVE} = Mask_{Merge} \wedge Mask_{Tissue} \wedge (Mask_{CEF,i} \oplus s_e), \quad (6)$$

where $\wedge$ represents the AND operation.

Since there are two possible types of each component of $Mask_{TestPVE}$ (soft tissue or PVE), the inspection was performed with the assumptions that the PVE voxels were the interface layer appearing between the air and CEF; otherwise they were defined as tissue. Eventually, the PVE regions was determined and labelled as $Mask_{PVE}$ (Figure 2(g)).

Colon Cleansing and Mucosa Reconstruction

The dilated $Mask_{PVE}$ and $Mask_{CEF}$ were combined together and then subtracted from the CT image, successfully eliminating the CEF and PVE voxels. Consequently, the reconstructed edge of the mucosal layer was generated on the adjacent pixels of the removed edge and denoted as $Edge_i$, where i is the adjacent pixels of the removed edge. Then the estimated intensity value of each voxel of $Edge_i$ was calculated, as in Eq. (7):

$$I_{Edge,i} = (I_{G5,i} + I_{GM3,i})/2, \quad (7)$$

where $I_{Edge,i}$ is the intensity value of each voxel of $Edge_i$, $I_{G5,i}$ is the intensity value at each voxel of $Edge_i$ after convolving the cleaned colon image by a Gaussian low-pass filter with a 5×5 voxels mask size, and $I_{GM3,i}$ is the intensity value at each voxel of $Edge_i$ after convolving the cleaned colon image by a Gaussian low-pass filter with a 3×3 voxels mask size and then performing median filtering to eliminate some noises of inharmonious intensity. Subsequently, $I_{Edge,i}$ was calculated and replaced on the $Edge_i$ to give a more natural appearance of the mucosal layer. From the experiment,

the Gaussian filter of both sizes could be applied to 512×512 voxels (standard size of CT image) and a larger or smaller size of this image. A larger mask size made the image more blurred whilst a smaller mask size could not completely reduce the effect of the rapid transition of the intensity level. However, the mask size of the Gaussian filter should not be more than 5×5 voxels since the intensity at the reconstructed edge areas would be obviously different from the surrounding tissue layers. Even if the median filter could remove noise, it should not be used with a smaller image size since it might cause the omission of small protrusions in the tissue layers.

Hybrid Edge Detection

The algorithm of the hybrid edge detection method was composed of three stages: (i) Canny edge detection [26] with automatic threshold setting, (ii) LoG edge detection [27] with automatic threshold setting, and (iii) hybrid edge construction. These are described in turn below.

Canny edge detection with automatic threshold setting

The gradient magnitude of the cleaned colon image was calculated. Afterwards, a non-maximum suppression was performed to track along the top of the ridges so that only the gradient magnitudes at the points of the greatest local change were identified. Hysteresis was then applied to track the edges and eliminate broken edges and streaks. Hysteresis as implemented here depended on the setting scale of the two thresholds, T_1 and T_2, for detecting the edge location. The value of threshold T_1 was automatically selected utilising Otsu's method [28], which is normally used with the intensity values of the CT image, but here the gradient magnitude of the cleaned colon image was applied instead. Then the between-class variance was determined from Eq. (8):

$$\sigma_b^2 = w_{g1}[\mu_{g1} - \mu_{gT}]^2 + w_{g2}[\mu_{g2} - \mu_{gT}]^2 . \quad (8)$$

where w_{g1} and w_{g2} are the probability distribution of the gradient magnitude value on the foreground and background respectively, μ_{g1} and μ_{g2} are the mean gradient magnitudes of the foreground and background respectively, and μ_{gT} is the net mean gradient magnitude. The threshold which corresponded to the maximum between-class variance was defined as T_{Otsu}. The threshold T_1 for hysteresis was set to equal to T_{Otsu}, whilst T_2 was then calculated from Eq. (9):

$$T_2 = kT_{Otsu} = kT_1 , \quad (9)$$

where k is a scaling factor which makes $T_2 < T_1$ (in this case $k = 0.4$) in order for the weak edges to be detected. When the gradient magnitude was greater than the T_1, it was identified as a strong edge, and when it was between T_1 and T_2, it was identified as a weak edge, unless there was a connecting path from the weak edge pixels to the strong edge pixels, in which case edge linking was then performed. The derived edges were then labelled as f_C. A sample result is shown in Figure 4(b).

LoG detection with automatic threshold setting

The cleaned colon image was smoothed by the use of a Gaussian filter and subsequently the LoG was calculated as the second spatial derivative of the smoothed image. Zero-crossing detection was utilised to estimate the edge locations. The threshold value for the zero-crossing operation, T_z, was automatically set by the mean absolute value of LoG, as derived from Eq. (10):

$$T_z = \frac{1}{mn}\sum_{x=1}^{m}\sum_{y=1}^{n}\left|LoG(x,y)\right| , \quad (10)$$

where $LoG(x,y)$ is the intensity level estimated by the LoG image at coordinates (x, y) of an image whose size is $m \times n$. The derived edges were then labelled as f_{LoG}. A sample result is shown in Figure 4(c) in grey and white. Afterwards, the LoG edges located at positions where the gradient magnitude was greater than T_{Otsu} were preserved; otherwise they were removed as noisy edges. Hence the final LoG edges were acquired by Eq. (11):

$$f_{LoG}(x,y) = \begin{cases} f_{LoG}(x,y) & \text{if } f_G(x,y) \geq T_{Otsu} \\ 0 & \text{if } f_G(x,y) < T_{Otsu} \end{cases}, \tag{11}$$

where $f_G(x,y)$ is the gradient magnitude of an image at coordinates (x, y). A sample image of LoG edges after elimination of the noisy edges is shown in Figure 4(c) in white.

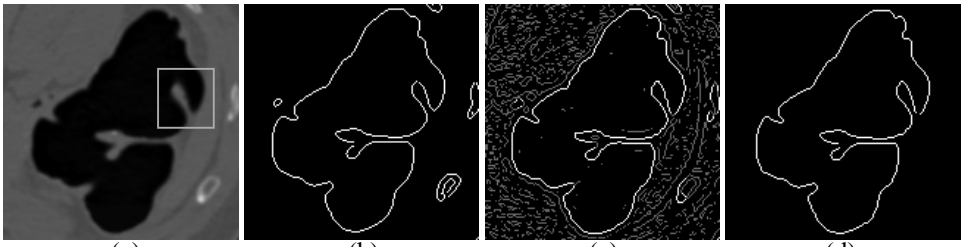

(a) (b) (c) (d)

Figure 4. (a) Original CT image slice; (b) after Canny edge detection by automatically-set threshold; (c) after LoG edge detection by automatically-set threshold (white) and discarded edge (grey); (d) hybrid edge obtained by (b) and (c)

Hybrid edge construction

Although the Canny edge detection could produce strong edges, it identified an edge without examining the deviations from its neighbours [29]. In contrast, the LoG edge detection defined the edge by examining an area nearby each pixel, but it was sensitive to noise [30, 31]. Consequently, the hybrid edge derived from both detectors could assist in edge localisation and noise reduction better than that from either detector alone. Only the edges obtained from both methods and contiguous to the air inside the colon were conserved, whilst those at the other locations were eliminated. If the edges detected by both detection were at the same location, they were preserved for the hybrid edges and assigned as f_{Hyb}. The remaining segments in the Canny edge and LoG edge images which were not preserved were called S_{Canny} and S_{LoG} respectively. Each segment of S_{LoG} and S_{Canny} which were contiguous to S_{LoG} was then analysed by Eqs. (12) and (13) respectively:

$$E_{LoG} = \sum_{i=i_0}^{i_{n-1}} \sum_{j=j_0}^{j_{n-1}} \frac{I_{LoG}(i,j)}{n}, \tag{12}$$

$$E_{Canny} = \sum_{k=k_0}^{k_{m-1}} \sum_{l=l_0}^{l_{m-1}} \frac{I_{Canny}(k,l)}{m}, \tag{13}$$

where n and m are the numbers of pixels of each segment of S_{LoG} and S_{Canny} respectively. The notation $I_{LoG}(i,j)$ represents the intensity of each pixel of S_{LoG} at coordinates i and j. Similarly, $I_{Canny}(k,l)$ is the intensity of each pixel of S_{Canny} that is contiguous to S_{LoG} at coordinates k and l. When E_{LOG} was less than E_{Canny} or when it was more than E_{Canny} and $(n\text{-}m)$ was between 0 and threshold k_s, S_{LoG} was gathered in f_{Hyb} and its contiguous S_{Canny} was ignored. Otherwise, S_{Canny} was gathered in f_{Hyb} and its contiguous S_{LoG} was ignored. Hence all the hybrid edges f_{Hyb} were acquired

by Eq. (14):

$$f_{Hyb}(a,b)=\begin{cases} S_{LoG}(i,j)\,|\,(a,b)=(i,j) & \text{if } (E_{LoG}<E_{Canny}) \\ S_{LoG}(i,j)\,|\,(a,b)=(i,j) & \text{if } (E_{LoG}>E_{Canny}\ and\ \ 0<n-m\le k_s), \\ S_{Canny}(k,l)\,|\,(a,b)=(k,l) & \text{otherwise} \end{cases} \tag{14}$$

where $S_{LoG}(i,j)$ is each segment of S_{LoG} at coordinates (i, j), $S_{Canny}(k,l)$ is each segment of S_{Canny} that is contiguous to $S_{LoG}(i,j)$ at coordinates (k,l), and k_s is the threshold to protect the oversize of S_{LoG}. Finally, all of the hybrid edges, f_{Hyb}, were acquired for calculating the enhanced edge map in the next process. A sample image of hybrid edges is shown in Figure 4(d).

Enhanced Gradient Vector Flow (EGVF)

The EGVF was composed of two stages: the first utilised an enhanced-edge map computation whilst the second was the EGVF field calculation.

Enhanced-edge map

The gradient magnitudes at the location of the hybrid-edge mask, f_{Hyb}, were enhanced while the other locations were kept unchanged. Then the enhanced gradient magnitude, f_e, was obtained by Eq. (15):

$$f_e(x,y)=\begin{cases} k_e\nabla(G(x,y)*I(x,y)) & \text{if } f_{Hyb}(x,y)=1 \\ \nabla(G(x,y)*I(x,y)) & \text{otherwise} \end{cases} \tag{15}$$

where k_e is the weight for the gradient magnitude enhancement (in this case k_e=1.15, which was selected as the optimal result following the experimental increasing of the value in 0.01 increments), $G(x,y)$ is the Gaussian filter, ∇ is the gradient operator and (x, y) are the coordinates of the image. The enhanced-edge map, f_{eh}, was then calculated from Eq. (16):

$$f_{eh}(x,y)=\left|f_e(x,y)\right|^2. \tag{16}$$

The enhanced-edge map preserved the gradient magnitude of real edges and decreased the gradient magnitude from noise. A sample image of an enhanced gradient magnitude is shown in Figure 5(c) and is different from the image obtained by the traditional gradient magnitude (Figure 5(b)) at the location where the hybrid edges are enhanced by the weight factor.

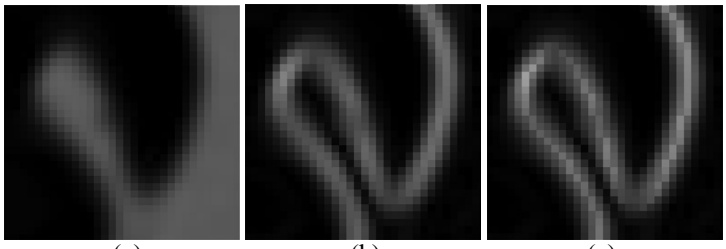

(a) (b) (c)

Figure 5. (a) Zoomed view image of square box of Figure 4(a); (b) traditional gradient magnitude of (a); (c) enhanced gradient magnitude of (a)

EGVF field

The EGVF field was obtained by applying the enhanced-edge map, f_{eh}, instead of the traditional edge map, as shown in Eq. (17):

$$V_t = \mu\nabla^2 V - \left(V - \nabla f_{eh}\right)\left|\nabla f_{eh}\right|^2, \tag{17}$$

where V_t is the partial derivative of V with respect to time t, μ is a regularisation parameter, and ∇ and ∇^2 are the gradient and Laplacian operators respectively. Then the EGVF deformable model was calculated and used to assist in pulling the curve towards the edge.

Colon Segmentation and 3D Model Reconstruction

Colon segmentation was computed by utilising the connected component in 3D space. The largest volume was assumed to be the colon and the other organs were eliminated. In the case that the small intestine was inflated and connected with the colon, removal of the small intestine was performed by the anatomical knowledge that the small intestine is smaller but longer than the colon and that it connects to the colon at the cecum. Finally, the reconstructed 3D colon model was acquired by applying the marching cubes algorithm [32].

RESULTS AND DISCUSSION

Colon Cleansing

The proposed colon cleansing method was examined in three assessments by a radiologist based on the capability of the cleansing method and the confidence in its accuracy. The assessment criteria for the evaluation of the colon cleansing were achieved by the guidance of the expert radiologist. The first assessment evaluated the capability of eliminating the CEF at each position inside the colon in the CT images. Assigned scores (1 to 5) corresponded to percentage ranges of cleansing (0-25%, 26-50%, 51-75%, 75-99% and 100% respectively). The second assessment evaluated the accuracy of the region cleansing of the colon lumen and was rated from 1 to 4, where 1 = uninterpretable due to artefacts from faecal tagging, 2 = obvious wall irregularity, 3 = equivocal wall irregularity, and 4 = no wall irregularity. The third assessment evaluated the confidence in the accuracy of the colon cleansing technique and was scored from 1 to 3, for a low, moderate and high confidence level respectively. The mean scores of each data set for the above three assessments are shown in Table 1.

Table 1. Results of cleansing assessment

Data set	Score of colon cleansing (1 to 5)	Accuracy of region cleansing (1 to 4)	Confidence in image accuracy (1 to 3)
1	4.18 ±1.58	3.37 ± 0.88	2.79 ± 0.41
2	4.80 ± 0.76	3.57 ± .0.81	2.91 ± 0.32
3	4.56 ± 1.25	2.92 ± 0. 91	2.88 ± 0.32
4	4.82 ± 0.80	3.29 ± 0.90	2.90 ± 0.30

Note: Data are shown as mean ± 1SD. Data-set sizes are 1352, 1637, 945 and 1201 segments for data sets 1-4 respectively.

The assessment of the percentage of colon cleansing shows that all of the four data sets had a high percentage of cleansing and so the colon cleansing was satisfactory, with most of the CEF and PVE voxels being successfully removed regardless of their size and form (Figure 6). Even artefacts of inhomogeneous contrast-enhanced materials (mixture of contrast-enhancing agent and residual faeces) were eliminated (arrowed in Figures 6(j, m)) and the mucosa layer between air and soft tissue after cleansing was smooth and reconstructed. However, in the case that the patients did not follow the diet instruction prior to bowel preparation, the data sets might contain some tiny regions

of artefacts that sometimes could not be completely removed (arrowed in Figure 6(h)).

The assessment of accuracy of the region cleansing shows that three of the four data sets had satisfactory scores, with only one data set (no. 3) having a lower score, which was due to the problem of a beam hardening artefact that rendered the residual material incompletely enhanced. Hence the colon wall was not smooth (arrowed in Figure 6(n)).

Finally, the assessment of the confidence in the accuracy of the images shows that the proposed method is satisfactory and sufficient to assist the radiologist in diagnosing colorectal cancer and could be used in 3D colon reconstruction.

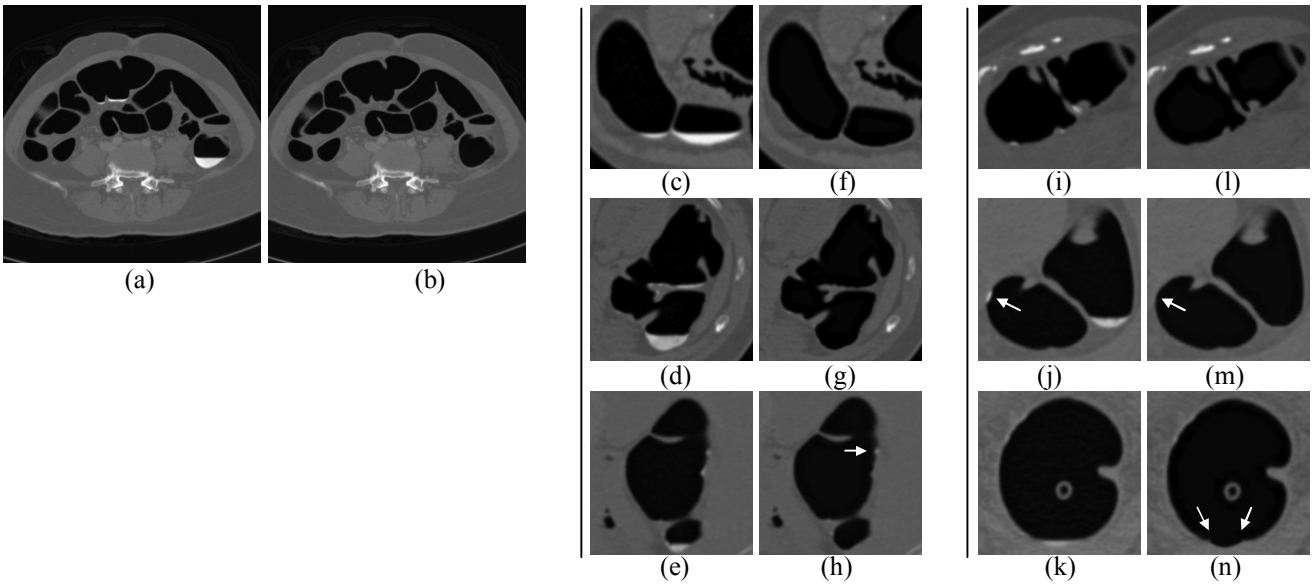

Figure 6. (a) CT image slice; (b) CT image after colon cleansing; (c-e, i-k) CT image slice (zoomed views); (f-h, l-n) corresponding CT image slice (zoomed views) after colon cleansing

The results of the comparison between the proposed cleansing method and the existing method of cleansing by threshold value selecting and vertical filter technique [4] are summarised in Figure 7. The existing methods produced a clear cleansed colon image when the selected threshold was 1,200 and 1,250 but they produced an oversegment on the CEF (square boxes in Figures 7(d, e, g, h)). When the selected threshold was slightly increased to 1,350, the oversegment was not found but instead it produced an undersegment on the CEF (square boxes in Figures 7(k, l)). Moreover, for all the selected threshold values operated with a vertical filter in the existing methods, the PVE of the interface layer between air and CEF that did not lie on the lower part of colon lumen due to gravity could not be removed (arrowed in Figures 7(f, i, l)). In contrast, the proposed cleansing method produced better results on removing the CEF and PVE from various image intensities and different locations of the CEF (Figures 7(m-o)), even if the CEF did not lie on the lower part of the colon lumen (arrowed in Figure 7(o)).

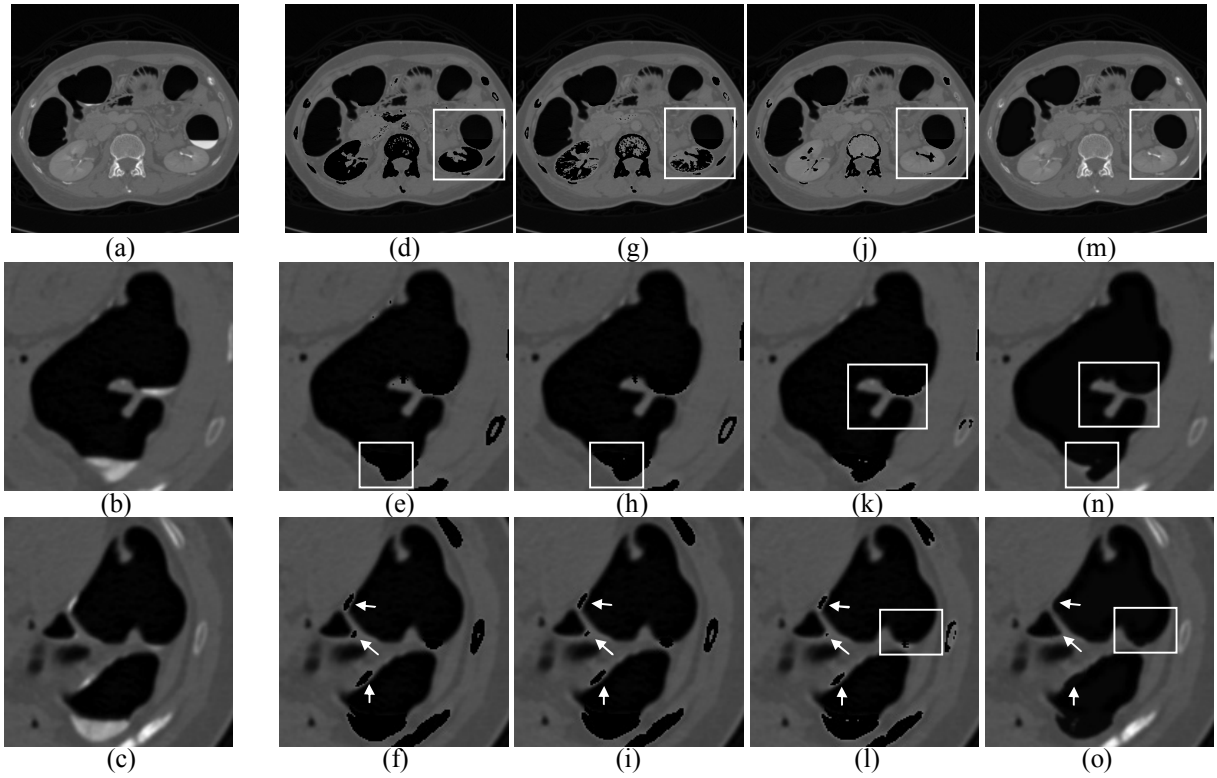

Figure 7. (a) CT image slice; (b, c) CT image slice (zoomed view); (d-l) CT image slice after colon cleansing by vertical filter method [4] with different thresholding values; (d-f) results from using threshold value = 1,200; (g-i) results from using threshold value = 1,250; (j-l) results from using threshold value = 1,350; (m-o) CT image slice after colon cleansing by proposed cleansing method

The intensity profiles along the cleaned colon lumen formed by the proposed cleansing method and those formed by the existing method of CEF and PVE voxel removal by threshold value selecting and vertical filter technique [4] are shown in Figure 8. Rapid intensity transitions along the cleaned colon wall were produced by the conventional method (Figure 8(a)), whereas the proposed cleansing method with mucosa layer reconstruction technique showed improvement in transitions of the intensity level of the colon lumen after colon cleansing (Figure 8(b)).

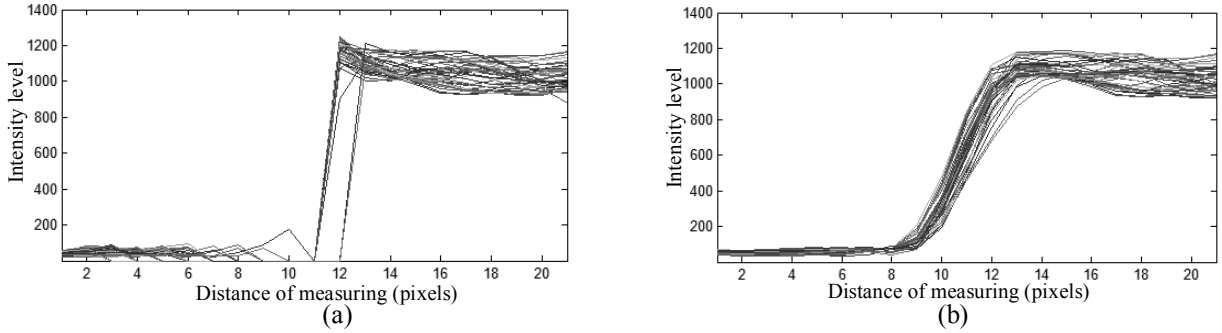

Figure 8. Intensity profiles of removed edge: (a) by selected threshold of 1,250 operated with vertical filter [4]; (b) by proposed cleansing method

Colon-Wall Detection and Colon Segmentation

The proposed EGVF was developed to obtain a better detection of the colon-wall boundary compared with the traditional GVF. An example of the results with the same weight parameters are

shown in Figure 9. Although the traditional GVF method can detect a variety of colon wall shapes with a diminishing shaded intensity, it sometimes produces incomplete edges on the colon boundary (arrowed in Figures 9(e-h)), whereas the proposed EGVF gives a more complete edge pattern (arrowed in Figures 9(i-l)) with the shape almost like the colon segment from the CT image slice. When the automatically derived initial contours are misplaced, however, the EGVF and the GVF methods may fail to detect the thin tissue layers between the two segmented colon (arrowed in Figures 9(g, k)).

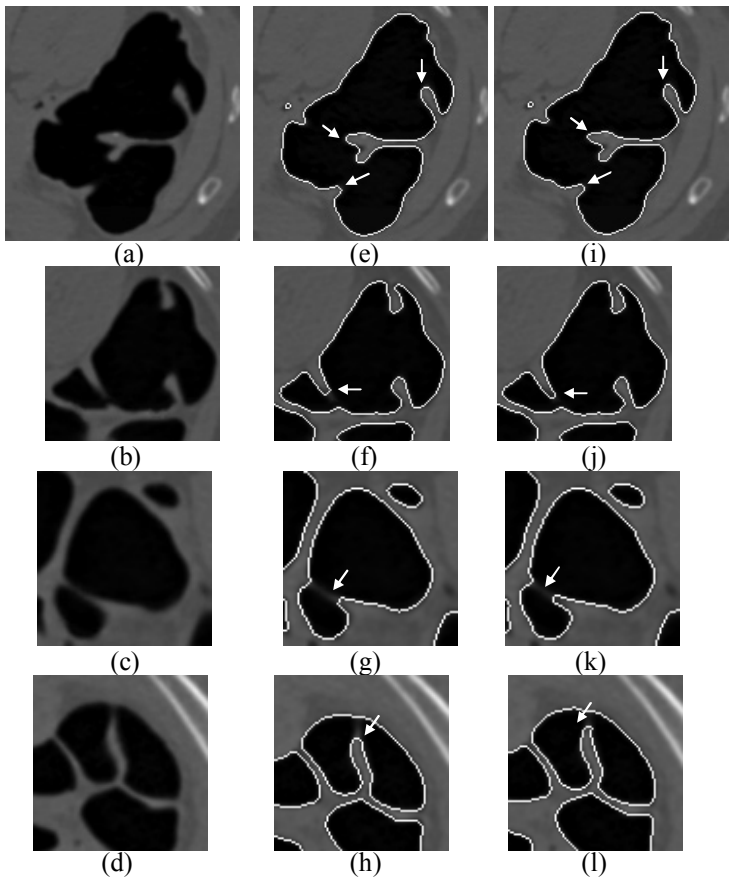

Figure 9. CT image slice (zoomed views) (a-d) and those after manipulation by GVF (e-h) and EGVF (i-l)

The performance of the proposed method for colon-wall detection and colon segmentation was compared with the existing segmentation methods of the watershed algorithm [10] and the level-set method [14]. The assessment was performed by comparing the results from all three techniques in terms of quality and accuracy of colon-wall detection, independently evaluated by two expert radiologists as a blind assessment—the radiologists did not know any information about the techniques which had been applied to each set of data. The assessment scores from the two radiologists were ranked on a scale from 1 (poor quality) to 10 (best quality), and in order to make the comparison reasonable, the initial contours from all techniques were automatically set in the same place by reference to the air inside the colon. The gradient magnitude and the standard deviation were used in the same range and the weight parameters of all techniques were increasingly adjusted in 0.01 increments and were selected from the best experimental results and employed to all data sets. For the proposed EGVF method, the weight parameters were $\mu = 0.01$, $\alpha =$

0.03, $\beta = 0.01$ and $k_e = 1.15$. The EGVF deformable model algorithm was stopped if the area inside the deformable model in the last 10 iterations had no progress. This stopping condition was also applied to the level-set method. In addition to the original four data sets used previously (1-4), four more data sets (5-8) were examined so as to allow for differently-shaped colons.

The comparative assessment scores of the quality of the colon-wall detection on each data set from both radiologists for each technique, including the *p*-value by Duncan's multiple means tests, are summarised in Table 2. The proposed method clearly gave better results (numerically and statistically) on the detection of the colon wall than those from the other two traditional techniques (watershed and level-set methods) for all of the eight data sets examined, including their net means. That the means of all the assessment scores of the quality of colon-wall detection across all data sets did not numerically differ much between the three techniques may reflect the large number of segments of the colon.

Table 2. Assessment scores by watershed algorithm, level-set method and proposed EGVF of the quality of colon-wall detection of all colon segments

	Radiologist 1				Radiologist 2			
Data set	Watershed	Level set	EGVF	*p*-value	Watershed	Level set	EGVF	*p*-value
1	9.77 ± 0.79	9.74 ± 0.66	9.88 ± 0.45	5.13E^{-08}*	9.94 ± 0.45	9.95 ± 0.28	9.99 ± 0.13	0.00035*
2	9.90 ± 0.49	9.91 ± 0.39	9.97 ± 0.19	3.56E^{-07}*	9.89 ± 0.57	9.88 ± 0.43	9.98 ± 0.20	7.02E^{-12}*
3	9.76 ± 0.89	9.87 ± 0.49	9.90 ± 0.35	3.80E^{-08}*	9.78 ± 0.93	9.89 ± 0.45	9.94 ± 0.32	2.55E^{-07}*
4	9.82 ± 0.96	9.91 ± 0.44	9.93 ± 0.37	1.14E^{-05}*	9.88 ± 0.89	9.97 ± 0.23	9.99 ± 0.10	3.12E^{-07}*
5	9.66 ± 1.31	9.80 ± 0.72	9.89 ± 0.51	1.25E^{-13}*	9.87 ± 0.80	9.94 ± 0.35	9.98 ± 0.22	6.66E^{-10}*
6	9.79 ± 1.02	9.93 ± 0.38	9.95 ± 0.30	5.39E^{-13}*	9.86 ± 0.89	9.95 ± 0.33	9.98 ± 0.22	1.64E^{-09}*
7	9.90 ± 0.59	9.91 ± 0.49	9.95 ± 0.40	0.00972*	9.96 ± 0.25	9.95 ± 0.22	9.99 ± 0.05	3.44E^{-11}*
8	9.85 ± 0.68	9.89 ± 0.38	9.92 ± 0.32	0.00016*	9.92 ± 0.57	9.96 ± 0.24	9.99 ± 0.12	1.56E^{-07}*
Mean	9.81 ± 0.53	9.87 ± 0.19	9.93 ± 0.16	6.19E^{-48}*	9.89 ± 0.54	9.94 ± 0.21	9.98 ± 0.11	2.22E^{-50}*

Note: Data are shown as mean ± 1 SD. Means followed by * are significantly different at $p < 0.01$ level (Duncan's multiple means test). Data-set sizes are 1352, 1637, 945, 1201, 1854, 1702, 1728 and 1661 segments for data sets 1-8 respectively.

In normal cases (segments without arrow in Figure 10), all techniques gave a broadly similar performance for the colon-wall segmentation. In special cases (segments with arrow in Figure 10), where the colon lumen had a small thin layer or a higher descending shaded intensity at the border of the colon lumen, however, each technique gave different results. The watershed algorithm could detect an obvious colon wall (Figure 10(h)), but it sometimes produced incomplete edges (arrowed in Figure 10(e)) and missed small tissue layers (arrowed in Figures 10(f, g)). Similarly, the level-set method could detect an explicit colon wall with a smooth curve (Figure 10(i)), but it could not move to the real shape with higher descending contrast intensity and concave regions (arrowed in Figures 10(j-l)). These could lead to false discrimination and misrepresent the size and shape of the colon-wall tissue layer, especially polyps. The EGVF gave a more completed edge (arrowed in Figures 10(m-p)) on capturing the concave regions, small tissue layers and colon boundary with diminishing shaded intensity.

With respect to the images from special conditions, segments of the colons were selected by both radiologists and then the comparative assessment scores of the quality of colon-wall detection for these special cases were analysed separately (Table 3). The mean assessment scores by both radiologists of the quality of the colon-wall detection in the selected special cases were all numerically and statistically better for the proposed method than the watershed and level-set

methods. Hence the proposed method seemed to give better results with various shapes of colon and even with special cases, except when the automatically allocated initial contours were misplaced, which resulted in rough edges.

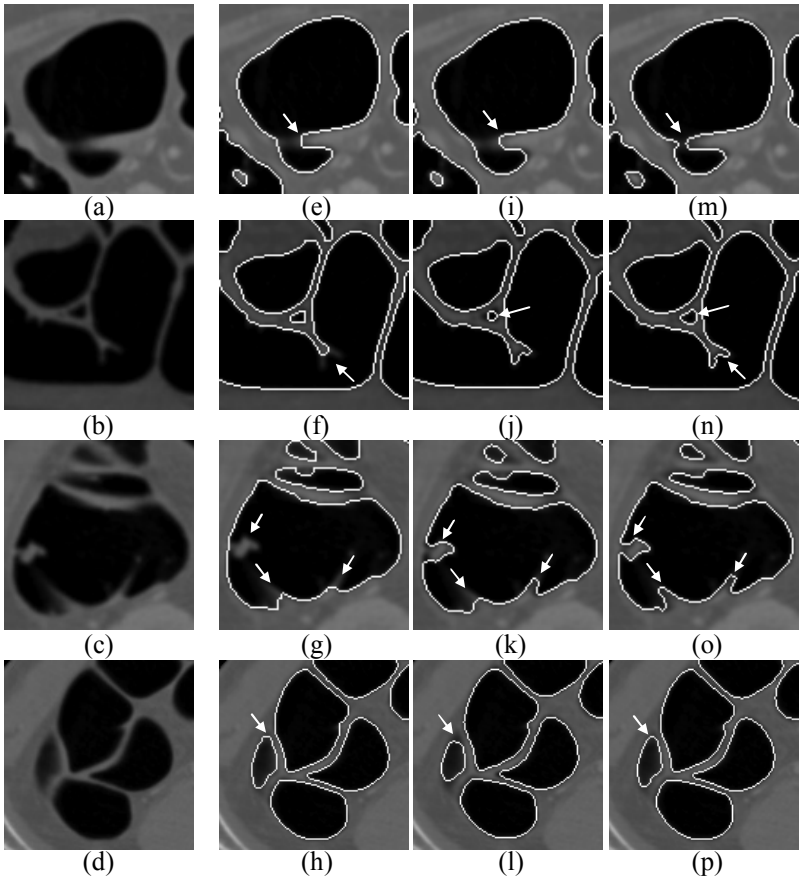

Figure 10. CT image slice (zoomed views) (a-d) and those after manipulation by watershed algorithm (e-h), level-set method (i-l) and EGVF (m-p)

Table 3. Assessment scores by watershed algorithm, level-set method and EGVF of quality of colon-wall detection in special cases

	Radiologist 1				Radiologist 2			
Data set	Watershed	Level set	EGVF	*p*-value	Watershed	Level set	EGVF	*p*-value
1	8.78 ± 1.46	8.62 ± 0.88	9.35 ± 0.84	$9.78E^{-14}$*	9.70 ± 1.00	9.72 ± 0.59	9.93 ± 0.30	0.000179*
2	9.20 ± 1.18	9.26 ± 0.87	9.74 ± 0.48	$8.06E^{-10}$*	9.09 ± 1.41	9.05 ± 0.86	9.83 ± 0.54	$1.17E^{-16}$*
3	8.09 ± 1.80	8.92 ± 0.95	9.42 ± 0.83	$7.45E^{-14}$*	8.26 ± 2.09	9.08 ± 0.94	9.52 ± 0.78	$1.14E^{-10}$*
4	7.33 ± 2.59	8.73 ± 1.10	9.02 ± 1.00	$9.27E^{-10}$*	8.27 ± 2.95	9.53 ± 0.77	9.92 ± 0.36	$1.17E^{-08}$*
5	7.01 ± 2.73	8.25 ± 1.35	9.05 ± 1.21	$4.10E^{-25}$*	8.82 ± 2.10	9.49 ± 0.94	9.80 ± 0.81	$9.27E^{-12}$*
6	7.30 ± 2.60	9.04 ± 1.01	9.30 ± 0.86	$8.57E^{-22}$*	8.21 ± 2.72	9.36 ± 1.01	9.73 ± 0.74	$4.89E^{-12}$*
7	8.85 ± 1.64	9.04 ± 1.33	9.41 ± 1.21	0.00169*	9.61 ± 0.76	9.47 ± 0.54	9.97 ± 0.18	$8.03E^{-15}$*
8	8.63 ± 1.63	9.02 ± 0.71	9.28 ± 0.70	$2.13E^{-07}$*	9.26 ± 1.61	9.66 ± 0.64	9.91 ± 0.37	$1.48E^{-08}$*
Mean	8.25 ± 2.11	8.84 ± 1.09	9.34 ± 0.94	$6.50E^{-76}$*	9.03 ± 1.88	9.44 ± 0.82	9.84 ± 0.56	$9.14E^{-61}$*

Note: Data are shown as mean $\pm$ 1 SD. Means followed by * are significantly different at the $p < 0.01$ level (Duncan's multiple means test). Data-set sizes are 257, 199, 118, 83, 209, 132, 157 and 179 segments for data sets 1-8 respectively.

In the final process the colon segmentation was performed based on anatomical structures and volume analysis, and the contiguous small intestine was removed. Then the surface rendering was performed to finally reconstruct the 3D colon model (Figure 11). The average time for each step is shown in Table 4; all calculations were performed in Matlab environmental on Windows 7 using a PC computer with a 2.0GHz Core i7 processor and 4 GB of RAM memory.

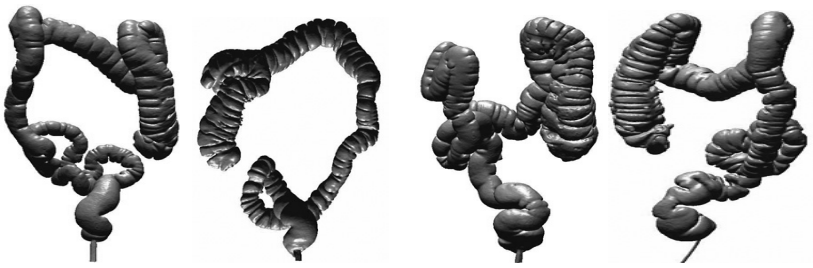

Figure 11. 3D model of the colon

Table 4. Average time for each step for a 512×512-voxel CT image size

Processing step	Time (second)	Time (%)
Colon cleansing		
Elimination of area outside abdomen	0.0957	1.3760
Image sharpening by Laplacian operator	0.0446	0.6413
K-means clustering for colon classification	1.1349	16.3180
Lungs removal	0.0411	0.5910
Automatic CEF and PVE segmentation	0.7563	10.8743
Colon cleansing and mucosa reconstruction	0.0897	1.2897
Colon-wall detection and colon segmentation		
Canny edge detection with automatic threshold setting	0.1188	1.7081
LoG detection with automatic threshold setting	0.0793	1.1402
Hybrid edge construction	0.0604	0.8685
EGVF for colon-wall detection and colon segmentation	4.5341	65.1929
Total	6.9549	100

CONCLUSIONS

In our hybrid framework for reconstructing a 3D colon model, the accuracy of the colon cleansing was satisfactory. All PVE and CEF were successfully removed and the mucosal layer was reconstructed just like in the natural colon lumen. Some troubles with the tiny artefacts were overcome by applying more features to extract. The accuracy of the colon-wall detection was better than the conventional watershed and level-set methods. The limitation imposed by misplaced initial contours could be improved by adding more features to adapt contours. The 3D model of the colon was successfully reconstructed and sufficient for the radiologist's diagnostic examinations.

ACKNOWLEDGEMENTS

The authors thank the Department of Radiology, Chulalongkorn University for providing the CT image data sets. We also thank Sareeya Ruamsup MD and Sumunta Thongtong MD for their helpful suggestions and discussions. Dr. Robert Butcher from the Publication Counselling Unit, Chulalongkorn University is thanked for comments on the manuscript and English proofreading.

REFERENCES

1. R. Nishihara, K. Wu, P. Lochhead, T. Morikawa, X. Liao, Z. R. Qian, K. Inamura, S. A. Kim, A. Kuchiba, M. Yamauchi, Y. Imamura, W. C. Willett, B. A. Rosner, C. S. Fuchs, E. Giovannucci, S. Ogino and A. T. Chan, "Long-term colorectal-cancer incidence and mortality after lower endoscopy", *N. Engl. J. Med.*, **2013**, *369*, 1095-1105.
2. J. P. Heiken, C. M. Peterson and C. O. Menias, "Virtual colonoscopy for colorectal cancer screening: Current status", *Cancer Imaging*, **2005**, *5*, S133-S139.
3. S. Wang, L. Li, H. Cohen, S. Mankes, J. J. Chen and Z. Liang, "An EM approach to MAP solution of segmenting tissue mixture percentages with application to CT-based virtual colonoscopy", *Med. Phys.*, **2008**, *35*, 5787-5798.
4. K. Y. Chang, H. H. Zhang, S. J. Chen, L. S. Chen and J. H. Chen, "Automatic colon segmentation using isolated-connected threshold", Proceedings of 1st International Conference on Robot, Vision and Signal Processing, **2011**, Kaohsiung, Taiwan, pp.44-47.
5. G. Slabaugh, X. Yang, X. Ye, R. Boyes and G. Beddoe, "A robust and fast system for CTC computer-aided detection of colorectal lesions", *Algorithms*, **2010**, *3*, 21-43.
6. A. Skalski, M. Socha, T. Zieliftski and M. Duplaga, "Colon cleansing for virtual colonoscopy using non-linear transfer function and morphological operations", Proceedings of 7th IEEE International Workshop on Imaging Systems and Techniques, **2007**, Krakow, Poland, pp.1-5.
7. V. Bevilacqua, M. Cortellino, M. Piccinni, A. Scarpa, D. Taurino, G. Mastronardi, M. Moschetta and G. Angelelli, "Image processing framework for virtual colonoscopy", Proceedings of 5th International Conference on Intelligent Computing, **2009**, Ulsan, South Korea, pp.965-974.
8. J. H. Bidgoli, A. Ahmadian, S. Akhlaghpor, N. R. Alam and S. Z. Mahmodabadi, "An efficient colon segmentation method for oral contrast-enhanced CT colonography", Proceedings of 2005 IEEE Engineering in Medicine and Biology 27th Annual Conference, **2005**, Shanghai, China, pp.3429-3432.
9. M. Ismail, S. Elhabian, A. Farag, G. Dryden and A. Seow, "Fully automated 3D colon segmentation for early detection of colorectal cancer based on convex formulation of the active contour model", Proceedings of IEEE Computer Vision and Pattern Recognition Workshops, **2012,** Providence, Rhode Island, pp.58-63.
10. A. Skalski, M. Socha, T. Zieliftski and M. Duplag, "Virtual Colonoscopy - Technical Aspects", in "Colonoscopy" (Ed. P. Miskovitz), InTech, Rijeka (Croatia), **2011**, Ch.17.
11. W. Cai, J. G. Lee, M. E. Zalis and H. Yoshida, "Mosaic decomposition: An electronic cleansing method for inhomogeneously tagged regions in noncathartic CT colonography", *IEEE Trans. Med. Imaging*, **2011**, *30*, 559-574.
12. S. Tan, J. Yao, M. M. Ward and R. M. Summers, ''Linear measurement of polyps in CT colonography using level sets on 3D surfaces", Proceedings of IEEE Engineering in Medicine and Biology Society, **2009**, Minneapolis, USA, pp.3617-3620.
13. D. Chen, H. Abdelmunim, A. A. Farag, R. Falk and G. Dryden, "Segmentation of colon tissue in CT colonography using adaptive level sets method", Proceedings of MICCAI 2008 Workshop on Computational and Visualization Challenges in the New Era of Virtual Colonoscopy, **2008**, New York, USA, pp.108-115.
14. K. Chunhapongpipat, L. Vajragupta, B. Chaopathomkul, N. Cooharojananone and R. Lipikorn, "Automatic colon cleansing in CTC image using gradient magnitude and similarity measure", *SIP Comm. Comp. Inform. Sci.*, **2009**, *61*, 82-89.

15. H. Zhu, M. Barish, P. Pickhardt and Z. Liang, "Haustral fold segmentation with curvature-guided level set evolution", *IEEE Trans. Biomed. Eng.*, **2013**, *60*, 321-331.
16. M. Kass, A. Witkin and D. Terzopoulos, "Snakes: Active contour models", *Int. J. Comput. Vision*, **1988**, *1*, 321-331.
17. C. Xu and J. L. Prince, "Snakes, shapes, and gradient vector flow", *IEEE Trans. Image Process.*, **1998**, *7*, 359-369.
18. B. Chen, J. Zhao, E. Dong, J. Chen, Y. Zhao and Z. Yuan, "An improved GVF snake model using magnetostatic theory", Proceedings of Computer, Informatics, Cybernetics and Applications, **2012**, Hangzhou, China, pp.431-440.
19. H. Zhou, X. Li, G. Schaefer, M. E. Celebi and P. Miller, "Mean shift based gradient vector flow for image segmentation", *Comput. Vis. Image Und.*., **2013**, *117*, 1004-1016.
20. T. K. Chuah, C. W. Lim, C. L. Poh and K. Sheah, "Bone segmentation of magnetic resonance images by gradient vector flow active contour with atlas based centroid forces", Proceedings of International Conference on Digital Image Computing: Techniques and Applications, **2010**, Sydney, Australia, pp.126-131.
21. S. Choi and C. Kim, "Automatic initialization active contour model for the segmentation of the chest wall on chest CT", *Healthcare Inform. Res.*, **2010**, *16*, 36-45.
22. A. M. Kop and R. Hegadi, "Kidney segmentation from ultrasound images using gradient vector force", *Int. J. Comput. Appl*., **2010**, *2*, 104-109.
23. M. K. A. Mahmoud and A. Al-Jumaily, "Segmentation of skin cancer images based on gradient vector flow (GVF) snake", Proceedings of International Conference on Mechatronics and Automation, **2011**, Beijing, China, pp.216-220.
24. S. Patil, V. R. Udupi and D. Patole, "A robust system for segmentation of primary liver tumor in CT images", *Int. J. Comput. Appl.*, **2013**, *75*, 6-10.
25. P. M. Patel, B. N. Shah and V. Shah, "Image segmentation using K-mean clustering for finding tumor in medical application", *Int. J. Comput. Trends Technol.*, **2013**, *4*, 1239-1242.
26. J. Canny, "A computational approach to edge detection", *IEEE Trans. Pattern Anal. Mach. Intell.*, **1986**, *8*, 679-698.
27. D. Marr and E. Hildreth, "Theory of edge detection", *Proc. R. Soc. Lond. B*, **1980**, *207*, 187-217.
28. R. C. Gonzalez and R. E. Woods, "Digital Image Processing", 2nd Edn., Prentice Hall, Englewood Cliffs, **2002**, pp.45-56.
29. M. Basu, "Gaussian-based edge-detection methods—A survey", *IEEE Trans. Syst. Man Cybern. C*, **2002**, *3*, 252-260.
30. M. Roushdy, "Comparative study of edge detection algorithms applying on the gray scale noisy image using morphological filter", *Int. J. Graphics Vis. Image Process.*, **2006**, *6*, 17-23.
31. M. Bennamoun, B. Boashash and J. Koo, "Optimal parameters for edge detection", Proceedings of IEEE International Conference on Systems, Man and Cybernetics, 1995. Intelligent Systems for the 21st Century, **1995**, Vancouver, Canada, Vol. 2, pp.1482-1488.
32. W. E. Lorensen and H. E. Cline, "Marching cubes: A high resolution 3D surface construction algorithm", *ACM SIGGRAPH Comp. Graphics*, **1987**, *21*, 163-169.

Maejo Int. J. Sci. Technol. **2015**, *9*(01), 82-92; doi: 10.14456/mijst.2015.9

Maejo International Journal of Science and Technology

ISSN 1905-7873
Available online at www.mijst.mju.ac.th

Full Paper

Weak efficiency of non-smooth multiobjective programming via an η-approximation method

Rekha Gupta * and Manjari Srivastava

Department of Mathematics, University of Delhi, Delhi 110007, India

* Corresponding author, e-mail: rekhagupta1983@yahoo.com

Received: 29 January 2014/ Accepted: 18 March 2015 / Published: 19 March 2015

Abstract: A non-smooth vector optimisation problem (VOP) over cones is considered. An η-approximated vector optimisation problem is constructed by modifying the objective and constraints of the VOP at a feasible point. An equivalence between their (weak) efficient solutions is given by assuming the functions involved in the VOP to be a generalised type I. Further, the definitions of Lagrange function L_η and saddle point are introduced for the η-approximated problem and saddle-point results are deduced. At the end, sufficient conditions for the existence of (weak) efficient solutions of the VOP and the saddle point of L_η are derived. Examples are given to support the results.

Keywords: non-smooth vector optimisation, η-approximation method, generalised type I functions, Lagrange function, saddle point

INTRODUCTION

Multiobjective programming has become an important area of investigation in recent times. This is because of its practical usage in the fields of economics, decision theory, optimal control, game theory and many more. Most of the optimisation problems are actually multiobjective programming problems where the objectives are conflicting. As a result, there is no single solution which optimises all objectives simultaneously. The concept of (weak) efficiency has played a useful role in the analysis of solutions of this type of optimisation problems. Many authors have studied necessary and sufficient optimal conditions of Fritz-John and Karush-Kuhn-Tucker type of (weak) efficient solutions of a multiobjective programming problem ([1-8] and references therein).

Recently, considerable attention has been given for devising new methods of solving a mathematical programming problem with the help of some associated optimisation problems which are in general easier to solve. One such method makes use of a modified objective function introduced by Antczak [9] to solve a differentiable multiobjective programming problem involving functions which are invex. Antczak [10] introduced an η-approximation method of solving a

differentiable multiobjective programming problem. This method is an extension of an approach with a modified objective function in the sense that here the η-approximation problem is obtained by a modification of both the objective and constraint functions in the original multiobjective programming problem at an arbitrary but fixed feasible point. Antczak [11] then extended the η-approximation method to the non-smooth case by constructing a family of η-approximated vector optimisation problems (VOPs) in terms of Clarke's generalised gradients of the objective and constraint functions [12]. Further Antczak [13] introduced a vector valued Lagrange function for the same η-approximation problem as considered previously [11] and obtained saddle-point results under invexity assumptions. Recently Suneja et al. [14] studied a modified objective function method for non-smooth VOP over cones and established the equivalence between the original problem and its modified objective function problem. Scalar valued Lagrange function was also introduced and saddle-point results were obtained under cone invex and cone pseudo-invex assumptions on the functions involved in the original problem.

Motivated by the above research work, the present paper develops an η-approximation method for solving a non-smooth VOP over cones. An η-approximated VOP over cones constructed in terms of Clarke's generalised gradients of the objective and constraint functions is associated with the original problem, and the equivalence between (weak) efficient solutions of both problems is established assuming the functions involved in the original problem is a generalised type I. Further, the definitions of Lagrange function and saddle point are given for the η-approximated problem and saddle-point results are deduced under generalised type I assumptions on the functions involved. Finally, existing results for (weak) efficient solutions of the considered problem and saddle points of the Lagrange function for the η-approximated problem under some Karush-Kuhn-Tucker type conditions are obtained. Examples are given to illustrate the results.

PRELIMINARIES AND DEFINITIONS

Let $K \subseteq \mathbb{R}^p$ be a closed convex cone with $\operatorname{int} K \neq \phi$, where $\operatorname{int} K$ denotes the interior of K. The positive dual cone K^* and the strict positive dual cone K^{s^*} of K are defined as follows:

$$K^* = \{y \in \mathbb{R}^p : x^T y \geq 0, \forall x \in K\}$$

and

$$K^{s^*} = \{y \in \mathbb{R}^p : x^T y > 0, \forall x \in K \setminus \{0\}\}.$$

Let X be a non-empty open subset of $\mathbb{R}^n$.

Definition 1. A real valued function $\phi : X \to \mathbb{R}$ is said to be locally Lipschitz at a point $\bar{x} \in X$ if there exists a real number $l > 0$ such that

$$|\phi(x) - \phi(y)| \leq l \| x - y \|$$

for all x, y in a neighbourhood of $\bar{x}$. A function ϕ is said to be locally Lipschitz on X if it is locally Lipschitz at each point of X.

Definition 2 [12]**.** Let $\phi : X \to \mathbb{R}$ be a locally Lipschitz function; then $\phi^o(\bar{x}; v)$ denotes the Clarke's generalised directional derivative of ϕ at $\bar{x} \in X$ in the direction v and is defined as

$$\phi^o(\bar{x}; v) = \limsup_{\substack{y \to \bar{x} \\ t \downarrow 0}} \frac{\phi(y + tv) - \phi(y)}{t}.$$

The Clarke's generalised subdifferential of ϕ at $\bar{x} \in X$ is denoted by $\partial\phi(\bar{x})$ and is defined as

$$\partial\phi(\bar{x}) = \{\xi \in \mathbb{R}^n : \phi^o(\bar{x}; v) \geq \langle \xi, v \rangle, \ \forall v \in \mathbb{R}^n\}.$$

Let $f=(f_1,f_2,\ldots,f_p):X\to\mathbb{R}^p$ be a vector valued function. Then f is said to be locally Lipschitz on X if each f_i is locally Lipschitz on X.

The Clarke's generalised directional derivative of a locally Lipschitz function $f:X\to\mathbb{R}^p$ at $\overline{x}\in X$ in the direction v is given by

$$f^o(\overline{x};v)=(f_1{}^o(\overline{x};v),f_2{}^o(\overline{x};v),\ldots,f_p{}^o(\overline{x};v)).$$

The Clarke's generalised subdifferential of $f:X\to\mathbb{R}^p$ at $\overline{x}\in X$ is the set

$$\partial f(\overline{x})=\partial f_1(\overline{x})\times\partial f_2(\overline{x})\times\ldots\times\partial f_p(\overline{x}),$$

where $\partial f_i(\overline{x})$ is the Clarke's generalised subdifferential of f_i at $\overline{x}$.

Every element $A=(A_1,A_2,\ldots,A_p)\in\partial f(\overline{x})$ is a continuous linear operator from $\mathbb{R}^n$ to $\mathbb{R}^p$. Let u be a vector in Euclidean space ¡ ^{n}, then define

$$Au=(\langle A_1,u\rangle,\langle A_2,u\rangle,\ldots,\langle A_p,u\rangle)^T.$$

Definition 3 [14]**.** A locally Lipschitz function $f:X\to\mathbb{R}^p$ is said to be K-generalised invex with respect to η at $\overline{x}\in X$ on X, if there exists $\eta:X\times X\to\mathbb{R}^n$ such that for every $x\in X$ and $\xi\in\partial f(\overline{x})$,

$$f(x)-f(\overline{x})-\xi\eta(x,\overline{x})\in K.$$

Consider the following non-smooth VOP:

$$K\text{-Minimise } f(x)$$
$$\text{subject to } -g(x)\in Q,$$

where $f:X\to\mathbb{R}^p$, $g:X\to\mathbb{R}^m$ are locally Lipschitz functions on X, and K and Q are closed convex pointed cones with non-empty interiors in $\mathbb{R}^p$ and $\mathbb{R}^m$ respectively. Let $D=\{x\in X:-g(x)\in Q\}$ denote the set of all feasible solutions of VOP.

Definition 4. A point $\overline{x}\in D$ is said to be a weak efficient solution of VOP if there exists no $x\in D$ such that

$$f(x)-f(\overline{x})\in-\operatorname{int}K.$$

Definition 5. A point $\overline{x}\in D$ is said to be an efficient solution of VOP if there exists no $x\in D$ such that

$$f(x)-f(\overline{x})\in-K\setminus\{0\}.$$

Now on the lines of Suneja et al. [6], we have the following definition:

Definition 6. (f,g) is said to be $(K\times Q)$ generalised type I with respect to η at a point $\overline{x}\in X$ if there exists $\eta:D\times X\to\mathbb{R}^n$ such that for every $x\in D$, $\xi\in\partial f(\overline{x})$ and $\zeta\in\partial g(\overline{x})$,

$$f(x)-f(\overline{x})-\xi\eta(x,\overline{x})\in K$$

and

$$-g(\overline{x})-\zeta\eta(x,\overline{x})\in Q.$$

Taking $X=\mathbb{R}^n$, Suneja et al. [15] proved the following result giving Karush-Kuhn-Tucker necessary optimality conditions for VOP.

Lemma 1. *Let f be K-generalised invex and g be Q-generalised invex with respect to the same $\eta:\mathbb{R}^n\times\mathbb{R}^n\to\mathbb{R}^n$ at $\overline{x}\in D$ on $\mathbb{R}^n$. Suppose that the generalised Slater constraint qualification is satisfied; that is, there exists $x^*\in D$ such that $g(x^*)\in-\operatorname{int}Q$. If $\overline{x}$ is a weak efficient solution of VOP, then there exist $\overline{\lambda}\in K^*\setminus\{0\}$ and $\overline{\mu}\in Q^*$ such that*

$$0\in\partial f(\overline{x})\overline{\lambda}+\partial g(\overline{x})\overline{\mu},\qquad(1)$$

$$\bar{\mu}^T g(\bar{x}) = 0. \tag{2}$$

EQUIVALENT VOP AND OPTIMALITY CONDITIONS

Let $\bar{x} \in D$ and $\bar{\xi}, \bar{\zeta}$ be Clarke's generalised gradients of the objective function f and constraint function g in VOP at $\bar{x}$ respectively. We consider an η-approximated VOP given by

$$\begin{aligned} \text{VOP}_\eta(\bar{x}, \bar{\xi}, \bar{\zeta}) \qquad & K\text{-Minimise } \bar{\xi}\eta(x, \bar{x}) \\ & \text{subject to } -(g(\bar{x}) + \bar{\zeta}\eta(x, \bar{x})) \in Q, \end{aligned}$$

where f, g, X are as defined in VOP, and $\bar{\xi} = (\bar{\xi}_1, \bar{\xi}_2, \ldots, \bar{\xi}_p)$, $\bar{\zeta} = (\bar{\zeta}_1, \bar{\zeta}_2, \ldots, \bar{\zeta}_m)$, $\bar{\xi}_i, i = 1, \ldots, p$, $\bar{\zeta}_j, j = 1, \ldots, m$ are Clarke's generalised gradients of $f_i, i = 1, \ldots, p$ and $g_j, j = 1, \ldots, m$ respectively at $\bar{x}$; that is, $\bar{\xi}_i \in \partial f_i(\bar{x}), i = 1, \ldots, p$, $\bar{\zeta}_j \in \partial g_j(\bar{x}), j = 1, \ldots, m$, and $\eta : X \times X \to \mathbb{R}^n$ is a vector valued function. Let $D(\bar{x}, \bar{\zeta}) = \{x \in X : -g(\bar{x}) - \bar{\zeta}\eta(x, \bar{x}) \in Q\}$ denote a feasible set of $\text{VOP}_\eta(\bar{x}, \bar{\xi}, \bar{\zeta})$.

Theorem 1. *Let $X = \mathbb{R}^n$, f be K-generalised invex and g be Q-generalised invex with respect to the same $\eta : \mathbb{R}^n \times \mathbb{R}^n \to \mathbb{R}^n$ at $\bar{x} \in D$ on $\mathbb{R}^n$ with $\eta(\bar{x}, \bar{x}) = 0$. Also assume that the generalised Slater constraint qualification is satisfied. If $\bar{x}$ is a weak efficient solution of VOP, then $\bar{x}$ is also a weak efficient solution of $\text{VOP}_\eta(\bar{x}, \bar{\xi}, \bar{\zeta})$, where $\bar{\xi} \in \partial f(\bar{x})$ and $\bar{\zeta} \in \partial g(\bar{x})$ are Clarke's generalised gradients of f and g at $\bar{x}$ respectively, satisfying the Karush-Kuhn-Tucker conditions* (1) *and* (2) *at $\bar{x}$ with Lagrange multipliers $\bar{\lambda}$ and $\bar{\mu}$.*

Proof. Suppose that $\bar{x}$ is not a weak efficient solution of $\text{VOP}_\eta(\bar{x}, \bar{\xi}, \bar{\zeta})$. Then there exists some $\hat{x} \in D(\bar{x}, \bar{\zeta})$ such that

$$\bar{\xi}\eta(\hat{x}, \bar{x}) - \bar{\xi}\eta(\bar{x}, \bar{x}) \in -\operatorname{int} K.$$

Since $\eta(\bar{x}, \bar{x}) = 0$, we get

$$\bar{\xi}\eta(\hat{x}, \bar{x}) \in -\operatorname{int} K.$$

As $\bar{\lambda} \in K^* \setminus \{0\}$, we obtain

$$\bar{\lambda}^T \bar{\xi}\eta(\hat{x}, \bar{x}) < 0. \tag{3}$$

Further $\hat{x} \in D(\bar{x}, \bar{\zeta})$ implies

$$-g(\bar{x}) - \bar{\zeta}\eta(\hat{x}, \bar{x}) \in Q.$$

As $\bar{\mu} \in Q^*$, we get

$$\bar{\mu}^T (g(\bar{x}) + \bar{\zeta}\eta(\hat{x}, \bar{x})) \le 0.$$

Using (2), the above inequality gives

$$\bar{\mu}^T \bar{\zeta}\eta(\hat{x}, \bar{x}) \le 0. \tag{4}$$

Adding (3) and (4), we get

$$(\bar{\lambda}^T \bar{\xi}^T + \bar{\mu}^T \bar{\zeta}^T)\eta(\hat{x}, \bar{x}) < 0.$$

This contradicts (1). Hence $\bar{x}$ is a weak efficient solution of $\text{VOP}_\eta(\bar{x}, \bar{\xi}, \bar{\zeta})$.

Theorem 2. *Let (f, g) be $(K \times Q)$ generalised type I at $\bar{x}$ with respect to η with $\eta(\bar{x}, \bar{x}) = 0$. If $\bar{x}$ is a weak efficient solution of $\text{VOP}_\eta(\bar{x}, \bar{\xi}, \bar{\zeta})$, then $\bar{x}$ is a weak efficient solution of VOP.*

Proof. Suppose, on the contrary, that $\bar{x}$ is not a weak efficient solution of VOP. Then there exists some $\hat{x} \in D$ such that

$$f(\hat{x}) - f(\bar{x}) \in -\operatorname{int} K$$

$$\Rightarrow \qquad f(\bar{x}) - f(\hat{x}) \in \operatorname{int} K. \tag{5}$$

Since (f, g) is $(K \times Q)$ generalised type I at $\bar{x}$; therefore, we get

$$f(\hat{x}) - f(\overline{x}) - \overline{\xi}\eta(\hat{x},\overline{x}) \in K \tag{6}$$

and

$$-g(\overline{x}) - \overline{\zeta}\eta(\hat{x},\overline{x}) \in Q, \tag{7}$$

as $\overline{\xi} \in \partial f(\overline{x})$ and $\overline{\zeta} \in \partial g(\overline{x})$.

Now (7) shows that $\hat{x} \in D(\overline{x},\overline{\zeta})$. From (5) and (6), we get

$$-\overline{\xi}\eta(\hat{x},\overline{x}) \in \operatorname{int} K$$

$$\Rightarrow \quad \overline{\xi}\eta(\hat{x},\overline{x}) \in -\operatorname{int} K .$$

As $\eta(\overline{x},\overline{x}) = 0$, we obtain

$$\overline{\xi}\eta(\hat{x},\overline{x}) - \overline{\xi}\eta(\overline{x},\overline{x}) \in -\operatorname{int} K ,$$

which contradicts the fact that $\overline{x}$ is a weak efficient solution of $\text{VOP}_\eta(\overline{x},\overline{\xi},\overline{\zeta})$. Hence the desired result follows.

Example 1. Consider the VOP:

$$K\text{-Minimise } f(x)$$
$$\text{subject to } -g(x) \in Q,$$

where $f: X \to \mathbb{R}^2$ $g: X \to \mathbb{R}^2$, $X =]-1,1[$, $f(x) = (f_1(x), f_2(x))$, $g(x) = (g_1(x), g_2(x))$, $K = \{(x,y): y \le x, y \le 0\}$ and $Q = \{(x,y): y \le -x, x \le 0\}$.

Define $\eta : D \times X \to \mathbb{R}$ as $\eta(x,\overline{x}) = x^2 - \overline{x}^2$. Let

$$f_1(x) = \begin{cases} x^2, & x \ge 0 \\ -x^2 - x, & x < 0 \end{cases}, \qquad f_2(x) = \begin{cases} -x^3, & x \ge 0 \\ x, & x < 0 \end{cases}$$

and

$$g_1(x) = \begin{cases} x^4 + x^2, & x \ge 0 \\ 5x, & x < 0 \end{cases}, \qquad g_2(x) = \begin{cases} x^2, & x \ge 0 \\ 2x, & x < 0. \end{cases}$$

Here $-g(x) \in Q \Rightarrow 0 \le x < 1$. Hence feasible set $D = \{x \in \mathbb{R} : 0 \le x < 1\}$.

Let $\overline{x} = 0 \in D$. Then $\partial f_1(0) = [-1,0]$, $\partial f_2(0) = [0,1]$, $\partial g_1(0) = [0,5]$ and $\partial g_2(0) = [0,2]$. Now (f,g) is $(K \times Q)$ generalised type I at $\overline{x} = 0$ because for every $x \in D$, $\xi \in \partial f(\overline{x})$ and $\zeta \in \partial g(\overline{x})$, we have

$$f(x) - f(0) - \xi\eta(x,0) \in K$$

and

$$-g(0) - \zeta\eta(x,0) \in Q.$$

Also, $\eta(\overline{x},\overline{x}) = 0$.

Now we construct a modified $\text{VOP}_\eta(\overline{x},\overline{\xi},\overline{\zeta})$ for $\overline{\xi} = (\overline{\xi}_1,\overline{\xi}_2) = (-\frac{1}{2},0)$ and $\overline{\zeta} = (\overline{\zeta}_1,\overline{\zeta}_2) = (\frac{3}{2},1)$ as follows:

$$K\text{-Minimise } \overline{\xi}\eta(x,\overline{x}) = (-\tfrac{1}{2}x^2,0)^T$$
$$\text{subject to } -(\tfrac{3}{2}x^2,x^2)^T \in Q.$$

Here $(-\frac{3}{2}x^2,-x^2)^T \in Q$ for every $x \in X$. Therefore, feasible set of modified problem is X; that is, $D(\overline{x},\overline{\zeta}) = X$. Since

$$\overline{\xi}\eta(x,\overline{x}) - \overline{\xi}\eta(\overline{x},\overline{x}) = \overline{\xi}\eta(x,\overline{x}) = (-\tfrac{1}{2}x^2,0)^T \notin -\operatorname{int} K$$

for any $x \in D(\overline{x},\overline{\zeta})$, $\overline{x} = 0$ is therefore a weak efficient solution of $\text{VOP}_\eta(\overline{x},\overline{\xi},\overline{\zeta})$. Hence by Theorem 2, $\overline{x} = 0$ is a weak efficient solution of VOP.

Theorem 3. *Let (f,g) be $(K \times Q)$ generalised type I at $\overline{x}$ with respect to η, with $\eta(\overline{x},\overline{x}) = 0$. If $\overline{x}$ is an efficient solution of $\text{VOP}_\eta(\overline{x},\overline{\xi},\overline{\zeta})$, then $\overline{x}$ is an efficient solution of VOP.*

Proof. The proof follows on the lines of Theorem 2.

SADDLE-POINT CRITERIA

In this section we use the η-approximation method to obtain saddle-point criteria for a class of non-smooth VOPs. First, we define the Lagrange function L_η for $\text{VOP}_\eta(\bar{x},\bar{\xi},\bar{\zeta})$ associated with the original problem VOP as follows:

$$L_\eta(x,\lambda,\mu,\bar{\xi},\bar{\zeta}) = \lambda^T\bar{\xi}\eta(x,\bar{x}) + \mu^T(g(\bar{x}) + \bar{\zeta}\eta(x,\bar{x})),$$

for all $x \in D, \lambda \in K^*, \mu \in Q^*$.

Now for the above Lagrange function, we give the definition of saddle point as follows.

Definition 7. A point $(\bar{x},\bar{\lambda},\bar{\mu}) \in D \times K^* \setminus \{0\} \times Q^*$ is said to be a saddle point of the Lagrange function L_η if for any $x \in D, \lambda \in K^*, \mu \in Q^*$,

$$L_\eta(\bar{x},\lambda,\mu,\bar{\xi},\bar{\zeta}) \le L_\eta(\bar{x},\bar{\lambda},\bar{\mu},\bar{\xi},\bar{\zeta}) \le L_\eta(x,\bar{\lambda},\bar{\mu},\bar{\xi},\bar{\zeta}).$$

Theorem 4. *Let (f,g) be $(K \times Q)$ generalised type I with respect to η at $\bar{x} \in D$ and $\eta(\bar{x},\bar{x}) = 0$. If $(\bar{x},\bar{\lambda},\bar{\mu})$ is a saddle point of the Lagrange function L_η of $VOP_\eta(\bar{x},\bar{\xi},\bar{\zeta})$, then $\bar{x}$ is a weak efficient solution of VOP.*

Proof. Let $(\bar{x},\bar{\lambda},\bar{\mu})$ be a saddle point of L_η. Then

$$L_\eta(\bar{x},\lambda,\mu,\bar{\xi},\bar{\zeta}) \le L_\eta(\bar{x},\bar{\lambda},\bar{\mu},\bar{\xi},\bar{\zeta}), \quad \forall\ \lambda \in K^*,\ \mu \in Q^* \tag{8}$$

and

$$L_\eta(\bar{x},\bar{\lambda},\bar{\mu},\bar{\xi},\bar{\zeta}) \le L_\eta(x,\bar{\lambda},\bar{\mu},\bar{\xi},\bar{\zeta}), \quad \forall\ x \in D. \tag{9}$$

From (8) and $\eta(\bar{x},\bar{x}) = 0$, we get that

$$\mu^T g(\bar{x}) \le \bar{\mu}^T g(\bar{x}), \quad \forall\ \mu \in Q^*.$$

Therefore, in particular for $\mu = 0$, we get $\bar{\mu}^T g(\bar{x}) \ge 0$. Also, as $\bar{\mu} \in Q^*$ and $\bar{x} \in D$, we have $\bar{\mu}^T g(\bar{x}) \le 0$. From these two inequalities, it follows that

$$\bar{\mu}^T g(\bar{x}) = 0. \tag{10}$$

Now let us suppose that $\bar{x}$ is not a weak efficient solution of VOP. Then there exists some $\hat{x} \in D$ such that

$$f(\hat{x}) - f(\bar{x}) \in -\operatorname{int} K$$

$$\Rightarrow \qquad f(\bar{x}) - f(\hat{x}) \in \operatorname{int} K. \tag{11}$$

Since (f,g) is $(K \times Q)$ generalised type I at $\bar{x}$, we get

$$f(\hat{x}) - f(\bar{x}) - \bar{\xi}\eta(\hat{x},\bar{x}) \in K \tag{12}$$

and

$$-g(\bar{x}) - \bar{\zeta}\eta(\hat{x},\bar{x}) \in Q, \tag{13}$$

as $\bar{\xi} \in \partial f(\bar{x})$ and $\bar{\zeta} \in \partial g(\bar{x})$.

From (11) and (12), we get

$$-\bar{\xi}\eta(\hat{x},\bar{x}) \in \operatorname{int} K.$$

As $\bar{\lambda} \in K^* \setminus \{0\}$, we obtain

$$\bar{\lambda}^T\bar{\xi}\eta(\hat{x},\bar{x}) < 0. \tag{14}$$

Now from (13) and $\bar{\mu} \in Q^*$, we get

$$\bar{\mu}^T(g(\bar{x}) + \bar{\zeta}\eta(\hat{x},\bar{x})) \le 0. \tag{15}$$

Using (10), (14), (15) and $\eta(\bar{x},\bar{x})) = 0$, we get

$$\begin{aligned} L_\eta(\hat{x},\bar{\lambda},\bar{\mu},\bar{\xi},\bar{\zeta}) &= \bar{\lambda}^T\bar{\xi}\eta(\hat{x},\bar{x}) + \bar{\mu}^T(g(\bar{x}) + \bar{\zeta}\eta(\hat{x},\bar{x})) \\ &< 0 \\ &= \bar{\lambda}^T\bar{\xi}\eta(\bar{x},\bar{x}) + \bar{\mu}^T(g(\bar{x}) + \bar{\zeta}\eta(\bar{x},\bar{x})) \\ &= L_\eta(\bar{x},\bar{\lambda},\bar{\mu},\bar{\xi},\bar{\zeta}), \end{aligned}$$

which contradicts (9). Hence $\bar{x}$ is a weak efficient solution of VOP.

Theorem 5. *Let (f,g) be $(K\times Q)$ generalised type I with respect to η at $\bar{x}\in D$ and $\eta(\bar{x},\bar{x})=0$. If $(\bar{x},\bar{\lambda},\bar{\mu})$ is a saddle point of L_η with $\bar{\lambda}\in K^{s^*}$, then $\bar{x}$ is an efficient solution of VOP.*

Proof. The proof follows on the lines of Theorem 4.

Example 2. Consider the VOP:

$$\begin{aligned} &K\text{-Minimise } f(x) \\ &\text{subject to } -g(x)\in Q, \end{aligned}$$

where $f: X\to\mathbb{R}^2$, $g: X\to\mathbb{R}^2$, $X=]-2,2[$, $f(x)=(f_1(x),f_2(x))$, $g(x)=(g_1(x),g_2(x))$, $K=\{(x,y): x\geq y, x\geq 0\}$ and $Q=\{(x,y): y\leq -x, y\leq 0\}$.

Define $\eta: D\times X\to\mathbb{R}$ as $\eta(x,\bar{x})=(x-\bar{x})^3$; then $\eta(\bar{x},\bar{x})=0$. Let

$$f_1(x)=\begin{cases} x^3, & x\geq 0 \\ -x^2-x, & x<0 \end{cases}, \qquad f_2(x)=\begin{cases} -\frac{x}{6}, & x\geq 0 \\ 0, & x<0 \end{cases}$$

and

$$g_1(x)=\begin{cases} x-x^2, & x\geq 0 \\ -x^3, & x<0 \end{cases}, \qquad g_2(x)=\begin{cases} \frac{7}{2}x, & x\geq 0 \\ -x^2, & x<0. \end{cases}$$

Here $-g(x)\in Q\Rightarrow 0\leq x<2$. Hence feasible set $D=\{x\in\mathbb{R}: 0\leq x<2\}$.
Let $\bar{x}=0\in D$. Then $\partial f_1(0)=[-1,0]$, $\partial f_2(0)=[-\frac{1}{6},0]$, $\partial g_1(0)=[0,1]$ and $\partial g_2(0)=[0,\frac{7}{2}]$.

Now (f,g) is $(K\times Q)$ generalised type I at $\bar{x}=0$ because for every $x\in D$, $\xi\in\partial f(\bar{x})$ and $\zeta\in\partial g(\bar{x})$, we have

$$f(x)-f(0)-\xi\eta(x,0)\in K$$

and

$$-g(0)-\zeta\eta(x,0)\in Q.$$

We construct the Lagrange function L_η for the $\text{VOP}_\eta(\bar{x},\bar{\xi},\bar{\zeta})$ for $\bar{\xi}=(\bar{\xi}_1,\bar{\xi}_2)=(-\frac{1}{10},-\frac{1}{6})$ and $\bar{\zeta}=(\bar{\zeta}_1,\bar{\zeta}_2)=(\frac{1}{2},\frac{1}{12})$, which is given as

$$\begin{aligned} L_\eta(x,\lambda,\mu,\bar{\xi},\bar{\zeta}) &= \lambda^T\bar{\xi}\eta(x,\bar{x}) + \mu^T(g(\bar{x}) + \bar{\zeta}\eta(x,\bar{x})) \\ &= (\lambda_1,\lambda_2)\,(-\tfrac{1}{10}x^3,-\tfrac{1}{6}x^3)^T + (\mu_1,\mu_2)\,(\tfrac{1}{2}x^3,\tfrac{1}{12}x^3)^T. \end{aligned}$$

It is easy to see that for $\bar{\lambda}^T=(\bar{\lambda}_1,\bar{\lambda}_2)=(\frac{1}{8},-\frac{1}{8})\in K^*\setminus\{0\}$ and $\bar{\mu}^T=(\bar{\mu}_1,\bar{\mu}_2)=(0,-\frac{1}{12})\in Q^*$, $(\bar{x},\bar{\lambda},\bar{\mu})$ is a saddle point of L_η. Hence by Theorem 4, $\bar{x}$ is a weak efficient solution of VOP.

Remark 1. If in Example 2, we take $\bar{\lambda}^T=(\bar{\lambda}_1,\bar{\lambda}_2)=(\frac{1}{8},-\frac{1}{9})\in K^{s^*}$, $\bar{\xi}=(\bar{\xi}_1,\bar{\xi}_2)=(-\frac{1}{12},-\frac{1}{6})$ and everything else as in Example 2, then by Theorem 5, it can be proved that $\bar{x}$ is an efficient solution of VOP.

Theorem 6. *Let $X=\mathbb{R}^n$, f be K-generalised invex and g be Q-generalised invex with respect to the same $\eta:\mathbb{R}^n\times\mathbb{R}^n\to\mathbb{R}^n$ at $\bar{x}\in D$ on $\mathbb{R}^n$ with $\eta(\bar{x},\bar{x})=0$. Also, assume that the generalised Slater constraint qualification is satisfied. If $\bar{x}$ is a weak efficient solution of* VOP, *then $(\bar{x},\bar{\lambda},\bar{\mu})$ is a saddle point of the Lagrange function L_η of* $\text{VOP}_\eta(\bar{x},\bar{\xi},\bar{\zeta})$, *where $\bar{\xi}\in\partial f(\bar{x})$ and*

$\bar{\zeta} \in \partial g(\bar{x})$ *are Clarke's generalised gradients of* f *and* g *at* $\bar{x}$ *respectively, satisfying the Karush-Kuhn-Tucker conditions* (1) *and* (2) *at* $\bar{x}$ *with Lagrange multipliers* $\bar{\lambda}$ *and* $\bar{\mu}$.

Proof. Since $\bar{x}$ is a weak efficient solution of VOP, therefore from Lemma 1 we have

$$\bar{\xi}\ \bar{\lambda} + \bar{\zeta}\ \bar{\mu} = 0 \tag{16}$$

and

$$\bar{\mu}^T g(\bar{x}) = 0. \tag{17}$$

Now for any $x \in D$, we have by using (16), (17) and $\eta(\bar{x},\bar{x}) = 0$ that

$$\begin{aligned} L_\eta(x,\bar{\lambda},\bar{\mu},\bar{\xi},\bar{\zeta}) &= \bar{\lambda}^T\bar{\xi}\eta(x,\bar{x}) + \bar{\mu}^T(g(\bar{x}) + \bar{\zeta}\eta(x,\bar{x})) \\ &= (\bar{\lambda}^T\bar{\xi}^T + \bar{\mu}^T\bar{\zeta}^T)\eta(x,\bar{x}) + \bar{\mu}^T g(\bar{x}) \\ &= 0 \\ &= \bar{\lambda}^T\bar{\xi}\eta(\bar{x},\bar{x}) + \bar{\mu}^T(g(\bar{x}) + \bar{\zeta}\eta(\bar{x},\bar{x})) \end{aligned}$$

$$\Rightarrow \quad L_\eta(x,\bar{\lambda},\bar{\mu},\bar{\xi},\bar{\zeta}) = L_\eta(\bar{x},\bar{\lambda},\bar{\mu},\bar{\xi},\bar{\zeta}),\ \forall\ x \in D. \tag{18}$$

Again, as $\bar{x} \in D$, we have for all $\mu \in Q^*$,

$$0 = \bar{\mu}^T g(\bar{x}) \geq \mu^T g(\bar{x}). \tag{19}$$

Now using $\eta(\bar{x},\bar{x}) = 0$ and (19), we have, for any $\lambda \in K^*$ and $\mu \in Q^*$,

$$\begin{aligned} L_\eta(\bar{x},\lambda,\mu,\bar{\xi},\bar{\zeta}) &= \lambda^T\bar{\xi}\eta(\bar{x},\bar{x}) + \mu^T(g(\bar{x}) + \bar{\zeta}\eta(\bar{x},\bar{x})) \\ &\leq \bar{\lambda}^T\bar{\xi}\eta(\bar{x},\bar{x}) + \bar{\mu}^T(g(\bar{x}) + \bar{\zeta}\eta(\bar{x},\bar{x})) \\ &= L_\eta(\bar{x},\bar{\lambda},\bar{\mu},\bar{\xi},\bar{\zeta})\ . \end{aligned} \tag{20}$$

Combining (18) and (20), we get

$$L_\eta(\bar{x},\lambda,\mu,\bar{\xi},\bar{\zeta}) \leq L_\eta(\bar{x},\bar{\lambda},\bar{\mu},\bar{\xi},\bar{\zeta}) = L_\eta(x,\bar{\lambda},\bar{\mu},\bar{\xi},\bar{\zeta}),$$

for all $x \in D$, $\lambda \in K^*$ and $\mu \in Q^*$. Hence $(\bar{x},\bar{\lambda},\bar{\mu})$ is a saddle point of L_η.

EXISTENCE OF WEAK EFFICIENT SOLUTIONS OF VOP AND SADDLE POINT OF L_η

Theorem 7. *Let* $\bar{x} \in D$*, for which there exist* $\bar{\lambda} \in K^* \setminus \{0\}$ *and* $\bar{\mu} \in Q^*$ *such that* (1) *and* (2) *hold and* (f,g) *is* $(K \times Q)$ *generalised type I at* $\bar{x}$ *with respect to* η*. Then* $\bar{x}$ *is a weak efficient solution of* VOP.

Proof. Suppose that $\bar{x}$ is not a weak efficient solution of VOP. Then there exists some $\hat{x} \in D$ such that

$$f(\hat{x}) - f(\bar{x}) \in -\operatorname{int} K$$

$$\Rightarrow \quad f(\bar{x}) - f(\hat{x}) \in \operatorname{int} K. \tag{21}$$

Since (f,g) is $(K \times Q)$ generalised type I at $\bar{x}$, we have for all $\xi \in \partial f(\bar{x})$ and $\zeta \in \partial g(\bar{x})$ that

$$f(\hat{x}) - f(\bar{x}) - \xi\eta(\hat{x},\bar{x}) \in K \tag{22}$$

and

$$-g(\bar{x}) - \zeta\eta(\hat{x},\bar{x}) \in Q. \tag{23}$$

From (21) and (22), we get

$$-\xi\eta(\hat{x},\bar{x}) \in \operatorname{int} K,\ \forall\ \xi \in \partial f(\bar{x}).$$

As $\bar{\lambda} \in K^* \setminus \{0\}$, we obtain

$$\bar{\lambda}^T\xi\eta(\hat{x},\bar{x}) < 0,\ \forall\ \xi \in \partial f(\bar{x})\ . \tag{24}$$

Using (23) and $\bar{\mu} \in Q^*$, we get

$$\bar{\mu}^T(g(\bar{x}) + \zeta\eta(\hat{x},\bar{x})) \leq 0,\ \forall\ \zeta \in \partial g(\bar{x}).$$

As (2) holds, the above inequality becomes

$$\bar{\mu}^T \zeta \eta(\hat{x}, \bar{x}) \leq 0, \ \forall \ \zeta \in \partial g(\bar{x}) . \tag{25}$$

Adding (24) and (25), we get

$$(\bar{\lambda}^T \xi^T + \bar{\mu}^T \zeta^T) \ \eta(\hat{x}, \bar{x}) < 0, \ \ \forall \ \xi \in \partial f(\bar{x}), \ \zeta \in \partial g(\bar{x}) \ ,$$

which contradicts (1). Hence $\bar{x}$ is a weak efficient solution of VOP.

Theorem 8. *Let $\bar{x} \in D$, for which there exist $\bar{\lambda} \in K^{s^*}$ and $\bar{\mu} \in Q^*$ such that* (1) *and* (2) *hold and (f, g) is $(K \times Q)$ generalised type I at $\bar{x}$ with respect to η. Then $\bar{x}$ is an efficient solution of* VOP.

Proof. The proof follows on the lines of Theorem 7.

Theorem 9. *Let $\bar{x} \in D$ at which Karush-Kuhn-Tucker conditions* (1) *and* (2) *are satisfied with Lagrange multipliers $\bar{\lambda} \in K^* \setminus \{0\}$ and $\bar{\mu} \in Q^*$. Then $(\bar{x}, \bar{\lambda}, \bar{\mu})$ is a saddle point of the Lagrange function L_η of $\text{VOP}_\eta(\bar{x}, \bar{\xi}, \bar{\zeta})$, where $\eta(\bar{x}, \bar{x}) = 0$ and $\bar{\xi} \in \partial f(\bar{x})$, $\bar{\zeta} \in \partial g(\bar{x})$ are Clarke's generalised gradients of f and g at $\bar{x}$ respectively, satisfying conditions* (1) *and* (2) *at $\bar{x}$ with Lagrange multipliers $\bar{\lambda}$ and $\bar{\mu}$.*

Proof. If $(\bar{x}, \bar{\lambda}, \bar{\mu})$ is not a saddle point of L_η, then at least one of the following two statements holds:

(a) There exists $(\hat{\lambda}, \hat{\mu}) \in K^* \times Q^*$ such that

$$L_\eta(\bar{x}, \hat{\lambda}, \hat{\mu}, \bar{\xi}, \bar{\zeta}) > L_\eta(\bar{x}, \bar{\lambda}, \bar{\mu}, \bar{\xi}, \bar{\zeta}) \ .$$

(b) There exists $\hat{x} \in D$ such that

$$L_\eta(\bar{x}, \bar{\lambda}, \bar{\mu}, \bar{\xi}, \bar{\zeta}) > L_\eta(\hat{x}, \bar{\lambda}, \bar{\mu}, \bar{\xi}, \bar{\zeta}) \ .$$

If (a) holds, then using the definition of L_η and $\eta(\bar{x}, \bar{x}) = 0$, we get

$$\hat{\mu}^T g(\bar{x}) > \bar{\mu}^T g(\bar{x}) .$$

Since $\bar{x} \in D$ and $\hat{\mu} \in Q^*$, therefore from (2) we have

$$0 \geq \hat{\mu}^T g(\bar{x}) > \bar{\mu}^T g(\bar{x}) = 0 ,$$

which is a contradiction. If (b) holds, then from $\eta(\bar{x}, \bar{x}) = 0$ we get

$$\bar{\mu}^T g(\bar{x}) > \bar{\lambda}^T \bar{\xi}(\hat{x}, \bar{x}) + \bar{\mu}^T (g(\bar{x}) + \bar{\zeta} \ \eta(\hat{x}, \bar{x}))$$

$$\Rightarrow \qquad (\bar{\lambda}^T \bar{\xi}^T + \bar{\mu}^T \bar{\zeta}^T) \ \eta(\hat{x}, \bar{x}) < 0,$$

which contradicts (1). Hence $(\bar{x}, \bar{\lambda}, \bar{\mu})$ is a saddle point of L_η.

Example 3. Consider the VOP:

$$K\text{-Minimise } f(x)$$
$$\text{subject to } -g(x) \in Q,$$

where $f : X \to \mathbb{R}^2$, $g : X \to \mathbb{R}^2$, $X =]-2, 2[$, $f(x) = (f_1(x), f_2(x))$, $g(x) = (g_1(x), g_2(x))$, $K = \{(x, y) : y \leq x, x \geq 0\}$ and $Q = \{(x, y) : y \leq -x, y \geq 0\}$.

Define $\eta : D \times X \to \mathbb{R}$ as $\eta(x, \bar{x}) = (x - \bar{x})^2$; then $\eta(\bar{x}, \bar{x}) = 0$. Let

$$f_1(x) = \begin{cases} -x^2, & x < 1 \\ -x, & x \geq 1 \end{cases}, \qquad f_2(x) = \begin{cases} -x^3, & x < 1 \\ -x, & x \geq 1 \end{cases}$$

and

$$g_1(x) = \begin{cases} x, & x < 1 \\ 1, & x \geq 1 \end{cases}, \qquad g_2(x) = \begin{cases} 0, & x < 1 \\ -x + 1, & x \geq 1. \end{cases}$$

Now $-g(x) \in Q \Rightarrow 0 \leq x < 2$. Hence $D = \{x \in \mathbb{R} : 0 \leq x < 2\}$.

Let us take $\bar{x} = 1 \in D$; then $\partial f_1(1) = [-2,-1]$, $\partial f_2(1) = [-3,-1]$, $\partial g_1(1) = [0,1]$ and $\partial g_2(1) = [-1,0]$

Now it is easy to see that for $\bar{\lambda}^T = (\bar{\lambda}_1, \bar{\lambda}_2) = (1, -\frac{2}{3}) \in K^* \setminus \{0\}$, $\bar{\mu}^T = (\bar{\mu}_1, \bar{\mu}_2) = (0, \frac{1}{2}) \in Q^*$, $\bar{\xi} = (\bar{\xi}_1, \bar{\xi}_2) = (-\frac{7}{4}, -3) \in \partial f(1)$ and $\bar{\zeta} = (\bar{\zeta}_1, \bar{\zeta}_2) = (\frac{1}{3}, -\frac{1}{2}) \in \partial g(1)$, we have

$$\bar{\lambda}^T \bar{\xi}^T + \bar{\mu}^T \bar{\zeta}^T = 0$$

and

$$\bar{\mu}^T g(\bar{x}) = 0.$$

Therefore, conditions (1) and (2) are satisfied at $\bar{x} = 1$. We construct the Lagrange function L_η for the $\text{VOP}_\eta(\bar{x}, \bar{\xi}, \bar{\zeta})$ (where $\bar{\xi}, \bar{\zeta}$ are as given above):

$$L_\eta(x, \lambda, \mu, \bar{\xi}, \bar{\zeta}) = \left(-\frac{7}{4}\lambda_1 - 3\lambda_2 \right)(x-1)^2 + \left(\frac{1}{3}\mu_1 - \frac{1}{2}\mu_2 \right)(x-1)^2 + \mu_1 .$$

Then with simple calculations, it can be seen that $(\bar{x}, \bar{\lambda}, \bar{\mu})$ is a saddle point of L_η, where $\bar{\lambda}, \bar{\mu}$ are the Lagrange multipliers given above, satisfying Karush-Kuhn-Tucker conditions (1) and (2).

ACKNOWLEDGEMENTS

The first author is thankful to the Council of Scientific and Industrial Research (CSIR), India for the financial support provided during the work.

REFERENCES

1. I. Ahmad, S. K. Gupta and A. Jayswal, "On sufficiency and duality for nonsmooth multiobjective programming problems involving generalized *V-r*-invex functions", *Nonlinear Anal.*, **2011**, *74*, 5920-5928.
2. M. A. Hanson and B. Mond, "Necessary and sufficient conditions in constrained optimization", *Math. Program.*, **1987**, *37*, 51-58.
3. A. Jayswal, "On sufficiency and duality in multiobjective programming problem under generalized α -type I univexity", *J. Glob. Optim.*, **2010**, *46*, 207-216.
4. N. G. Rueda and M. A. Hanson, "Optimality criteria in mathematical programming involving generalized invexity", *J. Math. Anal. Appl.*, **1988**, *130*, 375-385.
5. N. G. Rueda, M. A. Hanson and C. Singh, "Optimality and duality with generalized convexity", *J. Optim. Theory Appl.*, **1995**, *86*, 491-500.
6. S. K. Suneja, S. Khurana and M. Bhatia, "Optimality and duality in vector optimization involving generalized type I functions over cones", *J. Glob. Optim.*, **2011**, *49*, 23-35.
7. A. M. Stancu, "Mathematical Programming with Type-I Functions", Matrix Rom, Bucharest (Romania), **2013**.
8. A. Jayswal, A. K. Prasad and I. M. Stancu-Minasian, "On nonsmooth multiobjective fractional programming problems involving (p,r)-ρ-(η,θ)-invex functions", *Yugoslav J. Operat. Res.*, **2013**, *23*, 367-386.
9. T. Antczak, "A new approach to multiobjective programming with a modified objective function", *J. Glob. Optim.*, **2003**, *27*, 485-495.
10. T. Antczak, "An η -approximation method in nonlinear vector optimization", *Nonlinear Anal.*, **2005**, *63*, 225-236.
11. T. Antczak, "An η -approximation method for nonsmooth multiobjective programming problems", *Anziam J.*, **2008**, *49*, 309-323.
12. F. H. Clarke, "Optimization and Nonsmooth Analysis", Interscience, New York, **1983**.

13. T. Antczak, "Saddle points criteria in nondifferentiable multiobjective programming with *V*-invex functions via an η-approximation method", *Comput. Math. Appl.*, **2010**, *60*, 2689-2700.
14. S. K. Suneja, S. Sharma and M. Kapoor, "Modified objective function method in nonsmooth vector optimization over cones", *Optim. Lett.*, **2014**, *8*, 1361-1373.
15. S. K. Suneja, S. Khurana and Vani, "Generalized nonsmooth invexity over cones in vector optimization", *Eur. J. Operat. Res.*, **2008**, *186*, 28-40.

Maejo Int. J. Sci. Technol. **2015**, *9*(01), 93-107; doi: 10.14456/mijst.2015.8

Maejo International Journal of Science and Technology

ISSN 1905-7873
Available online at www.mijst.mju.ac.th

Full Paper

A modified wall-building-based compound approach for the knapsack container loading problem

Ampol Karoonsoontawong * **and Krongthong Heebkhoksung**

Department of Civil Engineering, Faculty of Engineering, King Mongkut's University of Technology Thonburi, 126 Pracha Uthit Road, Bang Mod, Thung Khru, Bangkok 10140, Thailand

* Corresponding author, email: ampolk@gmail.com, ampol.kar@kmutt.ac.th

Received: 27 January 2014 / Accepted: 25 March 2015 / Published: 3 April 2015

Abstract: This paper considers the knapsack container loading problem. Rectangular-shaped boxes with different sizes are packed in rectangular-shaped containers according to a specified container sequence. Each container is filled such that the total loaded volume is maximised. All boxes with the same origin-destination pair may be rotated in six orthogonal directions without load-related and positioning constraints. The proposed approach performs 36 wall-building heuristic methods based on three ranking functions, two priority rules and six orthogonal rotations of containers. Three real-world test problems from a furniture company are employed. There is not a winning heuristic that performs best on the three test problems. The typical wall-building approach does not perform well when compared with considering all six orthogonal rotations of a container. In terms of the number of containers, the proposed approach can save up to 33% on the three problems, and the highest fill percentages in the best solutions are improved by up to 70.96% when compared with the manual solutions. In an additional experiment the proposed approach yields slightly lower (up to 5.38% and 3.64%) average fill percentages, with 94.47% and 87.94% shorter CPU time than the existing tree-search heuristic for the respective weakly and strongly heterogeneous problem instances.

Keywords: heuristic algorithm, knapsack container loading problem, wall-building algorithm

INTRODUCTION

Container loading is a crucial function for an efficient supply chain [1]. Inefficient container loading may inevitably result in additional container costs as well as an unsatisfactory level of customer service. The problem considered in this paper is the knapsack container loading problem.

The problem definition is explicitly stated as follows. Given the user-specified rectangular-shaped containers and rectangular-shaped boxes, all boxes are packed into the containers in a specified sequence. To fill a container, the subset of boxes is selected to be packed in the container such that the total volume is maximised. The cargo boxes may be rotated in any orthogonal direction without load-related and positioning constraints. It is noted that in principle, the empty spaces could be filled up with foam rubber to ensure proper support of the boxes [2]. All boxes have the same origin-destination pair. It is assumed that the cargo weights are dominated by cargo volume in container packing, so box weights are not considered in the algorithm.

In our view the contributions of this paper are threefold. First, a modified wall-building-based compound approach is proposed in this paper. The modification of the original compound approach [3] is the consideration of six orthogonal rotations of the container in addition to the three existing ranking functions and two existing priority rules for determining layer depths and strip heights. The modification results in 36 modified wall-building heuristic methods. The compound approach performs the 36 heuristic methods while recording the best solution found. Second, three real-world test problems from a furniture company in Thailand are employed in the comparison of the proposed compound method against the manual solutions and the tree-search heuristic [2] in terms of three criteria: the number of containers, the fill percentage, and the CPU time. Lastly, a performance comparison experiment of the proposed compound approach and the tree-search heuristic is conducted on the weakly heterogeneous and strongly heterogeneous standard test problem instances with a single container in terms of the fill percentage and the CPU time.

LITERATURE REVIEW

The container loading problem was first studied by Gilmore and Gomory [4]. Dyckhoff [5] and Wäscher et al. [6] proposed the general classification of cutting and packing problems. Pisinger [2] categorised the packing and loading literature into four categories based on the objective function and side constraints: strip packing, knapsack container loading, bin packing and multi-container loading. Firstly, in the strip packing problem (e.g. [3, 7]) the container has a known width and height but unlimited depth, and the problem is to pack all boxes such that the container's depth is minimised. This problem category is applicable to multi-drop situations. Secondly, in the knapsack container loading problem (e.g. [8–11]) we select a subset of boxes to be packed in a single container such that the total box volume is maximised. Thirdly, in the bin packing problem (e.g. [12]) all boxes have to be packed into a minimum number of containers with fixed dimensions. Lastly, in the multi-container loading problem (e.g. [13, 14]) all boxes are packed into a minimum number of containers, which are chosen from containers with varying dimensions such that the total shipping cost is minimised. Since the container loading problem is a nondeterministic-polynomial- hard problem [2], there does not exist an efficient algorithm for obtaining the exact solution in polynomial time. Christensen and Rousøe [15] and Bortfeldt and Wäscher [1] provide a thorough review of heuristics for the container loading problem. The heuristics for the container loading problem can be subdivided into three categories: construction algorithms [3, 4, 7, 16], tree-search algorithms [2, 17, 18], and metaheuristic algorithms [19–25]. In this study the knapsack container loading problem is considered, and the proposed approach is a construction algorithm.

MODIFIED WALL-BUILDING-BASED COMPOUND APPROACH

The wall-building algorithm of George and Robinson [16] fills a single container by building layers (walls) across the container's depth. The layer depth is selected based on the rationale that a box with the largest size of the smallest dimensions may be difficult to accommodate later in the packing procedure. As such, the ranking rule sets the layer's depth equal to the largest size of the smallest dimensions of the unpacked boxes. Given a known layer's depth, horizontal strips are built across the container's height. To fill a horizontal strip, the algorithm inserts the box with the largest size of the smallest dimensions of an unpacked box. Bischoff and Marriott [3] proposed a compound approach that performs the wall-building algorithms with various ranking rules while recording the best solution found. In this paper we modify the compound approach by considering six orthogonal rotations of the container, Pisinger's three ranking functions and two priority rules [2], Pisinger's box pairing procedure [2], and Pisinger's dynamic programming-based algorithm for the exact solution of the 0-1 knapsack strip packing problem [26].

The dimensions $\overline{W}$, $\overline{H}$ and $\overline{D}$ refer to the typical width, height and depth of the container, whereas the current width, height and depth of container (*W*, *H* and *D*) refer to the dimensions considered in the modified wall-building algorithm along the x-, y- and z-axes respectively. In the same way the dimensions $\overline{w}_j$, $\overline{h}_j$ and $\overline{d}_j$ are the initial width, height and depth of box *j*, whereas the current dimensions of box *j* (w_j, h_j and d_j) refer to the dimensions considered in the algorithm along the three axes. All boxes can be rotated in six orthogonal directions (or rotations), as illustrated in Figure 1.

The modified wall-building-based compound approach further considers six possible container rotations in the procedure. As shown in Table 1, the container rotation types 1, 2, 5 and 6 correspond to wall-building approaches, whereas the container rotation types 3 and 4 correspond to floor-building approaches. Container rotation type 1 (i.e. typical container rotation) builds layers (walls) across the container's depth $\overline{D}$ and builds horizontal strips of length $\overline{W}$ across the container's height $\overline{H}$. For container rotation types 2–6, the procedure rotates the container in the other five orthogonal directions and performs the wall-building algorithm; these rotation types correspond to either wall or floor building and either horizontal- or vertical-strip building.

Specifically, container rotation type 2 corresponds to building layers (walls) across container's depth $\overline{D}$ and vertical strips of length $\overline{H}$ across container's width $\overline{W}$. Container rotation type 3 corresponds to building layers (floors) across container's height $\overline{H}$ and horizontal strips of length $\overline{D}$ across container's width $\overline{W}$. Container rotation type 4 corresponds to building layers (floors) across container's height $\overline{H}$ and horizontal strips of length $\overline{W}$ across container's depth $\overline{D}$. Container rotation type 5 corresponds to building layers (walls) across container's width $\overline{W}$ and horizontal strips of length $\overline{D}$ across container's height $\overline{H}$. Container rotation type 6 corresponds to building layers (walls) across container's width $\overline{W}$ and vertical strips of length $\overline{H}$ across container's depth $\overline{D}$.

The notations used in the proposed procedure, including the parameters and variables, are first given. Then the pseudo-code is described, followed by descriptions of the major components in the pseudo-code.

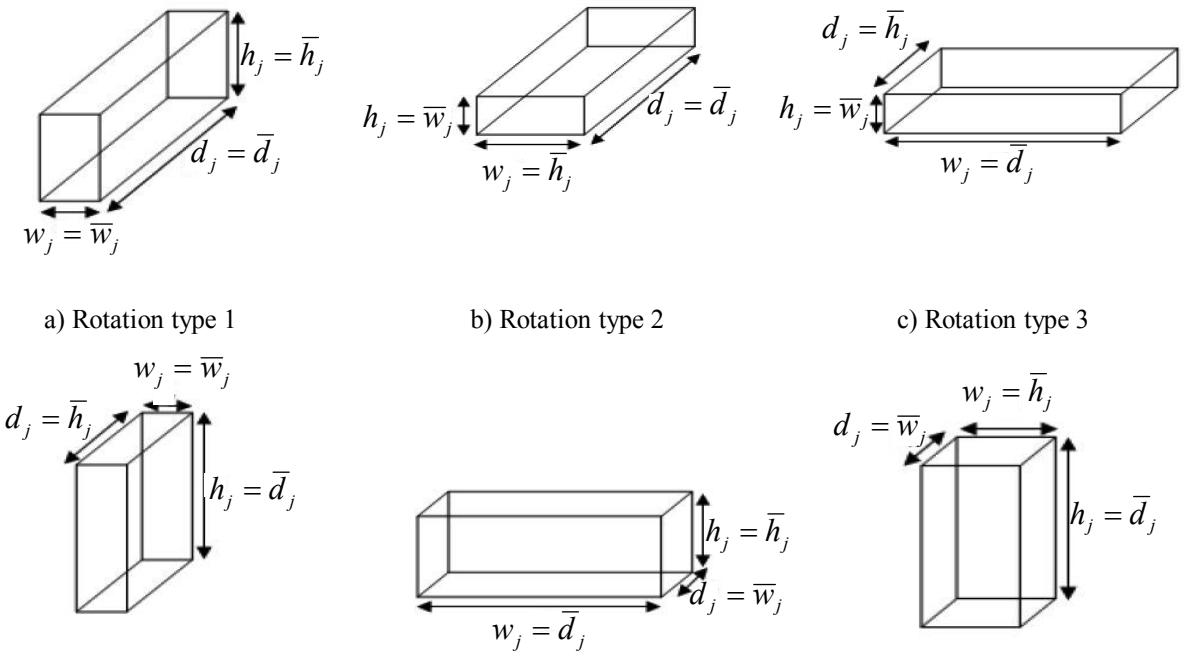

a) Rotation type 1 b) Rotation type 2 c) Rotation type 3

d) Rotation type 4 e) Rotation type 5 f) Rotation type 6

Figure 1. Six orthogonal rotations

Table 1. Container rotation types and associated descriptions

Container rotation type	W	H	D	Description
1	$\overline{W}$	$\overline{H}$	$\overline{D}$	Wall building: Layer building across depth $\overline{D}$ Horizontal strip (strip length = $\overline{W}$) building across height $\overline{H}$
2	$\overline{H}$	$\overline{W}$	$\overline{D}$	Wall building: Layer building across depth $\overline{D}$ Vertical strip (strip length = $\overline{H}$) building across width $\overline{W}$
3	$\overline{D}$	$\overline{W}$	$\overline{H}$	Floor building: Layer building across height $\overline{H}$ Horizontal strip (strip length = $\overline{D}$) building across width $\overline{W}$
4	$\overline{W}$	$\overline{D}$	$\overline{H}$	Floor building: Layer building across height $\overline{H}$ Horizontal strip (strip length = $\overline{W}$) across depth $\overline{D}$
5	$\overline{D}$	$\overline{H}$	$\overline{W}$	Wall building: Layer building across width $\overline{W}$ Horizontal strip (strip length = $\overline{D}$) across height $\overline{H}$
6	$\overline{H}$	$\overline{D}$	$\overline{W}$	Wall building: Layer building across width $\overline{W}$ Vertical strip (strip length = $\overline{H}$) building across depth $\overline{D}$

Notations

Parameters

OC = the user-specified ordered set of containers
$N = \{1,\ldots,n\}$ = set of boxes
$\overline{W}$, $\overline{H}$ and $\overline{D}$ = typical container width, height and depth
$\overline{w}_j$, $\overline{h}_j$ and $\overline{d}_j$ = initial width, height and depth of box j

Variables

N' = set of unloaded boxes
N'' = set of unloaded boxes that are feasible to fill the current layer
N''' = set of unloaded boxes that are feasible to fill the current strip
W = current container width in the algorithm
H = current container height in the algorithm
D = current container depth in the algorithm
w_j, h_j and d_j = current width, height and depth of box j
D_r = current residual container depth
H_r = current residual wall height
d' = current layer depth
sw' = current strip width
sh' = current strip height
strip_start_y = y-coordinate of the beginning of current strip
strip_end_y = y-coordinate of the ending of current strip
wall_start_z = z-coordinate of the beginning of current layer
wall_end_z = z-coordinate of the ending of current layer
(x_j, y_j, z_j) = (x,y,z)-coordinate of the referenced corner of loaded box j in the current solution
(dx_j, dy_j, dz_j) = (width, height, depth) of loaded box j in the current solution
(x_j^*, y_j^*, z_j^*) = (x,y,z)-coordinate of the referenced corner of loaded box j in the best solution found (dx_j^*, dy_j^*, dz_j^*) = (width, height, depth) of loaded box j in the best solution found

Pseudo-code

For each heuristic method c,u,v (i.e. container rotation type c, ranking function u and priority rule v), the following steps are performed, given the ordered set of containers OC. The variable indicating the ordinal number of container in OC is denoted by *con*.

Step 0: Set $con = 1$. Set $N' = N$.

Step 1: Initialise the following for the container *con*:

- set the current residual container depth to the current container depth: set $D_r = D$
- set the current strip width to the current container width: set $sw' = W$
- set *wall_end_z* = 0
- set (x_j, y_j, z_j) = (0,0,0) for all boxes j in N'
- set (dx_j, dy_j, dz_j) = ($\overline{w}_j$, $\overline{h}_j$, $\overline{d}_j$) for all boxes j in N'.

Step 2: Determine the current layer depth d' based on the ranking function f^u and the priority rule v and D_r. If d' can be determined:

- update the current residual container depth: set $D_r = D_r - d'$
- set the current residual wall height to the current container height: set $H_r = H$
- set *wall_start_z* = *wall_end_z*
- set *wall_end_z* = *wall_start_z* + d'
- set *strip_end_y* = 0

Otherwise, go to Step 7.
Step 3: Perform the box pairing procedure to obtain the set of feasible unloaded boxes (N'') to fill the current wall. Update (dx_j, dy_j, dz_j) for all rotated boxes j.
Step 4: Determine the current strip height (sh') based on the ranking function f^{α} and the priority rule v, given H_r. If sh' can be determined:

- update the current residual wall height: set $H_r = H_r - sh'$
- determine the set of feasible unloaded boxes (N''') to fill the current strip, and update (dx_j, dy_j, dz_j) for all rotated boxes j
- set *strip_start_y* = *strip_end_y*
- set *strip_end_y* = *strip_start_y* + sh'

Otherwise, go to Step 2.
Step 5: Perform the strip packing procedure to select boxes from N''' to fill the strip ($sw' \times sh' \times d'$) and update (x_j, y_j, z_j) and (dx_j, dy_j, dz_j) of each loaded box j. Update the sets of unloaded boxes N' and N''.
Step 6: If there is an unloaded box (i.e. $N' \neq \{\}$), go to Step 4. Otherwise, go to Step 8.
Step 7: Calculate the fill percentage of the current container *con*: fill percentage = volume of loaded boxes / volume of container. If *con* < |*OC*|, then set *con* = *con* + 1 and go to Step 1. Otherwise, go to Step 8.
Step 8: Calculate the fill percentage of the current container *con*.
Step 9: If the higher fill% in the current solution is higher than that in the best solution:

- set best heuristic method (c^*,u^*,v^*) = current heuristic method (c,u,v)
- set (x_j^*, y_j^*, z_j^*) = (x_j, y_j, z_j) and set (dx_j^*, dy_j^*, dz_j^*) = (dx_j, dy_j, dz_j) for all j in N.

Descriptions of Major Components

The major components of the proposed approach include the layer depth and strip height determinations, the box pairing procedure and the strip packing problem.

Layer depth and strip height determinations

In Step 2 we employ the ranking functions used by Pisinger [2], which are based on certain statistics of the dimensions of the unloaded boxes. The smallest and largest dimensions of the unloaded boxes are denoted by α and β respectively. Three different ranking functions are considered:

$$f_k^1 = \sum_{i=1}^{n} 1_{(w_i = k \vee h_i = k \vee d_i = k)} \quad \forall k = \alpha, \alpha+1, ..., \beta-1, \beta \tag{1.1}$$

$$f_k^2 = \sum_{i=1}^{n} 1_{(\max\{w_i, h_i, d_i\} = k)} \quad \forall k = \alpha, \alpha+1, ..., \beta-1, \beta \tag{1.2}$$

$$f_k^3 = \sum_{i=1}^{n} 1_{(\min\{w_i, h_i, d_i\} = k)} \quad \forall k = \alpha, \alpha+1, ..., \beta-1, \beta \tag{1.3}$$

Type-1 ranking function, Eq. (1.1), determines the number of occurrences of each dimension from all dimensions w_i, h_i and d_i of the remaining boxes. Type-2 ranking function, Eq. (1.2), determines the number of occurrences of each dimension from the largest dimensions of the unloaded boxes. Type-3 ranking function, Eq. (1.3), determines the number of occurrences of each dimension from the smallest dimensions of the unloaded boxes.

In Step 4 when the layer depth and the set of feasible unloaded boxes (N'') to fill the current wall have been determined, the ranking functions only consider the current width and the current

height of feasible unloaded boxes. The smallest dimension of the current widths and heights of the feasible unloaded boxes is denoted by α and the largest by β. Three different ranking functions are:

$$f_k^1 = \sum_{i=1}^{n} 1_{(w_i=k \vee h_i=k)} \quad \forall k = \alpha, \alpha+1, ..., \beta-1, \beta \tag{2.1}$$

$$f_k^2 = \sum_{i=1}^{n} 1_{(\max\{w_i,h_i\}=k)} \quad \forall k = \alpha, \alpha+1, ..., \beta-1, \beta \tag{2.2}$$

$$f_k^3 = \sum_{i=1}^{n} 1_{(\min\{w_i,h_i\}=k)} \quad \forall k = \alpha, \alpha+1, ..., \beta-1, \beta \tag{2.3}$$

The type-1 ranking function, Eq. (2.1), determines the number of occurrences of each dimension from all dimensions w_i and h_i of the feasible unloaded boxes. The type-2 ranking function, Eq. (2.2), determines the number of occurrences of each dimension from the largest dimensions of w_i and h_i of the feasible unloaded boxes. The type-3 ranking function, Eq. (2.3), determines the number of occurrences of each dimension from the smallest dimensions w_i and h_i of the feasible unloaded boxes.

In Steps 2 and 4 we consider two priority rules [2]. For priority rule 1, the largest dimension with positive ranking function value is selected, i.e. largest dimension k with $f_k > 0$. For priority rule 2, the most frequent dimension is selected, i.e. dimension k with the largest value of f_k. The motivation of priority rule 1 is that the largest dimension should be loaded early in the packing procedure; otherwise, it may be difficult to be packed later. The motivation of priority rule 2 is that a homogeneous layer or strip width may be tightly packed. It is noted that the procedure by George and Robinson [16] is equivalent to type-3 ranking function and priority rule 1.

Box pairing procedure

After the layer depth d' is determined, in Step 3 we employ the box pairing procedure [2] to determine the set of feasible unloaded boxes (N'') to fill the current wall. Pisinger [2] indicated that a box pairing procedure can be used to achieve an improved solution in his tree-search heuristic, and this is also adopted in our proposed algorithm. The complexity of the box pairing procedure is $O(n^2)$ and it is executed only once for each layer depth d'. The box pairing procedure is described below:

Step 3.1: Set $N''=\{\}$. If the smallest dimension of each box i in the set N' is bigger than the layer depth d', box i is not inserted in N'' and is not considered in the box pairing procedure. Otherwise, rotate each box i in the set N' such that its depth d_i is the largest dimension satisfying the constraint $d_i \le d'$. The filling ratio to pack box i in a layer with depth d' is $\mu(i)$:

$$\mu(i) = w_i h_i d_i / w_i h_i d' = d_i / d' \tag{3}$$

Step 3.2: Pair box i with another box j in the set N' where $j \neq i$. All orthogonal rotations of i and j are considered such that $d_i + d_j \le d'$, and the associated filling ratio, $\eta(i,j)$, is determined:

$$\eta(i,j) = \frac{w_i h_i d_i + w_j h_j d_j}{d' \cdot \max\{w_i, w_j\} \cdot \max\{h_i, h_j\}} \tag{4}$$

If $\eta(i,j) \le \mu(i)$ for all boxes $j \neq i$ in N' and all orthogonal rotations of boxes i and j, then box i remains alone and is inserted in N''. Otherwise, box j and the corresponding rotation with the largest value of $\eta(i,j)$ is selected to pair with box i in order to form a new box k with the following dimensions: $w_k = \max\{w_i, w_j\}$, $h_k = \max\{h_i, h_j\}$ and $d_k = d_i + d_j$. Then box k is inserted in N''.

Strip packing problem

In Step 5 strips are filled horizontally. The strip has a width equal to the current container width $sw' = W$, a depth equal to the current layer depth d', and a height of sh'. The procedure first determines the set of feasible unloaded boxes (N''') to fill the current strip as follows. Set $N''' = \{\}$. Each box j in the set N'' is rotated in one of six directions such that w_j is minimised subject to $d_j \le d'$ and $h_j \le sh'$. If it is possible to fit box j in the current strip, box j is inserted in the set N'''. If not, then box j is not considered for the current strip packing. The strip packing problem can be formulated as a 0-1 knapsack problem, as shown below [2]:

$$\max \sum_{j \in N'''} w_j \cdot h_j \cdot d_j \cdot s_j \quad \text{subject to} \quad \sum_{j \in N'''} w_j \cdot s_j \le W \quad \text{and} \quad s_j \in \{0,1\} \quad \forall j \in N'''$$

where s_j is a binary decision variable; s_j = 1 if box j is chosen to fill the current strip, and 0 otherwise. The 0-1 knapsack problem is a nondeterministic-polynomial-hard problem [27], so there does not exist an efficient algorithm for an exact solution in polynomial time. It can be solved in pseudo-polynomial time by dynamic programming [28]. In this study we employ the effective dynamic programming-based algorithm by Pisinger [26].

COMPUTATIONAL EXPERIENCES

Thirty-six modified wall-building heuristic methods were implemented in C by modifying the callable C code: the box pairing procedure was taken from the callable C code by Pisinger [29] and the dynamic programming heuristic for a 0-1 knapsack problem was taken from the callable C code by Pisinger [30]. These heuristic trials were run on a computer with a 1.73 GHz Intel Core i7 processor and 4 GB of RAM, running under Windows 7. We used three real-world test problems from a furniture company in Thailand. The origin of the cargos was Thailand and the destinations of the cargos in the three test problems were Brunei, Vietnam and Japan. The initial dimensions of the boxes for the three test problems are shown in Tables 2a-c. These three test problems were weakly heterogeneous since the number of box types was less than 20 [2]. The standard container types were 40' HQ, 40' and 20', as shown in Table 2d. For the first and second test problems, all heuristic methods employed 40' HQ containers. For the third test problem, all methods employed a 40' container as the first container and a 20' container as the second container.

Due to space limitation, we show only the results of test problem 1 in Table 3. It is noted that the cargo weights in each container in the solutions do not exceed the allowable weight. The heuristic method *c,u,v* refers to the container rotation type *c*, ranking function f^u and priority rule *v*. There is not a winning heuristic that performs best on the three test problems. On the first test problem, there are 11 heuristic methods that yield two 40' HQ containers and 25 methods that yield three 40' HQ containers. The method *c*=6,*u*=2,*v*=2 performs best on the first test problem with two 40' HQ containers and the highest fill percentage (87.82%) of container number 1. On the second test problem there are 34 heuristic methods that yield two 40' containers and only 2 methods (*c*=3,*u*=2,*v*=1 and *c*=5,*u*=2,*v*=1) that yield three 40' containers. The method *c*=6,*u*=3,*v*=1 performs best on the second test problem with two 40'-containers and the highest fill percentage (80.75%) of container number 1. In the best solution found, the fill percentage (20.50%) of container number 2 is equal to 15,908,120 cm^3, which can fill a 20' container. Thus, the best solution found becomes a 40' container with 80.75% fill and a 20' container with 41.03% fill. On the third test problem there are 33 methods that yield two containers (40' and 20'). The three methods (*c*=1,*u*=1,*v*=2; *c*=3,*u*=1,*v*=2; *c*=4,*u*=1,*v*=2) perform best on the third test problem, yielding a single 40' container with the highest

fill percentage (68.42%). Interestingly, the typical wall-building algorithms that are associated with container rotation type 1 (c=1) do not perform well; thus, this reiterates the improvement by considering the six orthogonal rotations of container.

The best solutions found on the three test problems by the proposed compound approach were subsequently compared with the manual solutions by the furniture company as well as the best solutions found by the tree-search heuristic [2], as shown in Table 4. The manual solutions by the furniture company employ three 40' HQ containers for the first test problem, two 40' containers for the second test problem, and a 40' container and a 20' container for the third test problem. In terms of the number of containers, the proposed compound approach can save 33.33%, 25% and 33.33% on the three test problems respectively. The highest fill percentages in the best solutions found are

Table 2. Initial dimensions of boxes for three test problems and dimensions of standard containers

a) Initial dimensions (cm) of boxes for test problem 1 (223 boxes and 16 box types)*

Box type	1	2	3	4	5	6	7	8	9	10	11	12	13	14	15	16
Width ($\overline{w}_j$)	100	70	96	100	85	85	85	102	80	212	80	102	102	145	70	69
Depth ($\overline{d}_j$)	100	70	70	100	190	148	195	160	155	80	170	102	102	67	68	69
Height ($\overline{h}_j$)	80	80	53	60	100	100	100	90	90	90	65	77	57	83	100	92
Number of boxes	1	3	2	3	3	4	3	3	3	4	3	6	1	16	11	157

* Total box volume = 129,402,900 cm^3

b) Initial dimensions (cm) of boxes for test problem 2 (113 boxes and 14 box types)*

Box type	1	2	3	4	5	6	7	8	9	10	11	12	13	14
Width ($\overline{w}_j$)	90	92	110	100	80	100	110	110	110	100	100	100	100	70
Depth ($\overline{d}_j$)	100	142	110	100	95	195	110	110	110	210	210	180	180	73
Height ($\overline{h}_j$)	101	101	75	115	92	70	90	55	45	55	60	60	26	92
Number of boxes	12	1	8	4	5	3	1	1	1	1	9	1	1	65

* Total box volume = 78,578,264 cm^3

c) Initial dimensions (cm) of boxes for test problem 3 (94 boxes and 11 box types)*

Box type	1	2	3	4	5	6	7	8	9	10	11
Width ($\overline{w}_j$)	120	120	120	91	130	90	130	110	80	110	70
Depth ($\overline{d}_j$)	120	120	190	210	244	170	170	190	80	210	73
Height ($\overline{h}_j$)	70	40	70	70	80	70	70	45	70	60	92
Number of boxes	1	1	1	1	1	2	2	1	3	1	80

* Total box volume = 53,097,700 cm^3

d) Typical dimensions of standard container types

Container type	$\overline{W}$	$\overline{H}$	$\overline{D}$
40' HQ	243 cm (8 ft)	292 cm (9.6 ft)	1219 cm (40 ft)
40'	243 cm (8 ft)	262 cm (8.6 ft)	1219 cm (40 ft)
20'	243 cm (8 ft)	262 cm (8.6 ft)	609 cm (20 ft)

Table 3. Computational results for test problem 1 (all containers are 40' HQ with 86,495,364 cm^3)

Heuristic method *c,u,v* (CPU time) t	Container no.	Fill %
1, 1, 1 (3.88 sec)	1	77.03
	2	72.13
	3	0.45
2, 1, 1 (3.23 sec)	1	70.7
	2	77.04
	3	1.87
3, 1, 1 (0.39 sec)	1	55.39
	2	80.7
	3	13.51
4, 1, 1 (4.79 sec)	1	76.97
	2	72.64
5, 1, 1 (8.73 sec)	1	61.42
	2	53.81
	3	34.37
6, 1, 1 (1.06 sec)	1	67.5
	2	66.69
	3	15.42
1, 1, 2 (0.61 sec)	1	81.11
	2	68.49
2, 1, 2 (0.46 sec)	1	72.95
	2	73.67
	3	2.99
3, 1, 2 (0.10 sec)	1	79.04
	2	67.24
	3	3.33
4, 1, 2 (0.39 sec)	1	81.28
	2	68.33
5, 1, 2 (0.28 sec)	1	81.48
	2	64.3
	3	3.83
6, 1, 2 (1.38 sec)	1	81.9
	2	63.88
	3	3.83
1, 2, 1 (0.48 sec)	1	77.03
	2	72.13
	3	0.45
2, 2, 1 (0.55 sec)	1	71.36
	2	77.8
	3	0.45
3, 2, 1 (0.23 sec)	1	55.39
	2	80.7
	3	13.51
4, 2, 1 (6.19 sec)	1	76.97
	2	72.64
5, 2, 1 (8.64 sec)	1	61.42
	2	53.81
	3	34.37
6, 2, 1 (0.27 sec)	1	58.84
	2	70.58
	3	20.19
1, 2, 2 (0.45 sec)	1	79.51
	2	70.1
2, 2, 2 (0.37 sec)	1	79.5
	2	69.65
	3	0.45
3, 2, 2 (0.09 sec)	1	78.17
	2	52.61
	3	18.82
4, 2, 2 (0.31 sec)	1	77.99
	2	24.86
	3	46.76
5, 2, 2 (0.10 sec)	1	86.13
	2	59.94
	3	3.53
6, 2, 2 (0.22 sec)	**1**	**87.82**
	2	**61.78**
1, 3, 1 (1.58 sec)	1	78.24
	2	71.37
2, 3, 1 (0.63 sec)	1	68.99
	2	62.42
	3	18.19
3, 3, 1 (0.36 sec)	1	79.66
	2	69.95
4, 3, 1 (2.39 sec)	1	79.15
	2	70.46
5, 3, 1 (0.35 sec)	1	86.5
	2	63.11
6, 3, 1 (4.03 sec)	1	82.4
	2	67.21
1, 3, 2 (0.89 sec)	1	73.21
	2	68.15
	3	8.25
2, 3, 2 (0.60 sec)	1	80.21
	2	66.83
	3	2.56
3, 3, 2 (0.12 sec)	1	79.52
	2	66.06
	3	4.02
4, 3, 2 (0.57 sec)	1	68.75
	2	71.12
	3	9.73
5, 3, 2 (3.57 sec)	1	79.92
	2	61.28
	3	8.41
6, 3, 2 (15.85 sec)	1	78.91
	2	63.83
	3	6.87

Note: *c* = container rotation type; *u* = ranking function; *v* = priority rule
Total CPU time = 74.14 sec; the best solution found is in bold and underlined

increased by 70.96%, 57.32% and 27.94% on test problems 1, 2 and 3 respectively when compared with the manual solutions. The tree-search heuristic yields the same results as the proposed compound approach in terms of the number of containers. The highest fill percentages by the proposed approach are only 2.47% and 8.57% lower than those by the tree-search heuristic on problems 1 and 2 respectively. The computational times by the proposed approach are only 74.49% and 98.10% less than those by the tree-search heuristic on problems 1 and 2 respectively.

Next, an experiment was conducted to compare the performance of the proposed approach and the tree-search heuristic [2] for the knapsack container loading problem. We employed only one container in the user-specified ordered set of containers (i.e. $|OC| = 1$) so that the proposed approach

Table 4. Comparison between manual solutions, best solutions found by tree-search heuristic, and best solutions found by proposed approach on three test problems

Container no.	Manual solution		Best solution by tree-search heuristic [2]		Best solution found by modified wall-building-based compound approach	
	Container type	No. of boxes Vol. of boxes Fill %	Container type	No. of boxes Vol. of boxes Fill %	Container type	No. of boxes Vol. of boxes Fill %
Test problem 1						
1	40' HQ	82 44,440,856 cm^3 51.37%	40' HQ	111 77,884,495 cm^3 90.04%	40' HQ	162 75,962,452 cm^3 87.82%
2	40' HQ	94 41,173,128 cm^3 47.60%	40' HQ	112 51,518,405 cm^3 59.56%	40' HQ	61 53,440,448 cm^3 61.78%
3	40' HQ	47 43,788,916 cm^3 50.63%	-		-	
Total CPU time	-		290.58 sec		74.14 sec	
Test problem 2						
1	40'	39 39,838,464 cm^3 51.33%	40'	93 68,541,604 cm^3 88.32%	40'	98 62,670,144 cm^3 80.75%
2	40'	74 38,739,800 cm^3 49.92%	20'	20 10,036,660 cm^3 25.89%	20'	15 15,908,120 cm^3 41.03%
Total CPU time	-		809.80 sec		15.38 sec	
Test problem 3						
1	40'	85 41,508,600 cm^3 53.48%	40'	94 53,097,700 cm^3 68.42%	40'	94 53,097,700 cm^3 68.42%
2	20'	9 11,589,100 cm^3 29.89%	-		-	
Total CPU time	-		0.04 sec		9.65 sec	

Note: Volume of 40' HQ container = 86,495,364 cm^3
Volume of 40' container = 77,608,854 cm^3
Volume of 20' container = 38,772,594 cm^3

solved the knapsack container loading problem. As in Pisinger [2], data instances were randomly generated using the scheme of Hemminki [31], which reflects typical properties of industrial loading problems. The container had width, height and depth of 230, 230 and 590 cm respectively. Two types of data instances were tested: the weakly heterogeneous and the strongly heterogeneous. For weakly heterogeneous instances, 20 different box types were generated, with the widths, heights and depths randomly distributed between 25-115 cm. Then the cargo was generated by randomly choosing a box as one of the 20 box types. For strongly heterogeneous instances, boxes were generated such that they may have different dimensions. For each instance, new boxes were generated until their overall volume exceeded the target volume percentage of the container volume (T_c). A series of tests were run where boxes were generated until the overall volume of the boxes exceeded T_c = 80, 85, 90, 95, 100, 110, 120, …, 200% of the container volume. These were run on a computer with a 3.4 GHz Intel Core i7-3770 processor and 8 GB of RAM, running under Windows 7. Table 5 shows the average results of 100 problem instances at each T_c level by the tree-search heuristic and the proposed approach for the weakly and strongly heterogeneous instances. For the

Table 5. Comparison of the modified wall-building-based compound approach and the tree search heuristic for the knapsack container loading problem (average values of 100 instances)

T_c	Weakly heterogeneous instances					Strongly heterogeneous instances				
	Average total number of boxes	Tree search heuristic [2]		Proposed approach		Average total number of boxes	Tree search heuristic [2]		Proposed approach	
		Avg. % volume filled	Avg. CPU time (sec)	Avg. % volume filled (% change)	Avg. CPU time (sec) (% change)		Avg. % volume filled	Avg. CPU time (sec)	Avg. % volume filled (% change)	Avg. CPU time (sec) (% change)
90	84.76	90.74	2.06	86.89 (-4.24)	1.34 (-34.95)	82.45	90.86	0.86	88.36 (-2.75)	0.90 (4.65)
95	89.34	92.75	26.05	87.76 (-5.38)	1.44 (-94.47)	86.78	92.35	2.6	89.15 (-3.47)	0.95 (-63.46)
100	94.09	93.34	24.06	88.45 (-5.24)	1.4 (-94.18)	91.27	93.07	3.45	89.76 (-3.56)	0.98 (-71.59)
110	103.28	93.96	20.29	89.37 (-4.89)	1.53 (-92.46)	100.23	93.99	5.24	90.57 (-3.64)	1.10 (-79.01)
120	113.03	94.28	16.38	89.95 (-4.59)	1.62 (-90.11)	109.54	94.59	7.17	91.22 (-3.56)	1.20 (-83.26)
130	122.56	94.46	13.66	90.72 (-3.96)	1.81 (-86.75)	118.4	95	8.78	91.91 (-3.25)	1.27 (-85.54)
140	131.73	94.61	11.13	90.91 (-3.91)	1.86 (-83.29)	127.36	95.3	10.49	92.35 (-3.10)	1.37 (-86.94)
150	140.66	94.66	10.5	91.32 (-3.53)	1.91 (-81.81)	136.76	95.54	12.11	92.73 (-2.94)	1.46 (-87.94)
160	149.78	94.79	10.41	91.72 (-3.24)	2.05 (-80.31)	145.91	95.74	12.19	93.08 (-2.78)	1.56 (-87.20)
170	159	94.87	10.18	92.02 (-3.00)	2.17 (-78.68)	155.28	95.91	12	93.46 (-2.55)	1.65 (-86.25)
180	168.27	94.97	9.85	92.37 (-2.74)	2.27 (-76.95)	164.53	96.04	11.08	93.64 (-2.50)	1.71 (-84.57)
190	177.57	95	10.55	92.52 (-2.61)	2.39 (-77.35)	173.74	96.14	10.06	93.89 (-2.34)	1.77 (-82.41)
200	186.84	95.08	10.35	92.75 (-2.45)	2.53 (-75.56)	182.78	96.18	9.46	94.05 (-2.21)	1.88 (-80.13)

weakly heterogeneous problem instances, the proposed approach yields up to 5.38% less average percentage of volume filled with 94.47% shorter CPU time than the tree-search heuristic, while for the strongly heterogeneous problem instances, it yields up to 3.64% less average percentage of volume filled with 87.94% shorter CPU time. Interestingly, as T_c increases, the proposed approach yields solutions closer to those by the tree-search heuristic in terms of average percentage of volume filled, with considerably shorter CPU time.

CONCLUSIONS

The modified wall-building-based compound approach that performs 36 wall-building heuristic methods (three ranking functions, two priority rules and six orthogonal rotations of containers) is proposed. It was tested on three real-world test problems which were weakly heterogeneous with less than 20 box types from a furniture company. There was not a winning heuristic that performed best on the three test problems. The typical wall-building heuristic methods associated with container rotation type 1 did not perform well; significant improvement was achieved by considering the six orthogonal rotations of a container in the modified approach.

The best solutions found on the three test problems were compared with the manual solutions by the furniture company. In terms of the number of containers, the proposed compound approach could save up to 33% on the three test problems. The highest fill percentages in the best solutions found were improved by up to 70.96% when compared with the manual solutions. Next, the best solutions found by the proposed approach were compared with the best solutions found by the existing tree-search heuristic method. They yielded the same results in terms of the number of containers. However, the proposed approach was slightly outperformed by the tree-search heuristic method in terms of solution quality but performed much better in terms of computational time. The best fill percentages by the proposed approach were up to 8.57% less than those by the tree-search heuristic method, while the total computational times on the three test problems were up to 98.10% shorter.

Furthermore, when compared in weakly and strongly heterogeneous instances at different levels of total box volume, the proposed approach yielded up to 5.38% and 3.64% less average percentage of volume filled with 94.47% and 87.94% shorter CPU time than the tree-search heuristic respectively. Interestingly, as the generated total box volume got higher, the proposed approach yielded solutions closer to those of the existing tree-search heuristic in terms of average percentage of volume filled with considerably shorter CPU time.

ACKNOWLEDGEMENTS

The authors gratefully acknowledge support from the National Research Council of Thailand and the Thailand Research Fund.

REFERENCES

1. A. Bortfeldt and G. Wäscher, “Constraints in container loading – A state-of-the-art review”, *Eur. J. Oper. Res.*, **2013**, *229*, 1-20.
2. D. Pisinger, “Heuristics for the container loading problem”, *Eur. J. Oper. Res.*, **2002**, *141*, 382-392.
3. E. E. Bischoff and M. D. Marriott, “A comparative evaluation of heuristics for container loading”, *Eur. J. Oper. Res.*, **1990**, *44*, 267-276.

4. P. C. Gilmore and R. E. Gomory, "Multistage cutting stock problems of two and more dimensions", *Oper. Res.*, **1965**, *13*, 94-120.
5. H. Dyckhoff, "A typology of cutting and packing problems", *Eur. J. Oper. Res.*, **1990**, *44*, 145-159.
6. G. Wäscher, H. Haubner and H. Schumann, "An improved typology of cutting and packing problems", *Eur. J. Oper. Res.*, **2007**, *183*, 1109-1130.
7. E. E. Bischoff and M. S. W. Ratcliff, "Loading multiple pallets", *J. Oper. Res. Soc.*, **1995**, *46*, 1322-1336.
8. H. Gehring, K. Menschner and M. Meyer, "A computer-based heuristic for packing pooled shipment containers", *Eur. J. Oper. Res.*, **1990**, *44*, 277-288.
9. K. He and W. Huang, "A caving degree based flake arrangement approach for the container loading problem", *Comput. Ind. Eng.*, **2010**, *59*, 344-351.
10. S. Liu, W. Tan, Z. Xu and X. Liu, "A tree search algorithm for the container loading problem", *Comput. Ind. Eng.*, **2014**, *75*, 20-30.
11. N. Wang, A. Lim and W. Zhu, "A multi-round partial beam search approach for the single container loading problem with shipment priority", *Int. J. Prod. Econ.*, **2013**, *145*, 531-540.
12. S. Martello, D. Pisinger and D. Vigo, "The three-dimensional bin packing problem", *Oper. Res.*, **2000**, *48*, 256-267.
13. C. S. Chen, S. M. Lee and Q. S. Shen, "An analytical model for the container loading problem", *Eur. J. Oper. Res.*, **1995**, *80*, 68-76.
14. L. Wei, W. Zhu and A. Lim, "A goal-driven prototype column generation strategy for the multiple container loading cost minimization problem", *Eur. J. Oper. Res.*, **2015**, *241*, 39-49.
15. S. G. Christensen and D. M. Rousøe, "Container loading with multi-drop constraints", *Master Thesis*, **2007**, Technical University of Denmark, Denmark.
16. J. A. George and D. F. Robinson, "A heuristic for packing boxes into a container", *Comput. Oper. Res.*, **1980**, *7*, 147-156.
17. M. Eley, "Solving container loading problems by block arrangement", *Eur. J. Oper. Res.*, **2002**, *141*, 393-409.
18. R. Morabito and M. Arenales, "An and/or-graph approach to the container loading problem", *Int. Trans. Oper. Res.*, **1994**, *1*, 59-73.
19. H. Gehring and A. Bortfeldt, "A genetic algorithm for solving the container loading problem", *Int. Trans. Oper. Res.*, **1997**, *4*, 401-418.
20. A. Bortfeldt and H. Gehring, "A hybrid genetic algorithm for the container loading problem", *Eur. J. Oper. Res.*, **2001**, *131*, 143-161.
21. A. Moura and J. F. Oliveira, "A GRASP approach to the container-loading problem", *IEEE Intell. Syst.*, **2005**, *20*, 50-57.
22. A. Bortfeldt, H. Gehring and D. Mack, "A parallel tabu search algorithm for solving the container loading problem", *Parallel Comput.*, **2003**, *29*, 641-662.
23. D. Mack, A. Bortfeldt and H. Gehring, "A parallel hybrid local search algorithm for the container loading problem", *Int. Trans. Oper. Res.*, **2004**, *11*, 511-533.
24. P. Thapatsuwan, P. Pongcharoen, C. Hicks and W. Chainate, "Development of a stochastic optimisation tool for solving the multiple container packing problems", *Int. J. Prod. Econ.*, **2012**, *140*, 737-748.

25. J. Liu, Y. Yue, Z. Dong, C. Maple and M. Keech, "A novel hybrid tabu search approach to container loading", *Comput. Oper. Res.*, **2011**, *38*, 797-807.
26. D. Pisinger, "A minimal algorithm for the 0-1 Knapsack Problem", *Oper. Res.*, **1997**, *45*, 758-767.
27. M. R. Garey and D. S. Johnson, "Computers and Intractability: A Guide to the Theory of NP-Completeness", W. H. Freeman, Los Angeles, **1979**.
28. C. H. Papadimitriou, "On the complexity of integer programming", *J. ACM*, **1981**, *28*, 765-768.
29. D. Pisinger, "A tree-search heuristic C code", **1998**, http://www.diku.dk/~pisinger/codes.html (Accession date: August 2012).
30. D. Pisinger, "The minknap algorithm callable C code", **1993**, http://www.diku.dk/~pisinger/codes.html (Accession date: August 2012).
31. J. Hemminki, "Container loading with variable strategies in each layer", Proceedings of 10th EURO Summer Institute on Combinatorial Optimization ESI-X. Groupe HEC (Ecole des Hautes Etudes Commerciales), **1994**, Jouy-en-Josas, France.

Maejo Int. J. Sci. Technol. **2015**, *9*(01), 108-120; doi: 10.14456/mijst.2015.7

Maejo International Journal of Science and Technology

ISSN 1905-7873
Available online at www.mijst.mju.ac.th

Technical Note

Privacy-preserving emergency access control for personal health records

Phuwanai Thummavet and Sangsuree Vasupongayya*

Department of Computer Engineering, Faculty of Engineering, Prince of Songkla University, P.O. Box 2 Kohong, Hatyai, Songkhla, 90112, Thailand

* Corresponding author, e-mail: vsangsur@coe.psu.ac.th

Received: 19 June 2014 / Accepted: 2 April 2015 / Published: 9 April 2015

Abstract: Recently, a flexible scheme for handling personal health records (PHRs) in emergency situations has been proposed. Under such a scheme, each PHR is classified as secure, restricted, or exclusive information. Secure PHRs are immediately available to the emergency response unit (ERU) staff. Restricted PHRs require additional approvals from a set of authorised people who are pre-selected by the PHR owner. Exclusive PHRs are only accessible by the owner. Previous work assumed that all ERU staff is trustworthy. To be practical, this work eliminates such an assumption. Several mechanisms are applied to ensure the usability and security of the newly proposed scheme. For example, an access-request authentication mechanism is applied to enhance the trustworthiness of the requests that are invoked by the ERU staff. Moreover, a transaction auditing mechanism is applied to provide a non-repudiation feature. This paper discusses the usability and security issues of the proposed scheme in practice and suggests how to classify a PHR considering the above-mentioned privacy levels.

Keywords: personal health record, privacy, security, ciphertext-policy attribute-based encryption, threshold cryptosystem

INTRODUCTION

Today, people are more aware of information concerning their health because of the rising cost of healthcare. Recently, alternative medicines such as dietary supplements and herbal products have gained popularity [1]. In addition, personal health record (PHR) system is emerging as a preventive healthcare method [2]. The PHR system allows an individual to collect, store, analyse, and share his/her personal health data with a group of trusted people such as family members, family doctors and caretakers [3]. The PHR system usually contains highly sensitive information

[4]; it can include information related to the PHR owner's health such as his/her mental health, disease risks and laboratory test results. Therefore, the PHR system must ensure the security and privacy of the PHR owner's information, and the actual PHRs must be protected from an unauthorised access or modification. Moreover, the PHR owner must be able to manage and control all authorised access to his/her PHRs. To achieve such features, the PHR system should allow the PHR owner to define an access control policy on his/her PHRs, which must be enforced by the PHR system. Thus, an individual can access a PHR if and only if that individual has been granted the authority by the PHR owner via an access control policy. For example, John can grant access to his family doctor, Jason, by defining a policy such as "Jason, who is a doctor, can access my records." Hence the PHR system will allow only Jason, who is a doctor, to access John's PHRs.

An interesting PHR management issue arises during an emergency [5, 6]. Generally, an emergency response unit (ERU) staff member is the first care provider to reach the victim. Providing correct and useful health information (e.g. personal diseases) about the victim in the emergency situation can increase the opportunity to provide proper treatment to save the victim's life or alleviate his/her critical conditions. Therefore, it is vital to allow the ERU staff to access the necessary PHR information of the victim in an emergency situation [7]. According to the above example, John can allow Dr. Jason to access his PHRs because John knows Dr. Jason. In an emergency, John may not know any ERU staff. Thus, John will not be able to define a policy to allow a specific ERU staff member to access his PHRs. During an emergency situation, John may be unconscious and may not be able to grant any permission to the ERU staff at the scene. Moreover, ERU staff should not access John's PHRs unless they are necessary to save his life. Thus, the question is how to allow ERU staff to access the victim's PHRs during an emergency situation.

A scheme to manage and handle PHRs during an emergency situation has been proposed in our previous work [8], which allows different access restrictions. Under such a scheme, each PHR is classified into secure, restricted, and exclusive categories. Different categories provide different access permissions to ERU staff for the victim's PHRs. Secure PHRs are freely available to ERU staff during an emergency situation. Restricted PHRs are accessible to an ERU staff member if and only if he/she was granted access permission by at least t out of n trusted people who are pre-selected by the PHR owner, where t is an acceptable threshold, pre-defined by the PHR owner and n is the total number of trusted people on the PHR owner's list. Exclusive PHRs are not accessible even during an emergency situation. With the proposed scheme, the PHR owners can selectively share their PHRs with the ERU staff while additional data can be requested if needed.

This work extends the previous scheme to cover external ERUs that were not included in the original design [8]. The ERU staff authentication process was not considered in the original design because the ERU staff was assumed to be trustworthy and part of the PHR system. However, in the real world ERU staff can be from various external sources such as public organisations, medical care institutions, private organisations, non-profit organisations or a group of volunteers. Therefore, the ERU staff must be verified by their authorised commander/manager. To guarantee the reliability of the verification process, an access request authentication (ARA) mechanism is proposed in this work as an extension of the previous scheme. Hence the PHR access request from any ERU staff can be performed if and only if the staff member is granted access permission by his/her authorised ERU commander/manager. In addition, a transaction auditing mechanism is used in this study to provide a non-repudiation feature. Furthermore, the security of all connections in the proposed scheme is provided by means of secure sockets layer protocols and secure shell protocols.

RELATED WORK

A database-level encryption was employed by Weerasinghe and Muttukrishnan [9] to provide an information exchange scheme between the ERU staff and the PHR service providers via a trusted third party. Under such a scheme, the actual PHRs are encrypted and stored by a PHR service provider. During emergency situations, the PHR service provider delivers the requested PHR to the ERU staff on behalf of the PHR owner. The authentication of each party should be done by the trusted third party. However, the use of a database key becomes an issue because such a technique can introduce a privacy risk for the PHR owner [10]. To access the information, the ERU staff has access to the key through which multiple access can be performed. Typically, the access permission under such a scheme is binary and the ERU staff can access the entire database. In other words, the ERU staff can access all records stored in a particular database even though some records may not be related to their tasks.

To solve the privacy concern of the database-level encryption technique, a digital pseudonym was introduced by Huda et al [11]. The pseudonym indexes the PHRs for each PHR owner, whose name (i.e. a field in the database) is replaced by a random pseudonym. Then the pseudonym is encrypted and stored on the PHR owner's health smart card. The ERU staff uses the pseudonym to retrieve the victim's PHRs during an emergency situation. Using the pseudonym, even though the database records are exposed to unauthorised users, the PHR owner's privacy is still preserved. However, the scope of the information accessed by the ERU staff cannot be limited because the ERU staff can access all records indexed by a particular pseudonym.

A backup mechanism at a trust centre for the PHR owner was proposed by the healthcare system for patient privacy [12]. Under such a scheme, the PHR owner can define the information that will be available during emergency situations and selects his/her PHRs to be stored at a trusted server. The information stored at the trust centre is freely available to the ERU staff during an emergency situation. Hence the privacy of the PHR owner and the secrecy of the PHR can be preserved. However, only static information pre-selected by the PHR owner is available. In our proposed scheme both static and additional information is available to the ERU staff. The static pre-selected information is the secure PHRs and the additional information is the restricted PHRs, which are available upon request.

A key-policy attribute-based encryption (KP-ABE) [13] was employed in the break-glass access [14, 15] to protect the PHR information. The KP-ABE enables a PHR owner to specify a set of attributes embedded in the encrypted PHR. The PHR owner selects a set of PHRs to be freely available to the ERU staff during emergency situations. Then a special 'emergency' attribute is added during the PHR encryption process. A set of PHRs can only be decrypted by a key that contains the 'emergency' attribute and is distributed to the ERUs during an emergency situation. However, only static pre-selected information is available.

The KP-ABE was also employed by Huang et al. [6] to offer the PHR information according to the severity level of the situation. The PHR owner can assign any of the three severity levels (mild, moderate and severe) to each PHR. Then each PHR is encrypted using the KP-ABE technique with a set of owner-desired attributes and the severity level. The KP-ABE private keys that are based on different severity levels can access the PHR information with different scopes. Under such a scheme, the availability of the pre-defined information is an issue. For example, if the ERU staff is allowed to access mild-level and moderate-level information, then the information is always available even when it is not required.

OUR PROPOSED PRIVACY-PRESERVING EMERGENCY ACCESS CONTROL SCHEME

Our proposed privacy-preserving emergency access control scheme for PHRs is illustrated in Figure 1. The scheme consists of five modules and three players. The modules comprises the user authority (UA), the emergency server (EmS), the PHR server, the audit server and the emergency authority (EA). The players include the PHR owner, the PHR trusted users and the ERU staff.

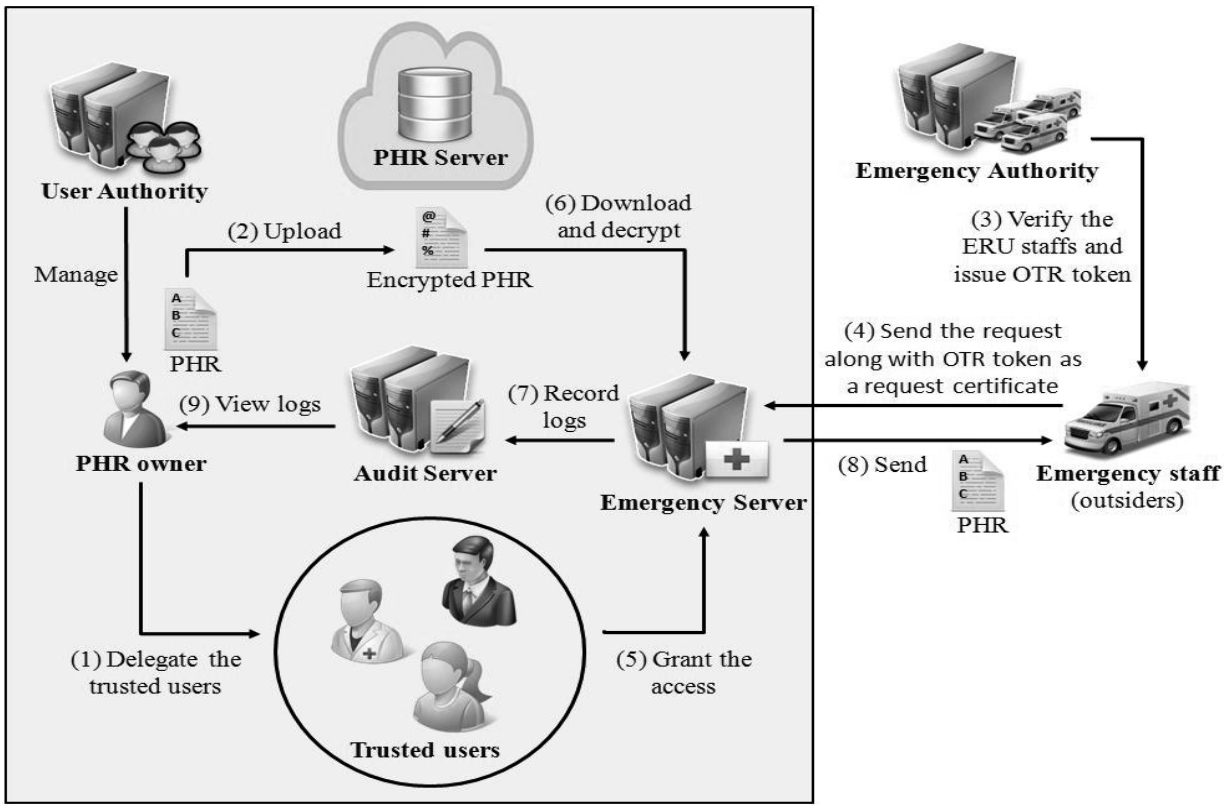

Figure 1. Proposed privacy-preserving emergency access control scheme

The UA is responsible for performing all PHR user management tasks such as creating a user, generating a user key, distributing the user key and revoking the user. The PHR server is an actual PHR storage, which can be internal or public storage. The PHRs are encrypted and uploaded to the storage. The EmS handles all tasks related to an emergency situation. These three modules were presented in the original design [8]. The next two modules are added in this work. The audit server records all activities performed by the ERU staff during emergency situations and produces reports for the PHR owner. The EA is responsible for managing tasks related to the ERU staff, such as verifying ERU staff identity, authorising ERU staff, revoking ERU staff access and generating a one-time request (OTR) token for ERU staff. The EA can be either distributed or centralised as long as it is registered with the proposed scheme.

The PHR owners can manage and track all activities conducted on their PHRs. Trusted users can be partially granted restricted access on behalf of the PHR owner during emergency situations. When the total number of approvals received from the pre-selected trusted users is equal to or greater than the pre-defined threshold, restricted PHR access permission is granted. The ERU staff must be verified and authorised by their corresponding EA.

The ARA mechanism ensures that only authorised ERU staff is allowed to access the PHR system. Each PHR access request invoked by the ERU staff must be verified by its commander/ manager (denoted as EA in Figure 1). Once the ERU staff member is verified, the OTR token, which is a certificate with a specific expiration time, is generated. The request with a valid OTR token is processed by the EmS. The ERU staff cannot reuse the token once it is expired. To expedite this process, the ERU staff can be verified and issued with the OTR token in an emergency vehicle before they arrive at the emergency location. Hence the delay time to access any secure PHR is eliminated because the secure PHRs can be immediately accessed once the valid OTR token is presented. In addition, a transaction auditing mechanism is employed to guarantee a non-repudiation feature of all access conducted by the ERU staff.

Under our proposed scheme, the PHRs are encrypted at the data origin using the ciphertext-policy attribute-based encryption (CP-ABE) technique [16]. Then the encrypted PHR is uploaded to the PHR server (denoted as (2) in Figure 1). Using the CP-ABE scheme, the access policy of each PHR is embedded during the PHR encryption process. The policy is defined by the PHR owner. Only the user who has the CP-ABE private key that satisfies the access policy can decrypt the encrypted PHR. In addition, the secure sockets layer protocol and the secure shell protocol are employed to provide a secure communication among the modules and players under the proposed scheme. The information collected by the network traffic eavesdropping technique remains protected. In the following section the assignment of a privacy level to each PHR is presented. Then the PHR pre-processing and accessing methods are described.

Defining Privacy Level

This section provides a guideline for the PHR owners in order to classify their PHRs into one of the three privacy levels: secure, restricted and exclusive. The guideline is created according to the sensitivity of the PHR information. Typically, health related information of an individual stored in a PHR system has different sensitivity levels. For example, some information such as mental health, domestic abuse/violence, drug abuse, disorders and disabilities is considered to be sensitive for some people. A person usually does not disclose such information to others. Such information can result in disgrace or even unfair job opportunities to its owner [4, 5]. However, other information such as congenital diseases, allergies and disease risks can help the ERU staff make a better decision in treating the victim during emergency situations [7].

The secure PHRs are available to the ERU staff during emergency situations. Therefore, the basic information of a person's health that is necessary to treat the person must be provided. Some people are allergic to simple medicine such as Paracetamol. Such information is important during a life-threatening condition. Thus, a list of information such as congenital diseases, allergies and disease risks is suggested to be under the secure-level category [17]. In addition, a list of emergency contact people for the victim is classified under this category so the people who know the victim can be informed about the situation.

The ERU staff is allowed to access the restricted-level information if an access permission is granted by a certain number of the victim's delegates. Unlike the secure-level information, the restricted-level information will not be available immediately. Thus, the information under this category can only be used by the physicians that are away from the emergency scene, in a fully equipped emergency vehicle or an intensive care unit at a hospital. This set of information should include the person's medical history, laboratory test results, physicians' recommendations, his/her

physicians' contact information, and some relevant health-monitoring data. Such information will help physicians make a better judgment on the next actions.

Finally, the exclusive-level information is considered to be highly sensitive according to the PHR owner judgment. Usually, this set of information includes mental health, domestic abuse/violence, drug abuse, disorders and disabilities [4, 5]. Note that this guideline is provided as a suggestion and the proposed scheme is not limited to it.

PHR Pre-processing

The proposed scheme uses the EmS to perform all PHR retrieving and decrypting tasks during emergency situations. The EmS attribute must be defined in the access policy of the secure and restricted PHRs. The exclusive PHR access policy does not include any attribute of the EmS. As a result, the ERU staff is not allowed to access exclusive PHRs even during emergency situations while the secure PHR is accessible by the authorised ERU staff during emergency situations. To assign a secure PHR, the EmS attribute must be added to the access policy of that particular PHR. Then the PHR is encrypted using the CP-ABE with a defined access policy and the encrypted PHR is securely uploaded to the PHR server. By adding the EmS attribute to the access policy, the EmS is able to decrypt a particular PHR. During an emergency situation, the authorised ERU staff can access the secure PHRs instantly via the EmS.

The restricted PHR is accessible by the authorised ERU staff if and only if they are granted an access permission by at least t (pre-determined threshold) out of n trusted users who are pre-selected by the PHR owner. To assign a restricted PHR, the PHR owner must first select a set of trusted users (denoted as (1) in Figure 1). These trusted users are asked to make a decision to grant access permission on any restricted PHR on behalf of the PHR owner. A restricted emergency key (REK) attribute is added to the access policy of that particular PHR. Then the PHR is encrypted using the CP-ABE with defined access policy. Next, a set of random secret keys associated with the number of trusted users are generated. The REK attribute is encrypted using threshold cryptosystem [18] with a set of random secret keys and a pre-determined threshold (t) as encryption parameters. A random secret key is assigned to each trusted user. Each secret key is encrypted using a corresponding trusted user's public key. The encrypted PHR is securely uploaded to the PHR server while the encrypted REK attribute and the set of encrypted secret keys are securely uploaded to the EmS. Thus, the EmS can decrypt any restricted PHR if and only if at least t trusted users provide their approval. Because each secret key is encrypted with a trusted user's public key, only the trusted user's private key can decrypt the secret key. With the threshold cryptosystem, the REK attribute can be decrypted if at least t secret keys are provided. Using the REK attribute, the EmS can decrypt the restricted PHRs.

PHR Accessing

In this section both secure and restricted PHR accessing sequences are explained. Figure 2 and Figure 3 show sequences of transactions occurring when accessing secure PHRs and restricted PHRs respectively. To enhance the trustworthiness of a request invoked by the ERU staff, the ARA mechanism guarantees that each request must be verified by his/her EA (steps 1–4 in Figure 2 and Figure 3). The OTR token ensures that the ERU staff is verified by his/her EA (step 3 in Figure 2 and Figure 3). The verification process can be expedited by issuing an OTR token to the ERU staff once the emergency case is assigned. Because the OTR token is a certificate with a specific expiration time, the token cannot be reused when its lifetime expires. Therefore, this mechanism

assures that only authorised ERU staff can access the PHRs. All requests and transactions are recorded. Figure 4 shows the transactions collected by the auditing system using our prototype software.

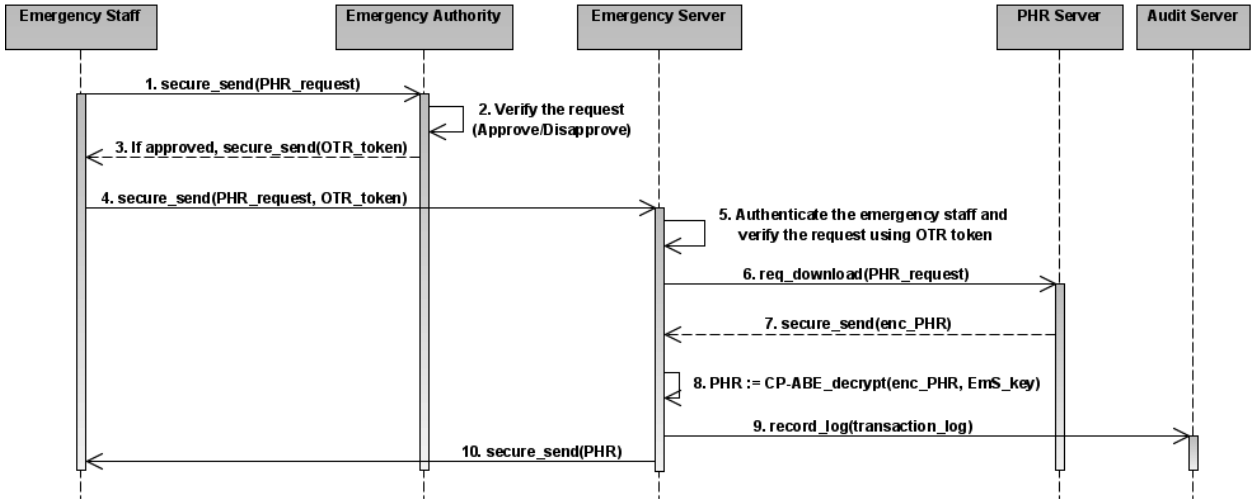

Figure 2. Secure PHR access sequences.

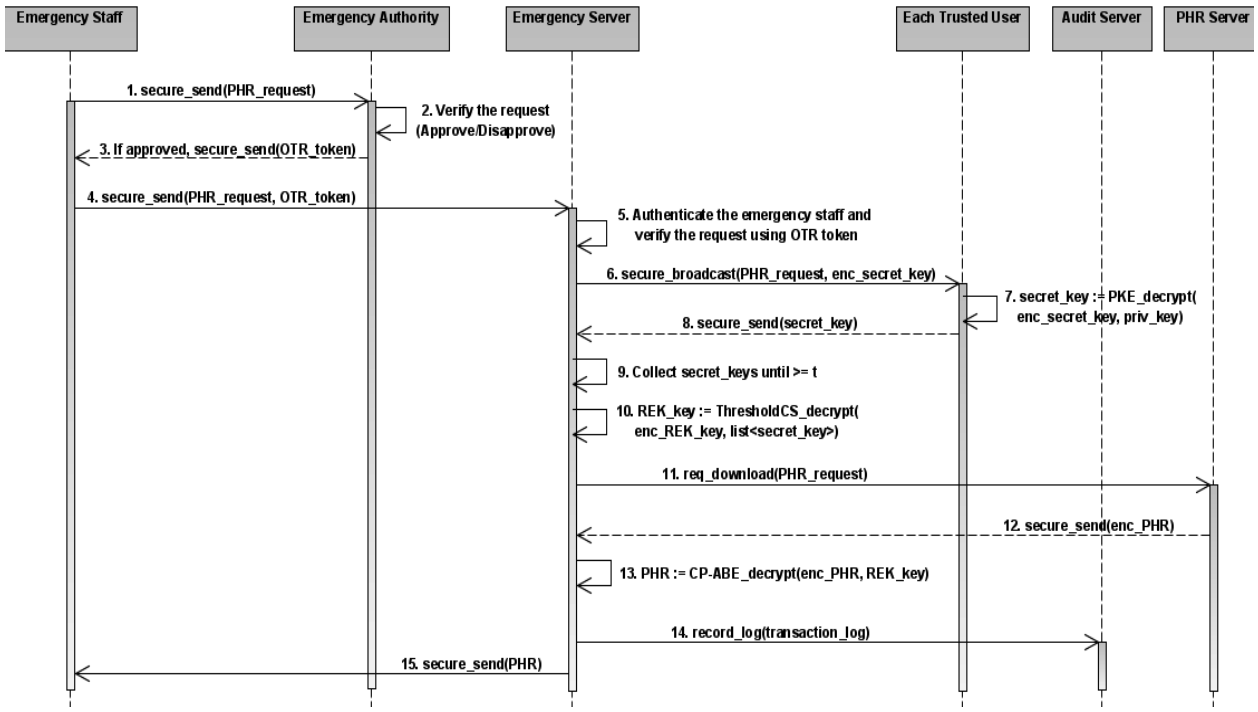

Figure 3. Restricted PHR access sequences

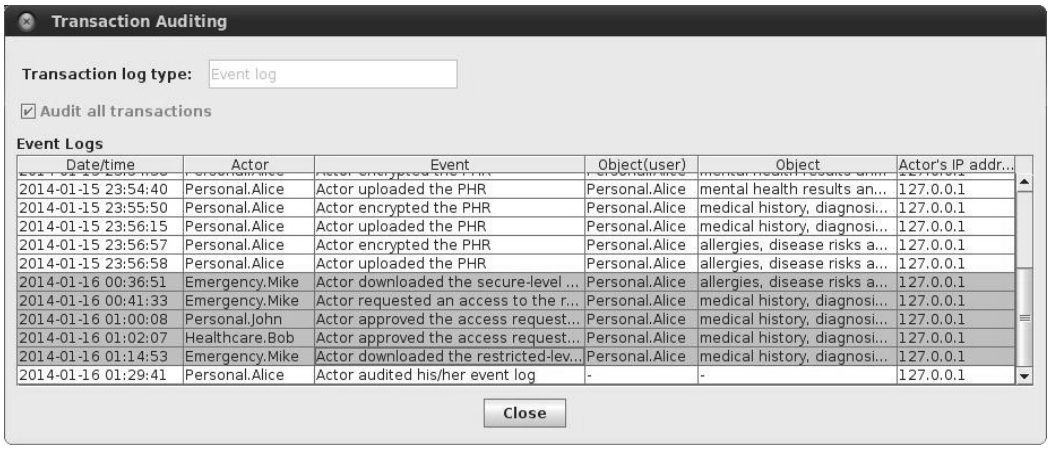

Date/time	Actor	Event	Object(user)	Object	Actor's IP addr...
2014-01-15 23:54:40	Personal.Alice	Actor uploaded the PHR	Personal.Alice	mental health results an...	127.0.0.1
2014-01-15 23:55:50	Personal.Alice	Actor encrypted the PHR	Personal.Alice	medical history, diagnosi...	127.0.0.1
2014-01-15 23:56:15	Personal.Alice	Actor uploaded the PHR	Personal.Alice	medical history, diagnosi...	127.0.0.1
2014-01-15 23:56:57	Personal.Alice	Actor encrypted the PHR	Personal.Alice	allergies, disease risks a...	127.0.0.1
2014-01-15 23:56:58	Personal.Alice	Actor uploaded the PHR	Personal.Alice	allergies, disease risks a...	127.0.0.1
2014-01-16 00:36:51	Emergency.Mike	Actor downloaded the secure-level ...	Personal.Alice	allergies, disease risks a...	127.0.0.1
2014-01-16 00:41:33	Emergency.Mike	Actor requested an access to the r...	Personal.Alice	medical history, diagnosi...	127.0.0.1
2014-01-16 01:00:08	Personal.John	Actor approved the access request...	Personal.Alice	medical history, diagnosi...	127.0.0.1
2014-01-16 01:02:07	Healthcare.Bob	Actor approved the access request...	Personal.Alice	medical history, diagnosi...	127.0.0.1
2014-01-16 01:14:53	Emergency.Mike	Actor downloaded the restricted-lev...	Personal.Alice	medical history, diagnosi...	127.0.0.1
2014-01-16 01:29:41	Personal.Alice	Actor audited his/her event log	-	-	127.0.0.1

Figure 4. List of transactions collected by the audit server

To access secure PHRs, the ERU staff must send a PHR access request along with the OTR token to the EmS (step 4 in Figure 2). The OTR token is sent to the ERU staff if he/she is verified by his/her corresponding EA. Once the EmS successfully verifies the OTR token, the requested secure PHRs are downloaded and decrypted using the EmS attribute (steps 5–8 in Figure 2). Then the EmS stores the transaction information on the audit server (step 9 in Figure 2) and securely sends the requested secure PHRs to the ERU staff (step 10 in Figure 2).

To access restricted PHRs, the ERU staff must send a PHR access request along with the OTR token to the EmS (step 4 in Figure 3). The OTR token is sent to the ERU staff if he/she is verified by his/her corresponding EA. Once the EmS successfully verifies the OTR token (step 5 in Figure 3), the EmS securely broadcasts the request message to each corresponding trusted user for approval (step 6 in Figure 3). If the trusted user approves the request, the corresponding encrypted random secret key will be decrypted by the trusted user's private key (step 7 in Figure 3). The random secret key is sent to the EmS through a secure channel (step 8 in Figure 3). If the total number of random secret keys collected by the EmS is equal to the pre-determined threshold (t), the EmS decrypts the encrypted REK attribute value using the threshold cryptosystem (steps 9-10 in Figure 3). Next, the EmS downloads the requested PHRs from the PHR server and uses the REK attribute to decrypt the PHRs (steps 11-13 in Figure 3). Finally, the ERU staff receives the requested PHRs from the EmS via a secure channel (step 15 in Figure 3). In addition, the EmS records a transaction log on the audit server (step 14 in Figure 3).

USABILITY AND SECURITY DISCUSSIONS

Usability Issues

Figure 5 shows a typical flow of events during an emergency situation. First, an emergency situation occurs. Second, the call is made to the emergency hotline centre. Third, the emergency location and victim's current conditions are provided to the assigned ERU staff. Fourth, the ERU staff reach the victim. Fifth, the victim is transferred to a hospital or a medical facility. The commonly accepted standard response time from the first call (step 2 in Figure 5) until the ERU staff reach the victim (step 4 in Figure 5) is 8 minutes [19]. This section will cover only secure and restricted PHRs because the proposed scheme allows the ERU staff to access only these types of PHRs.

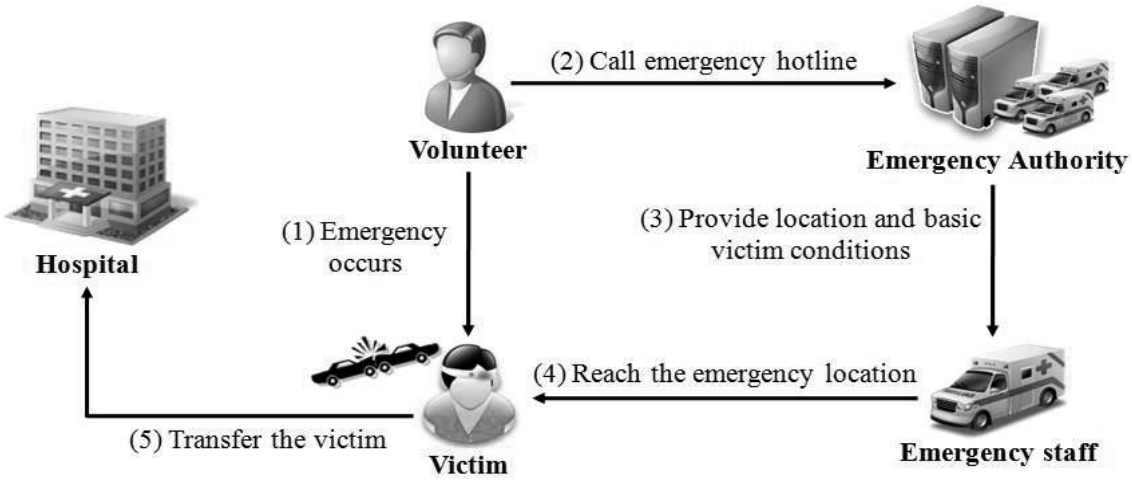

Figure 5. Typical flow of events during an emergency situation

According to the secure PHR access sequences shown in Figure 2, the total processing time to retrieve the secure PHRs includes the required time for: (1) the ERU staff to request an OTR token, (2) the EA to authorise and issue the OTR token, (3) the OTR token to be sent to the ERU staff, (4) the ERU staff to send the PHR request along with their OTR token to the EmS, (5) the EmS to download and decrypt the requested PHRs, and (6) the EmS to send the PHRs to the ERU staff. According to the cellular standard for the third generation [20], the data transmission rate in a moving vehicle is 348 kbps, meaning that 348,000 bits or 43.5 KB of data can be transferred each second. This amount of data can contain a text of approximately 10 novel-size pages. Therefore, the amount of time to transmit a request, an OTR token and a secure PHR is negligible. The EmS processing time depends on the PHR storage and the decryption process. The underlying encryption scheme of the CP-ABE is an advanced encryption standard (AES) [21] in cipher block chaining (CBC) mode [22], which takes less than 3.25 s to encrypt an image with the size of 468 KB [23]. Because the encryption and decryption time for AES-CBC is the same, the decryption processing time can be negligible. Using the current data storage technology, 50,000 records can be searched in 2.5 s [24]. Thus, the PHR storage processing time is not a problem. The only external factor to the total processing time is the EA processing time, which will be discussed later. Using the above supporting evidence, the secure PHR accessing time is reasonable in practical situations.

As described previously, the restricted PHRs are designed for the medical staff at the hospital to treat the victim when he/she is no longer at the emergency location. Therefore, there is a period of time between the call to the hotline and the victim arrival at the hospital during which the medical staff can obtain the necessary approval to access the necessary restricted PHRs. The processing time to retrieve the restricted PHRs includes the required time for: (1) the ERU staff to receive the OTR token, (2) the ERU staff to send the PHR request along with the OTR token, (3) the EmS to send the request to each trusted user, (4) each trusted user to respond to the request, (5) the partial secret key of each trusted user to be sent to the EmS, (6) the EmS to download and decrypt the requested PHRs, and (7) the EmS to send the PHRs to the ERU staff. The above factors discussed for the secure PHRs can also be applied to the restricted PHRs, the only difference being the response time of the trusted user. According to a study [25], the average response time of a person to an incoming text messaging is 431.28 s during simultaneous conversations and 391.88 s during non-simultaneous conversations. Therefore, it can take up to 7 min. for the trusted users to respond to a restricted PHR access approval request. Considering the 8-min. response time standard,

the medical staff at the hospital are able to access the restricted PHRs of the victim before the victim reaches the hospital.

To provide an additional assurance that the trusted users will respond to the request, the PHR owner should include at least one of the trusted users on the emergency contact list. Because the list is classified as a secure PHR, the ERU staff can contact the trusted user directly. The restricted PHRs are designed for the medical staff at the hospital; therefore, the medical staff can be added as an attribute in the access policy during the CP-ABE encryption of the PHRs and can thus access the PHRs. However, they must be a member of an authority that is recognised by the victim's PHR system.

Under the proposed scheme, the EA acts as a trusted agent to verify all of its ERU staff. Because the EA can be from various sources, the process of adding a new EA to the proposed scheme must be done carefully and the new EA must be verified. To ensure the performance of the ERU staff, each EA must be periodically evaluated. The request approval processing time and the OTR token generation time must be used as the key performance indicators to evaluate the EA. In addition, the OTR token lifetime may allow the ERU staff to perform a replay attack on the PHR system. Therefore, the ERU staff misconducts and performances can be used as another key performance indicator to evaluate the EA. The EA with poor performance must be removed.

Security Issues

Four attack models are discussed to account for possible security threats. The first model involves a database intruder. Under the proposed scheme, the actual PHR storage can be a public storage. Therefore, the database intruder or the storage administrator may try to access the information. However, the PHR is encrypted and the decryption keys are securely stored on separate trusted servers (i.e. the UA and the EmS). Hence the encrypted PHR stored on the PHR storage is protected with the assumption that the cryptographic primitives are not broken and the decryption key is not accessible.

The second attack model concerns an unauthorised access. The ERU staff may try to access the PHRs. However, the ARA mechanism prevents such access by allowing only the ERU staff with an approval from their corresponding EA to access the data. The approval is in the form of a valid OTR token. The ERU staff uses the received OTR token as a request certificate to access the requested PHRs through the EmS. An unauthorised access is prevented at the EmS and any attempt from the ERU staff is recorded by the audit server. Because the conduct of each ERU staff is used as a key performance indicator during the EA evaluation process, any misconduct by the ERU staff affects its EA performance. The EA evaluation process and the transaction auditing mechanism can indirectly prevent unauthorised access.

The third attack model is a replay attack. The ERU staff with a valid OTR token may conduct a replay attack. However, the OTR token is a certificate with a specific expiration time. Therefore, the ERU staff will not be able to reuse the OTR token once it is expired. However, this does not cover the period of time that the OTR token remains valid. Therefore, the lifetime of the OTR token must be short. The auditing information can show any misconduct of the ERU staff, which affects the performance of the corresponding EA.

The last attack model is a non-repudiation case. The audit server records all transactions invoked by the ERU staff and all activities can be tracked by the PHR owner. The transaction auditing mechanism is a very important mechanism to provide a non-repudiation feature.

CONCLUSIONS

This work has extended the original design of a PHR system for handling emergency situations to support a more practical scenario. In the original design all players were assumed to be trustworthy. In this work the ERU staff is considered an outsider and unknown to the system. Two mechanisms have been proposed to enhance the trustworthiness of the PHR access requests from an ERU staff member during an emergency situation. First, an ARA mechanism is designed to ensure the verification of the ERU staff by an on-duty emergency unit commander/manager. Any request invoked by an ERU staff member must be approved by his/her corresponding on-duty EA commander. Second, the transaction auditing mechanism is added to allow the PHR owners to track all transactions related to their PHRs. In addition, the auditing mechanism serves as a method for providing a non-repudiation feature for all PHR access performed by the ERU staff. Using the proposed extension, the trustworthiness of the requests invoked by the ERU staff is enhanced and the limitation of the previous work is eliminated.

The current data transmission rate and storage technology allows the proposed scheme to provide the requested PHRs within a commonly acceptable time and there is only one security limitation in the proposed scheme, which is the period of time that the OTR token remains valid. The suggested solution is to keep the lifetime of the OTR token short and to evaluate the EA based on its ERU staff performance and misconduct. Furthermore, a guideline on defining a proper privacy level for each PHR has been presented. The idea of collecting and storing transactions by an audit server is demonstrated using our developed prototype.

ACKNOWLEDGEMENTS

This work was supported by the Higher Education Research Promotion and National Research University Project of Thailand, Office of the Higher Education Commission (under the funding no. MED540548S at Prince of Songkla University).

REFERENCES

1. W. Wangcharoen, D. Amornlerdpison and K. Mengumphan, "Factors influencing dietary supplement consumption: A case study in Chiang Mai, Thailand", *Maejo Int. J. Sci. Technol.*, **2013**, *7*, 155-165.
2. A. A. Ozok, H. Wu, M. Garrido, P. J. Pronovost and A. P. Gurses, "Usability and perceived usefulness of personal health records for preventive health care: A case study focusing on patients' and primary care providers' perspectives", *Appl. Ergonom.*, **2014**, *45*, 613-628.
3. P. C. Tang, J. S. Ash, D. W. Bates, J. M. Overhage and D. Z. Sands, "Personal health records: Definitions, benefits, and strategies for overcoming barriers to adoption", *J. Am. Med. Inform. Assoc.*, **2006**, *13*, 121-126.
4. B. A. Malin, K. El Emam and C. M. O'Keefe, "Biomedical data privacy: Problems, perspectives, and recent advances", *J. Am. Med. Inform. Assoc.*, **2013**, *20*, 2-6.
5. K. Caine and R. Hanania, "Patients want granular privacy control over health information in electronic medical records", *J. Am. Med. Inform. Assoc.*, **2013**, *20*, 7-15.
6. J. Huang, M. Sharaf and C. T. Huang, "A hierarchical framework for secure and scalable EHR sharing and access control in multi-cloud", Proceedings of 41st International Conference on Parallel Processing Workshops, **2012**, Pittsburgh, USA, pp. 279-287.

7. J. L. Fernández-Alemán, I. C. Señor, P. Á. Lozoya and A. Toval, "Security and privacy in electronic health records: A systematic literature review", *J. Biomed. Inform.*, **2013**, *46*, 541-562.
8. P. Thummavet and S. Vasupongayya, "A novel personal health record system for handling emergency situations", Proceedings of 17th International Computer Science and Engineering Conference, **2013**, Nakorn Pathom, Thailand, pp.266-271.
9. D. Weerasinghe and R. Muttukrishnan, "Secure trust delegation for sharing patient medical records in a mobile environment", Proceedings of 7th International Conference on Wireless Communications, Networking and Mobile Computing, **2011**, Wuhan, China, pp.1-4.
10. Y. Ding and K. Klein, "Model-driven application-level encryption for the privacy of e-health data", Proceedings of 5th International Conference on Availability, Reliability and Security, **2010**, Krakow, Poland, pp.341-346.
11. M. N. Huda, S. Yamada and N. Sonehara, "Privacy-aware access to patient-controlled personal health records in emergency situations", Proceedings of 3rd International Conference on Pervasive Computing Technologies for Healthcare, **2009**, London, UK, pp.1-6.
12. J. Sun, X. Zhu, C. Zhang and Y. Fang, "HCPP: Cryptography based secure EHR system for patient privacy and emergency healthcare", Proceedings of 31st International Conference on Distributed Computing Systems, **2011**, Minneapolis, USA, pp.373-382.
13. M. Li, S. Yu, K. Ren and W. Lou, "Securing personal health records in cloud computing: Patient-centric and fine-grained data access control in multi-owner settings", Proceedings of 6th International Conference on Security and Privacy in Communication Networks, **2010**, Singapore, pp.89-106.
14. V. Goyal, O. Pandey, A. Sahai and B. Waters, "Attribute-based encryption for fine-grained access control of encrypted data", Proceedings of 13th ACM Conference on Computer and Communications Security, **2006**, Alexandria, USA, pp.89-98.
15. M. Li, S. Yu, Y. Zheng, K. Ren and W. Lou, "Scalable and secure sharing of personal health records in cloud computing using attribute-based encryption", *IEEE Trans. Parallel Distr. Syst.*, **2013**, *24*, 131-143.
16. J. Bethencourt, A. Sahai and B. Waters, "Ciphertext-policy attribute-based encryption", Proceedings of IEEE Symposium on Security and Privacy, **2007**, Berkeley, USA, pp.321-334.
17. S. Aguinaga and C. Poellabauer, "Method for privacy-protecting display and exchange of emergency information on mobile devices", Proceedings of International Conference on Collaboration Technologies and Systems, **2012**, Denver, USA, pp.596-599.
18. T. P. Pedersen, "A threshold cryptosystem without a trusted party", Proceedings of Workshop on Theory and Application of Cryptographic Techniques, **1991**, Brighton, UK, pp. 522-526.
19. P. T. Pons and V. J. Markovchick, "Eight minutes or less: Does the ambulance response time guideline impact trauma patient outcome?", *J. Emerg. Med.*, **2002**, *23*, 43-48.
20. International Telecommunication Union, "About mobile technology and IMT-2000", **2011**, http://www.itu.int/osg/spu/imt-2000/technology.html#Cellular Standards for the Third Generation (Accessed: April 2014).
21. National Institute of Standards and Technology, "Advanced encryption standard (AES)", **2001**, http://csrc.nist.gov/publications/fips/fips197/fips-197.pdf (Accessed: April 2014).
22. National Institute of Standards and Technology, "Recommendation for block cipher modes of operation", **2001**, http://csrc.nist.gov/publications/nistpubs/800-38a/sp800-38a.pdf (Accessed: April 2014).

23. R. Doomun, J. Doma and S. Tengur, "AES-CBC software execution optimization", Proceedings of International Symposium on Information Technology, **2008**, Kuala Lumpur, Malaysia, pp. 1-8.
24. K. K. Lee, W. Tang and K. Choi, "Alternatives to relational database: Comparison of NoSQL and XML approaches for clinical data storage", *Comput. Meth. Programs Biomed.*, **2013**, *110*, 99-109.
25. A. Battestini, V. Setlur and T. Sohn, "A large scale study of text-messaging use", Proceeding of 12th International Conference on Human Computer Interaction with Mobile Devices and Services, **2010**, Lisbon, Portugal, pp.229-238.

Maejo Int. J. Sci. Technol. **2015**, *9*(01), 121-135; doi: 10.14456/mijst.2015.10

Maejo International Journal of Science and Technology

ISSN 1905-7873
Available online at www.mijst.mju.ac.th

Full Paper

Analysis of frequency-based compact genetic algorithm (fb-cGA)

Sunisa Rimcharoen, Srichol Phiromlap and Nutthanon Leelathakul *

Faculty of Informatics, Burapha University, Chon Buri, 20131, Thailand

* Corresponding author, e-mail: nutthanon@buu.ac.th

Received: 19 June 2014 / Accepted: 30 March 2015 / Published: 9 April 2015

Abstract: A behaviour analysis of frequency-based compact genetic algorithm (fb-cGA) is proposed. The fb-cGA is a version of compact genetic algorithm (cGA) enhanced by the use of a new updating strategy. The algorithm counts the number of probability updates and the continuities of probability-update directions and uses them to adaptively update the algorithm's step sizes. This method requires fewer function evaluations and achieves solutions that are more accurate than those from the conventional cGA. It has been shown that fb-cGA can reduce the number of function evaluations to only one ninth of the number obtained from cGA on ten copies of a 3-bit trap function using a tournament size of 2. We conduct parameter studies and show that the use of one fourth of the population size (*psize/4*) as the algorithm's starting threshold can improve the overall efficiency of fb-cGA. The behaviour of fb-cGA on various problems is also examined. The results of the analysis show that information from the algorithm's past experience (i.e. the numbers of probability updates and continuities) can help the fb-cGA to update the probability vector towards a more promising direction, requiring fewer function evaluations.

Keywords: compact genetic algorithm, updating strategy, update frequency, update continuity

INTRODUCTION

Compact genetic algorithm (cGA) was proposed by Harik et al. [1]. It has been widely applied to various fields such as pipe network optimisation [2], parameter optimisation [3, 4], inventory planning [5], image recognition [6], traffic transportation management [7], communication [8-10], container loading [11], grid computing [12] and biology [13, 14]. The main contribution of this algorithm is to replace a whole set of candidate solutions (the so-called population) used by simple genetic algorithm (sGA) with a probability distribution. cGA requires

much less memory, as it does not need to maintain the population throughout the evolution process. The concept of cGA can be easily translated to hardware implementation by using the common very-large-scale integration [15-17]. Therefore, it opens up the application of genetic algorithm to new fields such as embedded systems. For example, Timmerman [18] used cGA to develop an insect-sized flapping-wing micro air vehicle.

However, for more difficult problems, cGA does not provide acceptable solutions. There have been many attempts to modify and improve cGA's probability updating strategy. Zhou et al. [19] proposed an improved cGA using mutation and named the algorithm mutated-by-bit-compact genetic algorithm (MBBCGA). At each generation, MBBCGA generates only one individual and then mutates this individual bit by bit. Ha et al. [20] proposed the use of more than one probability vector (PV) to enhance the exploration properties of the algorithm. Rimcharoen et al. [21] improved the updating strategy of cGA by using a moving average technique (mcGA). Ahn and Ramakrishna [22] adopted 'elitism', i.e. the idea of reserving the best solution in each generation. They proposed two variants: a persistent elitist compact genetic algorithm (pe-cGA) and a non-persistent elitist compact genetic algorithm (ne-cGA). The former stores the current best solution until a better solution is found, while the latter keeps the best solution just for a certain lifetime. In 2008 Lee et al. [23] introduced a new update strategy using augmented Bayesian networks. A few years later, they proposed compact genetic algorithm using a belief vector (cGABV) [24]. The new technique uses a belief vector (BV) instead of a probability vector. The difference between BV and PV is that each element of the BV stores a probability distribution (represented by associated mean and variance), whereas each of the PV keeps a probability value.

In our previous work [25], we proposed the usage of a frequency-based updating technique as the updating strategy of cGA. The technique collects and utilises information from the algorithm's past experience. Specifically, for each probability in the PV, the number of probability updates (in both up and down directions) are counted and used to adjust probability-updating step sizes, turning the vector towards the promising direction faster. Comparison results show that the frequency-based compact genetic algorithm (fb-cGA) requires substantially (up to nine times) fewer function evaluations when compared with traditional cGA. However, in-depth explanation and analysis of why this algorithm outperforms others remained lacking. Accordingly, in this paper, we conduct parameter studies and analyse how the algorithm behaves while solving various problems.

FREQUENCY-BASED COMPACT GENETIC ALGORITHM (fb-cGA)

cGA is one of various evolutionary algorithms. Instead of evolving the population for searching solutions, it employs a probabilistic model, PV, which requires relatively small amount of memory. Furthermore, the algorithm eliminates genetic operators such as crossover and mutation.

cGA keeps a PV over a chromosome to represent the population. The number of probabilities in the vector is equal to the chromosome length. Each probability is defined as the probability with the associated bit being equal to 1. The pseudo-code of cGA is shown in Figure 1. The two parameters are the chromosome length (l) and the population size (*psize*), which are used to further specify an updating step size (i.e. step size defined as 1 / *psize*). (Note that the relation between *psize* and the updating size in the cGA is analogous to the one between population size and evolving speed in sGA.)

```
initialise(p)
while (p does not converge) do
    individual1 := generate(p)
    individual2 := generate(p)
    evaluate(individual1, individual2)
    winner, loser := compete(individual1,
                             individual2)
    for i:=1 to l
    begin
        if winner[i] ≠ loser[i] then
            if winner[i] = 1 then
                p[i] := p[i] + 1/psize
            else
                p[i] := p[i] – 1/psize
    endfor
endwhile
```

Figure 1. Pseudo-code of cGA

```
s := tournament size
initialise(p)
while (p does not converge) do
    create(p, S[], s)
    evaluate(S[])
    rearrange(S[]) // S[1] is the best individual
    for i := 2 to s
    begin
        winner, loser := compete(S[1], S[i])
        for i:=1 to l
        begin
            if winner[i] ≠ loser[i] then
                if winner[i] = 1 then
                    p[i] := p[i] + 1/psize
                else
                    p[i] := p[i] – 1/psize
        endfor
    endfor
endwhile
```

Figure 2. Pseudo-code of tournament cGA

First, the cGA initially sets each of the probabilities in the vector to 0.5. According to the PV, the algorithm randomly generates two candidate solutions, denoted as *individual1* and *individual2*. Next, the solutions are evaluated, i.e. assigned fitness values. The winner, the one with the greater fitness value, is selected. In step 5, the PV is then updated towards the winner. The value of each probability changes if the winner's associated bit is not equal to the loser's: either increasing when the winner's bit is one, or decreasing otherwise. The loop continues to run until the PV converges, meaning that each probability in the vector is either zero or one.

Harik et al. [1] also modified cGA by adding more candidates, called tournament cGA, shown in Figure 2. The modified version randomly generates a set of s candidate solutions, denoted by an array *S* in the pseudo-code, and uses a tournament selection to choose the winner, which will be stored in *S*[1]. The PV is then updated by comparing *S*[1] with *S*[i] (for all *i* not equal to 1) in the same manner as the original cGA.

Both of the cGAs update each probability in the vector towards either one or zero. Some probabilities gradually increase while others drop. However, some might fluctuate, reflecting uncertainty in updating the PV. It is known that the PV fluctuates during the beginning period and converges to a certain direction at the end. The algorithms seem to work well in the case where problems have consistent information, leading the algorithms to turn the vector towards only one direction. However, if the problems are deceptive, they might delude the algorithms into searching for solutions in the wrong directions. Consequently, the cGAs could not provide the desired solution quality in spite of spending much of searching time. There has been much research aimed at modifying and improving the cGAs in such case.

In our previous work [25], we applied a frequency-based technique to update the PV, using the numbers of updates and the continuities of preceding updates as criteria. (The update continuity is

defined as the number of consecutive updates moving towards the same direction). We measured the uncertainty by observing the direction of each probability in the vector: if the direction is the same for a long time (high continuity), the uncertainty is low. The monitored continuities serve as a guideline or a promising trend that quickly leads to vector convergence.

Specifically, for each probability in the vector, the frequencies of two types of updates: stepping-up (increasing the probability towards 1) and stepping-down (decreasing the probability towards 0), were counted. Likewise, two types of update continuities were collected. The stepping-up continuity is reset to zero if the current update moves towards 0 and the stepping-down continuity is reset to zero if the current update moves towards 1. The fb-cGA technique is shown in Figure 3.

Updating strategy of fb-cGA

```
1:  for i := 1 to l
2:  begin
3:      if winner[i] ≠ loser[i] then
4:          if winner[i] = 1 then
5:              Ufreq[i] := Ufreq[i] + 1;
6:              Ucon[i] := Ucon[i] + 1;
7:              Dcon [i] := 0;
8:              if (Ufreq[i] > Dfreq[i] AND Gen > (psize/3)) then
9:                  p[i] := p[i] + ((1/psize)+(p[i] * (Ucon[i]/100));
10:             else
11:                 p[i] := p[i] + (1/ psize);
12:         else
13:             Dfreq[i] := Dfreq[i] + 1;
14:             Dcon [i] := Dcon [i] + 1;
15:             Ucon[i] := 0;
16:             if (Dfreq[i] > Ufreq[i] AND Gen > (psize/3)) then
17:                 p[i] := p[i] - ((1/psize) + (p[i]*(Dcon [i] / 100));
18:             else
19:                 p[i] := p[i] - (1/psize);
20:  endfor
```

Parameters:

Ufreq : number of stepping-up updates
Dfreq : number of stepping-down updates
Ucon : number of consecutive stepping-up updates
Dcon : number of consecutive stepping-down updates
Gen : generation number (incremented in Step 6)

Figure 3. Pseudo-code of fb-cGA

Figure 3 presents the pseudo-code of the frequency-based updating strategy in fb-cGA. *Ufreq* denotes the number of probability updates towards one (i.e. stepping-up updates). *Dfreq* denotes the number of probability updates towards zero (i.e. stepping-down updates). *Gen* denotes the generation number whose value is increased incrementally in step 6. The proposed updating strategy is performed when *Gen* is greater than 1/3 of the population size (*psize*). For the first third of the generations, fb-cGA works like the original method to explore solutions and find the right direction. It waits until the generation number reaches *psize*/3 because it needs time to gather sufficient information to see the trend. For the last two-thirds of the generations, the i^{th} probability is updated when the i^{th} bit of the winner (*winner*[*i*]) and the one of the loser (*loser*[*i*]) are not equal. If *winner*[*i*] is 1, the algorithm checks whether, from past experience, this probability is updated towards 1 most of the time (i.e. *Ufreq* greater than *Dfreq*). If so, the probability vector should be updated according to the majority with a larger step size. The step size can be determined by adding the term *Ucon*/100 multiplied by the previous value of i^{th} probability, where *Ucon* denotes the number of consecutive stepping-up updates. In contrast, when *winner*[*i*] is 0, the algorithm performs in a similar manner but considers *Dfreq* and *Dcon* instead. The i^{th} probability is updated by decreasing towards zero.

In this paper, we study the effects of the *psize* parameter and show that using *psize*/4 can improve the efficiency of fb-cGA. Thus, we use *psize*/4 instead of the previously proposed *psize*/3 [25] throughout the experiments conducted and presented in this paper.

PARAMETER STUDIES

As mentioned earlier, the proposed method performs the new updating strategy when the number of generations is greater than *psize*/4. The reason behind this strategy is that the statistics obtained during the beginning period are not reliable enough to capture the trend. In this section, empirical experiments are presented to explain why we set this parameter as *psize*/4. The algorithm on 4 benchmark problems, viz. 100-bits One-Max, 100-bits Random Max, 64-bits Royal Road and ten copies of 3-bits Trap problems, were tested. The characteristics of the four problems are explained below.

The One-Max problem is quite simple. The objective is to find the solution which is a bit string whose bits are all one. The fitness value is equal to the number of 1-bits in the bit string. The Random Max problem is similar to the One-Max problem in finding a bit-string solution whose bit pattern is exactly the same as the one of the target. However, instead of being all one, the target bit pattern is selected randomly. Obtained by comparing bit by bit, the fitness value is the number of bits equal to the associated ones of the target. Notice that this problem is designed to determine whether an algorithm is biased against one or zero.

The Royal Road is a group of bit patterns built up from sequences of short bit patterns. The bit pattern is called schema. There are 15 schemas for 64-bits royal road as shown in Figure 4. After comparing the bit string with each schema, the fitness value is calculated by summing up the numbers of bits equal to those of s_i for all i. For example, a fitness value of a bit string that contains all one (the optimum solution) is $(8 \times 8) + (4 \times 16) + (2 \times 32) + 64 = 256$.

The Trap problem is one of many difficult problems used for testing GAs. It is designed to fool gradient-based optimisers that favour zeroes, but the optimal solution is composed of all 1-bits. We can create a $k \times m$ Trap problem by combining the m groups of a k-bits trap. The fitness value is calculated by summing up the scores associated with all groups. For instance, a 3-bit Trap problem

gives a score of 3, 0, 1 and 2 for a group of three, two, one and zero 1-bits respectively. For example, a candidate solution '111 001 110 000 100' has a fitness value of 3 + 1 + 0 + 2 + 1 = 7.

Schema 1 = 11111111**********; $s1 = 8$
Schema 2 = ********11111111**********; $s2 = 8$
Schema 3 = ****************11111111**********; $s3 = 8$
Schema 4 = ************************11111111**********; $s4 = 8$
Schema 5 = ********************************11111111**********; $s5 = 8$
Schema 6 = **11111111**********; $s6 = 8$
Schema 7 = **11111111********; $s7 = 8$
Schema 8 = **11111111; $s8 = 8$
Schema 9 = 1111111111111111**********; $s9 = 16$
Schema10 =****************1111111111111111**********; $s10 = 16$
Schema11 =********************************1111111111111111**********; $s11 = 16$
Schema12 =**1111111111111111; $s12 = 16$
Schema13 =11111111111111111111111111111111**********; $s13 = 32$
Schema14 =********************************11111111111111111111111111111111; $s14 = 32$
Schema15 =1111111111111111111111111111111111111111111111111111111111111111; $s15 = 64$

Figure 4. Royal Road problem

We ran the proposed algorithm with all benchmark problems described above. For each tournament size of 2, 4 and 8, the parameter was varied among *psize*/2, *psize*/3, *psize*/4 and *psize*/5. The results shown in Table 1 are efficiency ratios [= (solution quality / number of evaluations) × 1000]. The efficiency ratio is used as a quantitative measurement to quantify a quality rate: the higher the rate, the better the efficiency. When the value of *n* is varied from 2 to 4, the efficiency ratio is better when *n* is large (4 or 5) in the case of solving the easy problems (i.e. One-Max and Random Max). For the harder but non-deceptive problem (i.e. Royal Road), a small value of *n* (2 or

Table 1. Efficiency ratio of varying tournament and population sizes in One-Max, Random Max, Royal Road and Trap problems

Problem		Efficiency ratio				Average
		One-Max	Random Max	Royal Road	Trap	
Tournament Size 2	*psize*/2	56.63	32.51	4.97	0.37	23.62
	psize/3	53.14	32.23	5.65	0.42	22.86
	psize/4	56.79	33.68	5.35	0.50	24.08
	psize/5	54.48	34.00	5.35	0.52	23.59
Tournament Size 4	*psize*/2	69.08	41.56	10.03	0.80	30.37
	psize/3	78.88	41.61	10.53	0.95	32.99
	psize/4	89.20	44.76	9.87	0.95	36.20
	psize/5	80.36	49.07	9.65	1.03	35.03
Tournament Size 8	*psize*/2	86.95	42.38	17.51	0.69	36.89
	psize/3	83.52	40.06	14.47	0.91	34.74
	psize/4	87.17	47.69	16.01	1.06	37.99
	psize/5	91.19	47.28	14.03	1.15	38.42

3) yields a slightly better ratio. This can be interpreted that the proposed algorithm needs more time to collect more diverse and higher fitness-valued samples before increasing its updating step size. For the deceptive problem (i.e. Trap), the efficiency ratio tends to be relatively high when *n* is large. This is because in the Trap problem the fb-cGA cannot find a good solution no matter what parameters are ─ the fitness value might remain similar. Therefore, the efficiency depends on the number of fitness evaluations more than the fitness value. In terms of tournament size, a larger size tends to provide a larger efficiency ratio. Overall, almost all of the best quality rates come from *psize*/4 and *psize*/5 (highlighted in Table 1). The average rate of *psize*/4 from all problems and all sizes of the tournament is 32.76, and that of *psize*/5 is 32.35. The *psize*/4 is therefore more desirable in terms of efficiency.

As shown in Figure 5, the convergence graphs, obtained from the One-Max problem experiments (*psize* = 100), reflect the algorithm behaviour. The dash lines are plotted at the generation numbers equal to *psize*/*n* (x = *psize/n*), showing when the proposed updating strategy is triggered. If *n* is larger, the proposed strategy starts sooner. Passing this line, the algorithm updates the PV with a larger step size when the winner's bit conforms to the majority direction (i.e. meeting the condition on line 8 or 16 in Figure 3). As the graphs show, the fitness values gradually improve in the early generations (generation number < *psize*/*n*) but increase abruptly after the trigger. This behaviour explains why the algorithm's PV converges to a solution using fewer function evaluations.

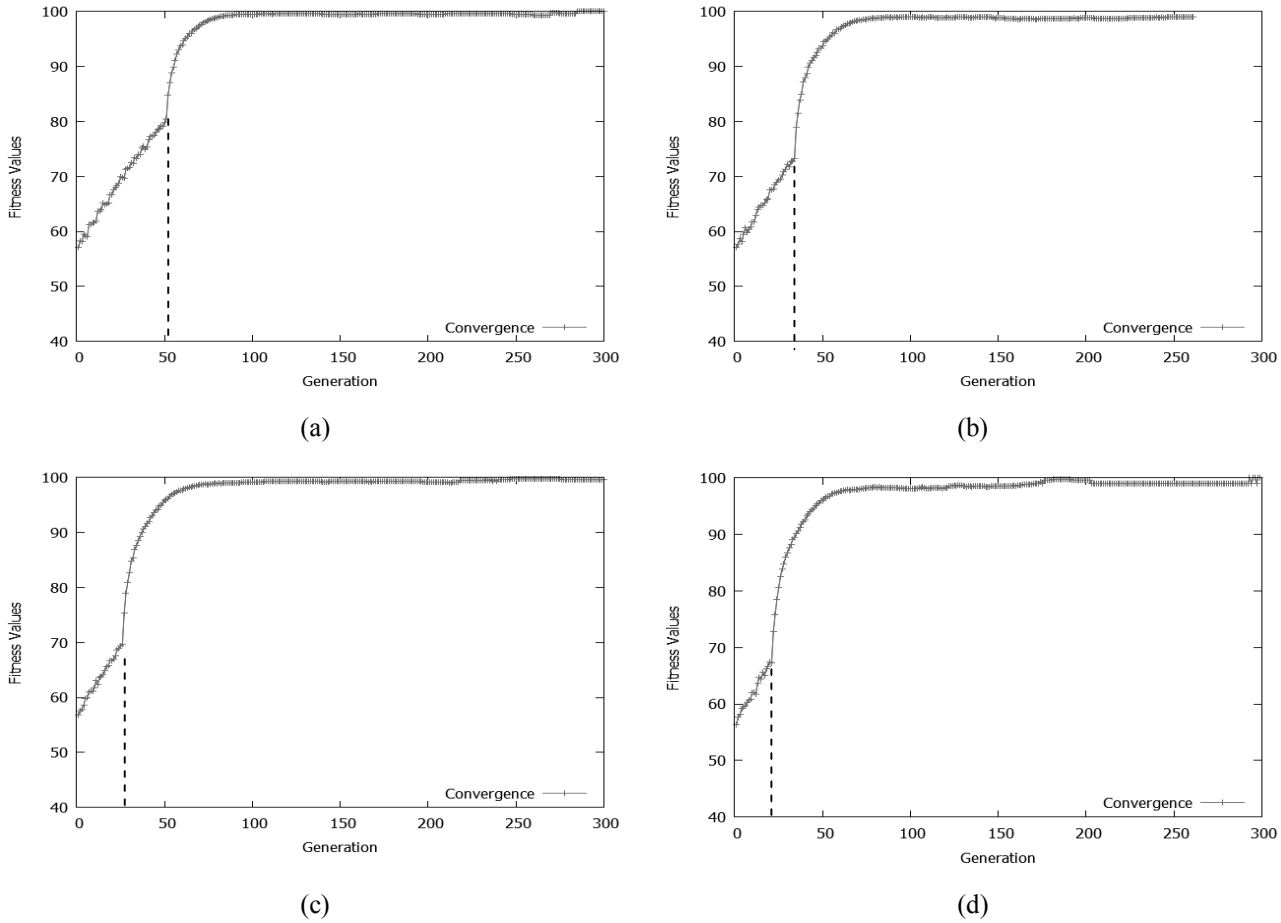

Figure 5. Convergence graphs of experiments with parameters: (a) psize/2, (b) psize/3, (c) psize/4 and (d) psize/5

PERFORMANCE COMPARISONS

At first, we tested all of the algorithms – sGA, cGA, mcGA, pe-cGA, ne-cGA and fb-cGA – with the 100-bit One-Max problem. Each graph in Figure 6 shows the results when the parameter *psize* (population size) varies between 4-100 with a step value of 8. All algorithms used the tournament size of 2. Each line shows an average result from 50 runs. In general, when the population size becomes larger, GAs take more function evaluations but yield better solutions.

Figure 6a shows that the solution quality (the numbers of correct bits) obtained from fb-cGA is comparable with those obtained from sGA, cGA and mcGA, while pe-cGA and ne-cGA have lower solution qualities. In terms of the number of function evaluations, Figure 6b shows that fb-cGA outperforms sGA, cGA and mcGA if the population size is large. When it is small (*psize* < 40), fb-cGA needs more function evaluations than do others. The example where *psize* is equal to 4 is used to explain this situation; the algorithm collects the statistics merely from one generation (*psize*/4 = 1) as a guide to update the PV with a large step size. The triggering time may be too early, leading the vector to a wrong direction. Consequently, the algorithm would spend more time (i.e. a larger number of function evaluations) searching before coming back to the right direction. Nevertheless, the number of fitness evaluations of fb-cGA does not increase as much as the population size and is comparable to those of pe-cGA and ne-cGA when the population size is 100.

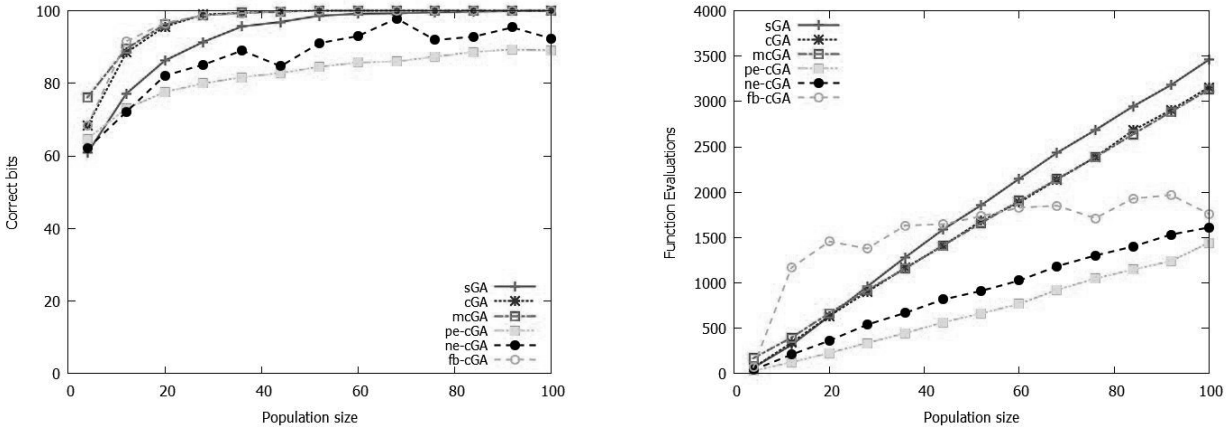

(a) Solution quality (b) Number of function evaluations

Figure 6. Correct bits and function evaluations (of all the algorithms) in One-Max problem

Figure 7 shows the performance of all the algorithms on the Random Max problem. The fb-cGA performance is moderate when compared with other techniques. It requires a large number of function evaluations to find the solution in the case of a small population, but when the population size increases the numbers of function evaluations tend to be comparable to those in cGA and mcGA.

Figure 8 shows the performance of all the algorithms on the Royal Road problem using tournament sizes of 2, 4 and 8. The number of population sizes varies between 4-100 with a step value of 8. Figures 8a, 8c and 8e show the solution quality in terms of fitness value. Figures 8b, 8d and 8f show the numbers of function evaluations. The fb-cGA yields comparable results in terms of solution quality with those from sGA, cGA and mcGA while requiring a much smaller number of function evaluations. When compared with ne-cGA in the case of tournament size of 2, fb-cGA has a higher fitness value than that of ne-cGA but requires more function evaluations. However, for

tournament sizes of 4 and 8, fb-cGA yields comparable fitness values with those of ne-cGA and needs fewer fitness evaluations. In this problem, pe-cGA requires the smallest number of function evaluations but yields lowest fitness values.

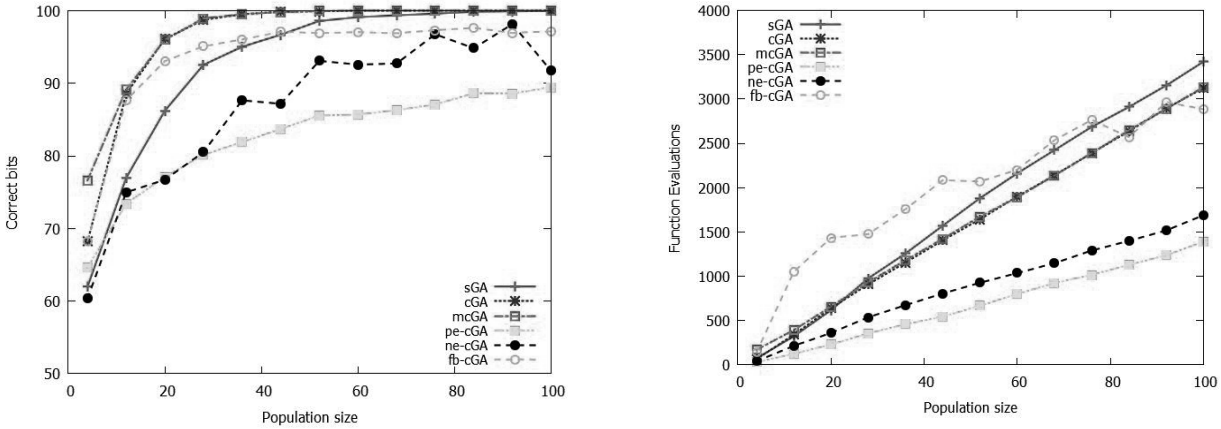

(a) Solution quality (b) Number of function evaluations

Figure 7. Correct bits and function evaluations (of all the algorithms) in Random Max problem

Figure 9 shows the algorithms' performance on the 3-Trap problem – the Trap problem with a group of 3 bits (k=3) – using tournament sizes of 2, 4 and 8, and population sizes of 8, 500, 1000, 1500, 2000, 2500 and 3000. Figures 9a, 9c and 9e show the solution quality in terms of the number of correct building blocks (the number of 3-bits blocks containing all 1-bits). Figures 9b, 9d and 9f show the numbers of function evaluations taken to find the solution. Figure 9a shows that the solution quality of fb-cGA is higher than that of sGA, cGA and mcGA, but lower than that of pe-cGA and ne-cGA. The fb-cGA requires the smallest number of function evaluations, using them approximately 14, 9, 12, 3 and 2 times fewer than do sGA, original cGA, mcGA, pe-cGA and ne-cGA respectively. This cofirms the efficiency of the proposed method in terms of the number of function evaluations saved.

ANALYSIS OF ALGORITHMS' CONVERGENCE AND BEHAVIOUR

The convergence analysis was carried out by using plots of the fitness values over time (generations). The behaviour analysis was performed through the graphic representation of all probability values in the PV from the first to the last generation to track how the probabilities change.

Figure 10 shows the fitness values and the probability values of cGA, mcGA, pe-cGA, ne-cGA and fb-cGA for the One-Max problem with tournament sizes of 2 and *psize* of 100. The graphs on the right show probability values in density of greyscale. Bearing in mind that the objective of the One-Max problem is to find a solution in which all bits are 1, all the shades representing probability values shown in the graphs on the right should fade to white (probability = 1) in the final generation.

The cGA, mcGA and fb-cGA can find the optimal solution (fitness value = 100), the ne-cGA yields a result very close to the optimal, while the pe-cGA's PV converges to one far from the optimal. The convergence graphs of cGA and mcGA are very similar. Their PV converges to the solution at nearly the same generation. However, the way in which the probabilities change is slightly different. The shades of mcGA fade quicker and more smoothly than do those of cGA. The

smooth change in the probability values of mcGA is in accordance with its updating rule in that the moving average approach waits to see the trend, thus slowing down the increase or decrease in the probability values.

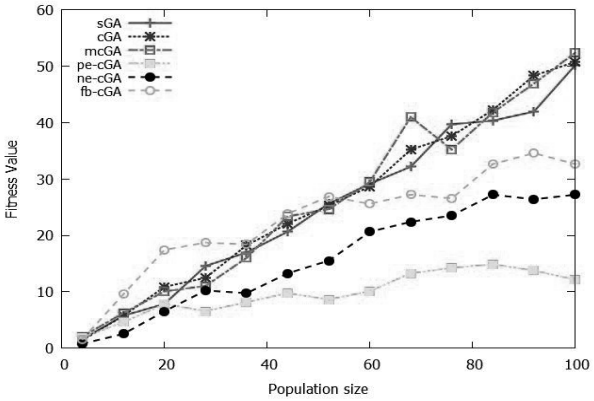

(a) Solution quality (tournament size 2)

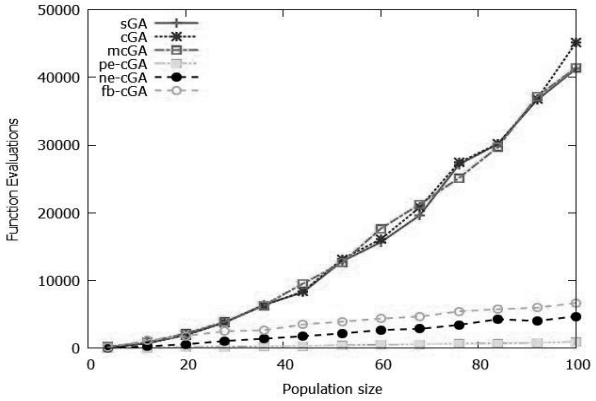

(b) Number of function evaluations (tournament size 2)

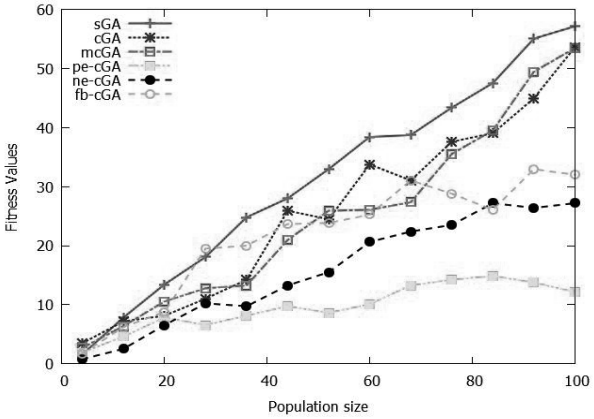

(c) Solution quality (tournament size 4)

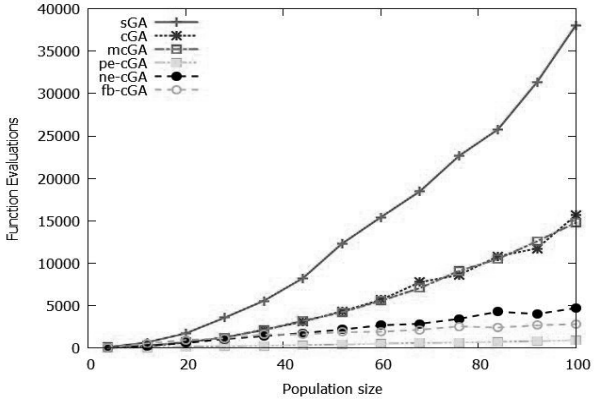

(d) Number of function evaluations (tournament size 4)

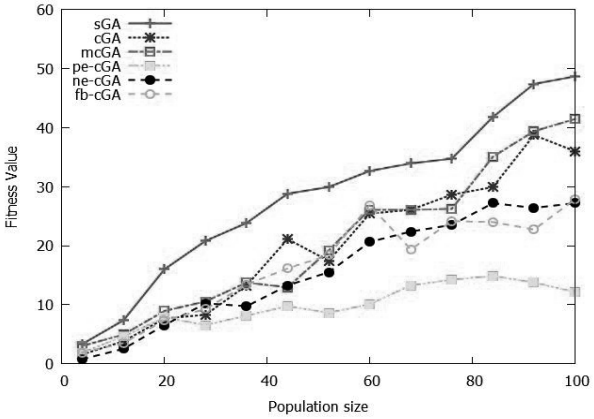

(e) Solution quality (tournament size 8)

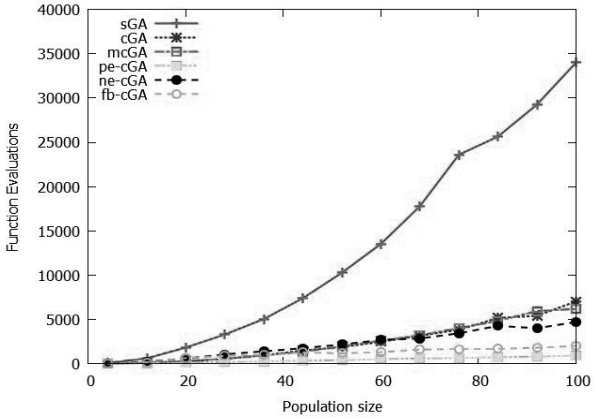

(f) Number of function evaluations (tournament size 8)

Figure 8. Fitness values and function evaluations (of all the algorithms) in Royal Road problem

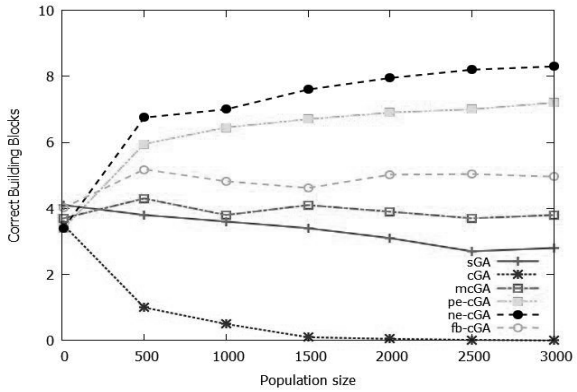

(a) Solution quality (tournament size 2)

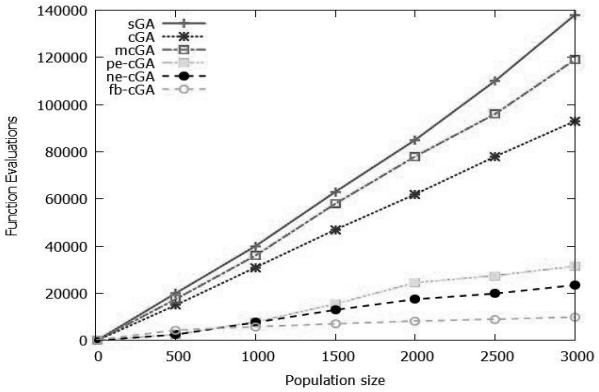

(b) Number of function evaluations (tournament size 2)

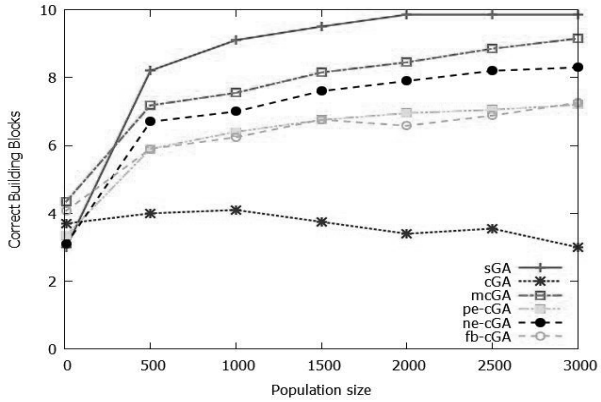

(c) Solution quality (tournament size 4)

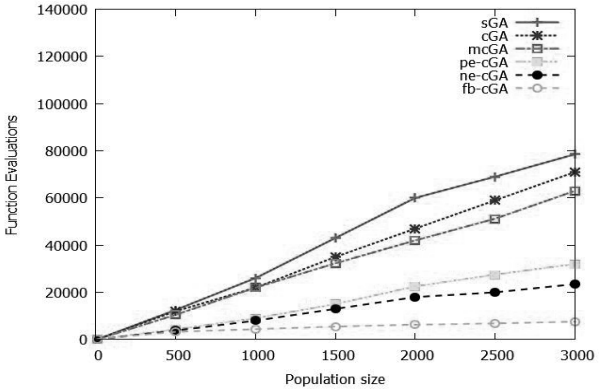

(d) Number of function evaluations (tournament size 4)

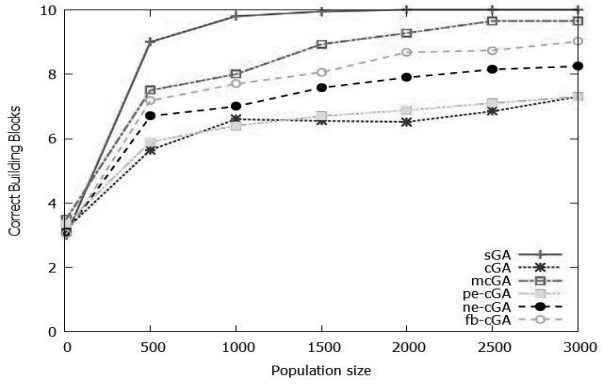

(e) Solution quality (tournament size 8)

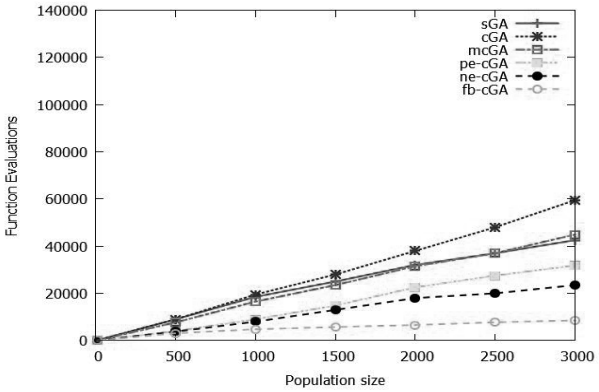

(f) Number of function evaluations (tournament size 8)

Figure 9. Correct building blocks and function evaluations (of all the algorithms) in Trap problem

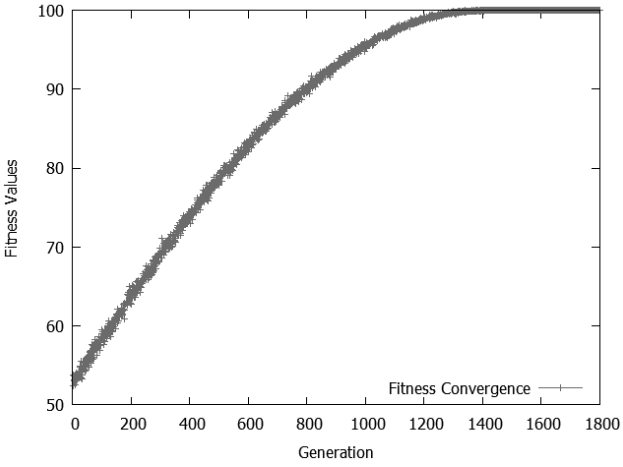

(a) Convergence of fitness values (cGA)

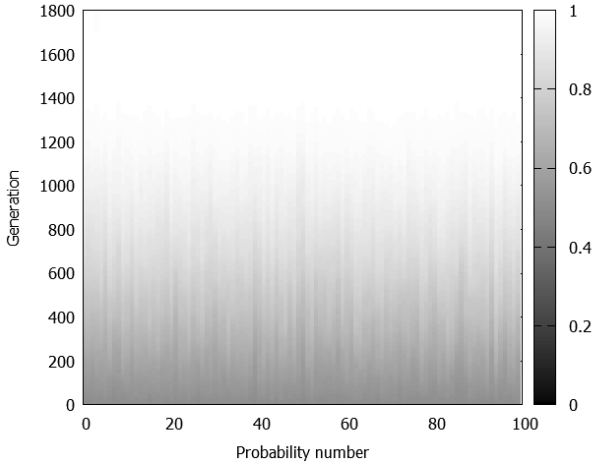

(b) 100 probability values of probability vector (cGA)

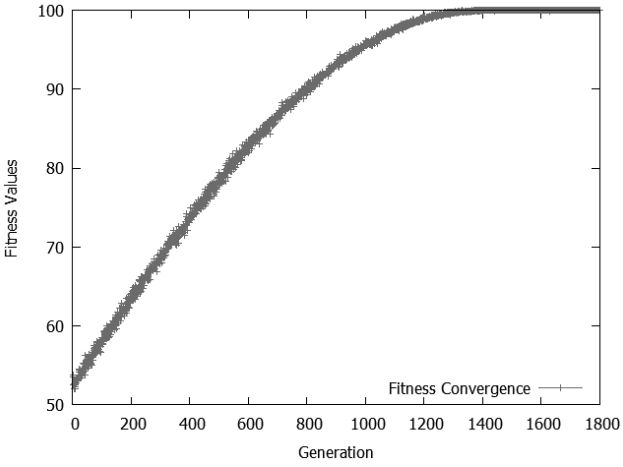

(c) Convergence of fitness values (mcGA)

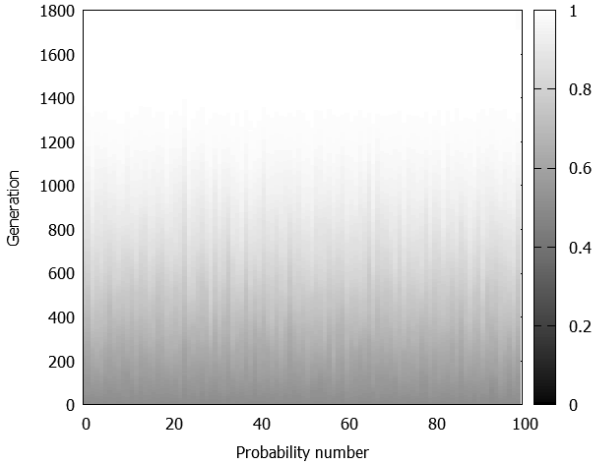

(d) 100 probability values of probability vector (mcGA)

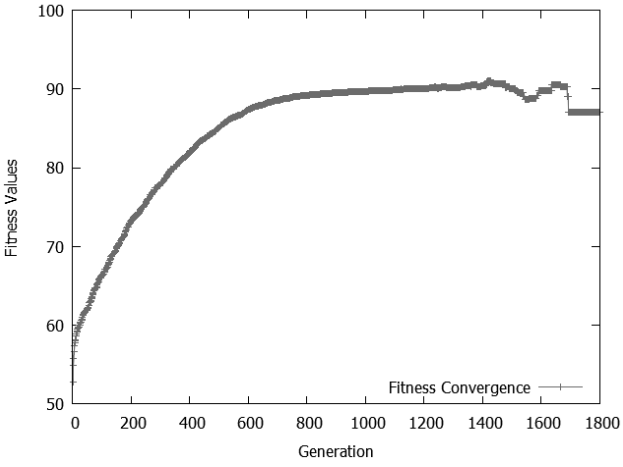

(e) Convergence of fitness values (pe-cGA)

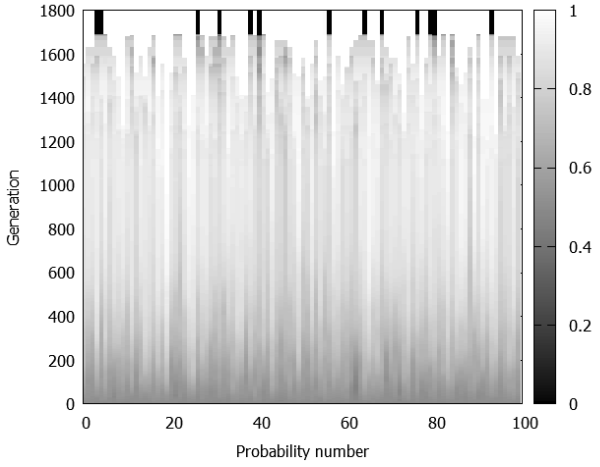

(f) 100 probability values of probability vector (pe-cGA)

Figure 10. Convergence of fitness values and change in 100 probability values in the probability vectors at each generation. Darker shading represents the probability closer to 0 while white represents the probability of 1. All probabilities are initialised to 0.5. All plots show the average values from 50 runs.

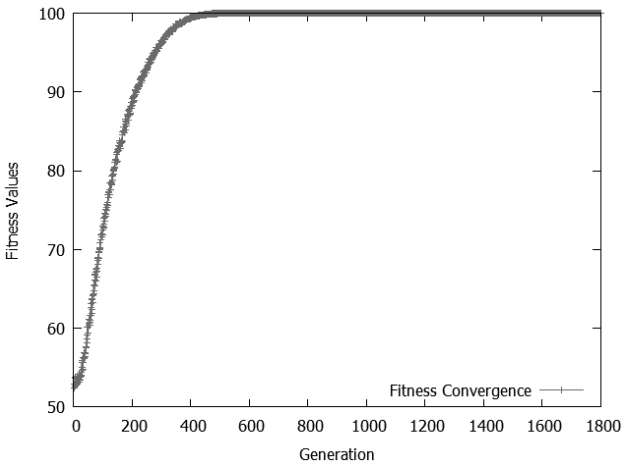

(i) Convergence (fb-cGA)

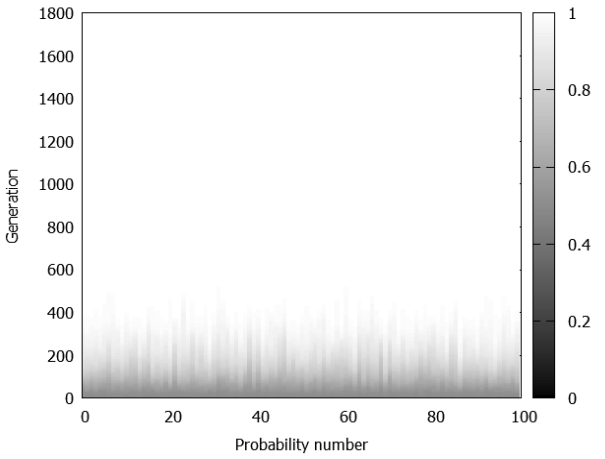

(j) Probability (fb-cGA)

Figure 10 (continued). The convergence and probability analysis

Both the pe-cGA's and ne-cGA's shades turn light grey faster than do the cGA's and mcGA's, as shown in the early generations of Figures 10f and 10h. However, the pe-cGA's final PV is unfavourable and the ne-cGA's approaches, but does not quite reach, the optimum. This is characteristic of elitism. The elite (the best solution so far) often contains zero bits in the chromosome, which deceives the algorithm into updating the probability towards zero. In the case where newly generated candidate solutions are worse than the elite, the PV is updated towards the elite again and the probability at the associated position may come closer to zero. This situation may lead the elitism-based algorithms to update the PV towards the wrong direction. Elitism affects the pe-cGA's performance more than the ne-cGA's due to its everlasting elite.

The fb-cGA's PV converges to the solution faster than the other algorithms (Figure 10i). The shade representing probability values in Figure 10j turns white in a small number of generations. To efficiently apply our proposed technique to a real-world problem, the chromosome should have all of its bits uncorrelated with one another. It is important to realise that the fb-cGA evolves its PV by updating all associated probabilities of all bits. The update is done only one bit at a time without taking into account the information of the other bits. The results of One-Max problem shown in Figure 10 serve as an example that supports this claim: fb-cGA can solve the problem using far fewer number of generations (approximately 400, instead of about 1300 generations required by the traditional cGA). This significant outperformance stems from the new dynamic updating strategy: the proposed technique decides to update the probabilities with a larger step size based on the collected statistics. However, if the chromosome bits of the real-world problem are correlated with one another, the proposed algorithm might not find the best solution, as shown in the Royal Road and the Trap problem.

For a real-world optimisation problem that has multiple local optima, there is a higher chance that the fb-cGA may get stuck at a local optimum. For example, in the field of computational vision, efficient algorithms such as cGA may be used to recognise objects in an image. However, if the input image is complex, it might introduce various local optima in the search space. Because fb-cGA uses a trend in early generations to quickly decide to update PV with a larger updating step size, it might prematurely decide to search towards a seemingly promising direction at a certain time. Once the proposed algorithm gets stuck, it is hard to escape from the local optimum because it already has a strong bias in favour of either zero or one. To handle this kind of problem, we should wait longer to

see a correct trend before using a large step size. In addition, the step size should be incrementally increased during the evolution.

CONCLUSIONS

This paper presents a behaviour analysis of fb-cGA. To update the PV, the fb-cGA collects and utilises the update number of each probability in both up and down directions. The numbers of updates are used to adjust probability-updating step sizes, turning the vector towards the promising direction faster. When the effect of parameter *psize*/*n* on the algorithm performance was investigated, the results suggested that the newly proposed updating strategy should be used when the generation number is greater than *psize*/4. The analysis, through graphic representation of all probabilities from the first to the last generation, shows that the fb-cGA updates the PVs towards the solution quicker than the other algorithms and also requires fewer function evaluations.

ACKNOWLEDGEMENTS

This work was funded by Thailand Research Fund, the Office of Higher Education Commission and the Faculty of Informatics, Burapha University (Grant No. TRG5680073). We also thank our mentor, Prof. Prabhas Chongstitvatana, for his guidance, support and encouragement.

REFERENCES

1. G. R. Harik, F. G. Lobo and D. E. Goldberg, "The compact genetic algorithm", *IEEE Trans. Evol. Comput.*, **1999**, *3*, 287-297.
2. M. H. Afshar, "Application of a compact genetic algorithm to pipe network optimization problems", *Transact. A*: *Civil Eng.*, **2009**, *16*, 264-271.
3. R. D. Al-Dabbagh, M. S. Baba, S. Mekhilef and A. Kinsheel, "The compact genetic algorithm for likelihood estimator of first order moving average model", Proceedings of 2nd International Conference on Digital Information and Communication Technology and Its Applications, **2012**, Bangkok, Thailand, pp.474-481.
4. R. D. Al-Dabbagh, A. Kinsheel, M. S. Baba and S. Mekhilef, "An integration of compact genetic algorithm and local search method for optimizing ARMA (1, 1) model of likelihood estimator", Proceedings of 2nd International Conference on Computer Science and Computational Mathematics, **2013**, Kuala Lumpur, Malaysia, pp.60-67.
5. C. F. M. Toledo, M. S. Arantes, R. R. R. Oliveira and A. C. B. Delbem, "A hybrid compact genetic algorithm applied to the multi-level capacitated lot sizing problem", Proceedings of 28th Annual ACM Symposium on Applied Computing, **2013**, Coimbra, Portugal, pp.200-205.
6. R. R. Silva, H. S. Lopes and C. R. E. Lima, "A compact genetic algorithm with elitism and mutation applied to image recognition", *Lect. Notes Comput. Sci.*, **2008**, *5227*, 1109-1116.
7. P. Olarthichachart, S. Kaitwanidvilai and S. Karnprachar, "Trip frequency scheduling for traffic transportation management based on compact genetic algorithm", Proceedings of International MultiConference of Engineers and Computer Scientists, **2010**, Hong Kong, pp.1072-1074.
8. R. D. H. Al-Dabbagh, "Compact genetic algorithm for cryptanalysis trapdoor 0-1 knapsack cipher", *J. Al-Nahrain Univ.*, **2009**, *12*, 137-145.
9. A. Azouaoui, A. Berkani and M. Belkasmi, "An efficient soft decoder of block codes based on compact genetic algorithm", *Int. J. Comput. Sci. Iss.*, **2012**, *9*, 431-438.
10. H. Xing and R. Qu, "A compact genetic algorithm for the network coding based resource minimization problem", *Appl. Intell.*, **2012**, *36*, 809-823.

11. P. Gupta and R. Tiwari, "Solving three dimensional bin packing problem using elitism based genetic algorithm", *Int. J. Adv. Res. Comput. Eng. Technol.*, **2012**, *1*, 471-475.
12. P. K. Singh and N. Sahu, "Task scheduling in grid computing environment using compact genetic algorithm", *Int. J. Sci. Eng. Technol. Res.*, **2014**, *3*, 107-110.
13. Y. C. Huang, C. F. Chang, C. H. Chan, T. J. Yeh, Y. C. Chang, C. C. Chen and C. Y. Kao, "Integrated minimum-set primers and unique probe design algorithms for differential detection on symptom-related pathogens", *Bioinformatics*, **2005**, *21*, 4330-4337.
14. A. Bade, I. M. Aref, B. M. Hussien and Y. Eman, "Solving protein folding problem using elitism-based compact genetic algorithm", *J. Comput. Sci.*, **2008**, *4*, 525-529.
15. C. Aporntewan and P. Chongstitvatana, "A hardware implementation of the compact genetic algorithm", Proceedings of IEEE Congress on Evolutionary Computation, **2001**, Seoul, Korea, pp.624-629.
16. J. C. Gallagher and S. Vigraham, "A modified compact genetic algorithm for the intrinsic evolution of continuous time recurrent neural networks", Proceedings of Genetic and Evolutionary Computation Conference, **2002**, New York, USA, pp.163-170.
17. J. C. Gallagher, S. Vigraham and G. Kramer, "A family of compact genetic algorithms for intrinsic evolvable hardware", *IEEE Trans. Evol. Comput.*, **2004**, *8*, 111-126.
18. K. M. Timmerman, "A hardware compact genetic algorithm for hover improvement in an insect-scale flapping-wing micro air vehicle", *Master Thesis*, **2012**, Wright State University, USA.
19. C. Zhou, K. Meng and Z. Qiu, "Compact genetic algorithm mutated by bit", Proceedings of 4th World Congress on Intelligent Control and Automation, **2002**, Shanghai, China, pp.1836-1839.
20. B. V. Ha, R. E. Zich, M. Mussetta, P. Pirinoli and C. N. Dao, "Improved compact genetic algorithm for EM complex system design", Proceedings of 4th International Conference on Communications and Electronics, **2012**, Hue, Vietnam, pp.381-392.
21. S. Rimcharoen, D. Sutivong and P. Chongstitvatana, "Updating strategy in compact genetic algorithm using moving average approach", Proceedings of IEEE Conference on Cybernetics and Intelligent Systems, **2006**, Bangkok, Thailand, pp.690-695.
22. C. W. Ahn and R. S. Ramakrishna, "Elitism-based compact genetic algorithms", *IEEE Trans. Evol. Comput.*, **2003**, *7*, 367-385.
23. J. Y. Lee, S. M. Im and J. J. Lee, "Bayesian network-based non-parametric compact genetic algorithm", Proceedings of 6th IEEE International Conference on Industrial Informatics, **2008**, Daejeon, Korea, pp.359-364.
24. J. Y. Lee, M. S. Kim and J. J. Lee, "Compact genetic algorithms using belief vectors", *Appl. Soft Comput.*, **2011**, *11*, 3385-3401.
25. S. Phiromlap and S. Rimcharoen, "A frequency-based updating strategy in compact genetic algorithm", Proceedings of International Computer Science and Engineering Conference, **2013**, Nakorn Pathom, Thailand, pp.207-211.